GEOWISSENSCHAFTLICHE MITTEILUNGEN

Heft Nr. 84, 2009

Kombination geodätischer Weltraumverfahren
für globale Karten der Ionosphäre

Sonya Todorova

Veröffentlichung
des Instituts für Geodäsie und Geophysik

Diese Arbeit wurde an der Fakultät für Mathematik und Geoinformation der Technischen Universität Wien zur Erlangung des akademischen Grades eines Doktors der technischen Wissenschaften eingereicht.

Begutachter:

Prof.Dr.-Ing. Harald Schuh
Institut für Geodäsie und Geophysik der Technischen Universität Wien
Gushausstrasse 27-29, A-1040 Wien, Österreich

Assoc. Prof. Dr. Manuel Hernandez-Pajares
Dept. of Applied Mathematics IV
Group of Astronomy and Geomatics (gAGE/UPC)
Technical University of Catalonia
Barcelona, Spain

Tag der mündlichen Prüfung: 21.04.2008

Abstract

In the last two decades rapid changes have occurred in modern space geodesy by the implementation of new observation techniques and the significant improvement of the existing methods. This creates the objective of integrating the results derived by the different geodetic techniques and methods in order to achieve a better understanding of the processes in the System Earth as a whole. Following this global objective in geodetic science, the thesis aims at the development of an integrated two-dimensional model of the upper part of the Earth's atmosphere, the ionosphere, by using and combining different space geodetic data, in particular observations derived by the Global Navigation Satellite System (GNSS) and by satellite altimetry missions operating at two distinct frequencies, such as Topex/Poseidon and Jason-1. Both geodetic techniques allow the observation and modelling of the ionosphere, but each of them has its specific characteristics which influence the derived ionosphere parameters. The classical input data for development of Global Ionosphere Maps (GIM) of the Total Electron Content (TEC) is obtained from dual-frequency GNSS observations. Such maps in general achieve good quality of the ionosphere representation. However, the GNSS stations are inhomogeneously distributed, with large gaps particularly over the sea surface, which lowers the precision of the GIM over these areas. On the other hand, the dual-frequency satellite altimetry missions provide information about the parameter of the ionosphere precisely above the sea surface, where the altimetry observations are performed. Due to the limited spread of the measurements and some open issues related to systematic errors, the ionospheric data from satellite altimetry is used only for cross-validation of the GNSS GIM. However, some specifics of the ionosphere parameters derived by satellite altimetry can partly balance the inhomogeneity of the GNSS data. Such important features are complementing the global coverage, different biasing and the absence of additional mapping, as it is the case with GNSS. The combination of ionosphere parameter on normal equation basis presented within the thesis allows making best use of the advantages of every particular method, providing a more homogeneous global coverage and higher accuracy and reliability than the results of each single technique.

Zusammenfassung

Die Einführung neuer Beobachtungstechniken und die signifikante Optimierung der bestehenden Methoden haben in den letzten zwei Dekaden eine rapide Entwicklung der modernen Weltraumgeodäsie hervorgerufen. Somit wurde auch eine neue Zielsetzung angelegt - die Integration der Resultate verschiedener geodätischen Techniken und Methoden, um die Prozesse im System Erde als Ganzes besser zu erfassen. Diese globale Zielsetzung in der modernen Geodäsie folgend, wird in dieser Dissertation ein kombiniertes zwei-dimensionales Modell des oberen Teils der Erdatmosphäre, die Ionosphäre, entwickelt. Dabei werden Daten aus verschiedenen geodätischen Weltraumverfahren herangezogen und kombiniert, insbesondere Beobachtungen des Globalen Satellitengestützten Navigationssystems (GNSS) und Messungen von Satellitenaltimetrie-Missionen, die auf zwei Frequenzen operieren, wie Topex/Poseidon und Jason-1. Beide oben genannten Weltraumverfahren erlauben die Beobachtung und Modellierung der Ionosphäre. Sie zeichnen sich aber durch spezifische Charakteristiken aus, die Einfluss auf die erhaltenen Ionosphärenparameter haben. Die klassischen Einganswerte für die Entwicklung Globaler Ionosphärenkarten (Global Ionosphere Maps, GIM) des Totalen Elektronengehalts (Total Electron Content, TEC) werden von Zweifrequenz GNSS Beobachtungen gewonnen. Solche Karten gewährleisten im Allgemeinen gute Qualität der Ionosphärenrepräsentierung. Jedoch ist die Verteilung der GNSS Stationen nicht homogen, mit großen Lücken vor allem über den Ozeanen, was zur Verringerung der GIM Genauigkeit in diesen Regionen führt. Ihrerseits liefern Zweifrequenz Satellitenaltimetrie-Missionen Information über die Ionosphärenparameter ausschlielich über der Meeresoberfläche, wo die Beobachtungen durchgeführt werden. Aufgrund der begrenzten Spannweite der Messungen und einigen offenen Fragen bezüglich der systematischen Fehler, wird die Ionosphäreninformation aus Satellitenaltimetrie nur zur Vergleichsprüfung der GNSS GIM eingesetzt. Allerdings können bestimmte Besonderheiten der aus Satellitenaltimetrie gelieferten Ionosphärenparameter die Inhomogenität der GNSS Daten ausbalancieren. Solche wichtigen Eigenschaften sind das Komplementieren der globalen Abdeckung, die unterschiedliche systematische Fehlerbehaftung und das Fehlen zusätzlichen Mappings, wie im Falle von GNSS. Die Kombination von Ionosphärenparametern auf Normalgleichungsebene, die in dieser Arbeit durchgeführt wird, ermöglicht es, die Vorteile jedes einzelnen Verfahrens am Besten auszunutzen und somit eine homogenere globale Abdeckung, höhere Genauigkeit und Zuverlässigkeit der GIM zu erreichen.

Contents

List of Figures

List of Tables

Acronyms

AAC	Associate Analysis Center
ADS	Altimeter Database System
AIUB	Astronomical Institute of the University of Berne, Switzerland
BIPM	International Bureau of Weights and Measures
C/A-code	Coarse/Acquisition code (1.023 MHz)
CDDIS	Crustal Dynamics Data Information System
CDMA	Code Division Multiple Access
CGNC	Coast Guard Navigation Center, USA
CHAMP	Challenging Minisatellite Payload
CNES	Centre National d'Etudes Spatiales
CPAR	Centre for RF Propagation and Atmospheric Research
CODE	Center for Orbit Determination in Europe, AIUB, Berne, Switzerland
COSMIC	Constellation Observing System for Meteorology, Ionosphere and Climate
DCB	Differential Code Bias
DORIS	Doppler Orbitography and Radiopositioning Integrated by Satellite
DOY	Day Of Year
ESA	European Space Agency, Darmstadt, Germany
EU	European Union
FDMA	Frequency Division Multiple Access
FORMOSAT-3	Formosa Satellite 3
FTP	File Transfer Protocol
GFZ	GeoForschungsZentrum, Potsdam, Germany
GGOS	Global Geodetic Observing System
GIM	Global Ionosphere Map
GLONASS	GLObal NAvigation Satellite System
GNSS	Global Navigation Satellite System
GOCE	Gravity Field and Steady State Ocean Circulation Explorer
GOLPE	GPS Occultation and Passive Reflection Experiment
GPS	Global Positioning System
GPSTk	GPS Toolkit
GRACE	Gravity Recovery and Climate Experiment
GSFC	Goddard Space Flight Center, USA
IAC	Information-Analytical Center
IAG	International Association of Geodesy
ICD	Interface Control Document
IDS	International DORIS Service
IERS	International Earth Rotation Service

IGEX	International GLONASS Experiment
IGG	Institute of Geodesy and Geophysics
IGRF	International Geomagnetic Reference Field
IGS	International GNSS Service
IONEX	IONosphere Map EXchange Format
IRI	International Reference Ionosphere
ITRF	International Terrestrial Reference Frame
IVS	International VLBI Service for Geodesy and Astrometry
JOE	Jason-1 Offset Estimate
JPL	Jet Propulsion Laboratory, Pasadena, California, USA
L1	L1 carrier (1575.42 MHz)
L2	L2 carrier (1227.60 MHz)
LC	Linear Combination
LEO	Low Earth Orbiter
LSTID	Large-Scale Travelling Ionospheric Disturbance
MSLM	Modified Single Layer Model
MSTID	Medium-Scale Travelling Ionospheric Disturbance
NASA	National Aeronautics and Space Administration, USA
NSO	National Solar Observatory, USA
P-code	Precision code (10.23 MHz)
PRN	Pseudo-Random Noise
RF	Radio Frequency
RINEX	Receiver INdependent EXchange format
RMS	Root Mean Square
SAC-C	Satelite de Aplicanciones Cientificas-C
SCC	System Control Centre
SH	Spherical Harmonic
SLM	Single Layer Model
SLR	Satellite Laser Ranging
SOPAC	Scripps Orbit and Permanent Array Center
SPDIR	Space Physics Interactive Data Resource
SPP	Single-Point Positioning
SSB	Sea State Bias
SSH	Sea Surface Height
SSTID	Small-Scale Travelling Ionospheric Disturbance
STEC	Slant Total Electron Content
SWH	Significant Wave Height
TAI	International Atomic Time (from French: Temps Atomique International)
TEC	Total Electron Content
TECU	Total Electron Content Unit/s
TID	Travelling Ionospheric Disturbance
T/P	Topex/Poseidon
UCAR	University Corporation for Atmospheric Research
UPC	Polytechnical University of Catalonia, Barcelona, Spain
UT	Universal Time
UTC	Coordinated Universal Time
VLBI	Very Long Baseline Interferometry

VTEC	Vertical Total Electron Content
WG	Working Group
WGS-84	World Geodetic System 1984

Chapter 1

Introduction and motivation

In the last two decades rapid changes have occurred in space geodesy by implementing new observation techniques and significantly improving the existing methods. The modern space geodetic techniques, such as the Global Navigation Satellite System (GNSS), Low Earth Orbiters (LEOs), Very Long Baseline Interferometry (VLBI), and others (see Figure 1.1) find various applications for a wide range of commercial and scientific purposes. Some of the basic uses of satellite geodesy are the navigation and positioning of vehicles and persons, as well as in civil engineering. From scientific point of view, the space geodetic techniques are an irreplaceable tool for global monitoring of the complex processes in the System Earth.
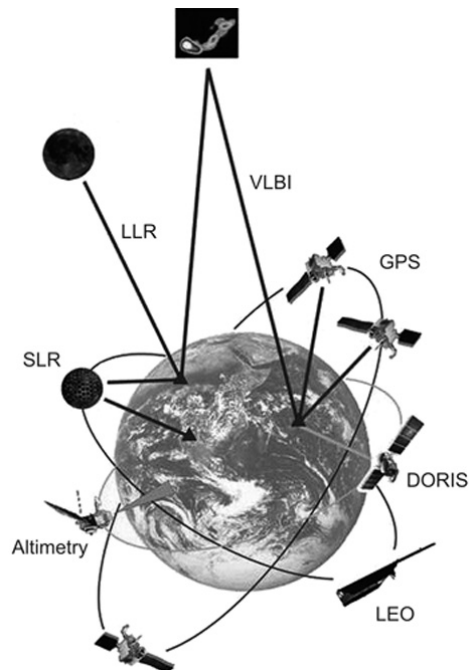
Figure 1.1: Space geodetic techniques (source: GGOS, 2007)

The steady increase in using space geodesy rises the demand for achieving the highest possible accuracy and reliability of the results. On the one hand, this can be done by technical improvement of the measuring and processing instruments. On the other, the optimisation of

the error sources modelling can significantly reduce the error budget. The integration of the results derived by different geodetic techniques and methods gives the possibility to account better for the different error sources and also enables an improved understanding of the processes in the System Earth as a whole. For this purpose, a special project was established in 2003 within the IAG (International Association of Geodesy). The main vision of the project, named Global Geodetic Observing System (GGOS, 2007), is: "GGOS integrates different geodetic techniques, different models, different approaches in order to ensure a long-term monitoring of the geodetic observables in agreement with the Integrated Global Observing Strategy (IGOS)."

Following this global objective in geodetic science, this dissertation aims at the development of an integrated model of the upper part of the Earth's atmosphere, the ionosphere, by using and combining different space geodetic data. Several geodetic techniques allow the observation and modelling of the ionosphere, but each of them has its specific characteristics which influence the derived ionosphere parameters. The combined model should make best use of the advantages of every particular method, have a more homogeneous global coverage and be more accurate and reliable than the results of each single technique.

The ionosphere is the part of the upper atmosphere where the density of free electrons and ions is high enough to influence the propagation of electromagnetic radio frequency waves (Hargreaves, 1992). The ionosphere extends to a height of over 1000 km above the Earth's surface, starting from about 50 to 90 km for day and night, respectively. It is a dispersive medium for the observables of all space geodetic techniques operating in the microwave band and affects both, their group and phase velocity. The effect is known as ionospheric refraction (Hartmann & Leitinger, 1984). It has to be considered in the determination of the propagation velocity of the signals of all space geodetic techniques operating with electromagnetic waves. Therefore, the measurements of nearly all space geodetic techniques operating with electromagnetic waves are carried out at two different radio frequencies. This allows the ionospheric influence, which in extreme cases can cause a signal path delay of several hundreds of meters, to be eliminated by linear combinations of the observations. On the other hand, in this way information about the ionosphere parameters can be obtained. If the behaviour of the ionosphere is known, the ionospheric refraction can be computed and global and regional models of the ionosphere can be developed.

For many of the commercial and scientific applications in the navigation and positioning field single frequency measurements are used. For them an accurate and reliable ionosphere model is essential. Furthermore, the technique specific instrumental offsets influencing the different measurements are of a high importance for the geodetic community and are obtained as a by-product when estimating global ionosphere parameters. The theoretical models of the ionosphere, such as the International Reference Ionosphere (IRI), are permanently updated by integration of real observations. The involvement of precise empirical results improves the theoretical models towards a higher temporal and spatial resolution and increases their accuracy. Theoretical models are widely used in radio science and for climate and plasma studies as well as from civil users (drivers, tourists), for aviation and marine navigation. Generally, a better understanding of the ionosphere, which is the main goal of this study, is fundamental for all studies of the upper atmosphere and the solar-terrestrial environment.

Information about the parameters of the ionosphere can be derived from the following space geodetic techniques:

- the Global Navigation Satellite System (GNSS), including the Global Positioning System (GPS), the GLObal NAvigation Satellite System (GLONASS), and with Europe's global navigation satellite system Galileo coming;

- satellite altimetry missions like TOPEX/Poseidon and Jason-1;

- Very Long Baseline Interferometry (VLBI);

- Doppler Orbitography and Radiopositioning Integrated by Satellite (DORIS);

- Low Earth Orbit Satellites (LEOs), e.g. FORMOSAT-3/COSMIC, CHAMP, GRACE.

The different observation principles of these techniques result in specific features of the ionosphere parameters derived by each of them. As a first step towards a common ionospheric model, the present work concentrates on investigating and combining ionosphere data from GNSS and satellite altimetry.

So far, the classical input data for the development of Global Ionosphere Maps (GIM) is obtained from dual-frequency GNSS observations. However, the GNSS stations are inhomogeneously distributed with large gaps particularly over the sea surface, which lowers the precision of the GIM over these areas. On their part, dual-frequency satellite altimetry missions such as Jason-1 provide information about the ionosphere precisely above the sea surface. Yet, due to the limited spread of the measurements and some open questions related to their systematic errors, the ionospheric data from satellite altimetry is used only for cross-validation of the GNSS GIM. It can be anticipated however, that some specifics of the ionosphere parameters derived by satellite altimetry will partly balance the inhomogeneity of the GNSS data. In this work two-hourly GIM from GNSS data are created and additionally satellite altimetry observations are introduced, which help to compensate the insufficient GNSS coverage of the oceans. Furthermore, the combination method allows the independent estimation of systematic instrumental errors, affecting both types of measurements. Thus, besides the daily values of the Differential Code Biases (DCB) for all GNSS satellites and receivers, also a constant daily offset of the altimetry satellites is estimated and investigated.

For a better overview of the subsequent chapters, a brief outline of each of them will be given:

Chapter 2: *Basic concepts*

This chapter overviews the basic theoretical background for ionospheric research, giving a short overview of the main processes in the Earth's ionosphere and their spatial and temporal dynamics. Since the dissertation deals with the ionosphere as an affecting factor for the signals of various space geodetic techniques, the wave propagation in this medium is also concerned with. In particular, the impact of the ionosphere on electromagnetic waves is regarded. The second part of the chapter describes the Single Layer Model and mapping function, which are used for ionosphere modelling in this work, as well as the spherical harmonics utilised for global representation of the Total Electron Content (TEC).

Chapter 3: *Ionospheric information from different space geodetic techniques*

The chapter is divided in three parts, focusing on GNSS, satellite altimetry, and several other space geodetic techniques, as sources of information about the ionosphere. It introduces the satellite positioning systems GPS and GLONASS, giving an overview of their historical development, current status, and future. The impact of the ionosphere on the observables of the two systems is reviewed and, consequently, the way for extracting ionosphere parameters from GPS and GLONASS measurements. Similarly, the second part deals with satellite altimetry missions, including a discussion on the differences between the ionosphere parameters derived by satellite altimetry and GNSS. In addition, several other techniques are outlined, which give the opportunity for ionosphere modelling. These are the Low Earth Orbiters (LEOs), Very Long Baseline Interferometry (VLBI), and the Doppler Orbitography and Radiopositioning Integrated by Satellite (DORIS).

Chapter 4: *Inter-technique combination*

The utilised method for parameter estimation and combination of ionosphere data from different techniques is introduced in this chapter. It consists of a short recapitulation of the least squares adjustment and the normal equation stacking. Eventually, the constraints and weighting applied in the work are revealed.

Chapter 5: *Global ionospheric maps from GNSS data*

As a first step of the research, global maps of the ionosphere are developed utilising only GNSS data, for being used afterwards as basis for the combination. This chapter shows the results of this initial estimation, describing the TEC parameterisation and estimation and giving examples of the outcomes. The obtained ionosphere maps and DCB values are discussed, with a detailed focus on the impact of using GLONASS data along with GPS observations. Furthermore, one-month time series of selected TEC parameters and of satellite and receiver DCB are shown and investigated. For validation of the results, comparisons with GIM and DCB provided by the International GNSS Service (IGS) are performed. The obtained TEC values are also compared with ionosphere data derived from satellite altimetry measurements.

Chapter 6: *Combined Global Ionospheric Maps*

The key part of the research is presented in this chapter. First of all, the main problems that have to be solved in the course of combining ionosphere data from GNSS and satellite altimetry are revealed. These are the relative weighting of the different kinds of observations, and the systematic errors affecting the altimetry derived VTEC. The adopted strategy for dealing with these two issues is substantiated on the basis of several test, the results of which are exemplified. In the second part of the chapter the results of the combination are shown. The combined GIM are compared with the GNSS-only maps on daily and monthly basis, as it is done with the corresponding RMS maps. Some ideas for further optimisation of the integrated GIM, arising in the course of the investigations and regarding mainly the altimetry satellite offset, are defined. The consistency of the combined ionosphere models is proven through comparison with the IGS GIM and with "raw" altimetry data. Finally, for an objective assessment of their accuracy, the combined GIM are applied for single-point positioning from single-frequency GNSS observations.

Chapter 7: *Summary and outlook*

Gives a summary of the essential results of the dissertation and discusses the benefits provided by the integration of ionosphere data, as well as the remaining open questions. As a consequence, the direction of the further work is outlined, along with some ideas that might be of interest for more detailed investigation.

Appendices

Appendix A shows an excerpt of the resulting IONEX-file for the combined GIM on day 182 in 2006. In Appendix B, examples of the global ionosphere models obtained for four weeks in different ionospheric conditions are given. It includes: daily combined GIM for one day of each week; the average weekly differences between the VTEC delivered by satellite altimetry and the corresponding values interpolated from the IGG GNSS-only and combined GIM; weekly time series of the estimated constant altimetry offsets. In the last part of Appendix B the results of the validation with raw altimetry data and the IGS AAC GIM carried out at the UPC are summarised. Eventually, Appendix C shows an example of combined GIM with integrated GNSS, Topex/Poseidon, and Jason-1 observations.

Part I

Using space geodetic techniques for ionosphere mapping - Theory

Chapter 2

Basic concepts

2.1 The ionosphere

The Earth's ionosphere is defined as that part of the upper atmosphere where the density of free electrons and ions is sufficient to influence the propagation of electromagnetic radio frequency waves (Hargreaves, 1992). The lower boundary of the ionosphere is observed at about 50 km above the Earth's surface at day time and at about 90 km at night; below these limits the solar radiation is completely absorbed by the Earth's atmosphere. The maximum electron density occurs at about 200 to 700 km above the surface of Earth, afterwards the intensity of the ionisation processes gradually diminishes with increasing height. Therefore, the upper limit of the ionosphere can not be explicitly defined and is considered at a height of about 1000 km. Beyond that border the medium becomes practically fully ionised but its density decreases. The ionosphere is a dispersive medium for electromagnetic waves since the integration between the electromagnetic field and the free electrons influences both the speed and propagation direction of the signal. This effect is called ionospheric refraction (Hartmann & Leitinger, 1984) and has to be considered in determination of the propagation velocity of the signals of all space geodetic techniques operating with electromagnetic waves. The magnitude of the ionospheric refraction depends on the number of free electrons along the ray path and varies strongly with time and geographical location, as well as with the magnetic and solar conditions. This chapter gives a brief description of the main features of the ionosphere, based mostly on Brunini (1997), and Hobiger (2003). For more details on physics of the ionosphere refer to e.g. Ratcliffe (1972), Davies (1990), and Kelley (1989).

2.1.1 Ionisation

The upper part of the Earth's atmosphere consists mainly of oxygen atoms (O) and molecules (O_2), nitrogen (N_2), hydrogen (H), and helium (He). The atomic nuclei comprise neutrons and protons; the electrons surrounding the nucleus are negatively charged with a total charge equal to the positive charge of the protons in it. Under the influence of external forces one or more electrons can be removed from the atomic electron shell, the atom becomes positively charged and turns to an ion. The process of breaking away of electrons from the atomic shell is called ionisation. The ionisation process in the upper atmosphere depends primarily on the Sun and its activity. The major part of the ionisation is produced by solar X-ray and ultraviolet radiation, which has wave length $\lambda < 0.1\,\mu\mathrm{m}$, and by corpuscular radiation.

2.1.2 Spatial and temporal variations

The Earth's ionosphere is driven mainly by the solar radiation and therefore, when studying the electron density it is beneficial to use a coordinate system which compensates the apparent solar motion (Brunini, 1997). In order to keep the change in the Sun's position minimal, the coordinate system should co-rotate with it, so the temporal variation of the electron content is slow and can be averaged for a short period, e.g. one to two hours. The origin of this sun-fixed coordinate system is set in the centre of mass of the Earth, the terrestrial rotation axis is chosen for Z-axis and the X-axis is defined by the mean solar meridian; the Y-axis completes the coordinate system to a right-handed one. In that way the geographical longitude and latitude (λ_g, β_g) can be transformed into sun-fixed longitude and latitude (λ_s, β_s) as follows:

$$\lambda_s = s = \lambda_g + UT - \pi = \lambda_g + UT - 12\,hours \tag{2.1}$$

$$\beta_s = \beta_g \tag{2.2}$$

with UT being the Universal Time. After the transformation the latitude remains unchanged (2.2) and the sun-fixed longitude (2.1) matches the hour angle of the Sun.

Furthermore, the behaviour of the ionosphere strongly depends on the geomagnetic field, so for global description of the electron density the usage of geomagnetic instead of geographical latitude is more convenient (Schaer, 1999; Hobiger, 2005). Within an altitude of few terrestrial radii the geomagnetic field can be approximated by a magnetic dipole, centred in the geocentre. The intersection points of the magnetic dipole axis and the Earth's surface define the north and south magnetic poles; the intersection with the plane orthogonal to the dipole axis is called the geomagnetic (or dip) equator, from which the geomagnetic latitude is measured. If the geographical coordinates of the geomagnetic north pole (λ_0, β_0) are known, the geomagnetic latitude β_{gm} corresponding to the geographical coordinates (λ_g, β_g) can be computed via:

$$sin\beta_{gm} = sin\beta_g\,sin\beta_0 + cos\beta_g\,cos\beta_0\,cos(\lambda_g - \lambda_0) \tag{2.3}$$

According to the 10th Generation International Geomagnetic Reference Field (IGRF-10), which is the latest version of a standard mathematical description of the Earth's main magnetic field, the coordinates of the north magnetic pole for the year 2005 are $\beta_0 = 79.7°$ (N) and $\lambda_0 = 71.8°$ (W), and move slowly according to the secular variation of the geomagnetic field. The predicted coordinates of the north geomagnetic pole for 2008 are $\beta_0 = 79.9°$ (N) and $\lambda_0 = 71.9°$ (W) (see IGRF, 2007). In that work the sun-fixed longitude and geomagnetic latitude are used. For the investigation of spatial ionospheric variations the time in (2.1) is fixed and for the analysis of temporal processes the coordinates (λ_g, β_{gm}) are retained.

The Chapman law and profile

The strongest variations in the free electrons and ions density in the ionosphere occur depending on the altitude above the Earth's surface (H) and the angle of incidence of the solar radiation (χ) with changing sun-fixed coordinates. These ionisation effects are approximated by the so-called Chapman law, formulated by S. Chapman in 1931 (Davies, 1990). The Chapman law describes the direct relation of the density of free electrons and ions to height

and daily solar motion. The production rate of ion pairs is given by the Chapman function (2.4) under the following simplifying assumptions, which barely hold especially for the upper atmosphere:

- only the solar radiation is taken into account, i.e. the impact of the cosmic rays, which are the second main (but less strong) cause of ionisation, is neglected;

- the atmosphere consists of a one-component isothermal gas distributed in horizontally stratified shells with constant scale height;

- the solar radiation is monochromatic and absorbed proportionally to the concentration of gas particles.

For this simple case, the Chapman function is defined as (Schaer, 1999):

$$q(H, \chi) = q_0 \, e^{(1 - z - sec\chi \, e^{-z})} \qquad \text{and} \qquad z = (H - H_0)/\Delta H \qquad (2.4)$$

where:

$q(H, \chi)$	ion production rate,
z	scaled altitude,
q_0	ion production rate at $z = 0$,
H_0	reference height of maximum ion production at $\chi = 0$, i.e. the Sun is in zenith,
ΔH	scale height.

The ion production rate is defined as:

$$q_0 = \frac{\phi(\infty) \, \eta}{\Delta H \, e} \qquad (2.5)$$

where:

$\phi(\infty)$	solar flux density outside the atmosphere (in photons/area),
η	number of ion pairs produced per proton.

The differentiation of (2.4) gives the altitude at which the ion production reaches its maximum:

$$H_{max} = H_0 + \Delta H \, z_{max} \qquad \text{and} \qquad z_{max} = ln \, sec\chi \qquad (2.6)$$

The maximum of the ion production is obtained as follows:

$$q_{max} = q_0 \, cos\chi \qquad (2.7)$$

Figure 2.1 shows the free electron and ion production rate (2.4) in [electrons/m^{3}sec] for different values of χ. Though at lower latitudes there is a large amount of ionisable molecules, the ion production rate decreases due to the ionisation of the high atmospheric layers and the reduction of photons. The potential of the increased quantity of photons at higher latitudes however, is limited by the low molecules density. Therefore, the altitude of maximum ion production is found at heights of about 200 to 700 km.
The electron density N_e depends on the recombination rate of ions and electrons in a relation, which - neglecting the term due to the transportation processes - can be expressed as:
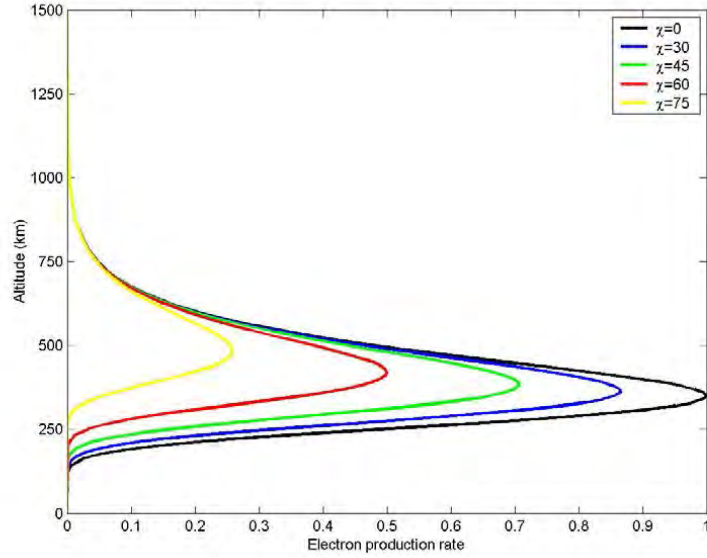
Figure 2.1: Chapman electron production rate for different angles of incidence of the solar radiation (χ)

$$\frac{dN_e}{dt} = q - L \tag{2.8}$$

with L being the loss rate due to the recombination. At altitudes of about $150\text{-}200\,\text{km}$ this term includes the square of the electron density, whereas at higher altitudes with low density of ionisable molecules the loss rate depends on N_e linearly.

In the case of equilibrium, the continuity equation (2.8) has the form $dN_e/dt = 0$ and the distribution of the electron density corresponding to (2.4) is:

$$N_e(z,\chi) = N_{e,0}\, e^{\frac{1}{2}(1-z-sec\chi\, e^{-z})} \tag{2.9}$$

where $N_{e,0} = \sqrt{\frac{q_o}{\alpha}}$ is the electron density at scaled altitude $z = 0$.

Such distribution is called α-Chapman layer (Hargreaves, 1992). The maximum electron density is reached at the altitude (2.6) and is:

$$N_{e,max}(\chi) = N_{e,0}\, cos^{\frac{1}{2}}(\chi) \tag{2.10}$$

In spite of the simplifying assumptions under which the Chapman theory is derived, it is able to explain the main characteristics of the ionosphere and provides a reliable reference for the basics in the ionosphere modelling (Kelley, 1989). As shown by the altitude profiles, the maximum electron density is concentrated in a relatively thin layer, typically located at a height of about 300 - 500 km above the Earth's surface. Based on that result, the so-called Single Layer Model (SLM) has been introduced. It assumes that all free electrons are concentrated in an infinitesimally thin layer at a fixed height. Usually, this height slightly exceeds the altitude of maximum electron density in order to balance the effect of the more

extended topside ionosphere. SLM is widely used as a basis for the development of Global Ionospheric Maps (GIM) and is also adopted in that work (for more details see section 2.2.1). The essential impact of the daily solar motion on the ionisation rate is also substantiated by the Chapman law and justifies the usage of the sun-fixed reference frame, presented in the beginning of that section.

Vertical structure of the ionosphere

The different transportation processes in the ionosphere lead to a vertical structure fairly different from the profile foreseen by the Chapman law and demonstrated in Figure 2.1. The actual vertical profile exhibits several peaks of the electron density N_e in different heights and at different times of the day. These maxima result from the differences in the chemical and physical processes affecting the various ions and atoms of which the medium is composed. The electron density peaks define the ionospheric layers, which are labelled with D, E and F (Figure 2.2). The highest electron density is observed in the F layer (Table 2.1). During day time it is divided in the F1 and F2 layers, formed under the influence of the ultraviolet radiation. The region below the densest F2 region is usually called bottomside and the region above it - topside ionosphere.
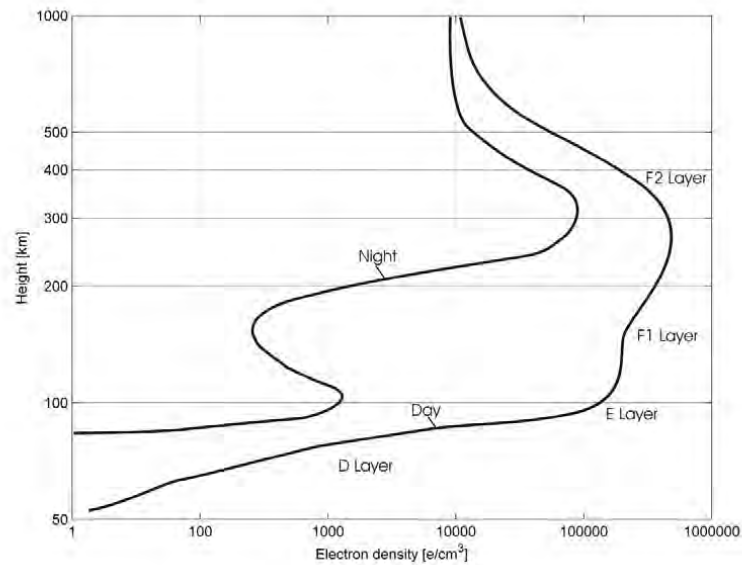
Figure 2.2: Vertical profile of the ionosphere at times of sunspot minimum after Hargreaves (1992)

Layer	D	E	F1	F2
Altitude [km]	60-85	85-140	140-200	200-1000
Day time N_e [cm^{-3}]	10^2-10^4	10^5	3×10^5	5×10^5
Night time N_e [cm^{-3}]	-	2×10^3	10^3	3×10^5

Table 2.1: Main ionospheric layers: altitude and electron density

Magnetic field

There are several important effects causing variations in the ionosphere, which can not be explained by the simplified Chapman theory. A large and very complex impact on the ionosphere is exerted by the processes in the outer terrestrial magnetic field. There, many interactions take place - between solar radiation and terrestrial matter, the Earth's magnetic field and the charged particles, and between the solar and terrestrial magnetic fields (Brunini, 1997; Hargreaves, 1992). The magnetism influences the electron density distribution provided in the Chapman's theory. This influence increases with height, as the number of ionisable molecules gets lower and the ionisation increases. At altitudes of some thousands of kilometres the impact of the terrestrial magnetic field becomes predominant and the medium is defined as magnetosphere. A widely used indicator for the level of perturbation of the geomagnetic field is the so-called K_p index (see also section 5.2).

The interaction between the solar wind and the force lines of the Earth's magnetic field determines the main geographical regions of the ionosphere. When the high energetic particles carried by the solar wind reach the terrestrial magnetic field, they experience an acceleration, which makes them rotate in a circular orbit around the magnetic force lines. The velocity vector of the charged particles approaching the Earth in the equatorial region is almost perpendicular to the magnetic lines, causing a rotation with nearly steady centre (Hargreaves, 1992). On the contrary, if the particles enter the magnetic field slightly afar the equatorial plane, their velocity component becomes parallel to the force lines and they move around them towards the corresponding (south or north) pole. The magnetic force lines in the polar regions are virtually vertical and the intensity of the charged particles is up to three times higher than over the equator. The particles reach low altitudes and collide with the atmospheric molecules. This is the reason for the barely predictable permanent ionospheric variations in the polar regions. When accelerated protons from the solar wind collide with molecules in the atmosphere and release energy in the form of light, the aurora phenomena can be observed in the regions near the geomagnetic poles (see e.g., Eather, 1980).

Figure 2.3: Electric currents in the day time ionosphere (source: United States Geological Survey, 2005)

Following the behaviour of the charged particles interacting with the force lines of the terrestrial magnetic field, the main geographical regions of the ionosphere can be defined:

- Low latitudes or equator regions (about $\pm 20°$ of the magnetic equator) are characterised by the highest free electron density, high spatial gradients and scintillations. This is where the so-called equatorial anomaly is observed in the form of a trough of concentrated ionisation in the F2 layer (see Figure 2.3);

- Mid latitudes exhibit regular and predictable ionosphere variations, with the times of magnetic storms being an exception;

- High latitudes (aurora regions) - considerably lower free electrons density but strong and nearly unpredictable short-time variations.

The impact of the geomagnetic field on the electron density variations constitutes the need of using the geomagnetic latitude (2.3) for better global representation of the ionosphere.

Temporal variations

Besides the variations due to height and geographical location, the ionosphere varies also with time. The most noticeable effect is seen as the Earth rotates with respect to the Sun. The ionisation increases in the sunlit hemisphere, reaching a peak shortly after noon local time, and decreases on the shadowed side. In addition to the diurnal effect reproduced by the Chapman function (2.4), there is also a seasonal periodicity coinciding with the equinoxes when the free electrons and ions reach a maximum.

The long-period temporal variations in the ionosphere depend on the solar activity. The basic indicator for the level of solar activity is the sunspot number. Due to their relatively low temperature, the sunspots are visible on the solar surface as darker regions and are usually located between $5°$ and $30°$ solar latitude (Hobiger, 2005). A widely used quantity is the Wolf sunspot number R:

$$R = k\,(f + 10g) \tag{2.11}$$

where:

f total number of the observed single spots,
g number of sunspot groups,
k constant, depending on the instrumental sensitivity.

The magnetic storms, during which the emittance of charged particles, ultraviolet and X-rays from the Sun increases and affects all geomagnetic field components and the number of electrons in the ionosphere, occur more frequently during sunspot number maximums. Generally, the average electron density is higher in periods of sunspot maximum. Sunspots are first noticed around 325 BC and have been recorded for several centuries. The spectral analysis of sunspot number time series shows a very prominent period of about 11.1 years as well as a noticeable 27-days period corresponding to the solar rotation (Figure 2.4). The latest solar maximum was recorded in the period 2001-2002. In the current period the solar activity is low.
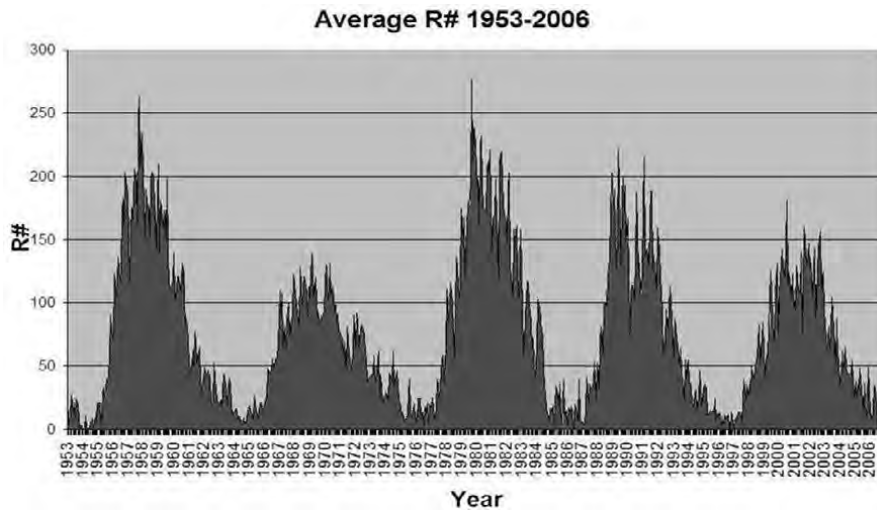
Figure 2.4: Average sunspot number over 53 years (credit: NSO (2007))

Further temporal phenomena are the so-called Travelling Ionospheric Disturbances (TIDs). They can change the value of the integrated electron density in the region of their occurrence in the range of several percent (Schaer, 1999). Three types of TIDs are defined: large- (LSTID), medium- (MSTID) and small-scale (SSTID). Their main classifications are listed in Table 2.2. TIDs occur mostly in mid latitudes (Hobiger, 2005) and are more evident close to solar maximum (Hernández-Pajares et al., 2006).

Classification	**LSTID**	**MSTID**	**SSTID**
Horizontal wavelength [km]	> 1000	> 100	> 10
Period [minutes]	30-180	10-60	> 1
Phase velocity [ms^{-1}]	300-1000	100-300	-

Table 2.2: Travelling ionospheric disturbances

2.1.3   Wave propagation in the ionosphere

In a dispersive medium the velocity of wave propagation is frequency-dependent. The ionosphere is a dispersive medium for the electromagnetic waves, and frequencies below 30 MHz are fully reflected by it - an effect utilised in radio communications. The refractive impact of the ionosphere on frequencies higher then 100 MHz is less strong and therefore the signals of the space geodetic techniques operating with microwaves are in the higher frequency band. The wave propagation in the ionosphere is discussed briefly in this section, for more information refer to e.g. Budden (1985).

The relation between the velocity v, the frequency w and the wave number k is given by:

$$v = \frac{w}{k} \tag{2.12}$$

The propagation velocity of a pure sinusoidal wave is denoted as phase velocity. The relation

between the phase velocity in vacuum and in a given medium yields the refraction index of the medium:

$$n = \frac{c}{v} \tag{2.13}$$

where c is the speed of light. The sinusoidal wave does not contain any information, since it is not modulated. For data transfer usually phase modulation is used, as it is the case in GNSS. A modulated carrier can consist of several pure sinusoidal waves with different frequencies. Passing through a dispersive medium, every single phase propagates with a different speed, depending on the frequency of each wave. Therefore, the propagation speed of such carrier is the so-called group velocity:

$$v_g = \frac{dw}{dk} \tag{2.14}$$

and the group refraction index can be expressed as:

$$n_g = \frac{c}{v_g} = c\frac{dw}{dk} = ... = n + w\frac{dn}{dw} \tag{2.15}$$

In a non-dispersive medium the phase and group velocity are identical and equal to the speed of light. In a dispersive medium the phase velocity is higher than the speed of light in vacuum and the travelling time of a pure carrier (τ_ϕ) shortens in the following way:

$$\tau_\phi = \int_S \frac{1}{v}dS - \int_{S'} \frac{1}{c}dS' \tag{2.16}$$

where S is the bent path of the carrier in the medium and S' - the straight path in vacuum. For the linear range we obtain:

$$d_\phi = c\tau_\phi = \int_S \frac{c}{v}dS - \int_{S'} dS' = \int_S (n-1)dS + \left[\int_S dS - \int_{S'} dS' \right] \tag{2.17}$$

The group velocity in a dispersive medium is lower than the speed of light in vacuum. The propagation time and the linear range in that case are expressed as follows:

$$\tau_g = \int_S \frac{1}{v_g}dS - \int_{S'} \frac{1}{c}dS' \tag{2.18}$$

and

$$d_g = \int_S (n_g - 1)dS + \left[\int_S dS - \int_{S'} dS' \right] \tag{2.19}$$

The complex phase refraction index in an ionised medium consisting of equal number of positive ions and free electrons and on which a regular magnetic field is applied, can be written following the Appelton-Hartee theory as (de Munck & Spoelstra, 1992):

$$n = \left[1 - \frac{X}{1 - iZ - \frac{Y_T^2}{2(1-X-iZ)} \pm \left[\frac{Y_T^4}{4(1-X-iZ)^2} + Y_L^2 \right]^{1/2}} \right]^{1/2} \tag{2.20}$$

with:

$$X = \frac{\omega_P^2}{\omega^2} \ , \ Y_L = \frac{\omega_{GL}}{\omega} \ , \ Y_T = \frac{\omega_{GT}}{\omega} \ , \ Z = \frac{\omega_C}{\omega} \qquad (2.21)$$

and

ω gyro frequency of the carrier,
ω_P electron plasma gyro frequency,
ω_G electron gyro frequency,
ω_C electron collision frequency.

The subscripts T and L refer to the transversal and longitudal components of the wave propagation.

The minimal frequency, with which an electromagnetic wave can penetrate an ionospheric layer, is called critical or plasma frequency of that layer and its square is proportional to the maximum electron density in the layer. The maximum plasma frequency of the whole ionosphere is called penetration frequency. A ground station could receive signals from space only if their frequency is higher than the penetration frequency of the ionosphere, which is (Hargreaves, 1992):

$$\omega_P = \sqrt{\frac{N_e e^2}{\epsilon_0 m_e}} \qquad (2.22)$$

with:

N_e electron density,
e charge of one electron,
ϵ_0 permittivity in vacuum,
m_e electron mass.

For frequencies ω considerably higher than ω_P, ω_G and ω_C, equation (2.20) can be approximated to:

$$n = \left[1 - \frac{X}{2(1 \pm Y_L)} \right]^{1/2} \cong \left[1 - \left(\frac{\omega_P}{\omega} \right)^2 \left(1 \pm \frac{\omega_{GL}}{\omega} \right)^{-1/2} \right]^{1/2} \qquad (2.23)$$

The phase refraction index is smaller than one, i.e. the propagation of the carrier phase accelerates. The phase refraction index is:

$$n = 1 - \frac{f_P^2}{2f^2} = 1 - \underbrace{\frac{e^2}{8\pi^2 \epsilon_0 m_e}}_{const} \frac{N_e}{f^2} \qquad (2.24)$$

where $f = \omega/2\pi$ denotes the carrier frequency in Hz, and $f_P = \omega_P/2\pi$ is the electron plasma frequency. Evaluating the constant factor in (2.24), we obtain:

$$C = \frac{e^2}{8\pi^2 \epsilon_0 m_e} \approx 40.28 \quad [\text{m}^3/\text{s}^2] \qquad (2.25)$$

and the phase refraction index can be written as:

$$n = 1 - 40.28 \, \frac{N_e}{f^2} \tag{2.26}$$

Considering (2.17) and (2.26), we obtain the linear advance in the distance, which has to be passed through by the phase carrier:

$$d_\phi = \int_S (n-1)dS = -\frac{40.28}{f^2} \int_S N_e dS \tag{2.27}$$

The negative sign in (2.27) shows that the carrier phase is advanced when passing through the ionosphere. The group refraction index (2.15) is bigger than one and so the group propagation is delayed:

$$n_g = 1 + 40.28 \, \frac{N_e}{f^2} \tag{2.28}$$

Consequently, by taking into account (2.19) the linear group delay in the ionosphere can be written as:

$$d_g = \int_S (n_g - 1)dS = +\frac{40.28}{f^2} \int_S N_e dS \tag{2.29}$$

Integrated electron density

As already mentioned, the quantity representing the ionospheric conditions is the electron density N_e expressed in [electrons/m^3]. If one is interested in signal propagation in the ionosphere however, the integral of the electron density along the ray path becomes relevant (e.g. Schaer, 1999). This quantity is defined as Total Electron Content (TEC) and represents the total amount of free electrons in a cylinder with a cross section of 1m^2 and the slant signal path as axis. TEC is measured in Total Electron Content Units (TECU), with 1 TECU equivalent to 10^{16} electrons/m^2. For an arbitrary ray path the slant TEC (STEC) can be obtained via:

$$STEC = \int N_e(S)dS \tag{2.30}$$

with $N_e(S)$ being the electron density along the line of sight.

In that way, the direct relation between the total electron content in TECU and the linear change in the distance in meters can be obtained. Taking into account (2.27), for the carrier phase the equation has the form:

$$d_\phi = -\frac{40.28 \cdot 10^{16}}{f^2} STEC \quad [\text{m}] \tag{2.31}$$

In the case of group propagation the result is the same (see (2.29)), but with positive sign, indicating that the group propagation is delayed:

$$d_g = +\frac{40.28 \cdot 10^{16}}{f^2} STEC \quad [\text{m}] \tag{2.32}$$

Finally, using the constant (2.25) the factor ϑ can be defined, so that it gives the ionospheric path delay in meter per one TECU, related to a certain frequency f in Hz:

$$\vartheta = \frac{C \cdot 10^{16}}{f^2} = \frac{40.28 \cdot 10^{16}}{f^2} \quad [\text{m/TECU}] \tag{2.33}$$

2.2 Global modelling of the Total Electron Content

The measurements of nearly all space geodetic techniques operating with electromagnetic waves - such as the Global Navigation Satellite System (GNSS) - are carried out at two different radio frequencies. This allows the ionospheric influence to be eliminated by linear combinations of the observations (see section 3.1.2). As a consequence, also information about the electron content can be obtained and used for modelling and monitoring of the ionosphere. The section gives a summary of the strategy for global TEC modelling applied in this work.

2.2.1 Single Layer Model and mapping function

GNSS alone does not easily allow vertical electron density profiles to be derived from its ground based observations (see section 3.1). Relaying on the results provided by the Chapman law - (2.5) and (2.6), the ionosphere models obtained from GNSS observations are developed in the form of a single layer, set at the height of the maximum electron density. However, the launch of different Low Earth Orbiter (LEOs) with GNSS receivers on board (see section 3.3) made ionosphere profiling through GNSS radio occultation possible (Syndegaard, 2000; Jakowski et al., 2004). The radio occultation principle is the measurement of the refractivity or bending of GPS signals slicing through the Earth's atmosphere and ionosphere (Figure 2.5). This observations provide information about the vertical variations throughout the ionosphere and give the opportunity for developing four dimensional ionosphere models - in latitude, longitude, time, and height (Hernández-Pajares et al., 2000).
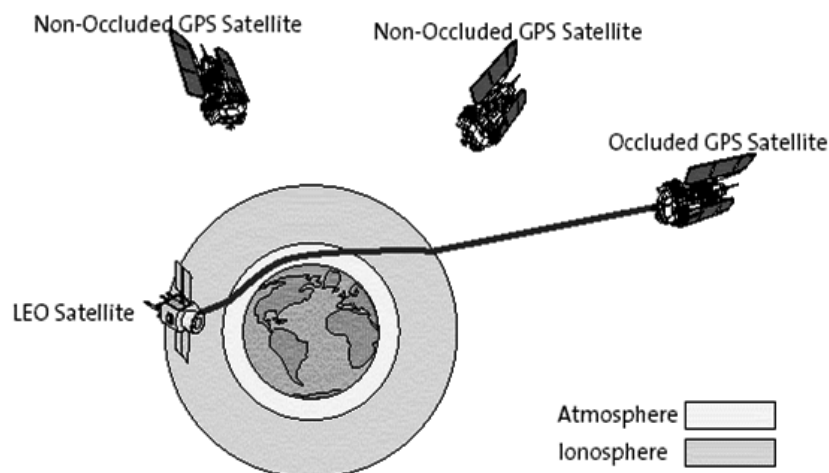
Figure 2.5: The radio occultation technique (credit: CPAR (2007))

There are two basic approaches for four dimensional ionosphere modelling:

- application of regional B-spline modelling and multi-resolution representation: the electron density is decomposed into a reference part, computed from a given model and an unknown correction term. The latter is expanded in a multi-dimensional series in terms of localizing base functions. The correction term can be modelled regionally by a tensor-product spline expansion. The monitoring of the ionosphere at different resolution levels is enabled by multi-resolution representation derived from wavelet analysis (Schmidt et al., 2006; Schmidt, 2007);

- four dimensional ionospheric tomography using voxels: combination of ground and occultation GNSS data is used to increase the vertical resolution of the global model. The ionosphere is represented as a four dimensional array of voxels with a certain resolution and the electron density is computed separately for the ray path through every voxel (e.g. Meza, 1999; Ruffini et al., 2002).

The bold goal of our future study is the development of a combined four dimensional global ionosphere model (section 7.2). As a first step towards this goal, the combination of GNSS and satellite altimetry ionospheric data is developed and investigated by means of global maps of the TEC representing the ionosphere in longitude, latitude and time based on the Single Layer Model (SLM).

SLM assumes that all free electrons are concentrated in an infinitesimally thin layer above the Earth's surface (Schaer, 1999). The height H of that shell is usually set slightly above the height where the highest electron density is expected (see section 2.1.2). A signal transmitted from the satellite to the receiver crosses the ionospheric shell in the so-called ionospheric pierce point. The zenith angle at that point is z' and the signal arrives at the ground station with zenith angle z (Figure 2.6).
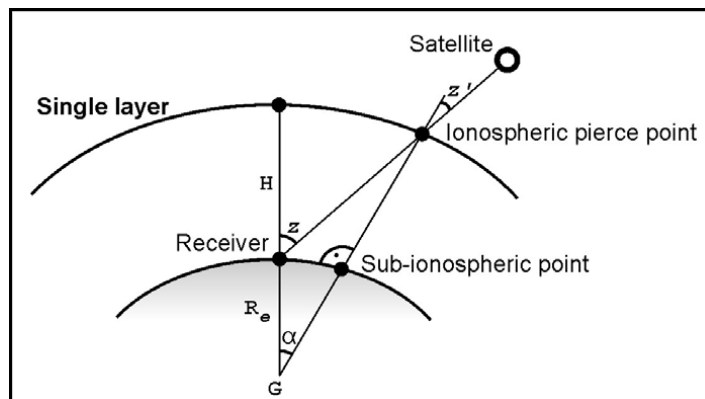
Figure 2.6: Single Layer Model

The relation between the measured slant TEC along the ray path and the vertical TEC value (VTEC) at the pierce point is given by a mapping function. In this study the Modified Single Layer Model Mapping Function (MSLM) is adopted (as in CODE (2007a), see also Dach et al. (2007)), and the mapping function for the transformation between STEC and VTEC can be written as:

$$F(z) = \frac{STEC}{VTEC} \cong \frac{1}{\cos z'} = \frac{1}{\sqrt{1 - \sin^2 z'}} = \frac{1}{\sqrt{1 - \left(\frac{R_e}{R_e + H}\sin(\alpha\,z)\right)^2}} \qquad (2.34)$$

where $\alpha = 0.9782$, $H = 506.7$ km, and $R_e = 6371$ km is the mean Earth radius. The MSLM approximates the JPL (Jet Propulsion Laboratory) extended slab model mapping function. Based on results showing that a single layer height of 550 km tends to be the best choice overall, the extended slab model provides an approximation which closely matches a single layer model with a shell height of 550 km (Sparks et al., 2000).

VTEC is obtained from the electron density along the ray path (2.30) by applying the mapping function (2.34):

$$STEC = F(z)VTEC \qquad (2.35)$$

The formula for computing the SLM mapping function is similar to (2.34) but the α coefficient is missing and the height H is usually set to 450 km. For more details of ionospheric mapping functions refer to Schaer (1999).

2.2.2 Global TEC representation through spherical harmonics

In order to develop a global ionosphere model, the vertical TEC has to be represented as a function of longitude, latitude and time, or according to the definition of the adopted coordinate system given in section 2.1.2 - as a function of the geomagnetic latitude β and sun-fixed longitude s. For the global VTEC parameterisation in this work the Spherical Harmonic (SH) expansion is adopted, as proposed by Schaer et al. (1995):

$$VTEC(\beta, s) = \sum_{n=0}^{n_{max}} \sum_{m=0}^{n} \tilde{P}_{nm}(\sin\beta)(a_{nm}\cos(ms) + b_{nm}\sin(ms)) \qquad (2.36)$$

where:

$VTEC(\beta, s)$	vertical TEC in TECU,
$\tilde{P}_{nm} = N_{nm}P_{nm}$	normalised Legendre function from degree n and order m,
N_{nm}	normalising function,
P_{nm}	classical Legendre function,
a_{nm} and b_{nm}	unknown coefficients of the SH expansion,

with the normalising function written as:

$$N_{nm} = \sqrt{\frac{2(2n-1)(n-m)!}{(n+m-2)!}} \qquad (2.37)$$

In case that the maximum degree and order of the spherical harmonic are defined as $n_{max} = m_{max}$, the number of unknown coefficients of the SH expansion (2.36) is given by:

$$u = (n_{max} + 1)^2 \qquad (2.38)$$

The SH expansion resolution in latitude ($\Delta\beta$) and longitude (Δs) is respectively:

$$\Delta\beta = \frac{2\pi}{n_{max}} \ , \ \Delta s = \frac{2\pi}{m_{max}} \tag{2.39}$$

An analysis of the global parameterisation (2.36) and the normalising function (2.37) shows that the zero-degree SH coefficient a_{00} represents the mean VTEC (Schaer, 1999):

$$VTEC_{mean} = \frac{1}{4\pi} \int_0^{2\pi} \int_{-\frac{\pi}{2}}^{\frac{\pi}{2}} VTEC(\beta, s)cos\beta d\beta ds = N_{00} \, a_{00} = a_{00} \tag{2.40}$$

2.2.3 Applications of the ionosphere models

Single frequency measurements are used in many commercial and scientific applications of navigation and positioning. When using single frequency observations, an accurate and reliable ionosphere model is essential. Another aspect is the global objective in modern geodesy for integration of different measurements, methods and models for a better understanding of the geodetic, geodynamic and global change processes in the entire System Earth, a goal which will be realised in the frame of the IAG project GGOS in the next 5 to 10 years (see GGOS, 2007). The theoretical models of the ionosphere, such as the International Reference Ionosphere (IRI) (Bilitza, 2001), are permanently updated by integration of real data. The assimilation of global ionosphere maps improves the theoretical models towards a higher temporal and spatial resolution and increases their accuracy. Another interesting application of ionosphere models with high spatial resolution for detection of seismic activity is shown by Ducic et al. (2003). Generally, a better understanding of the ionosphere, which is the main goal of the project, is fundamental for all studies of the upper atmosphere and the solar-terrestrial environment.

Chapter 3

Ionospheric information from different space geodetic techniques

3.1 Parameters of the ionosphere derived by GNSS

The Global Navigation Satellite System (GNSS), presently consisting of GPS (Global Positioning System) and GLONASS (GLObal NAvigation Satellite System), provides information about the ionospheric refraction enabling high resolution ionosphere imaging in longitude, latitude, and time (e.g. Brunini, 1997; Schaer, 1999). Both observables of the system - carrier phase and code measurements - are affected by the ionosphere. The measurements are carried out at two different radio frequencies, which allows the ionospheric influence to be eliminated by linear combinations of the observations. On the other hand, in this way information about the ionosphere parameters can be obtained. If the behaviour of the ionosphere is known, the ionospheric refraction can be computed and used to correct single-frequency measurements. In this section a recapitulation of the basic features of the two satellite navigation systems is provided. For more details on GPS refer to e.g. Hofmann-Wellenhof et al. (2001). An extensive description of the GLONASS system is given in Habrich (1999).

3.1.1 The positioning systems GPS and GLONASS

The basic principle of satellite navigation systems is the simultaneous observation of minimum four satellites, of which the positions are known. The measurements are carried out through correlation of the received satellite signal with an identical signal generated in the ground receiver. The difference between them is directly proportional to the time needed from the satellite signal to cover the distance between the satellite and the receiver. Since the receiver's clock differs from the clock on-board the satellite by an unascertained value, an additional unknown appears in the observation equation (see section 3.1.2). Therefore, only the simultaneous observation of at least four satellites enables the equation to be solved for all positioning parameters - latitude, longitude, height, and clock correction.

The Global Positioning System (GPS)

According to Wooden (1984), "the NAVSTAR Global Positioning System (GPS) is an all-weather, space-based navigation system under development by the Department of Defense (DoD) to enable users to accurately determine their position, velocity, and time in a common reference system, anywhere on or near the Earth on a continuous basis." GPS consists of three basic segments - space, control and user. Initially designated for military deployment, in 1983 a directive was issued for making the system available for free for civilian use. The full operational capability was declared in July 1995, when a constellation of 24 satellites was operating. Later on, technological advances and increasing demands constituted the need for modernisation of the GPS system. Therefore, in 2000 the GPS III program was launched. Goal of the project is to improve the system's accuracy and availability for all users, involving new ground stations, new satellites, and four additional navigation signals - three civilian and one military code. The initial operational capability of the first new civilian code is expected in 2008 (Tiberius & de Jong, 2002); the final term for the entire program is in 2013.

The GPS terrestrial reference system is the World Geodetic System 1984 (WGS-84). The system time of GPS is related to the atomic time system and referenced to the coordinated universal time (UTC) (Hofmann-Wellenhof et al., 2001). The GPS time is corrected for the UTC lag, being defined as:

$$GPS\ time = UTC + \underbrace{(n - 19.000)}_{seconds} \tag{3.1}$$

In (3.1) n is an integer number of seconds defined by the International Earth Rotation Service IERS. In November 2007 its value is $n = 33$, so the difference between the GPS time and UTC is 14 seconds.

The space segment

The nominal constellation of the GPS space segment consists of 24 operational satellites (Wasle, 2007). They are located in six orbital planes labelled from A to F, with an inclination of about $55°$ with respect to the Earth equator (Figure 3.1). The orbit planes are equally separated by $60°$ and nearly circular, with semi-major axis of about 26 600 km, which results in an altitude of 20 200 km above the surface of Earth. The orbital revolution period is 11 h 58 min. The current GPS constellation consists of 32 satellites from the types Block II, IIA (Figure 3.2), IIR and IIR-M. The first Block II satellite was launched in February 1989; the most recent Block IIR-M satellite was launched on 17 October 2007 and is operational since 31 October 2007. The full constellation allows the simultaneous observation of four to eight satellites with an elevation higher than $15°$ from every point on the Earth throughout the day. If the restriction for the elevation angle is set at $5°$, up to twelve satellites can be observed at the same time. The satellites are identified by plane/slot and PRN numbers from 1 to 32, and usually denoted as "G" and the PRN number (`G1, G2, ..., G32`).
The current status of the GPS constellation can be seen in Table 3.1.

The signal components of the system are controlled by highly accurate atomic (caesium or rubidium) clocks with long-term frequency stability of 10^{-13} to 10^{-14} over one day. They
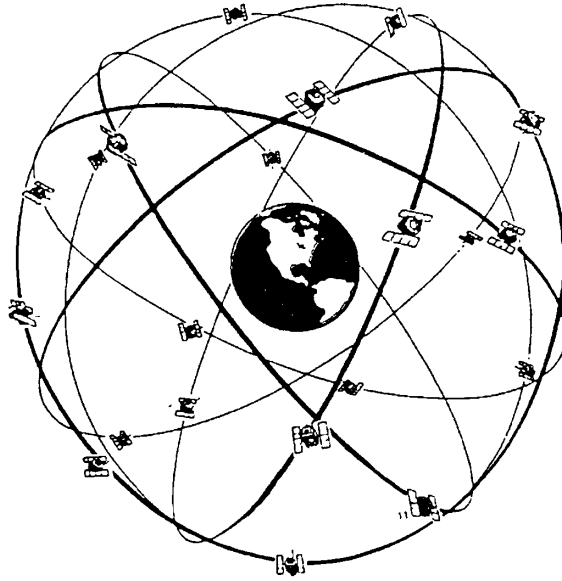
Figure 3.1: GPS nominal constellation (source: Grüller, 2007)
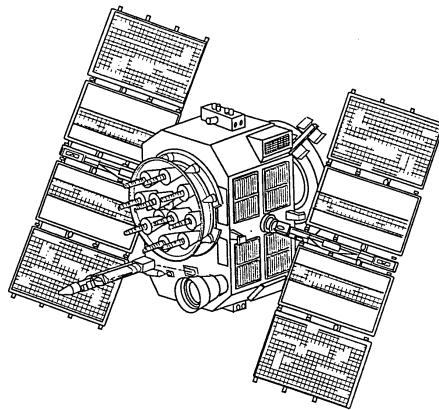
Figure 3.2: Block IIA GPS satellite (source: Grüller, 2007)

PRN	1	2	3	4	5	6	7	8	9	10	11	12	13	14
plane/slot	F6	D1	C2	D4	B5	C1	C5	A3	A1	E3	D2	B4	F3	F1
clock	Cs	Rb	Cs	Rb	Rb	Rb	Rb	Cs	Cs	Rb	Rb	Rb	Rb	Rb
PRN	15	16	17	18	19	20	21	22	23	24	25	26	27	28
plane/slot	F2	B1	C4	E4	C3	E1	D3	E2	F4	D5	A5	F5	A4	B3
clock	Rb	Rb	Rb	Rb	Rb	Rb	Rb	Rb	Rb	Cs	Rb	Rb	Cs	Rb
PRN	30	31	32											
plane/slot	B2	A2	E5											
clock	Cs	Rb	Rb											

Table 3.1: Current GPS satellites, planes and clocks (Cs - caesium, Rb - rubidium), source: CGNC (2007)

produce the fundamental frequency of 10.23 MHz. The signals on the $L1$ and $L2$ carriers are coherently derived by multiplying the fundamental frequency by 154 and 120 respectively: $f_{L1} = 1575.42$ MHz with wavelength 19 cm, and $f_{L2} = 1227.60$ MHz with wavelength 24 cm. The main reason for using two different frequencies is the elimination of the ionospheric refraction through linear combinations (see section 3.1.2). On the $L1$ carrier two pseudo-random noise (PRN) codes are generated: the Coarse/Acquisition code (C/A-code) with an effective wavelength of about 300 m, and the Precision code (P-code) with effective wavelength 30 m. On $L2$ only the P-code is modulated. At present, the P-code is encrypted to the Y-code in order to make it available only for authorised users. If a measurement resolution of 1% of the chip length is assumed, an uncertainty of 3 m for the C/A-code and 0.3 m for the P-code results. A resolution of 1% of the wavelength however, yields a 2 mm uncertainty of the phase observations. Therefore, for high-precision applications the carrier phase has to be utilised. The so-called navigation message, containing information about the system status and GPS time, the satellite clock bias and ephemerides, is modulated on both carriers.

The control segment

The operation control segment of GPS consists of one master control station located in Colorado Springs, USA, and six main monitor stations. At the master control station the tracking data from the monitor stations is collected and the satellite orbits and clock parameters are calculated, using a Kalman estimator. The results are transmitted to one of the ground antennas, located at four of the monitor stations, for potential upload to the satellites. Normally, the satellite ephemerides and clock information are uploaded three times per day to every satellite. Each of the six main monitor stations is provided with a precise atomic clock and measures the pseudorange to all satellites in view every 1.5 seconds. The smoothed observations are passed to the master control station in 15-minutes interval. The maximum duration of positioning service without contact to the operation control segment is: 14 days for the satellites of Block II, 180 days for satellites of Block IIA, and more than 180 days for satellites of Block IIR (Wasle, 2007).

The user segment

The GPS user segment can be divided in two main types - military and civil users. The civilian applications of GPS are mainly in the area of navigation, control and coordinate determination of persons and vehicles - airplanes, vessels, cars, etc. The GPS receivers differ depending on the producer and the purpose of use, but can generally be classified as one- or double-frequency receivers, and according to their ability to receive pseudorange and/or carrier phase. To the user segment belong also several governmental and private information services, providing the users with GPS information and data. The main information service is the International GNSS Service (IGS) (Dow et al., 2005), formerly the International GPS Service, established in 1993 by the International Association of Geodesy (IAG). IGS is a voluntary federation of more than 200 worldwide agencies that pool resources and permanent station data to generate precise GPS and GLONASS products. As of November 2007, the IGS global tracking network consists of 341 active tracking stations (Figure 3.3). The data obtained at these stations are processed at the ten IGS Analysis Centres (Hugentobler et al., 2006), which form submissions to the IGS products:

- GPS satellite ephemerides and satellite and station clocks including final, rapid, and ultra-rapid solutions for GPS, as well as final satellite ephemerides for GLONASS;

- geocentric coordinates and velocities of the IGS tracking stations;

- final, rapid, and ultra-rapid earth rotation parameters: length-of-day, polar motion and polar motion rates;

- atmospheric parameters, including ionospheric TEC grid. The IGS TEC maps are considered in more detail in section 3.1.3.
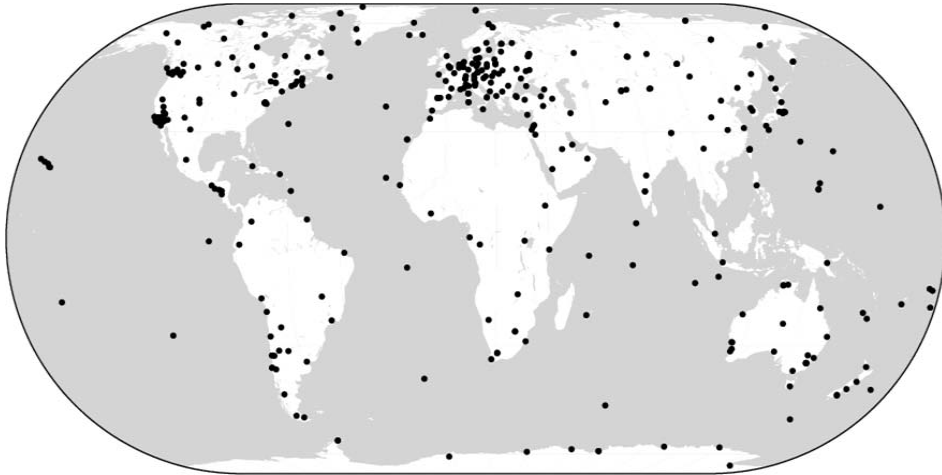
Figure 3.3: IGS tracking stations (source: IGS, 2007)

The IGS data and products can be obtained free of charge from the servers of the IGS data centres (IGS, 2007) via anonymous ftp. The GNSS observation data is stored in daily station-specific files in the Receiver INdependent EXchange (RINEX) format. The standard data sampling rate is every 30 sec. Besides the RINEX data files, the daily broadcast ephemeris file (BRDC navigation file) is used in this work. The BRDC files are a merge of the individual site navigation files into one non-redundant file, and are provided by the Crustal Dynamics Data Information System (CDDIS) at NASA GSFC (CDDIS, 2007).

The GLObal NAvigation Satellite System (GLONASS)

GLONASS (from Russian: GLObal'naya NAvigatsionnaya Sputnikovaya Sistema) is the Russian counterpart to the US navigation system GPS, based on the same principles in terms of data transmission and positioning methods. It is managed by the Russian Space Forces and operated by the Coordination Scientific Information Center of the Ministry of Defense of the Russian Federation. Established in 1976, till 1988 GLONASS is a purely military system. The next ten years civil users are restricted to one available signal. Eventually, in February 1999 a presidential directive makes both frequencies of the system disposable "with no direct user fees for civil GLONASS service" (Revnivykh, 2005). As stated in the recent GLONASS Interface Control Document (ICD, 2002), "the purpose of the Global Navigation Satellite System GLONASS is to provide unlimited number of air, marine, and any other type of users

with all-weather three-dimensional positioning, velocity measuring and timing anywhere in the world or near-earth space". Though the system was declared operational in 1993, the nominal constellation of 24 satellites was primarily present in 1996 (Wasle, 2007). However, right afterwards the system rapidly went in decline, with only six to eight satellites available in 2001. In August 2001 the Federal GLONASS Program for 2002-2011 was launched, aiming at the completion and modernisation of the system. According to Revnivykh (2005), the minimal operation capability (18 satellites in orbit) will be reached by 2008, and the full operation capability (24 satellites) shall be achieved by 2010 (Figure 3.4). The performance of the space and control segments of the system will be considerably improved, with main focus on the system's clocks stability and dynamical model. Furthermore, the introduction of a third civil carrier frequency and a substantial increase of the number of ground monitoring stations are planned.
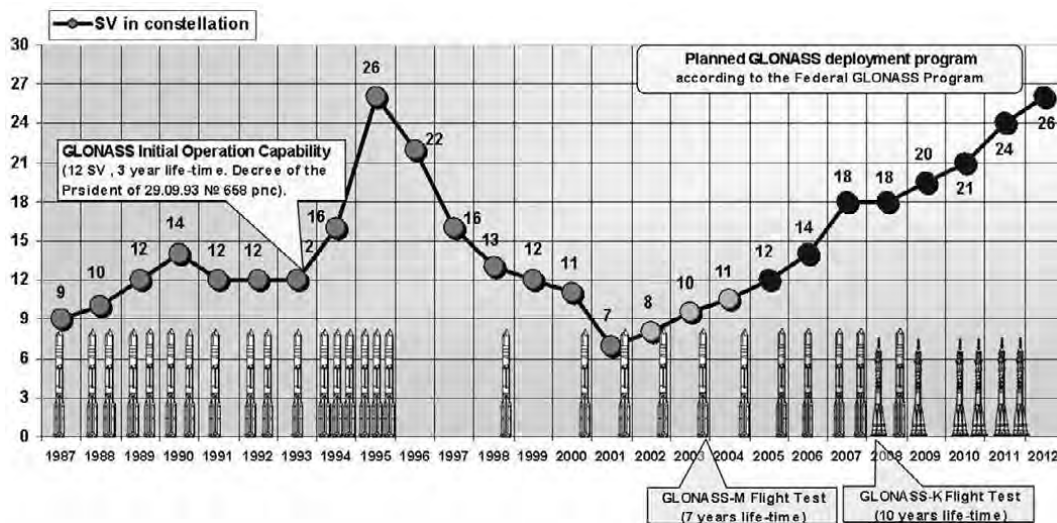
Figure 3.4: GLONASS constellation: history and perspective (source: GLONASS, 2007)

The terrestrial reference system of GLONASS is referred to as PE-90 (Parameters of the Earth 1990), or seldom as PZ-90. It is an Earth-centred reference frame, defined as follows (ICD, 2002):

- the Z-axis is directed to the Conventional Terrestrial Pole as recommended by the International Earth Rotation Service (IERS);

- the X-axis is directed to the point of intersection of the Earth's equatorial plane and the zero-meridian, established by the International Bureau of Weights and Measures (BIPM);

- the Y-axis completes the coordinate system to a right-handed one.

The main parameters of the common terrestrial ellipsoid PE-90 are listed in Table 3.2.

The transformation parameters between PE-90 and the systems ITRS and WGS 84 are shown by Boucher & Altamimi (2001). This comparison was among the objectives of the International GLONASS Experiment (IGEX). It started in October 1998 as the first coordinated

Parameter	Value
Semi-major axis	6 378 136 m
Flattening	1/298.257 839 303
Gravitational constant	398 600.44×109 m^3/s^2
Earth rotation rate	7.292115×10^{-5} rad/s

Table 3.2: Parameters of the common terrestrial ellipsoid PE-90

international effort to monitor GLONASS satellites on global basis, and supported by about 40 institutions worldwide. An important achievement of IGEX was the quality and consistency increase of the calculated GLONASS orbits, reaching an improvement from several tens of meters to about 25 cm in early 2000, even after the end of the official IGEX field campaign (Weber & Springer, 2001).

Similar to the GPS time (3.1), the GLONASS time is related to TAI and referenced to UTC with a constant offset of three hours, due to the difference between the Moscow and Greenwich Time. The rest of the difference between the GLONASS time and UTC is denoted as τ_c and caused by the time scales keeping of the different clocks. The parameter τ_c must not be higher than one millisecond and is contained in the GLONASS navigation message, which provides various information about the satellites and the system to the receiver. The GLONASS time is generated on the base of hydrogen clocks with daily instability of about $1 - 5 \cdot 10^{-14}$. Its relation to UTC can by expressed by:

$$GLONASS\,time = UTC - \tau_c + 3\,hours \qquad (3.2)$$

The correction of the GLONASS time to integer number of seconds due to the leap second is performed by the BPIM simultaneously with the UTC corrections. GLONASS users are notified for the latter in advance (at least three months before) through relevant bulletins, notifications etc. (ICD, 2002).

The space segment

The nominal GLONASS constellation consists of 24 satellites located in three orbital planes, with ascending nodes separated by 120° and inclination of 64.8° to the equator. The orbits are circular with an altitude of 19 100 km. Eight satellites are situated in each plane, so the argument of latitude displacement within the plane amounts 45°. The argument of latitude displacement between two planes is 15°. The position of each satellite within the constellation is indicated by a slot number. The individual satellites are usually denoted as "R" and the slot number (`R1, R2, ..., R24`). The orbital period is approximately 11 h 16 min, corresponding to 8/17 of a sidereal day. The constellation of 24 satellites guarantees that at least five satellites are seen from 99% of the Earth's surface at the same time. The expected life time is four years for the older GLONASS satellites and seven years for the new generation GLONASS-M satellites. The latest GLONASS-K version, with expected first launch in 2009 (as of June 2007, see Russian Space Web (2007)), will have a life span of 12-15 years and features a third L-band transmitter for civilian users. Additionally, all GLONASS satellites are provided with laser reflectors for satellite laser ranging (SLR). A summary of the GLONASS orbit characteristics compared to the ones of GPS can be seen in Table 3.3 (Habrich, 1999).
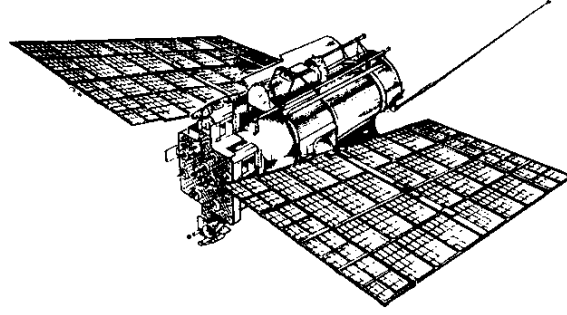
Figure 3.5: GLONASS satellite (source: Grüller, 2007)

Characteristic	**GLONASS**	**GPS**
Nominal number of satellites	24	24
Orbital planes	3, spaced by 120°	6, spaced by 60°
Orbital plane inclination	64.8°	55°
Satellites per orbital plane	8, equally spaced	6, unequally spaced
Orbital height	19 100 km	20 200 km
Revolution period	11 h 16 min	11 h 58 min
Ground track repeatability	every 8^{-th} sidereal day	every sidereal day

Table 3.3: GLONASS and GPS orbit characteristics

At present, two navigation signals are continuously provided by each GLONASS satellite: the standard accuracy C/A-code with effective wavelength of about 600 m, and the high accuracy P-code with wavelength of about 60 m. The C/A-code is modulated only on the first carrier $L1$, and the P-code is modulated on both, $L1$ and $L2$[1]. In the GLONASS-M satellites, which are operating since 2004, the C/A-code is added on $L2$ as well. Contrary to GPS, the GLONASS P-code signal is not encrypted, but the ranging code was never published officially. A basic difference between GLONASS and GPS is the signal structure. In GPS the Code Division Multiple Access (CDMA) is used: every satellite transmits the same two carriers, which are modulated by satellite-specific PRN-codes. GLONASS uses the Frequency Division Multiple Access (FDMA): two individual carrier frequencies are assigned to each satellite and the PRN-codes are the same for all satellites. Therefore, the GPS carrier frequencies are invariable ($f_{L1} = 1575.42$ MHz and $f_{L2} = 1227.60$ MHz), whereas the carrier frequencies of the GLONASS satellites are defined as:

$$f_{L1} = (1602.0 + k \cdot 0.5625)\text{MHz} \tag{3.3}$$
$$f_{L2} = (1246.0 + k \cdot 0.4375)\text{MHz}$$

with k being the frequency channel number. The ratio of the carrier frequencies on the GLONASS $L1$ and $L2$ sub-bands is $f_{L1}/f_{L2} = 9/7$; in the case of GPS the ratio is $f_{L1}/f_{L2} = 77/60$. Since two antipodal satellites can not be observed simultaneously from the same site of the Earth's surface, such pairs of satellites can transmit their signals at the same frequency

---

[1]the GLONASS carriers are often denoted also as $G1$ and $G2$ for differentiation from the GPS $L1$ and $L2$ carriers.

for preventing an interference between signals used for GLONASS, radio astronomy, and mobile satellite services (Habrich, 1999). Also therefore, a three-step shift of the GLONASS frequency band is carried out. The first step lasted until 1998: frequency channels 0 to 12, 22, 23 and 24 have been used for normal operation, and frequency channels 13, 14 and 21 were used only under exceptional circumstances. The second step was realised in the period 1998 - 2005: frequency channels 0 to 12 were in use and frequency channel 13 was allowed to use under exceptional circumstances. The recent third step is planned for beyond 2005: frequency channels -7 to +6 will be in use, with frequency channels 5 and 6 being used for special technical purposes for limited periods of time.

Information about the current GLONASS constellation status, including the slot and frequency channel numbers of the individual satellites, can be obtained from the Russian Space Agency Information-Analytical Center (IAC) web site (GLONASS, 2007). The constellation status as of mid of November 2007 is shown in Table 3.4.

Plane	Slot	k	Launch date	Input date	Outage date	Life [months]	Note
	1	07	26.12.04	06.02.05		30.3	
	2	01	10.12.03	02.02.04	19.04.07	38.3	decommissioning
	3	12	01.12.01	04.01.02	25.08.07	61.0	temporary off
I	4	06	10.12.03	29.01.04		44.9	
	5	07	01.12.01	13.02.03	09.07.06	36.1	decommissioning
	6	01	10.12.03	08.12.04		29.7	
	7	05	26.12.04	07.10.05		22.3	
	8	06	26.12.04	06.02.05		31.8	
	10	04	25.12.06	03.04.07		6.7	
II	14	04	25.12.06	03.04.07		7.2	
	15	00	25.12.06	12.10.07		0.9	
	18	10	13.10.00	05.01.01	25.05.07	66.5	decommissioning
	19	03	25.12.05	22.01.06	09.07.07	17.4	temporary off
III	21	08	25.12.02	31.01.03		53.3	
	22	10	25.12.02	21.01.03	07.02.07	46.5	decommissioning
	23	03	25.12.05	31.08.06		12.4	
	24	02	25.12.05	31.08.06		10.9	

Table 3.4: GLONASS constellation status in November 2007

The control segment

The GLONASS satellite system is operated by the System Control Centre (SCC) near Moscow and several command tracking stations located throughout the territory of Russia. The ranging data from all GLONASS satellites observed by the tracking stations are transferred to the SCC for processing. The obtained results - clock corrections, navigation messages and status information for each satellite - are transmitted back to the Command Tracking Stations and uploaded to the satellites (Habrich, 1999).

User segment

The different available GLONASS receiver types can be classified similar to GPS as single (only $L1$ signal) and dual ($L1$ and $L2$) frequency receivers, and as C/A- and/or P-Code receivers. For measuring the different satellites frequencies, the GLONASS antennas require an increased bandwidth. This must be taken into account when using combined GLONASS/GPS receivers. At present, about 60 of the permanent stations in the IGS tracking network are equipped with GLONASS/GPS receivers. Approximately half of them are located in Europe (Figure 3.6).
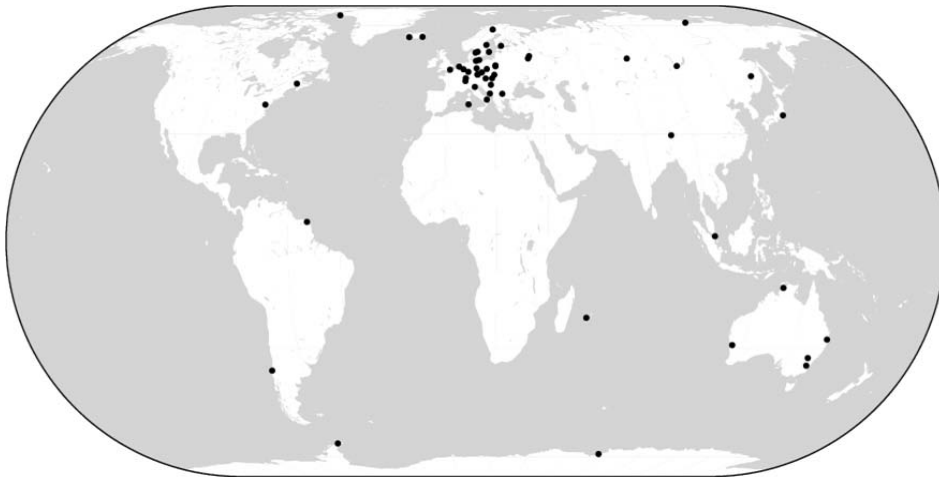
Figure 3.6: GLONASS tracking IGS stations (source: IGS, 2007)

GALILEO

With the approval of the GALILEO project financing in March 2002, the European Union (EU) initiated a new epoch of satellite navigation and geodesy. GALILEO is the future European Satellite Navigation System, to be built by the European Satellite Navigation Industries for the EU and the European Space Agency (ESA). It is expected to become operational in 2010. For more details on Galileo refer to the program's web site (GALILEO, 2007).

3.1.2 Impact of the ionosphere on the GNSS-observables

The observables of both the GPS and GLONASS navigation systems are ranges derived from measured differences in time or phase. The measurements are carried out by comparison of the signals generated by the receivers and the ones transmitted by the satellites. Since always two different clocks - at the receiver and on the satellite - are involved, the ranges are biased by the two clock errors and are thus denoted as pseudoranges. They can be modelled using fundamental observation equations and building differences in such way, that the various biases are eliminated or mitigated. Since both the time and phase ranges are affected by the ionosphere, an important task is to abolish the ionospheric bias. In this process however, the parameters of the ionosphere can be extracted and used for its monitoring. Thus, the basic steps of the GNSS observations modelling are outlined in this section, with main focus on the component related to the ionosphere study, following Schaer (1999) and Dach et al.

(2007). There are many comprehensive sources of detailed information on the topic, e.g. Hofmann-Wellenhof et al. (2001) or Kleusberg & Teunissen (1996).

Observation equations

A pseudorange, obtained when the satellite k transmitted a C/A- or P-code (respectively Y-code) and it has been registered by the receiver i, can be formulated as:

$$P = c\,(t_i - t^k) \tag{3.4}$$

where:

P	code pseudorange between the satellite k and the receiver i in length units,
c	speed of light,
t_i	time at which the signal was registered by the receiver i (as measured by the receiver clock),
t^k	time at which the signal was transmitted by the satellite k (as measured by the satellite clock),
$(t_i - t^k)$	the signal travelling time irrespective of the receiver and satellite clock errors.

The code pseudorange P can be regarded as a function of the geometric distance ρ between the satellite k and the receiver i, present at a certain GPS system time, and the delays caused by the media surrounding the Earth. Then, the code observation equation reads as:

$$P = \rho + c\,(\Delta t_i - \Delta t^k) + \Delta\rho_{trop} + \Delta\rho_{iono} + c\,(b^k - b_i) + \epsilon \tag{3.5}$$

with:

Δt^k	the satellite clock offset to the GPS system time,
Δt_i	the receiver clock offset to the GPS system time,
$\Delta\rho_{trop}$	the signal delay caused by the troposphere (i.e. the neutral atmosphere),
$\Delta\rho_{iono}$	the signal delay caused by the ionosphere,
b_i and b^k	additional delays caused by the hardware of the receiver and the satellite,
ϵ	random (residual) error.

The hardware delays b_i and b^k can not be separated from the clock offsets Δt of the individual receivers and satellites, and are therefore usually ignored, i.e. implicitly compensated by the clock corrections in single-frequency processing. The temporal stability of the hardware delays is in the order of several weeks, but in general they evolve in time.

There are several other effects that are not taken into account in (3.5) and are thus still included in the term ρ:
- relativistic effects due to the orbit eccentricity or the gravitational field;
- offsets and variations of the antenna phase centre;
- phase wind-up;
- the so-called multipath, caused by reflection of the arriving signals from terrestrial objects, such as mountains and buildings, so the signals reach the receiving antenna by two or more paths. Being a systematic effect over time spans from several minutes, over long time periods the multipath can be regarded as measurement noise. Thus, it is not an integral part

of the observation equation (3.5).

Similar to the code pseudorange, the observation equation for a carrier phase observation L can be written as:

$$L = \rho + c\left(\Delta t_i - \Delta t^k\right) + \Delta\rho_{trop} - \Delta\rho_{iono} + \lambda B + \epsilon \qquad (3.6)$$

with:

λ wavelength,
B_i^k constant bias (in cycles), which contains the carrier phase ambiguity N.

Again, the hardware delays b_i and b^k are present in the bias term λB, but can not be separated from the initial carrier phase ambiguity N. Using the substitution λB, where B is a real-valued number, one bias parameter B has to be estimated per one satellite pass registered from a receiver at one frequency. If the so-called cycle-slips occur, which are irreparable discontinuities in the carrier phase observations, additional B parameters have to be included.

The equations (3.5) and (3.6) are the fundamental GNSS observation equations. The term ρ contains geometrical information, which enables the positioning and orbit determination, as well as the recovery of the Earth rotation parameters. The information included in Δt_i and Δt^k allows time and frequency transfer over very long distances. Finally, the terms $\Delta\rho_{trop}$ and $\Delta\rho_{iono}$ contain information about the atmo- and ionosphere. It has to be noted, that the terms $\Delta\rho_{iono}$ in (3.5) and (3.6) have equal size but opposite signs, corresponding to the group delay and phase advance in the ionosphere, discussed in section 2.1.3.

Ionospheric refraction

Since the ionosphere is a dispersive medium for the electromagnetic waves, the ionospheric refraction represented by the term $\Delta\rho_{iono}$ depends on the signal frequency. The major rate of the ionospheric effect on the signals is proportional to the ratio $1/f^2$, with f being the carrier frequency. In extreme cases, this so-called first order ionospheric term can cause a positioning error of up to 20 m. The higher order ionospheric terms (Bassiri & Hajj, 1993) have a much weaker impact on the observations, and are therefore usually ignored. As shown by Hernández-Pajares et al. (2007), the effect of the second order ionospheric term appears mainly for the satellite clocks. Depending on the geographical location it can reach more than 10 mm. The impact of the second order ionospheric term on the satellite orbits consists of a global contribution of several millimetres, and the effect on the positioning is at the sub-millimetre level. In this study the second order ionospheric term will not be examined, but it has to be noted that for precise positioning with GNSS the higher order terms have to be taken into account (Mainul Hoque & Jakowski, 2007).

In order to concentrate on the ionospheric refraction in the observation equations (3.5) and (3.6), the frequency independent terms will be substituted by:

$$\rho' = \rho + c\left(\Delta t_i - \Delta t^k\right) + \Delta\rho_{trop} + \epsilon \qquad (3.7)$$

For representing the ionospheric delay related to the first frequency f_{L1} the variable I will be introduced. The effect of the ionised medium on phase and group signal propagation is

derived in section 2.1.3. Considering the relation between the total electron content in TECU and the linear change in the distance in meters given by equations (2.31) and (2.32), the absolute ionospheric delay in length units can be expressed as:

$$I = \frac{40.28 \cdot 10^{16}}{f_{L1}^2} STEC \qquad (3.8)$$

Substituting (3.7) and using the ionospheric variable I in the fundamental observation equations (3.5) and (3.6), for the P-code (P_j) and carrier phase (L_j) observations at the two different frequencies ($j = 1, 2$) we obtain:

$$P1 = \rho' + I + c\,(b_1^k - b_{i,1}) \qquad (3.9)$$
$$P2 = \rho' + \xi I + c\,(b_2^k - b_{i,2})$$

and

$$L1 = \rho' - I + \lambda_1 B_1 \qquad (3.10)$$
$$L2 = \rho' - \xi I + \lambda_2 B_2$$

The factor ξ depends on the carrier frequency ratio in the following way:

$$\xi = f_{L1}^2 / f_{L2}^2 \qquad (3.11)$$

In the case of GPS this ratio is $f_{L1}/f_{L2} = 77/60$ and the substitution yields $\xi \approx 1.647$; for GLONASS the relation is $f_{L1}/f_{L2} = 9/7$ and $\xi \approx 1.653$.

Except for the hardware delays b^k and b_i, the code observations (3.9) are unambiguous. However, the phase observations (3.10) are two to three orders of magnitude more accurate than the code measurements, which have a much higher noise. Moreover, the phase multipath is much more limited, being less than 1/4 of the wavelength (Hofmann-Wellenhof et al., 2001).

Code pseudorange smoothing

For using phase observations (3.10) instead of the noisier code pseudoranges (3.9) without carrying out an ambiguity resolution, the so-called code pseudorange smoothing can be applied. The phase-smoothed pseudorange observations are adapted from statistic comparison of continuous time series of dual-frequency code and phase measurements. This method allows the approximate determination of the ambiguities of the $L1$ and $L2$ carriers and leads to a significant reduction of the noise of the original code measurements (Schaer, 1999). The smoothed code measurements $\tilde{P}$ at the two frequencies for a certain epoch t can be derived as follows:

$$\tilde{P}1(t) = \bar{P}1 + \Delta L1(t) + 2\frac{f_{L2}^2}{f_{L1}^2 - f_{L2}^2}\,(\Delta L1(t) - \Delta L2(t)) \qquad (3.12)$$

$$\tilde{P}2(t) = \bar{P}2 + \Delta L2(t) + 2\frac{f_{L1}^2}{f_{L1}^2 - f_{L2}^2}\,(\Delta L1(t) - \Delta L2(t))$$

using the notations:

$$\Delta L1(t) = L1(t) - \bar{L}1 \tag{3.13}$$
$$\Delta L2(t) = L2(t) - \bar{L}2$$

where:

$L1(t), L2(t)$	phase measurements at epoch t,
$\bar{L}1, \bar{L}2$	mean phase measurements over a time period that encloses the epoch t, and in which no cycle-slips occurred during the satellite pass,
$\bar{P}1, \bar{P}2$	mean code measurements over the same "cycle-slips free" time interval.

The phase pseudoranges $L1(t)$ and $L2(t)$ are assumed to be free of errors. The noise of the smoothed code measurements $\tilde{P}1(t)$ and $\tilde{P}2(t)$ is reduced by a factor of about $\sqrt{k}$, with k being the number of epochs included in the terms $\bar{P}$ and $\bar{L}$, respectively. As a rule, the high temporal correlation of the smoothed code measurements results in underestimation of the standard deviations, when the observations are treated as uncorrelated.

Linear combinations

On closer examination of the fundamental observation equations (3.5) and (3.6) it appears that the differencing of one-way phase or code measurements taken quasi-simultaneously by one, two, or more receivers to one, two, or more satellites can eliminate various groups of the biasing terms. Since in this study only non-differenced observations (or the so-called zero differences) are utilised, the single, double and triple differences will not be explicated. Another method for elimination of error terms is the forming of linear combinations (LC) of the basic double-frequency carrier phase (or code) observations.

The ionosphere-free linear combination

A widely used LC is the so-called ionosphere-free linear combination, which cancels the ionospheric refraction terms I and ξI in the equations (3.9) and (3.10). The ionosphere-free liner combination is denoted as $L3$ and build as follows:

$$L3 = k_{1,3}L1 + k_{2,3}L2 \tag{3.14}$$

The coefficients $k_{j,3}$ ($j = 1, 2$) are:

$$k_{1,3} = +f_{L1}^2/(f_{L1}^2 - f_{L2}^2) \tag{3.15}$$
$$k_{2,3} = -f_{L2}^2/(f_{L1}^2 - f_{L2}^2)$$

The ionosphere-free linear combination from phase measurements on the two frequencies (3.10) with the notation (3.7) yields:

$$L3 = \rho' + \lambda_3 B_3 \tag{3.16}$$

with:

$\lambda_3 = c\,(f_{L1} + f_{L2})$ the so-called narrow-lane wavelength,

B_3 real-valued ambiguity parameter, in narrow-lane cycles.

Neglecting the hardware delays b, for the code observations (3.9) we obtain:

$$P3 = \rho' \tag{3.17}$$

The linear combination $L3$ is the most often used one, but it has to be noted that its observation noise is about three times larger than the $L1$ and $L2$ noise (Schaer, 1999). Under the assumption $\sigma(L2) = \sigma(L1)$, the $L3$ observation noise is:

$$\sigma(L3) = \sqrt{k_{1,3}^2 \sigma^2(L1) + k_{2,3}^2 \sigma^2(L2)} = \sqrt{k_{1,3}^2 + k_{2,3}^2}\,\sigma(L1) \approx 3\sigma(L1) \tag{3.18}$$

The geometry-free linear combination

For extracting the ionospheric information from the GNSS observations a linear combination is needed, which eliminates the "geometric" term ρ'. This is enabled by the so-called geometry-free linear combination $L4$, also called "ionospheric" observable. It is formed by subtracting simultaneous observations at the two carriers $L1$ and $L2$, and in this way removing all frequency-independent effects (such as clock errors, troposphere delay etc.). This leads to an observable, which contains only the ionospheric refraction and the differential inter-frequency hardware delays Δb^k and Δb_i, associated with the satellite k and the receiver i. The differential inter-frequency hardware delays are referred to as Differential Code Bias (DCB) and are usually given in ns (see section 5.4). The "ionospheric" observable has the form:

$$L4 = k_{1,4}L1 + k_{2,4}L2 = L1 - L2 \tag{3.19}$$

with $k_{1,4} = 1$ and $k_{2,4} = -1$.

Applied on the code and phase observation equations (3.9) and (3.10), the geometry-free linear combination has the form:

$$P4 = +\xi_4 I + c\left(\Delta b^k - \Delta b_i\right) \tag{3.20}$$

$$L4 = -\xi_4 I + B_4 \tag{3.21}$$

where:

$\xi_4 = 1 - \xi = 1 - f_{L1}^2/f_{L2}^2$ factor for relating the ionospheric refraction on $L4$ to $L1$,

ξ the factor (3.11),

$B_4 = \lambda_1 B_1 - \lambda_2 B_2$ ambiguity parameter with undefined wavelength, thus defined in length units,

$\Delta b^k = b_1^k - b_2^k$ differential inter-frequency hardware delay of the satellite k in time units,

$\Delta b_i = b_{i,1} - b_{i,2}$ differential inter-frequency hardware delay of the receiver i in time units.

According to (2.35) and (2.36) and using the notation (2.33), the absolute ionospheric refraction I (3.8) can be related to the vertical TEC as a function of the geomagnetic latitude and the sun-fixed longitude, and be written in the following way:

$$I = \vartheta STEC = \vartheta F(z) VTEC(\beta, s) \tag{3.22}$$

with:

$F(z)$ the mapping function (2.34) evaluated at zenith distance z,
β geomagnetic latitude,
s sun-fixed longitude.

Related to the first GPS frequency, the factor (2.33) has the value $\vartheta \approx 0.162$ m/TECU.

Consequently, the equations for the ionospheric code and phase observables (3.20) and (3.21) become:

$$P4 = +\xi_4 \vartheta F(z) VTEC(\beta, s) + c \left(\Delta b^k - \Delta b_i \right) \tag{3.23}$$

and

$$L4 = -\xi_4 \vartheta F(z) VTEC(\beta, s) + B_4 \tag{3.24}$$

The geometry-free linear combination applied on the phase smoothed code observations (3.12) can be accordingly rewritten and the result is identical with (3.23):

$$\tilde{P}4 = +\xi_4 \vartheta F(z) VTEC(\beta, s) + c \left(\Delta b^k - \Delta b_i \right) \tag{3.25}$$

Since in this study the function $VTEC(\beta, s)$ is represented as a spherical harmonic expansion (2.36), the unknown parameters in the observation equations (3.23), (3.24), and (3.25) are:

- the unknown coefficients of the SH expansion a_{nm} and b_{nm} (see section 2.2.2);

- the satellite and receiver DCB or the ambiguity parameter B_4.

In order to separate the unknown SH coefficients from the DCB or the ambiguity parameter, GNSS data over a longer time span need to be processed.

For a general overlook, the influence of ionospheric refraction from 1 TECU on the different linear combinations, formed as $LC = k_1 L1 + k_2 L2$, is given in Table 3.5. $L1$ and $L2$ are the basic carriers, $L3$ is the ionosphere-free linear combination, $L4$ the geometry-free, and $L5$ - the so-called wide-lane linear combination. The combinations $L3$ and $L4$ shown in the table, are the so-called narrow-lane LCs, where the ambiguities are previously resolved.

40

LC	k_1	k_2	Ionospheric path delay		
			[m]	[ns]	[cycles]
$L1$	1.00	0.00	-0.162	-0.542	-0.853
$L2$	0.00	1.00	-0.267	-0.892	-1.095
$L3$	2.55	-1.55	-	-	-
$L4$	1.00	-1.00	0.105	0.354	1.948
$L5$	4.53	-3.53	0.208	0.695	0.248

Table 3.5: Ionospheric delay on different linear combinations caused by 1 TECU (after Schaer, 1999)

3.1.3 Ionosphere Working Group at the International GNSS Service

In 1998 a special Ionosphere Working Group (WG) of the IGS was initiated for developing ionospheric products, as described by Feltens & Schaer (1998) and Hernández-Pajares (2004). The main products provided on a regular basis by the IGS ionospheric WG are Global Ionospheric Maps (GIM), representing the vertical TEC over the entire Earth as a two-dimensional raster in latitude and longitude in two-hourly snapshots, as well as the corresponding RMS maps. Additionally, daily and monthly values of the satellites and receivers DCB are provided.

At present, four IGS Associate Analysis Centres (AAC) evaluate global maps of the vertical TEC and provide them in the IONospheric EXchange (IONEX) format (Schaer et al., 1998). For each day 13 two-hourly maps are developed and stored in one daily file. The first reference epoch of each map is 0:00 UT on the regarded day, the last reference epoch is 0:00 UT on the next day. A brief description of the estimation strategy of the individual AAC is given in the header of each IONEX file:

- Centre for Orbit Determination in Europe (CODE), (Schaer, 1999): the GIM are generated on a daily basis using GPS and GLONASS data from about 150 stations of the IGS and other institutions (GLONASS observations are introduced in the maps since mid 2003). The VTEC is modelled in a solar-geomagnetic reference frame using a spherical harmonics expansion with maximum degree and order 15, i.e. 13×256, or 3328 parameters are computed for representing the global VTEC distribution. For representation in the time domain piece-wise linear functions with time spacing of their vertices of two hours, conforming with the epochs of the VTEC maps, are used. The differential P1-P2 code biases (DCB) for all GPS and GLONASS satellites and for the ground stations are estimated as constant values for each day; the DCB datum is defined by a zero-mean condition imposed on the satellite bias estimates. If needed, P1-C1 bias corrections are taken into account. A modified single-layer model mapping function approximating the JPL extended slab model mapping function, evaluated at geodetic satellite elevation angles, is adopted to convert the slant into vertical TEC. For the computation of the ionospheric pierce points, a spherical layer with a radius of 6821 km is assumed, implying geocentric, not geodetic IONEX latitudes. The GIM results correspond to the results for the last day of a 3-day combination analysis solving for 37×256, or 9472 VTEC parameters and one 24-hours common set of satellite and receiver DCB constants. The used observable is one-way carrier phase levelled to code.

- European Space Agency (ESA), (Feltens, 1998): a spherical harmonic model using data

from about 170 GPS stations is developed. The maximum degree and order of the spherical harmonic expansion is 15. Carrier phase levelled to code observables are used. The DCB are estimated in a separate fit and the values are related to the mean over all PRNs for which the DCB were estimated.

- Jet Propulsion Laboratory (JPL), (Mannucci et al., 1998): Global Ionospheric Maps are generated on an hourly and daily basis using data from up to 100 GPS sites of the IGS and others institutions. The vertical TEC is modelled in a solar-geomagnetic reference frame using bi-cubic splines on a spherical grid. A Kalman filter is used to solve simultaneously for instrumental biases and VTEC on the grid as stochastic parameters. One-way carrier phase levelled to code observables are used.

- Universidad Politécnica de Cataluña (UPC), (Hernández-Pajares et al., 1999): the VTEC is modelled independently for each station with a three-dimensional voxel model consisting of 72×9×2 cells in local time, latitude and height, with height boundaries of 59-739-1419 km. The used observables are phase differences (*L*1-*L*2). The DCB vanish in this approach and are thus computed as post-fit residuals.

At present, the combined IGS solution, which is available since the end of 2005, is evaluated at UPC. The combined TEC is calculated as weighted mean of the input TEC values; the reference for the DCB is $\sum DCB_{sat} = 0$.

Two types of ionospheric TEC grid are provided by the IGS AAC: rapid maps, updated daily and with a latency of less than 24 hours, and final GIM updated weekly and with latency of about eleven days. The provided accuracy is 2 - 9 TECU for the rapid and 2 - 8 TECU for the final GIM. The ionospheric grid maps can be downloaded via anonymous ftp from the Crustal Dynamics Data Information System (CDDIS) at NASA GSFC (CDDIS, 2007).

The IONospheric EXchange (IONEX) format

The GIM produced by the IGS AAC within the ionospheric WG are provided in the IONospheric EXchange (IONEX) format, described in Schaer et al. (1998). The vertical TEC is represented as a function of geocentric longitude and latitude (λ, β), and time (t) in UT in the form of a raster grid. The raster resolution is $\Delta\lambda = 5°$, $\Delta\beta = 2.5°$ and $\Delta t = 2^h$. The method for interpolation of the VTEC for a given epoch T_i with $i = 1, 2, ..., n$, recommended in Schaer et al. (1998), is interpolating between consecutive rotated TEC maps. It can be formulated as follows:

$$VTEC(\beta, \lambda, t) = \frac{T_{i+1} - t}{T_{i+1} - T_i} VTEC_i(\beta, \lambda_i') + \frac{t - T_i}{T_{i+1} - T_i} VTEC_{i+1}(\beta, \lambda_{i+1}') \qquad (3.26)$$

with $T_i \leq t < T_{i+1}$ and $\lambda_i' = \lambda + (t - T_i)$. When using this interpolation method the GIM are rotated by $t - T_i$ around the Z-axis. The aim of that rotation is to compensate the strong correlation between the ionospheric activity and the position of the Sun. As for the grid interpolation, a simple four-point interpolation formula can be applied, since the IONEX grid is sufficiently dense:

$$VTEC(\lambda_0 + p\Delta\lambda, \beta_0 + q\Delta\beta) = (1-p)(1-q)VTEC_{0,0} +$$
$$+ p\,(1-q)VTEC_{1,0} + (1-p)\,q\,VTEC_{0,1} + p\,q\,VTEC_{1,1} \qquad (3.27)$$

$\Delta\lambda$ and $\Delta\beta$ denote the grid widths in longitude and latitude; $0 \le p < 1$ and $0 \le q < 1$.

The header section of the IONEX file contains global information about the GIM, such as estimation method, contributing stations, DCB values, etc. In the mandatory section "`IONEX VERSION / TYPE`", which is the first record in the IONEX file, also the used technique or theoretical method must be specified. Up to now, the techniques used by the Analysis Centres are either "`'GPS'`", or "`'GNSS'`" (in the case of the AAC CODE). Nevertheless, an entry of the type "`'MIX': MIXed/combined`" is allowed as well. It is used in the IGS combined GIM, denoting that the solution is derived as a combination of the different AAC's GIM. In the case of the combined GIM computed within this study however, the entry "`'MIX'`" in the "`IONEX VERSION / TYPE`" section of the IONEX files stands for a combined GNSS/satellite altimetry GIM (see Appendix A).

3.2 Observing of the ionosphere with satellite altimetry

The satellite altimetry is a particular way of ranging; what is measured is the vertical distance between a satellite and the ocean surface (Seeber, 1993). The specific characteristic of the method is that no ground stations are required - the measurements are carried out from the altimeter on-board the satellite directly to the Earth's surface. The range between the satellite and the Earth surface is derived from the travelling time of the radar impulse transmitted by the radar-altimeter and reflected from the ground. The method is best applicable over the oceans, due to the good reflective properties of water. The signals are transmitted permanently in the high frequency domain (about 14 GHz) and the echo from the sea surface received by the satellite is used for deriving the round-trip time between the satellite and the sea. The satellite-to-ocean range is obtained by multiplication of the travelling time of the electromagnetic waves with the speed of light and averaging the estimates over a second. The pulse length is a few ns, resulting in a single range measurement resolution of about 0.1 to 1 m. After correcting for the tropo- and ionospheric refractions, the accuracy of the final range is within 20 mm. The knowledge of the satellite orbital trajectory allows obtaining the separation between the mean sea level and the Earth's ellipsoid as difference between the satellite's altitude above the ellipsoid and the measured range (Figure 3.7). Generally, the altitude of the satellite above the reference ellipsoid is provided with an accuracy of about 30 mm. The height from the real sea surface to the reference ellipsoid is denoted as Sea Surface Height (SSH). For a more precise evaluation, the separation between the instantaneous sea surface height and the geoid, as well as the deviations between the real satellite orbital trajectory and the computed orbit, have to be modelled.

Though the initial aim of the space-borne altimeters is the accurate measurement of the sea surface height, the two separate operation frequencies give the opportunity for obtaining information about the total electron content along the ray path as well. Further geodetic

applications of the satellite altimetry are e.g.:

- mapping the sea surface and monitoring the global seasonal and mean sea level changes;

- determination of the Earth's gravity field;

- detection of reference system offsets through investigation of crossovers (crossing of two sub-satellite tracks);

- unification of height systems;

- monitoring the geocentre variations.

Detailed information on satellite altimetry applications can be found in e.g. Hwang et al. (2004).
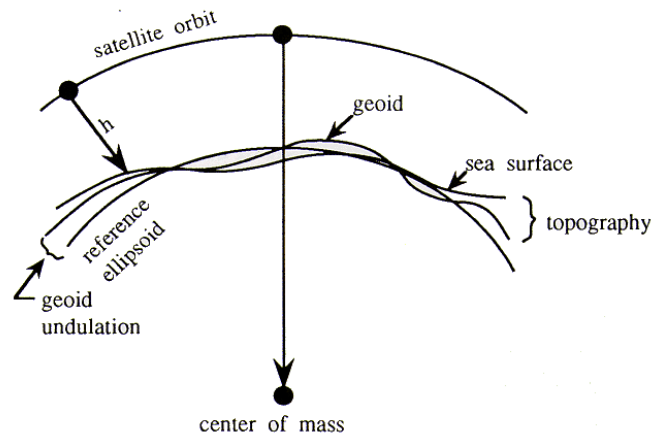
Figure 3.7: Schematic principle of satellite altimetry

3.2.1 Satellite altimetry missions

The first satellite-borne altimeter missions were the US SKYLAB, consisting of three satellites launched in the period 1973-1974, and GEOS-3 (launched 1975), followed by SEASAT in 1978 and GEOSAT in 1985. As part of several international oceanographic and meteorological programmes a number of satellite altimetry missions were launched in the nineties: ERS-1 (1991-1996), Topex/Poseidon (1992) and ERS-2 (1995). The most recent Jason-1 mission, which is the follow-on to Topex/Poseidon, was launched in 2001. On the contrary to the ERS-1 and ERS-2 missions, the satellites Topex/Poseidon and Jason-1 carry two-frequency altimeters, which give the opportunity to measure the electron density along the ray path. The planed launch date of Jason-2 - the next-generation NASA ocean altimetry mission which will be the follow-on to Jason-1, is the 16th of June 2008 (AVISO, 2007). Jason-2's orbit will be identical to that of Jason-1.

The Topex/Poseidon and Jason-1 missions

The Topex/Poseidon satellite (Figure 3.8) was launched on 10 August 1992 with the objective of "observing and understanding the ocean circulation" (AVISO, 2007), as a joint project be-

tween NASA and the French space agency CNES. The satellite was equipped with two radar altimeters and precise orbit determination systems, including the DORIS system. In September 2002 Topex/Poseidon assumed a new orbit midway between its original ground tracks, so the former Topex/Poseidon ground tracks could be taken over by the Jason-1 mission, launched in December 2001. The tandem mission ended in October 2005, due to a failure in a Topex/Poseidon pitch reaction wheel. Nevertheless, the mission exceeded by far its planned life time of five years.
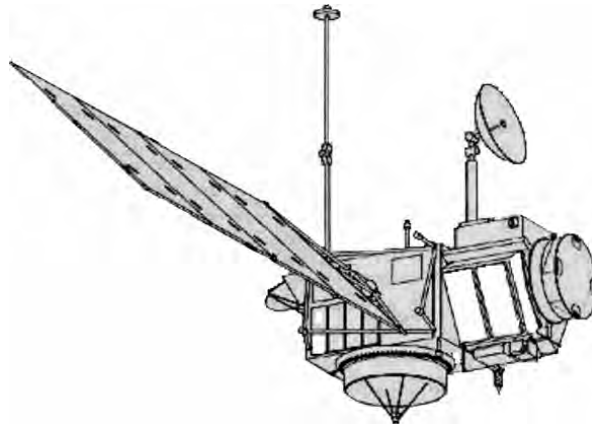
Figure 3.8: The Topex/Poseidon satellite

Jason-1 (Figure 3.9) is the first satellite of a series designed to ensure continuous observation of the oceans for several decades. It has inherited its main features - orbit, instruments, measurement accuracy, etc. - from its predecessor Topex/Poseidon. The orbit altitude of the two missions is 1336 km with an inclination of 66°. Being on the so-called "repeat orbit", the satellite passes over the same ground position every ten days. The orbit is prograde and not Sun synchronous. The adopted reference ellipsoid has an equatorial radius of 6378.1363 kilometres and a flattening coefficient of 1/298.257.
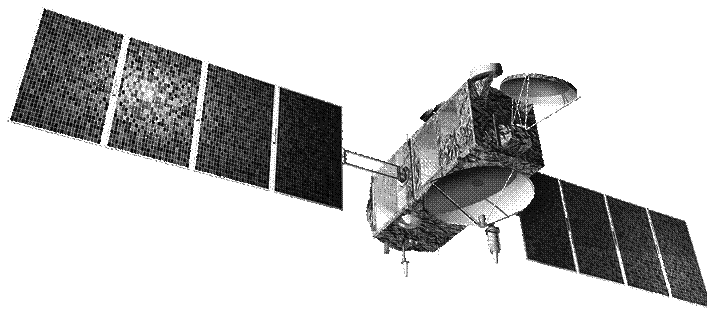
Figure 3.9: The Jason-1 satellite, credit: AVISO (2007)

3.2.2 Ionosphere parameters gained from dual-frequency observations

The primary sensor of both Topex/Poseidon and Jason-1 is the NASA Radar Altimeter, operating at 13.6 GHz (Ku-band) and 5.3 GHz (C-band), simultaneously (Fu et al., 1994). It is

the first space-borne altimeter that uses two-channel measurements to compute the effect of ionospheric free electrons in the satellite range measurements (AVISO/Altimetry, 1996). The measurements obtained from the radar altimeter are: the altimeter range, the significant wave height, the wind speed magnitude, the backscatter coefficient, and the ionospheric correction, since the two widely separated frequencies allow TEC to be detected directly from the nadir altimetry sampling data along the satellite track (Imel, 1994).

Similar to GNSS, the ionospheric effect on the Topex/Poseidon and Jason-1 measurements is proportional to the TEC along the ray path and inversely proportional to the square of the altimeter frequency. At the Ku-band (13.6 GHz), the sensitivity of the range delay to the TEC is 2.2 mm/TECU. Thus, the range at this signal can be over-estimated with 2 to 40 cm due to the ionosphere (Brunini et al., 2005). The ionospheric effect estimated in millimetre from measurements at two frequencies is expected to be negative, but positive values are allowed up to +40 mm to accommodate instrument noise effects. According to Imel (1994), the precision of the Ku-band range delay correction in one-second data averages is about 5 TECU or 1.1 cm. In fact, the precision of the satellite altimetry derived TEC estimates is a more complex issue, since it might be affected by systematic effects. A systematic error which might bias the TEC estimates due to its frequency dependence is the so-called Sea State Bias (SSB) (Chelton et al., 2001).

The Sea State Bias (SSB)

For typical wave heights, the diameter of the altimeter footprint on the sea surface is about 3-5 km. The measurements are taken approximately once per second along track, which gives a spacing of about 6 km. Due to this large footprint of the radar measurements, the sea surface scattering elements do not contribute equally to the radar return. Since troughs of waves tend to reflect altimeter pulses better than do crests, the centroid of the mean reflecting surface is shifted away from mean sea level towards the troughs of the waves. Due to this shift, the altimeter over-estimates the height of the satellite above the sea surface and the SSB emerges as difference between the apparent sea level as measured by the altimeter and the true mean sea level (AVISO/Altimetry, 1996). Being a function of the significant wave height and other sea-state related parameters linked to the electromagnetic properties of the sea surface, the SSB varies with the radar frequency. Still, the theoretical understanding of the SSB is quite limited and the most accurate SSB estimates are obtained through empirical models (Gaspar et al., 1994). In AVISO (2007) the SSB at the Ku-band is represented as:

$$\text{SSB} = \text{SWH} \left(a_1 + a_2 U + a_3 U^2 + a_4 \, \text{SWH} \right) \quad [\text{m}] \tag{3.28}$$

where:

U	wind intensity in m/s,
SWH	Significant Wave Height in meters,
a_i	empirically derived parameters.

The typical SWH values are between 1 and 5 m, whereas the lower values occur close to the equator and the highest - in the southern polar ocean (Brunini et al., 2005). According to Chelton et al. (2001), the level of the SSB is at about 1% of the SWH, which in extreme cases can lead to an error of up to 5 TECU in the TEC estimates. The corresponding errors in the

estimation of the absolute sea surface height can reach 5 cm and thus, the uncertainty of the SSB is regarded as one of the major challenges in the satellite altimetry.

For this work the ionospheric corrections derived from the Topex/Poseidon and Jason-1 missions are provided by the Altimeter Database System (ADS), operated by the Geo-ForschungsZentrum Potsdam (GFZ) (ADSCentral, 2007). In particular, the so-called "DUFT" correction is used. It is derived from the double-frequency altimeter measurements provided by the data centers, and filtered with a median of 100 km filter length. The range data used for the calculation of the correction is corrected for the SSB using the standard SSB correction. The ionospheric range delay dR derived from the altimeter measurements at the two frequencies is directly provided in mm, and has to be transformed into TECU according to (2.33). It has to be noted, that in the case of satellite altimetry derived TEC no mapping function is needed, since the measurements are carried out normal to the sea surface and thus, the ray path is assumed vertical. Consequently, the transformation formula is:

$$VTEC_{alt} = -dR \cdot 10^{-3} \frac{f_{Ku}^2}{40.28 \cdot 10^{16}} \quad [\text{TECU}] \tag{3.29}$$

with f_{Ku} being the Ku-band carrier frequency in Hz. The rough outliers in the "raw" VTEC estimates obtained from ADS are removed using a simple polynomial-fitting procedure.

3.2.3 TEC from satellite altimetry versus GNSS TEC - key issues

The TEC estimates from GNSS and from satellite altimetry measurements have often been compared in order to asses the precision of the two techniques (e.g. Brunini et al., 2005). Generally, the agreement between GNSS and altimetry derived TEC is good, but there are still some contradictions, which need further investigation. One important topic is the better understanding of the frequency-dependent systematic errors in the altimetry measurements, which would bias both the sea-level height and the TEC estimates (Chelton et al., 2001). Theoretically, the TEC values obtained by satellite altimetry are expected to be lower than the ones coming from GNSS, since opposite to GNSS the altimetry satellites do not sample the topside ionosphere due to their lower orbit altitude. However, several studies have shown that T/P and Jason-1 systematically overestimate the vertical TEC by about 3-4 TECU compared to the values delivered by GNSS (e.g. Azpilicueta et al., 2006; Brunini et al., 2005). On the other hand, most of the ionosphere models from GNSS data are based on the single layer model described in section 2.2.1, which does not account well for the ionospheric contribution above the altitude of the altimetry missions (Brunini et al., 2005). Furthermore, it has to be pointed out that when using SLM the STEC values derived from GNSS measurements have to be converted into vertical TEC, while the altimetry missions deliver directly the vertical values. The mapping function (2.34) used for this convertion is a potential error source for the GNSS TEC estimates. Finally, for comparing with altimetry TEC the values derived from GNSS have to be interpolated for regions above the oceans, which are usually far from the observing stations, i.e. such comparisons are performed in the worst scenario for GNSS. The differences between GNSS and altimetry derived TEC as well as the systematic error of the Jason-1 and Topex/Poseidon satellites are investigated in more detail in Part II.

3.3 Other space geodetic techniques providing ionosphere information

Along with GNSS and the satellite altimetry missions, several other space geodetic techniques can be used for investigation of the ionosphere. Their different observation principles result in specific features of the derived ionosphere parameters. The appropriate handling of these specifics would allow the integration of the provided ionospheric data and the development of a combined model with global coverage, higher accuracy and reliability. Such integration follows the global objective in geodetic science defined by IAG in the GGOS project (GGOS, 2007) and is the matter of our further studies. In this section a brief outline of the techniques LEO, VLBI, and DORIS and their potential in terms of ionosphere modelling will be given.

Low Earth Orbiters (LEOs)

Low Earth orbiting satellites operate at orbital altitudes between 500 and 2 000 km. One of their primary science objectives is the global sounding of the vertical layers of the neutral atmosphere and the ionosphere. The mission CHAMP, launched in 2000, and the follow-up missions GRACE (2001) and GOCE (2007) are equipped with ion drift meters and magnetometers in order to study the solar terrestrial environment. However, the most important issue of the LEOs concerning the ionosphere modelling is the opportunity for global monitoring of the vertical electron density distribution by using GPS radio occultation (Wickert et al., 2006). The radio occultation technique, based on the observation of the refractivity or bending of GPS signals, allows the extension of the three dimensional global ionosphere maps based on the SLM to a four dimensional model of the ionosphere, representing it in latitude, longitude, time, and height (see also section 2.2.1 and references there).
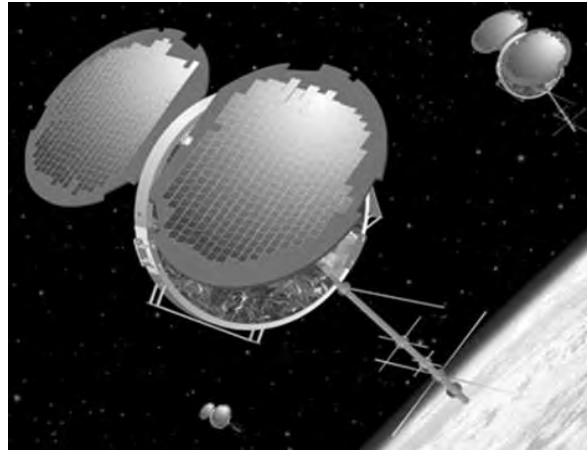
Figure 3.10: FORMOSAT-3/COSMIC satellites, artists' illustration (source: UCAR, 2007)

One of the primary scientific goals of the spacecrafts SAC-C (2000), equipped with the GPS Occultation and Passive Reflection Experiment (GOLPE) instrument, and the FORMOSAT-3/COSMIC mission launched in 2006 (Figure 3.10) is to obtain vertical profiles of the electron density in near real time through GPS radio occultation. The joint Taiwan - US project Constellation Observing System for Meteorology Ionosphere and Climate (COSMIC)/Formosa Satellite 3 (FORMOSAT-3) is a six-satellite radio occultation mission. Through the GPS

radio occultation technique FORMOSAT-3/COSMIC provides up to 2 500 ionospheric electron density profiles daily. The TEC between the COSMIC and the GPS satellites in view is derived from phase and pseudorange measurements, which are sampled in one-second intervals. In the early phase of the mission, the displacement between the COSMIC satellites was smaller than it will be in the final configuration. Hence, the unique opportunity for estimating the precision of the radio occultation remote sensing technique from closely collocated occultations (with separation of the tangent points smaller than 10 km) was provided. According to Schreiner et al. (2007), the RMS difference of electron density in the ionosphere between 150 and 500 km altitude for collocated occultations is about 10^3 cm^{-3}. By the end of 2007, the COSMIC satellites are expected to reach their final configuration in six different orbital planes and provide the projected global coverage.

Very Long Baseline Interferometry

After the first intercontinental experiments with Very Long Baseline Interferometry (VLBI) in the seventies it became clear, that besides the astronomical and astrophysical applications the method has also a big potential in the field of geodesy and geophysics. VLBI allows the measurement of distances in the magnitude of several thousands of kilometres with millimetre accuracy, ensuring highly precise coordinates. The technique is based on the observation of radio signals from extragalactic sources (galaxies or quasars), which are detected after travelling to the Earth for millions of light-years. Virtually, the sources are endlessly distant from the Earth and it can be therefore accepted that the signals reach the radio telescopes in the form of parallel wave fronts (Figure 3.11). The difference τ between the arrival of the signals at telescopes A and B is measured with hydrogen maser clocks with an accuracy of about 10^{-11} sec. By multiplying the time difference τ with the radio signal velocity, the difference in the paths of the two wave fronts is obtained and the distance between the telescopes can be calculated. The relative positions of points A and B are derived from multiple observations to sources in three or more different directions. The data are then processed in the so-called correlators (Hobiger, 2005).
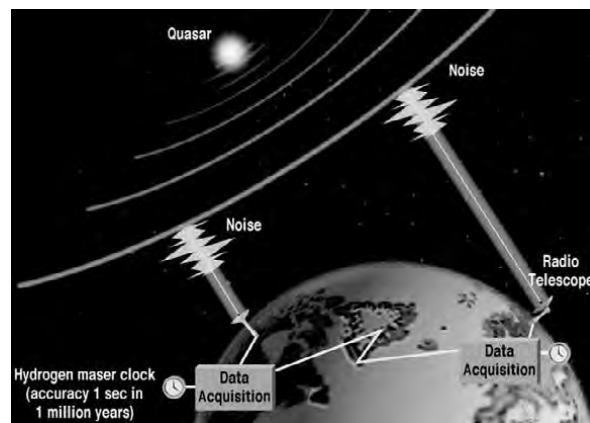
Figure 3.11: Principle of VLBI (source: IVS, 2007)

Geodetic VLBI observations are carried out at two distinct frequencies - 8.4 GHz and 2.3 GHz or the so-called S- and X-band - in order to determine ionospheric delay corrections. The ionospheric delay corresponds to the TEC along the ray path through the ionosphere. Since

VLBI is a differential technique however, the observed ionospheric delays represent the differences in the behaviour of the propagation media above each two stations. Additionally, there is a constant instrumental delay offset per baseline that contributes to the observed ionospheric delay. The instrumental offset is independent on the azimuth and elevation in which the antenna points, so one can separate it from the variable ionospheric parameters for each station and estimate it as an additional unknown. The observation equation at a certain time t can be written as (Hobiger et al., 2006):

$$\tau_{model}(t) = \tau_{ion,1}(t) - \tau_{ion,2}(t) + \tau_{offset,1}(t) - \tau_{offset,2}(t) \tag{3.30}$$

Consequently, the ionospheric refraction over station i at the X-band - with f_x being the carrier frequency in Hz - can be modelled as:

$$\tau_{ion,i} = \frac{1.34 \cdot 10^{-7}}{f_x^2} STEC_i \tag{3.31}$$

As shown by Hobiger et al. (2006), the TEC values derived by VLBI agree well with the outcomes from GPS and satellite altimetry measurements. Therefore, after considering its specific characteristics VLBI can be incorporated in a combined model for complementing the data derived from other techniques.

Doppler Orbitography and Radiopositioning Integrated by Satellite (DORIS)

DORIS is a Doppler satellite tracking system, developed for precise orbit determination and precise ground location. In 2003 the International DORIS Service (IDS) was established as an IAG service (IDS, 2007). DORIS is incorporated on board the Jason-1 and ENVISAT altimetry satellites and the remote sensing satellites SPOT2, SPOT4, and SPOT5; it also flew with SPOT3 and Topex/Poseidon. The satellites Jason-1, ENVISAT and SPOT5, launched in the period 2001-2002, are equipped with the new generation of DORIS receivers. The increase in the satellite constellation significantly improved the performance in the precise point positioning, achieving a precision of about 10 mm for weekly station coordinates (Tavernier et al., 2005). The main measuring frequency of DORIS is set at 2036.25 MHz; a second frequency for error corrections is set at 401.25 MHz, which allows deriving the ionospheric correction (Berthias, 2000). Most notably, the homogeneous global distribution of the more than 50 DORIS ground stations (Figure 3.12) would be of great value for the regular resolution of a future integrated ionosphere model.

Figure 3.12: DORIS ground stations network (source: Tavernier et al., 2007)

Chapter 4

Inter-technique combination

4.1 Recapitulation of the Least Squares Adjustment

The least squares adjustment is used in this work for deriving ionosphere models. In this section the utilised algorithm for parameter estimation will be presented in brief, mostly following Schaer (1999). For more details on parameter estimation refer to e.g. Koch (1999).

Having a one-dimensional array of actual observations L with the array of their corrections V (called also residual vector), we can fit them to a vectorial model function $\Phi(x)$ using the observation equation system:

$$L + V = \Phi(x) \tag{4.1}$$

and obtain the adjusted observations $\bar{L} = L + V$. Here, $x = x_0 + dx$ are the unknown parameters of the adjustment with:

$\quad x_0 \quad$ array of approximate values of the model parameters,
$\quad dx \quad$ array of the model parameters corrections with respect to the approximate values x_0.

The vector x is also referred to as solution vector.

Through linearising (4.1) we obtain:

$$L + V = \Phi(x_0) + A\,x \tag{4.2}$$

A is the first design matrix, defined as:

$$A = \left. \frac{\partial \Phi(x)}{\partial x} \right|_{x=x_0} \tag{4.3}$$

When the linearised equation system (4.2) is solved for the vector V, the following equation system results:

$$V = A\,x - (L - \Phi(x_0)) = A\,x - l \tag{4.4}$$

The term $l = L - \Phi(x_0)$ is denoted as "observed minus computed".

The corresponding stochastic model is formulated as:

$$P = Q_{ll}^{-1} = \sigma_0^2 \, C_{ll}^{-1} \tag{4.5}$$

with:

P	weight matrix of the observations,
Q_{ll}	cofactor matrix of the observations,
σ_0	a priori standard deviation of unit weight,
C_{ll}	covariance matrix of the observations.

For uncorrelated observations the matrix P is a diagonal matrix with diagonal elements $P_{ll} = \sigma_0^2/\sigma_l^2$ and σ_l^2 being the a priori variance of the l-th observation. If the observations are not only uncorrelated but also of equal accuracy the weight matrix P is replaced by the identity matrix I.

Following the basic principle of the least squares adjustment, the equation system (4.4) is solved by minimising the scalar function $V^T P V$:

$$[V^T P V] = min \tag{4.6}$$

Taking into account (4.4), the scalar function can be rewritten in the following way:

$$\begin{aligned} V^T P V &= (x^T A^T - l^T) P (Ax - l) = \\ &\quad x^T A^T P A x - x^T A^T P l - l^T P A x + l^T P l \end{aligned} \tag{4.7}$$

For achieving the minimum, the first derivative with respect to x must be set to zero:

$$\frac{\partial(V^T P V)}{\partial x} = 2 A^T P A x - 2 A^T P l = 0 \tag{4.8}$$

From the derivation we obtain the so-called normal equation:

$$(A^T P A)x - A^T P l = N x - b = 0 \tag{4.9}$$

where:

$N = A^T P A$	normal equation matrix,
$b = A^T P l$	right hand side of the normal equation system.

Hence, the solution vector is:

$$x = (A^T P A)^{-1} A^T P l = N^{-1} b \tag{4.10}$$

The estimated standard deviation of unit weight (also referred to as σ a posteriori) results from:

$$\bar{\sigma}_0 = \sqrt{\frac{V^T P V}{r}} \qquad \text{for} \qquad r > 0 \tag{4.11}$$

where $r = n - u$ denotes the degree of freedom of the least squares adjustment with n being the total number of observations and u - the number of unknown parameters.

The estimated covariance matrix of the adjusted parameters can be obtained as:

$$C_{xx} = \bar{\sigma}_0^2 \, Q_{xx} = \bar{\sigma}_0^2 \, N^{-1} \tag{4.12}$$

and Q_{xx} is called cofactor matrix of the model parameters.
The standard deviation of each individual model parameter is estimated as:

$$\bar{\sigma}_x = \sqrt{C_{xx}} = \bar{\sigma}_0 \sqrt{Q_{xx}} \tag{4.13}$$

with C_{xx} and Q_{xx} being the corresponding diagonal elements of the covariance and cofactor matrices.

For a particular function $f = Bx + f_0$ the general variance-covariance propagation law is:

$$C_{ff} = B \, C_{xx} \, B^T \tag{4.14}$$

Due to the relation between the covariance and cofactor matrices (which is $C = \sigma_0^2 \, Q$), equation (4.14) can be accordingly rewritten using the cofactor matrices Q instead of the covariance matrices C.

In the particular case of that work, the function Φ corresponds to the spherical harmonic expansion (2.36), described in section 2.2.2. The unknown model parameters are the coefficients of the SH expansion a_{nm} and b_{nm}, as well as the satellite and receiver DCB (see section 3.1.2).

4.2 Combination strategy

For the combination of GNSS and altimetry data the least-squares adjustment is applied on each set of observations and then the individual normal equations are combined. This is done by adding the relevant normal matrices N obtained from the two types of observations:

$$N_{comb} = N_{gnss} + N_{alt} = A_{gnss}^T \, P_{gnss} \, A_{gnss} + A_{alt}^T \, P_{alt} \, A_{alt} \tag{4.15}$$

where N and A are the corresponding normal and design matrices, and P is the weight matrix.

It has to be pointed out that with the chosen mathematical approach the development of daily global VTEC maps based only on altimetry data is unfeasible. When using spherical harmonic expansion as a model function, the observations must be to a greater or lesser extent globally distributed. Even if data from more than one satellite altimetry mission is available, the daily data coverage in the sun-fixed reference frame will be quite limited. As an illustration, Figure 4.1 shows the VTEC obtained from the missions Topex/Poseidon, Jason-1, ERS and GFO for the day 296 in 2002. In the case of ERS and GFO the VTEC values are based on external models; from Topex/Poseidon and Jason-1 the original measurements are shown. The upper two plots in Figure 4.1 demonstrate the VTEC as a function of the

geographical latitude β and longitude λ on the left hand side, and of the geographical latitude β and the sun-fixed longitude s on the right hand side. In the lower plots the corresponding altimeter footprints are shown.
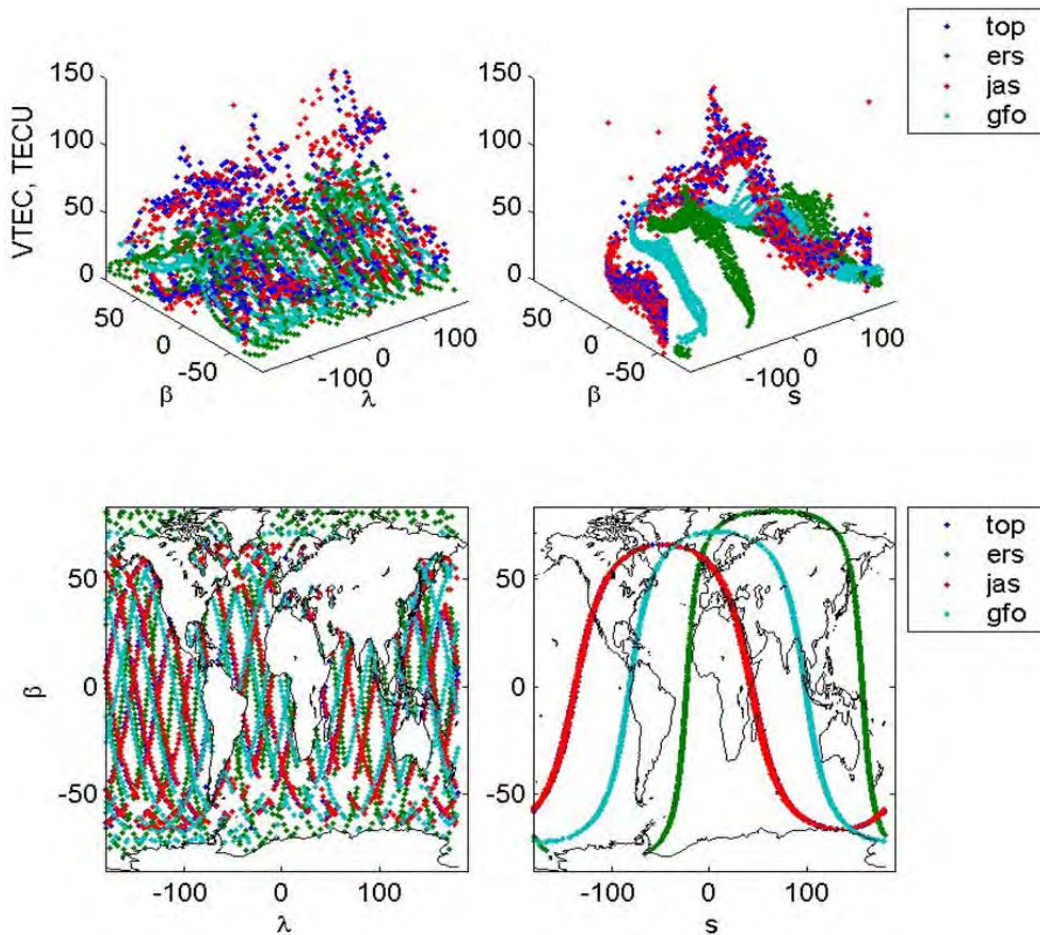
Figure 4.1: Upper plot: altimetry derived VTEC data in geographical (right) and sun-fixed (left) reference frame; lower plot: altimeter footprints in geographical (right) and sun-fixed (left) reference frame

The combination on normal equation level allows the independent estimation of the technique-specific constant time delays, such as the DCB, and can thus be used to indicate and model the technique-specific systematics. Taking into account that Jason-1 and Topex/Poseidon seem to generally overestimate the TEC compared to GNSS (see section 3.2.3), it can be assumed that the altimetry measurements are biased by a constant instrumental offset. Using the combination procedure, realised by stacking of the normal equations (4.15), it is possible to develop combined ionosphere models with additional estimation of daily offsets for the altimetry satellites, similar to the GNSS DCB. As illustrated in Figure 4.2, only the spherical harmonic coefficients are affected by the combination, whereas the DCB and the altimetry offsets remain independent. If these altimetry offsets are computed daily as a single value per altimetry satellite, they will include the plasmaspheric component additionally to the actual instrumental delay. This issue is discussed in more detail in chapter 6.
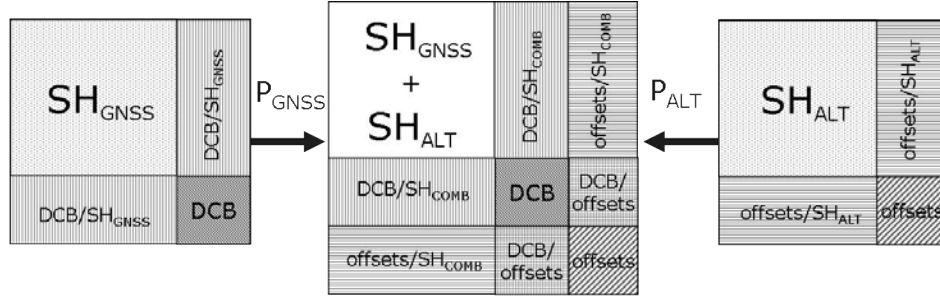
Figure 4.2: Combination of normal equations - schematic representation of the normal equation matrices

4.3 Constraints and weighting

Constraining single parameters

In the course of a parameter estimation problem, it might become necessary certain "artificial" observations to be added to the system. Such terms, also called "pseudo" observations, are used for introducing particular a priori information - such as predisposed values - for some of the model parameters. The pseudo observations have a certain variance and have to be applied to the observation equation system (4.2). For them, the "observed minus computed" value is usually zero (e.g. when the change of the pseudo observation with respect to the a priori value is used as parameter). Therefore, the corresponding diagonal element of the normal equation matrix N has to be extended by the weight:

$$W = \frac{\sigma_0^2}{\sigma_{abs}^2} \tag{4.16}$$

Eventually, the observations number n as well as the degree of freedom r have to be increased by the number of the pseudo observations. In that work, such constraint is used for defining the DCB datum (see section 5.4.1).

Constraining linear combinations of parameters

If instead of a single model parameter, the difference of two parameters has to be constrained, the weight W becomes a 2×2 weight matrix in the form:

$$W = \begin{pmatrix} W & -W \\ -W & W \end{pmatrix} \qquad \text{where} \qquad W = \frac{\sigma_0^2}{\sigma_{abs}^2} \tag{4.17}$$

For introducing the matrix (4.17) in the normal equation matrix N, the values W and $-W$ have to be added to the diagonal and off-diagonal elements that correspond to the pair of parameters concerned. Again, the observations number n as well as the degree of freedom r have to be incremented by one. Any linear combination of model parameter can be constrained

in that way. The above-quoted pseudo observations are used in that work for limiting the variability of consecutive VTEC maps, as described in section 4.3.

Weighting

At this stage of the work equal weights ($P_{gnss} = 1^2$) for all GNSS observations in both the GNSS-only and the combined solution are adopted. As a further step, a more elaborate weighting of the GNSS data must be performed, accounting for the difference between the time in which every single observation has been made and the reference epoch of the corresponding ionosphere map. As for altimetry data, a common a priori variance of $\sigma_0^{alt} = 0.25$ TECU (corresponding to $P_{alt} = 4^2$) is adopted. The relative weighting of the satellite altimetry observations is discussed in more details in sectin 6.1.2.

Part II

Global models of the ionosphere - Results

Chapter 5

Global ionospheric maps from GNSS data

The first step of the work comprises the development of Global Ionosphere Maps from GNSS data only. Afterwards, these maps are used as basis for the combination. Twelve two-hourly global maps of the ionosphere are estimated daily from GPS and GLONASS data using an autonomous Matlab-based software. The computations are carried out on a Linux computer (CPU Intel Core 2 Duo 2×2.67 GHz; 4096 MB RAM) and take altogether about seven hours for one daily solution. The final outputs - global VTEC and the corresponding RMS (Root Mean Square) maps, as well as daily DCB values for all the GNSS satellites and receivers - are in the IONEX format.

5.1 Parameterisation and estimation of the VTEC

The basic conditions of the GIM development from GNSS data performed within the research will be outlined in this section.

The computation is carried out day-by-day, using GNSS observations with sampling rate of 30 seconds and elevation cut-off angle of $10°$. The twelve GIM estimated for each day represent the ionosphere in longitude, latitude and time, with spatial resolution of $\Delta\beta = 2.5°$ in latitude and $\Delta\lambda = 5°$ in longitude. The temporal resolution of the GIM is $\Delta t = 2^h$, with the reference epoch of the first daily map being 1:00 UT and of the last - 23:00 UT. The slant TEC is normalised using the MSLM mapping function (2.34); for the computation of the ionospheric pierce points a spherical layer with height $H = 450$ km is adopted. The parameterisation is carried out through spherical harmonic expansions (2.36) in the solar-geomagnetic frame (2.1) and (2.3). The maximum degree and order of the SH expansions are both set to 15, which leads to the estimation of 256 SH coefficients for every two-hourly set of VTEC representations, according to (2.38). In the IONEX format, in which the final results are stored, the estimated global VTEC values are related to a grid in the Earth-fixed geographic frame. This allows the interpolation of VTEC for any geographic coordinates and points in time. In addition, one constant (P1-P2) DCB value per day is estimated for each GNSS satellite and receiver; hence, two different values are assigned to stations receiving both, GPS and GLONASS signals. A zero-mean condition is imposed on the satellite bias estimates for defining the DCB datum (see section 5.4.1).

Developing several global sets of VTEC per day often leads to faulty values - either negative or too high - in areas with no observations available for the given time interval. In order to avoid this effect, the variations of consecutive VTEC maps are limited by adopting "relative" a priori constraints (specified in section 4.3) between successive parameters of same degree and order (Schaer, 1999). The use of normalised SH coefficients (2.37) allows the a priori standard deviation (σ_0^{rel}) of these constraints to be equal for all VTEC parameters. The adopted value for the a priori variance of the pseudo observations is $\sigma_0^{rel} = 0.003$ TECU. It was determined experimentally, by introducing wide range of different σ_0^{rel} values in the GIM estimation and evaluation of their impact on the number and extent of the negative VTEC values. The variations limitation between consecutive maps is based on the assumption that the ionosphere remains invariable above areas not covered with data when co-rotating with the Sun. Therefore, the "relative" constraints have no effect on the absolute determination of VTEC. Being not bonded by the variations limitation, the first and the last two-hourly maps of one daily GIM sequence can display higher instability and slightly lower precision. The problem can be overcome by implementing a three-day solution, as shown by Schaer (1999). The latter has not been done in this work in order to keep the computation time low.

5.2 Used GNSS data

An optimal set of about 160 GNSS stations is chosen from a basic list of 325 IGS sites for each of the two-hourly GIM. Figure 5.1 shows the location of the GNSS stations used for estimating the twelve two-hourly GIM for the 1st of July 2006 (doy 182). The corresponding list of four-character station identifiers can be found in the header of the IONEX-file, excerpted in Appendix A. The adopted GNSS stations provide an adequate amount of observations and ensure a possibly global coverage at any time. For that purpose, the large amount of available stations in the northern hemisphere is reduced to one site per a $5° \times 5°$ grid space. Still, the number of observations performed there is about two times higher than in the southern hemisphere.

With regard to the ongoing modernisation of the GLONASS system, as well as to the upcoming Galileo, it is important to facilitate the deployment of different types of satellite navigation systems in the GIM estimation. At present, the GLONASS observations rate is considerably lower than GPS but nevertheless, the combination of the GPS constellation and the presently up to 15 operational GLONASS satellites is considerable (see also section 5.3). On average, GLONASS observations are carried out at about 40 GNSS stations used in this work and in July 2006 constitute approximately 9.3% of the total amount of GNSS data, utilised for the GIM estimation (Figure 5.2).

The daily RINEX observation files of the chosen stations are downloaded from the SOPAC public ftp GNSS archive server (SOPAC, 2007). The GPS observations are pre-processed with the GPSTk open source suite (Tolman et al., 2004); the GLONASS data is handled separately. The pre-processing step comprises the building of the geometry-free linear combination from every pair of double-frequency code and phase observations as well as the computation of the ionosphere pierce points coordinates. For both GPS and GLONASS, the daily broadcast ephemeris files downloaded from (CDDIS, 2007) are used.
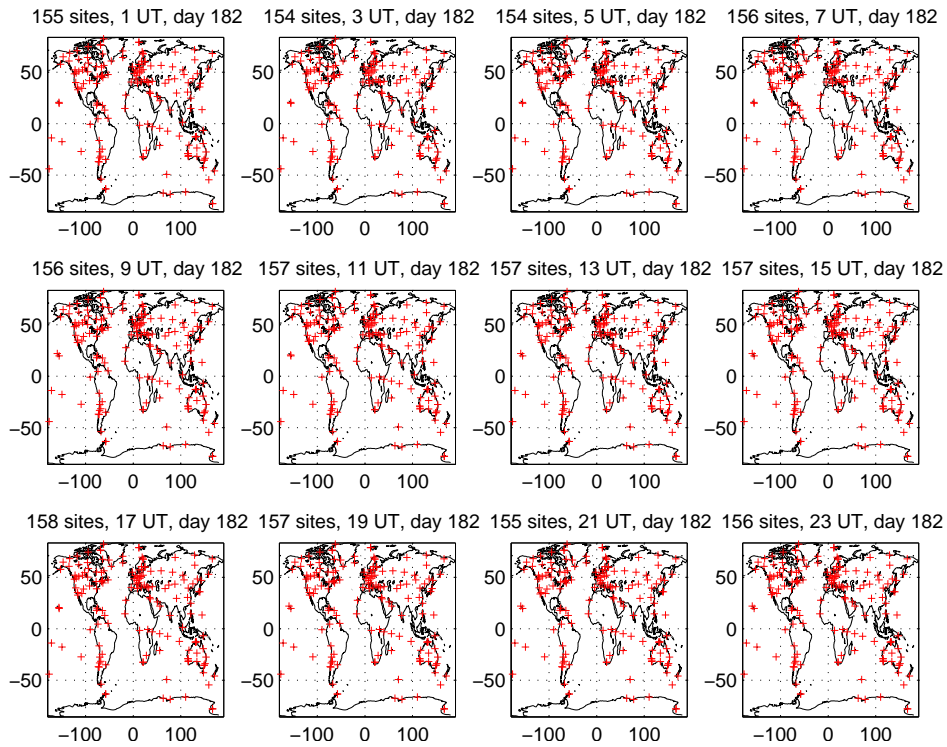
Figure 5.1: GNSS stations used for the twelve two-hourly GIM, day 182 in 2006
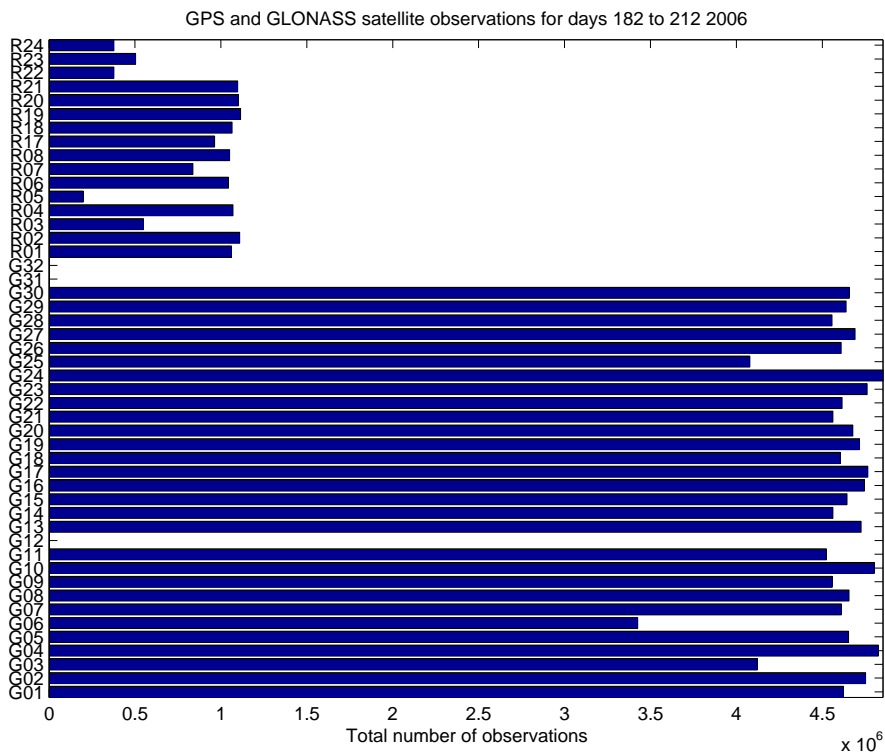
Figure 5.2: Total number of observations used for the GIM, July 2006

The GNSS-derived STEC values are extracted from the geometry-free linear combination applied on carrier-phase smoothed code GPS and GLONASS observations (3.25), as shown in section 3.1.2. An example of the "pseudo" STEC derived from GLONASS and GPS phase-smoothed pseudoranges obtained at the station `SOFI` can be seen in Figures 5.3 and 5.4. The "pseudo" STEC, shown in the figures per each satellite in TECU and as a function of the UT, is still affected by the DCB. The separation of the DCB is carried out next, in the least squares adjustment.
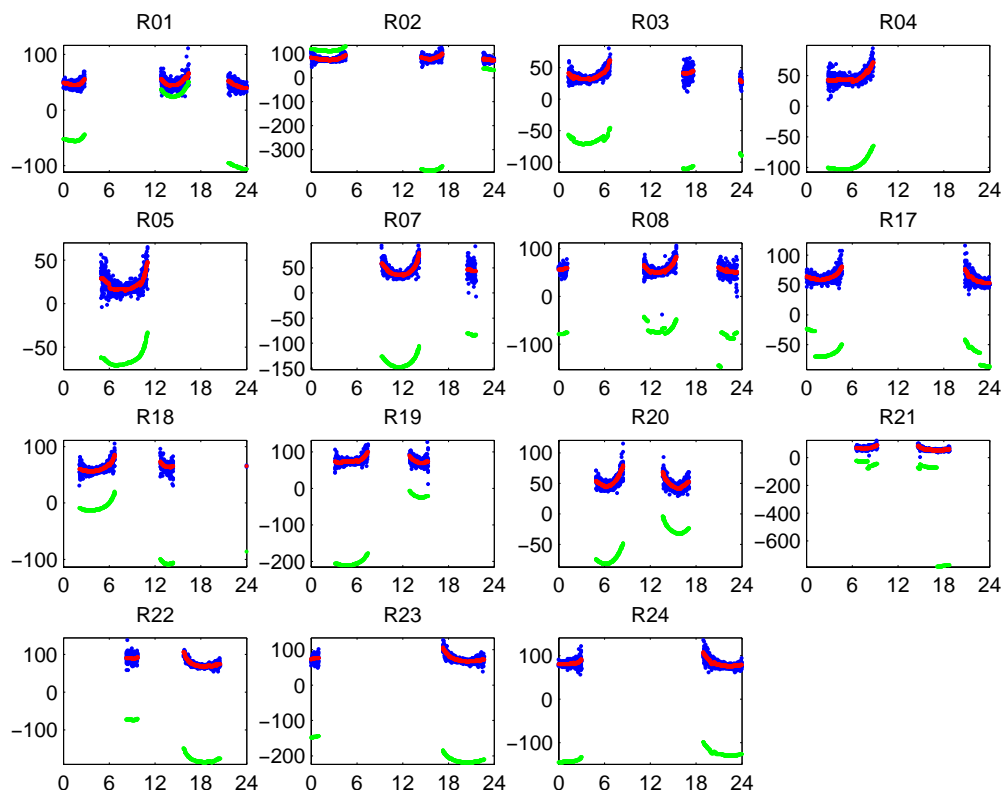
Figure 5.3: "Pseudo" STEC derived from GLONASS observations at station `SOFI` on day 182 2006 (red - STEC from phase-smoothed code observations; green - STEC from phase observations; blue - STEC from code observations)
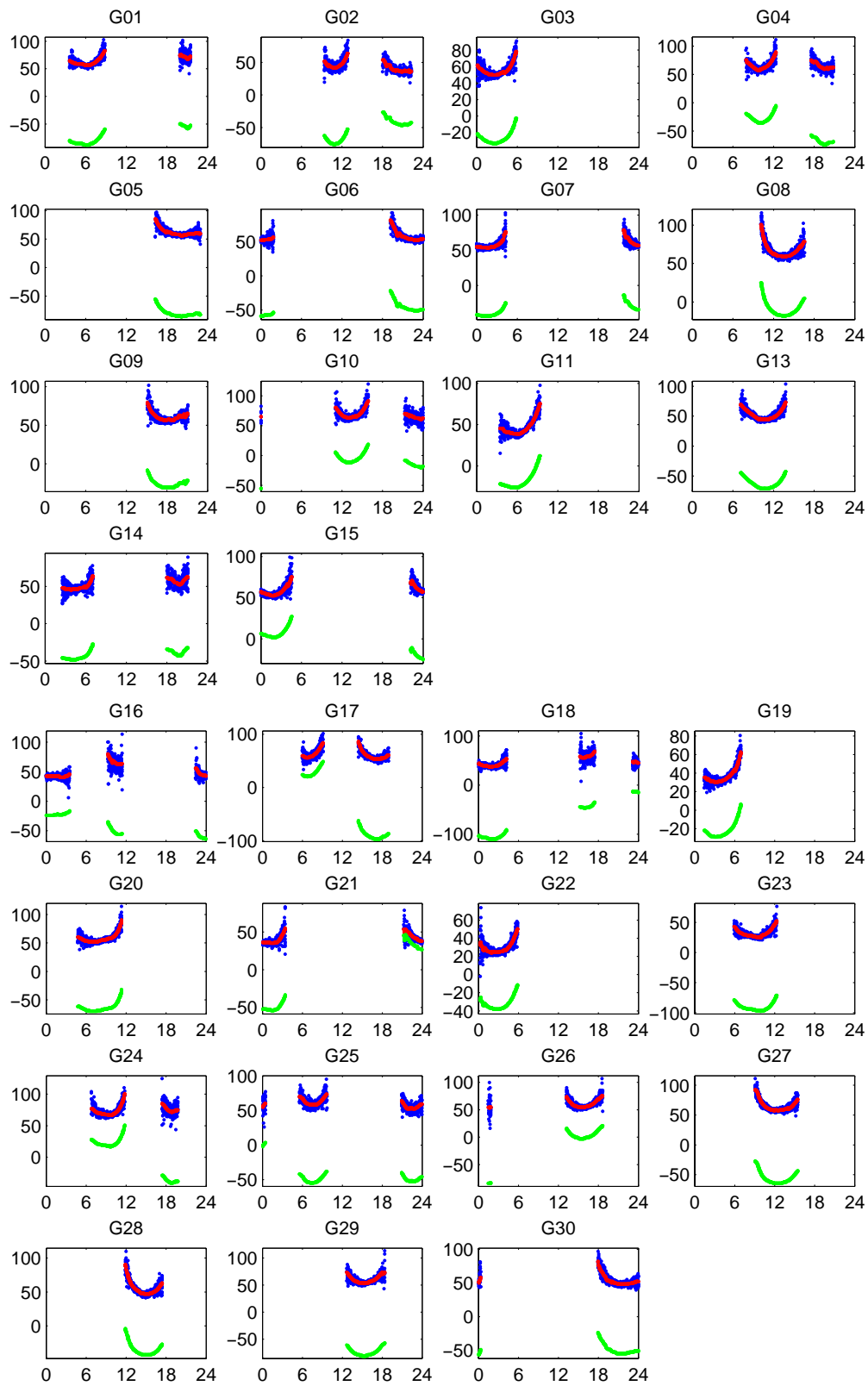
Figure 5.4: "Pseudo" STEC derived from GPS observations at station `SOFI` on day 182 2006 (red - STEC from phase-smoothed code observations; green - STEC from phase observations; blue - STEC from code observations)

To examine the performance of the developed GIM under various ionospheric conditions, the estimations are carried out in four weeks with different combinations of either remarkably high or low solar and magnetic activity. The Kp index and sunspot number for the chosen weeks in the years 2001, 2002, 2005, and 2006 are shown in Figure 5.5. The daily sunspot number indicates the solar activity, and the magnetic activity is characterised by the Kp index. The latter quantifies the disturbances in the horizontal component of the Earth's magnetic field in three-hours intervals (see section 2.1.2). The Kp index value is an integer reaching from 0 to 9, with 1 being calm. Kp index of 5 or more indicates a geomagnetic storm. In general, 2001 and 2002 are years of high solar activity (see also Figure 2.4), with 2001 being the year of the recent sunspot maximum. Afterwards, the solar activity decreases and is quite moderate for 2005 and 2006.
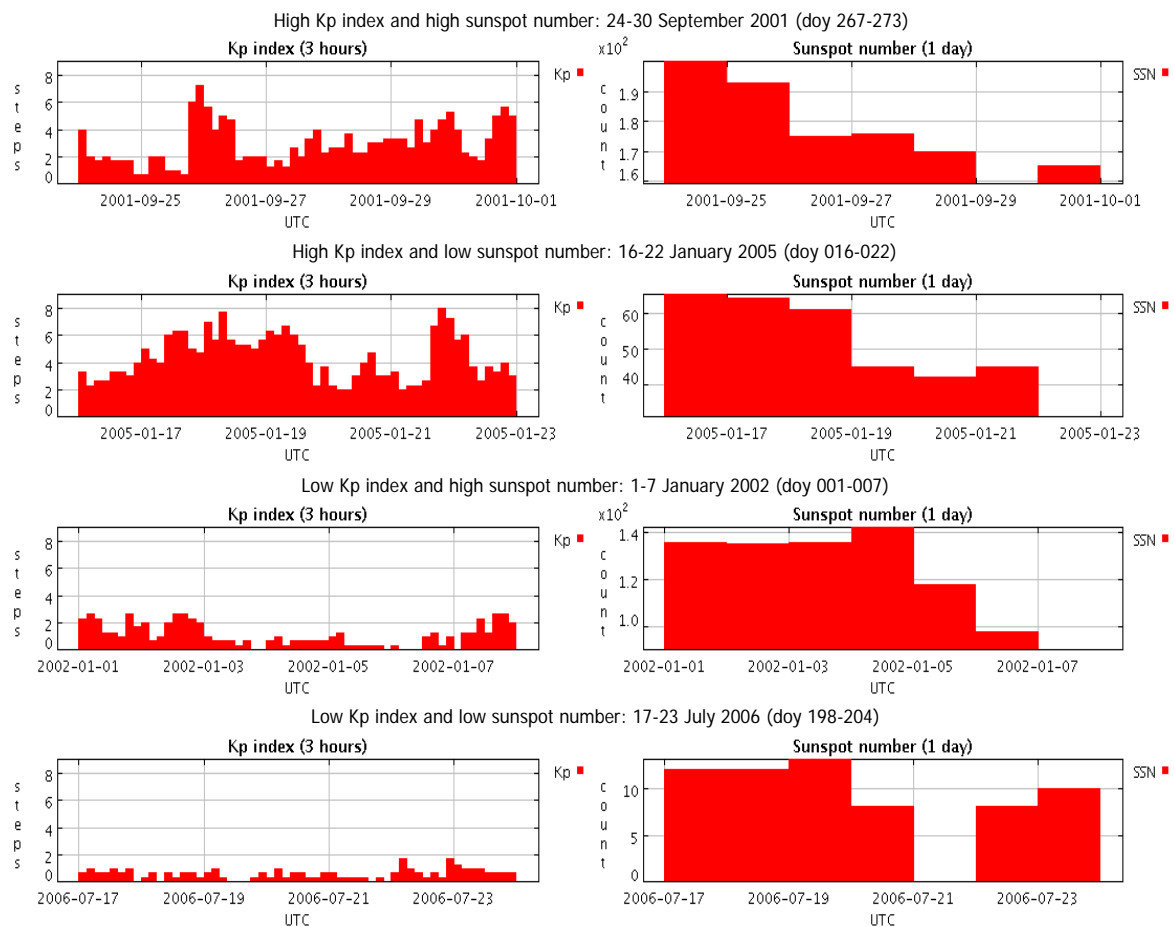
Figure 5.5: Kp index and sunspot number for the four chosen weeks (source: SPDIR, 2007)

5.3   Global VTEC derived from GNSS data

The daily global VTEC maps from GNSS data are estimated in two-hourly snapshots, taken in the middle of every time interval (in UT). The result for the 1st of July 2006, a day of moderate ionospheric activity, can be seen in Figure 5.6. The ionospheric maximum is evident along the geomagnetic equator as co-rotating with the Sun. According to (2.39), the chosen degree of the spherical expansion $n_{max} = 15$ ensures a $\Delta\beta = 360°/15 = 24°$ latitudal resolution of the VTEC structures. This allows reproducing the equatorial anomaly, which features a peak-to-peak distance of the order of 30°, as mentioned in section 2.1.2.
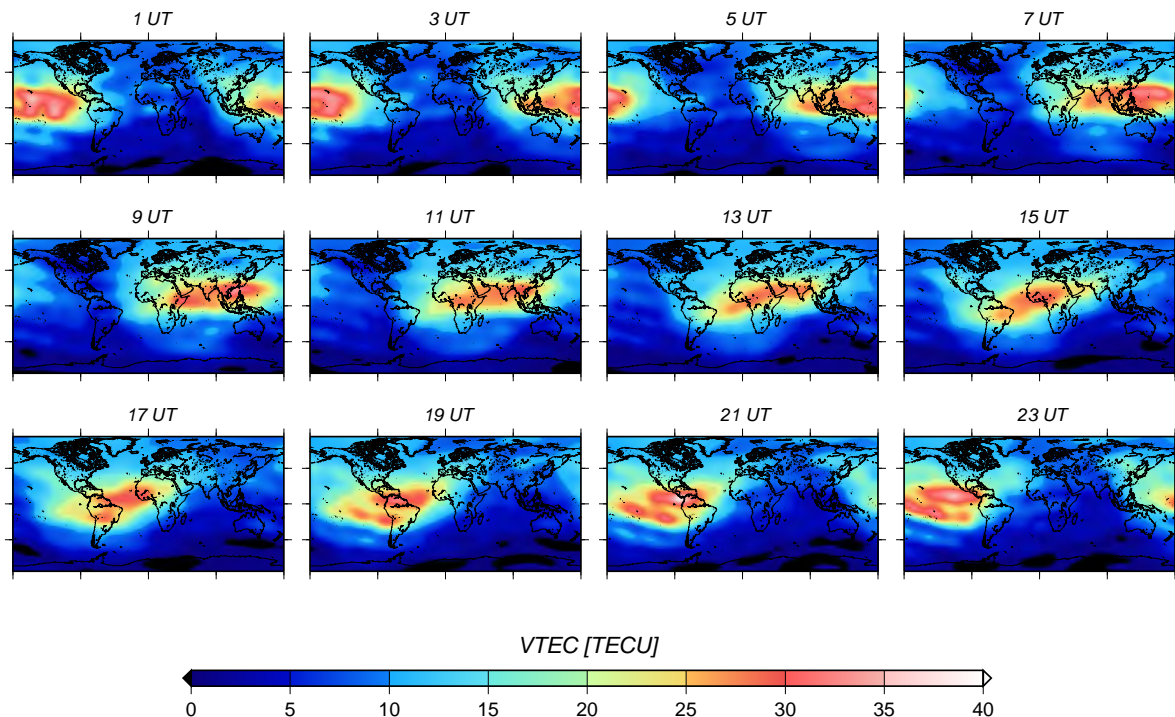
Figure 5.6: Global VTEC maps from GNSS data in two-hourly snapshots for day 182 2006

Impact of the GLONASS data on the GIM estimation

For assessing the impact of GLONASS data on the global VTEC maps, the GIM estimated for the investigated periods in 2005 and 2006 are recomputed using the same configuration of IGS stations, but ignoring the GLONASS observations. The two solutions are referred to as GNSS GIM and GPS-only GIM, accordingly. The map of the used GNSS stations on day 182 in 2006 (Figure 5.7) gives an overview of the GPS/GLONASS stations configuration. The GPS receivers are marked by crosses and the GPS/GLONASS ones - by crosses enclosed in circles. It can be seen that nearly half of the GPS/GLONASS receivers are located in the European region, which is densely covered by GNSS stations. However, the location of several of the other combined receivers - such as `OHI3`, `REUN`, `LHAS`, and `CRAR` - is quite isolated.

The effect of the GLONASS observations can not be entirely assessed through comparison
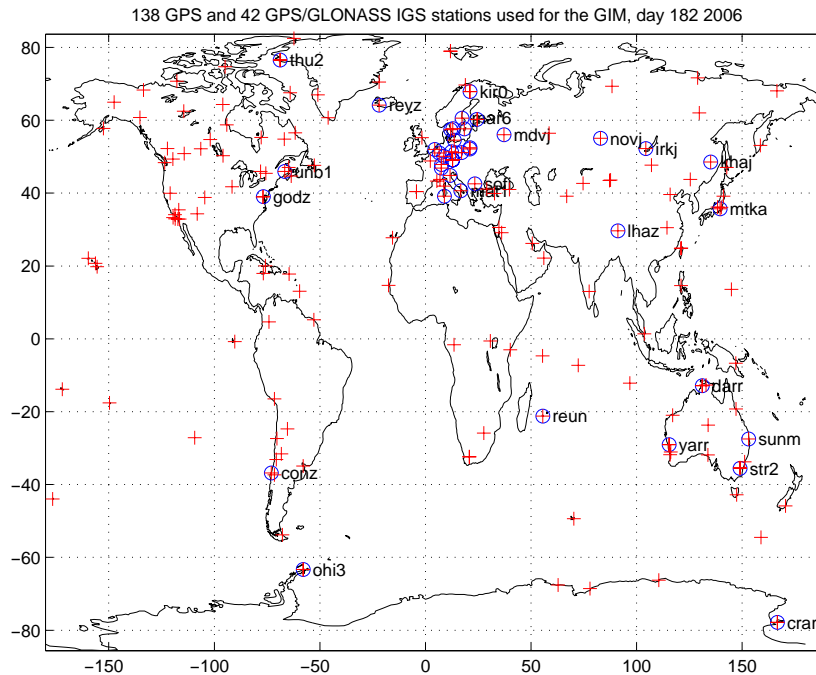
Figure 5.7: GPS (crosses) and GPS/GLONASS (crosses enclosed in circles) receivers used for the computations on day 182 2006

between the GNSS and GPS-only GIM, since in the GNSS solution the information from the two navigation systems is mixed. Nevertheless, such a comparison can visualise the general trend. Therefore, the daily average of the maximal, minimal, and mean differences ΔVTEC GNSS minus GPS-only GIM for the 31 days of July 2006 are displayed in Figure 5.8. It can be seen that for the regarded period the differences between the two types of maps are in the order of ±1 to ±2 TECU, with an average mean of about 0.01 TECU. Positive differences denote an increase of the VTEC values when adding GLONASS data and vice versa.

For a more detailed view, the sequence of two-hourly maps of the ΔVTEC between the GNSS and the GPS-only GIM for the 1st of July 2006 (doy 182) is shown in Figure 5.9. On the regarded day 42 of the 180 GNSS stations used for the GIM estimation were tracking GLONASS satellites (cf. Figure 5.7).

Negative values of the differences denote a lowering of the VTEC when GLONASS observations are included, and positive differences indicate an increase of the estimated VTEC under deployment of GLONASS data. The bias between the GNSS and the GPS-only GIM for the whole day is $\Delta VTEC_{mean} = 0.01$ TECU. In the two-hourly ΔVTEC maps shown in Figure 5.9, negative differences of up to −3 TECU (in blue and dark blue) appear in the map for 9 UT and in those for 19, 21 and 23 UT. In the 9 UT map the negative area roughly coincides with the location of the GPS/GLONASS receiver REUN in the Indian Ocean (see Figure 5.7). As for the other three maps, the higher negative differences appear around the GPS/GLONASS receivers NOVJ and IRKJ, located in Northern Asia. The positive differences GNSS minus GPS-only VTEC, rendered by red to white colours, are more blurred and appear predominately in the northern hemisphere. The peaks of positive differences (up to
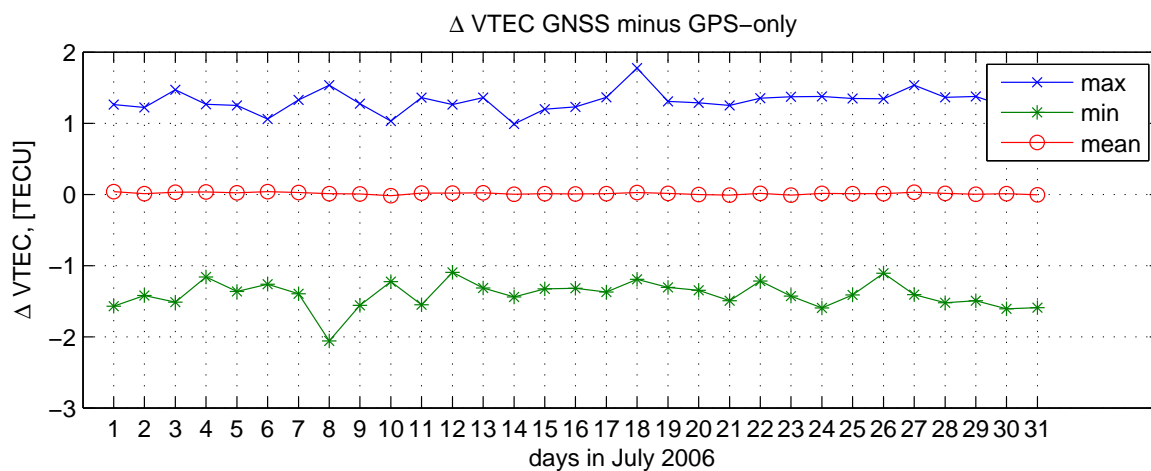
Figure 5.8: ΔVTEC GNSS minus GPS-only GIM for July 2006
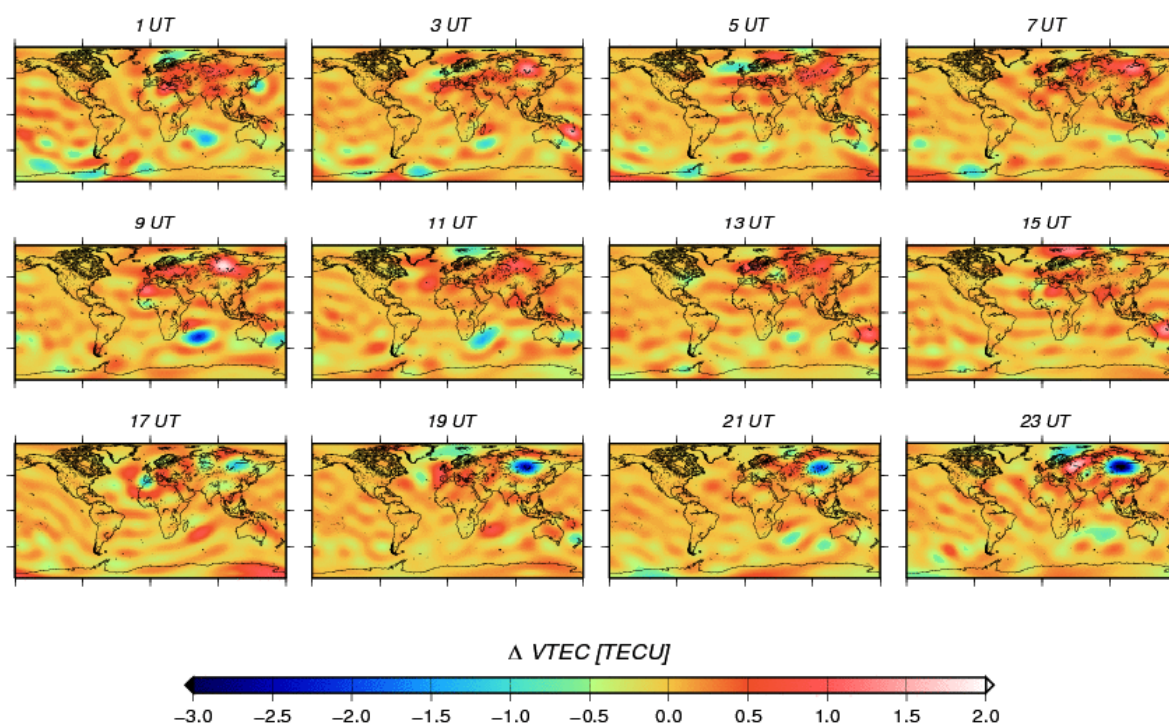
Figure 5.9: Global maps of the ΔVTEC between the GNSS and GPS-only GIM in two-hourly snapshots for day 182 2006

1.8 TECU) generally coincide with the locations of several GLONASS receiving stations, e.g.:

- OHI3 (β = -63.3°, λ = -57.9°) in the maps for 9 and 11 UT;

- CRAR (β = -77.8°, λ = 166.7°) - maps from 3 to 7 UT and at 17 UT;

- NOVJ (β = 55.0°, λ = 82.9°), IRKJ (β = 52.2°, λ = 104.3°) and LHAS (β = 29.7°, λ = 91.1°) in Asia in the maps from 1 to 13 UT;

- REUN (β = -21.2°, λ = 55.6°) in the Indian Ocean - 17, 19 UT;

- SUNM (β = -27.5°, λ = 153.0°) in Australia for the maps at 3, 15 and 19 UT UT.

All of the listed receivers are located in areas sparely covered by GNSS stations. On the contrary, in the European region where approximately half of the GLONASS receivers are located, the differences between the GNSS and the GPS-only solution are near to zero or slightly positive, pointing at a good agreement of the GPS and GLONASS data. The behaviour of the ΔVTEC is similar throughout the investigated period and leads to the conclusion that in spite of their relatively low number, the GLONASS observations can have an effect on the GIM of up to ± 3 TECU just in regions with lack of GNSS stations.

Time series of mean VTEC

In Figure 5.10 the difference in the mean VTEC, represented by the zero-degree spherical harmonic coefficients a_{00}, from the GNSS and the GPS-only GIM over one month (July 2006) can be seen. The difference between the two time series of mean VTEC is minimal, being in the range of -0.04 to 0.08 TECU. The bias of the difference is 0.02 TECU, and the standard deviation amounts 0.03 TECU, showing that the GLONASS data causes a slight increase in the mean VTEC. The correlation coefficient of the two time series is 0.9997.
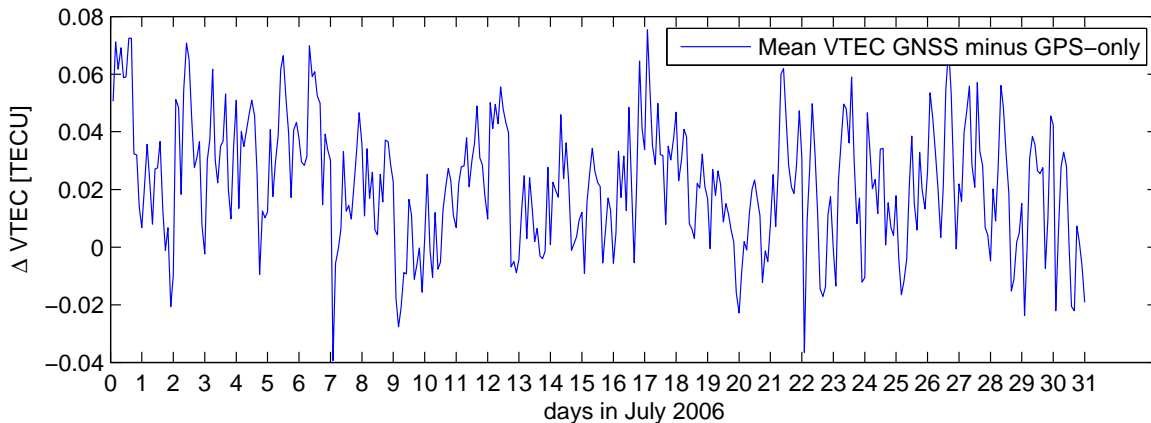
Figure 5.10: Difference of the mean VTEC values obtained from the GNSS and GPS-only GIM for July 2006

The mean daily VTEC (i.e. the average of the twelve zero-degree spherical harmonic coefficients a_{00} of each daily solution) for the same period is plotted versus the Kp index (Figure 5.11, top) and the sunspot number (Figure 5.11, bottom). TEC time series have been compared to solar and geomagnetic indices in several works. In Schaer et al. (1996) a time series including 427 days of mean VTEC is compared to the Kp index and the sunspot number. The authors observe a high correlation of the times of increasing and decreasing mean VTEC with the times when the solar activity level changes. Moreover, the dominant peaks in the analysed mean VTEC series can be recognised in both the Kp index and sunspot number series. According to Jakowski et al. (1999), TEC observations at different latitudes show an evident negative correlation to the Kp index. Based on the results of their study, the authors propose temporal and spatial gradients to be derived from global TEC maps and used for estimation of the perturbation degree of the ionosphere, along with the solar and geomagnetic activity indices.
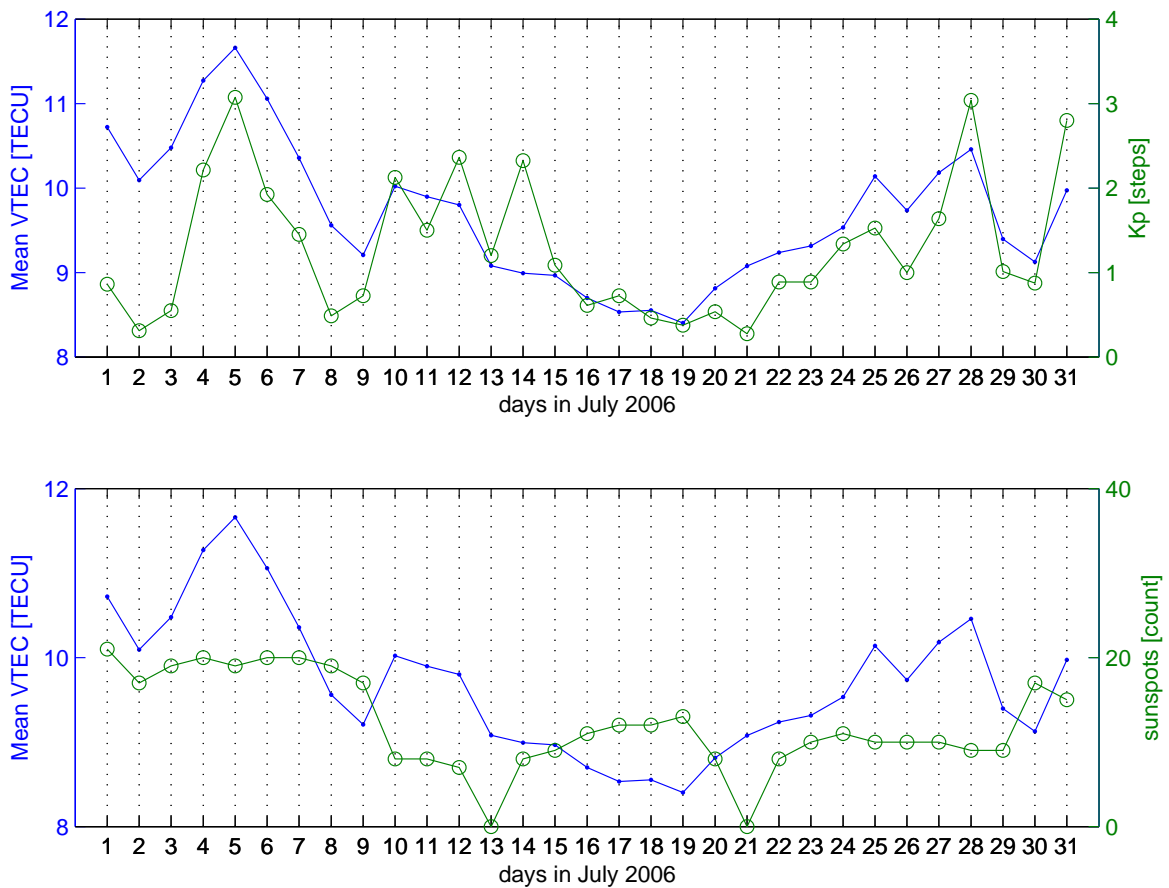
Figure 5.11: Mean VTEC versus the Kp index (upper plot) and the sunspot number (lower plot) for July 2006

Looking at the upper plot of Figure 5.11, one can see a positive correlation between the mean VTEC and the Kp index almost during the whole month, except for the 11th, 14th, 17th and 21st. The correlation coefficient between the estimated time series of mean VTEC and the corresponding values of the Kp index is $C_{a_{00},Kp} = 0.60$. The probability of getting a corre-

lation as large as the observed value by random chance, when the true correlation is zero, is $P_{a_{00},Kp} = 0.0004$. Being small enough (considerably less than 0.05), the obtained probability P substantiates that the correlation between the mean VTEC and the Kp index time series is significant. The comparison in the lower plot exhibits a positive correlation only during the first seven days of the period, in which also the sunspot number is higher than for the rest of the month. Afterwards, the correlation gets mostly negative. The correlation coefficient between the time series of sunspot number and mean VTEC is $C_{a_{00},sunsp} = 0.53$. It has to be noted, that the sunspot number does not exceed 20 during the whole month, which points at a moderate solar activity. The magnetic conditions for the regarded period are also calm with Kp index lower than 4.

The weekly averages of the mean and maximum VTEC derived from the GIM for the four periods with different combinations of solar and magnetic activity (see section 5.2) are summarised in Table 5.1. Due to the unavailability of reliable GLONASS navigation data for the years 2001 and 2002, GLONASS observations are introduced only for two of the four periods - the weeks in 2005 and 2006.

Period (doy, year)	Kp index	sunspot number	$VTEC_{mean}$ GPS-only GIM	$VTEC_{max}$ GPS-only GIM	$VTEC_{mean}$ GNSS GIM	$VTEC_{max}$ GNSS GIM
267-273, 2001	*high*	*high*	48.06	140.53	-	-
001-007, 2002	*low*	*high*	41.44	128.89	-	-
016-022, 2005	*high*	*low*	17.68	72.70	17.67	72.75
198-204, 2006	*low*	*low*	8.83	30.60	8.85	30.85

Table 5.1: Weekly averages of the mean and max VTEC (in TECU) from the GIM obtained for periods with different ionospheric conditions

Figure 5.12 shows the mean VTEC in two-hourly intervals, represented by the zero-degree spherical harmonic coefficient a_{00}, obtained for the same four weeks. As expected, the periods of high sunspot number are characterised by considerably higher total electron content.
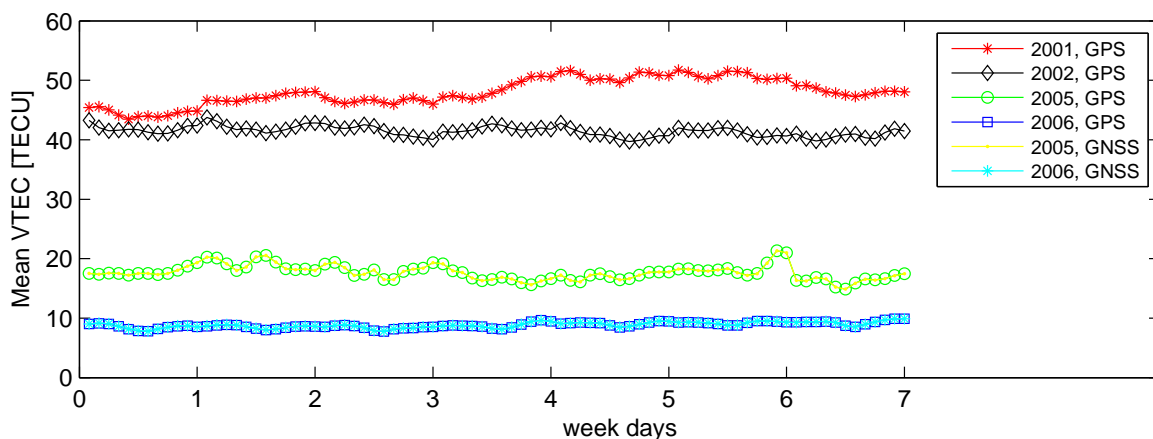
Figure 5.12: Mean VTEC obtained from the GNSS and GPS-only GIM for four weeks in different ionospheric conditions

The maximum values obtained for the weeks in 2001 and 2002 exceed 120 TECU, and the mean VTEC for both periods is above 40 TECU. Related to the first GPS frequency by using equation (2.33), a total electron content of 120 TECU corresponds to the remarkable ionospheric path delay of about 19.50 meters. The VTEC for the other two periods (in 2005 and 2005) is considerably lower, whereas the week in 2005 - characterised by high Kp index and sunspot number of about 50 - exhibits values more than twice higher than the period in 2006, when the Kp index is low and the sunspot number does not exceed 15 (as shown in Figure 5.5). For the latter two periods both GPS-only and GNSS (GPS and GLONASS) GIM are estimated. The differences between the mean and maximum VTEC obtained in the two cases are in the range of ± 0.25 TECU (see Table 5.1).

5.3.1 Formal error of the results

Using the variance-covariance error propagation law (4.14) the formal precision (or RMS) of the global VTEC estimates can be computed. The RMS maps for the 1$^{\text{st}}$ of July 2006, corresponding to the global GIM in Figure 5.6, are shown in Figure 5.13. Due to the lack of GNSS observations above the oceans and in the southern polar regions, the precision of the global VTEC maps is lower in these areas. The a posteriori sigma of the GNSS derived daily GIM is in the range of 3-8 TECU, generally depending on the overall ionospheric activity in the particular day. For the regarded example (day 182 in 2006) of moderate ionospheric conditions the a posteriori sigma of the global solution is $\sigma_{ap} = 4.08$ TECU.
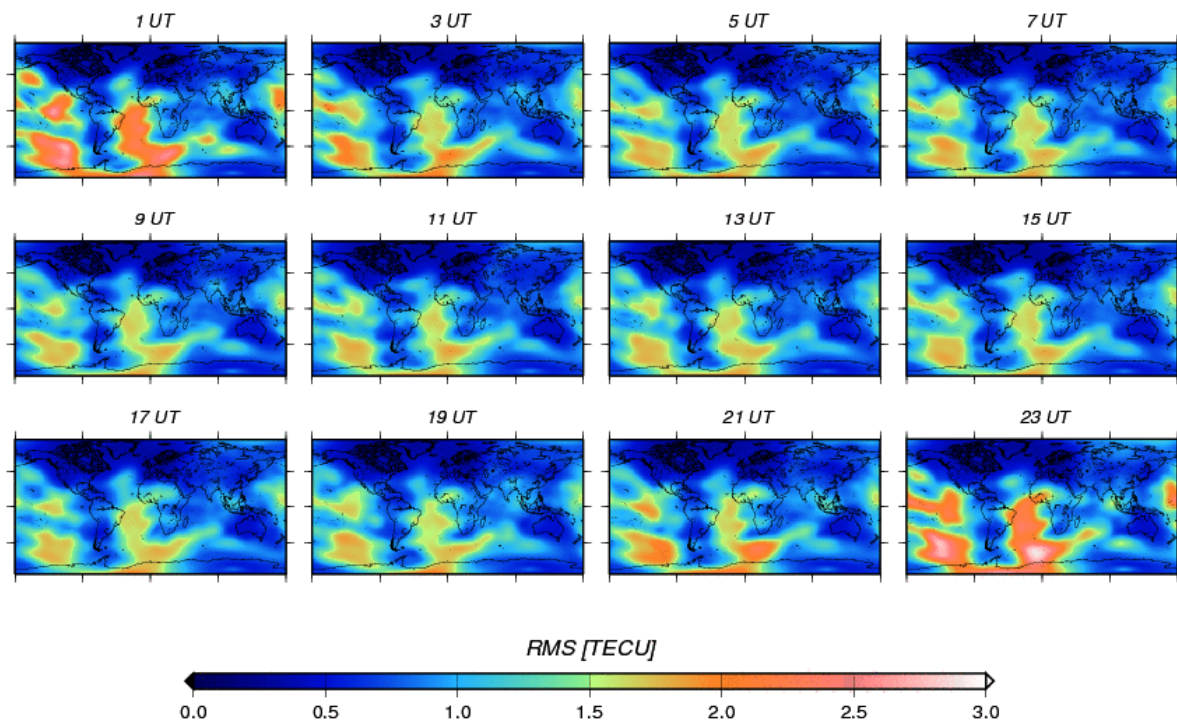
Figure 5.13: Global RMS maps from GNSS data in two-hourly snapshots for day 182 2006

The differences in the formal precision ΔRMS of the GNSS and GPS-only GIM for the same day (Figure 5.14) show an increase of the RMS within a range of 0.04 to 0.9 TECU when

using GLONASS observations. The worsening of the formal precision in the GNSS case occurs predominantly over the areas with lack of data that were mentioned above. Adding GLONASS data to the model leads to an increase of the observations number only in the areas already covered by GPS and hence, it can be expected that the system becomes more unstable for the sparsely covered regions.
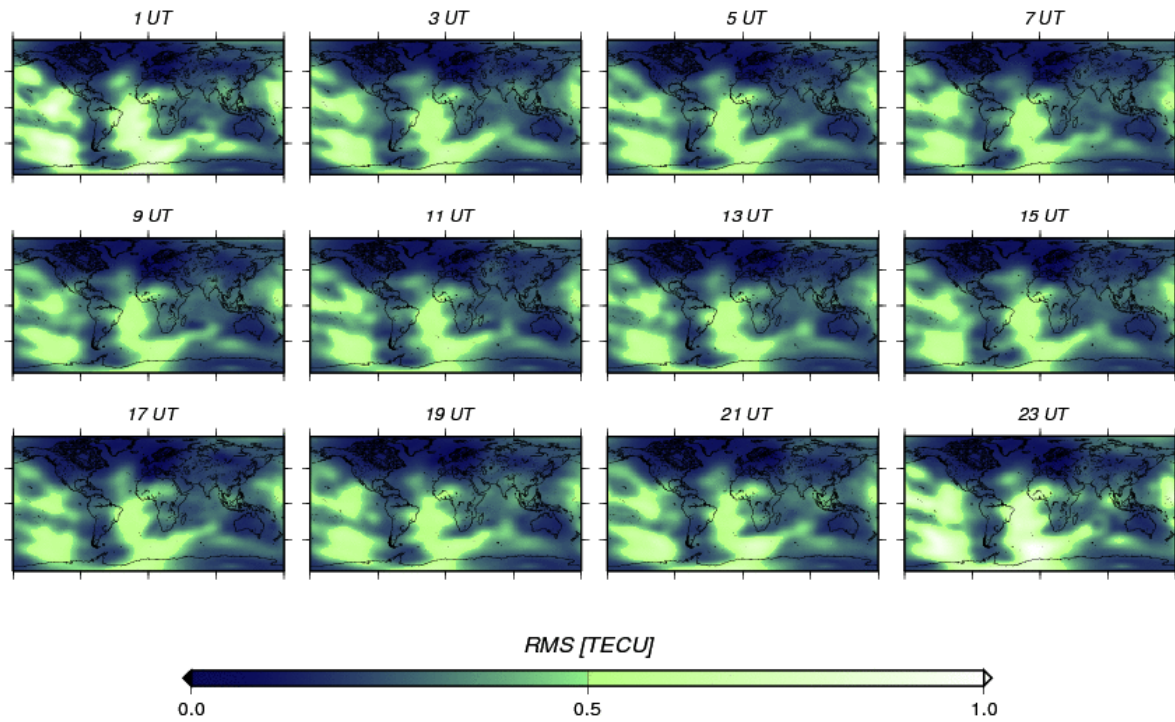
Figure 5.14: Global maps of the ΔRMS between the GNSS and GPS-only GIM, day 182 2006

The daily average of the maximal and minimal differences ΔRMS GNSS minus GPS-only GIM for July 2006 is displayed in Figure 5.15. Again, the RMS of the GNSS GIM is generally higher than the one of the GPS-only GIM with up to 0.8 TECU. The mean Δ RMS GNSS minus GPS-only GIM for the whole month is 0.2 TECU.
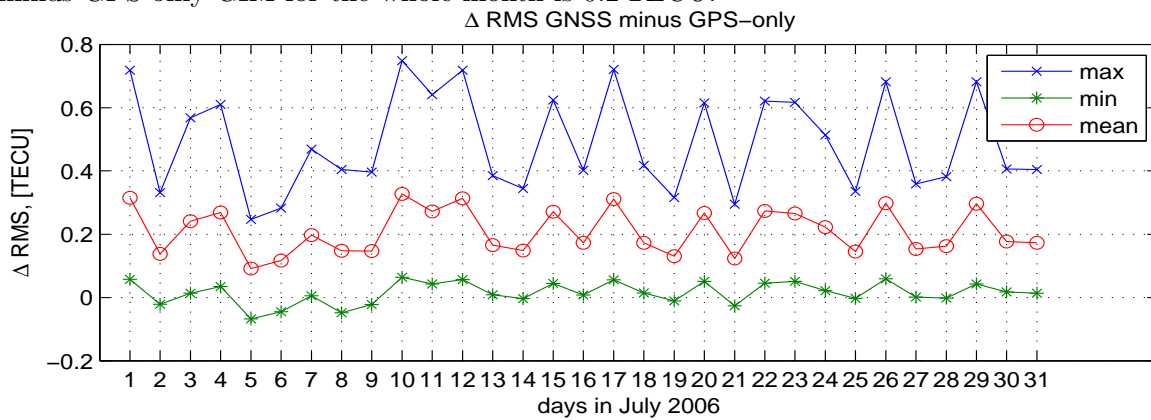
Figure 5.15: ΔRMS GNSS minus GPS-only GIM for July 2006

5.4   Differential Code Biases

The ionospheric parameters derived from the geometry-free linear combination of code measurements (3.23) or (3.25) are affected by the inter-frequency hardware biases Δb, also called Differential (P1-P2) Code Biases (DCB). When the ionosphere is modelled in- or directly using one-way code observations, it is necessary to estimate the satellites and receivers DCB as additional unknowns. The DCB can not only influence the quality of the VTEC estimation, but provide an insight into the stability of the instrumental biases when studied over long time periods. Furthermore, information about the DCB is required for the precise time transfer. It has to be noted, that only P1-P2 DCB are estimated in this work and hence stations receiving no P1 but only C/A-code are not involved in the computations.

5.4.1   Satellites DCB

All DCB might be shifted by a common bias and therefore, only the relative biases have an effect on the VTEC estimation. A particular satellite can be chosen as reference, or one can relate the individual satellite DCB estimates to a total mean. In this research the latter is done, by introducing the condition $\sum DCB_{sat} = 0$. While the receiver DCB are ascertained only from the observations made by each receiver itself, it can be anticipated that every satellite was observed by all receivers from the chosen global network during a 24 hours period. Therefore, the satellite DCB are determined more definite and a zero-mean of the satellite DCB is a very stable - though virtual - bias (Schaer, 1999). That does not fully apply for the GLONASS satellite DCB due to the limited number of observing receivers. To avoid singularities however, two zero-mean conditions must be set - one for the GPS and one for the GLONASS set of satellites DCB. The GPS and GLONASS DCB are estimated in daily sets, i.e. there is one reference zero-mean per day for each set. Hence, if for some reason the DCB of one satellite was not estimated in a 24 hours period, the reference slightly changes. This can happen when a satellite is not observable due to maintenance, manoeuvres, or - as it is at times the case with some GLONASS satellites - the number of observations with acceptable quality level to one particular satellite is too low. For the optimal determination of the DCB, the daily values have to be aligned to a reference, based on all involved satellites in a further post-processing step. Nevertheless, building the monthly median of the daily DCB estimates provides a result of sufficient reliability, as it is shown in section 5.5.1.

GPS satellites DCB

Figure 5.16 shows the daily estimates (dots) and the monthly median (crosses) for the GPS satellites DCB in July 2006. The mean standard deviation of the daily DCB values of the GPS satellites is $\text{std}_{mean} = 0.05\,\text{ns}$, being maximum (0.08 ns) for PRN 10 and minimum (0.03 ns) for PRN 9 (see Figure 5.17). At the time of estimation - July 2006 - PRN 9 is a Block II-A satellite operating on a rubidium standard, whereas PRN 10 is having a caesium clock. The Block IIR-M satellites PRN 12 and PRN 31 were launched in September and November 2006 and are therefore missing in July 2006.

The mean RMS of the GPS satellites DCB in the regarded period is 0.004 ns, corresponding to 0.01 TECU.
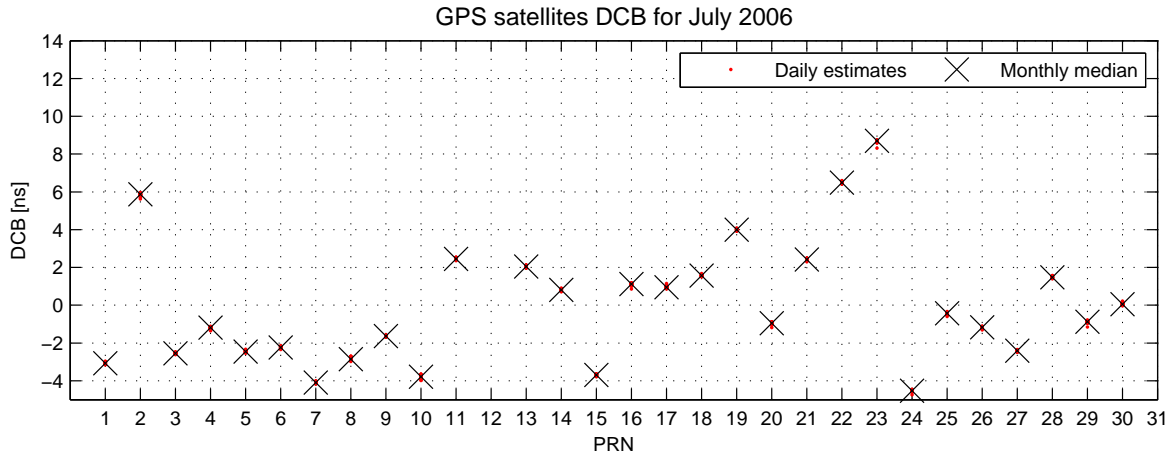
Figure 5.16: Daily estimates and monthly median of the GPS satellites DCB for July 2006
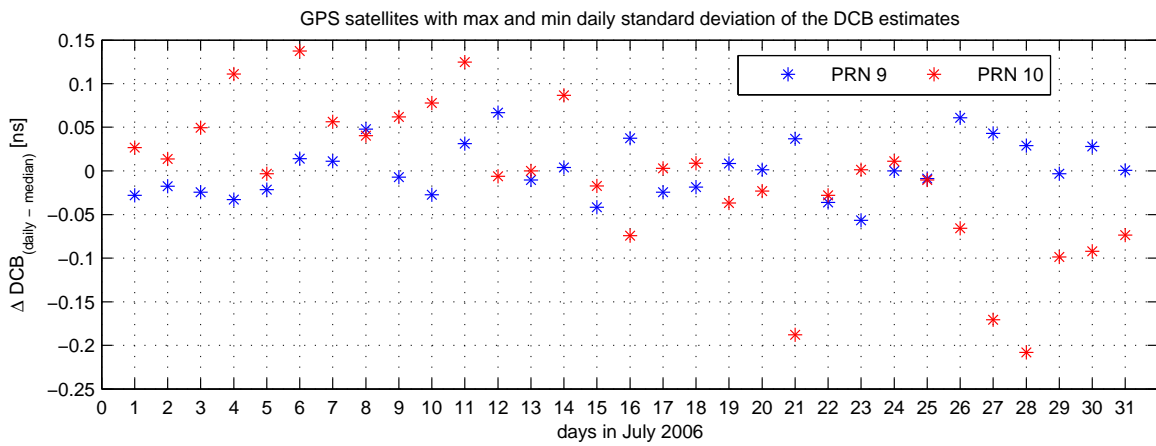
Figure 5.17: Difference between the daily estimates and the monthly median of the most and the least stable GPS satellites DCB for July 2006

GLONASS satellites DCB

As already mentioned, slight changes in the daily zero-mean reference can lead to higher variability of the daily DCB estimates. This is more often the case when estimating the GLONASS satellites DCB, due to the lower number of observations to some of the satellites. The higher daily scatter is evident in Figure 5.18 (top), showing the daily estimates and the monthly median of the GLONASS satellites DCB for July 2006. Apparently, there is a relation between the variability of the DCB and the value of the corresponding formal precision (Figure 5.18, bottom), which indirectly represents the number of observations to each satellite for a particular day.
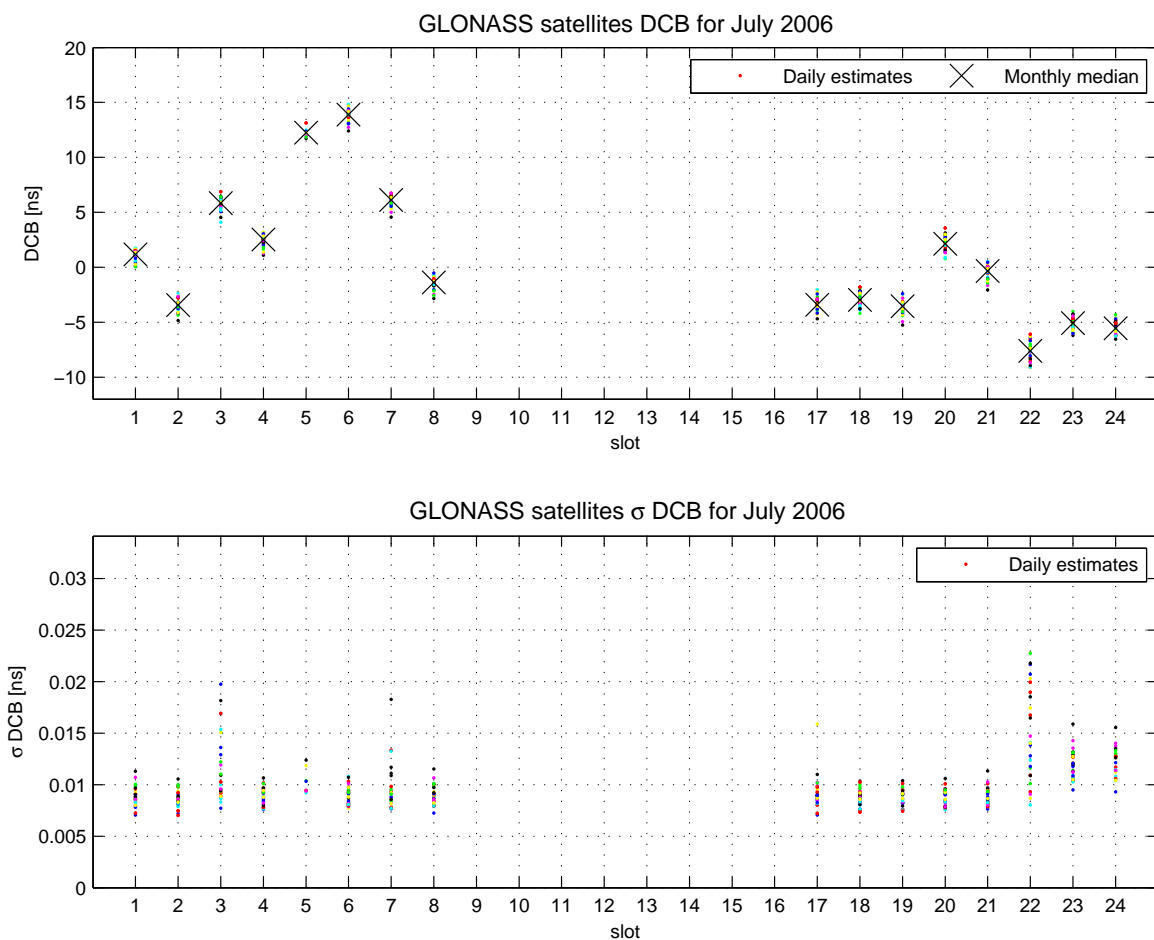
Figure 5.18: Daily estimates and monthly median of the GLONASS satellites DCB (top); daily estimates of their formal precision (bottom) for July 2006

From the 15 GLONASS satellites, to which observations were carried out on at least 15 days of the regarded period, slot 22 exhibits the maximum standard deviation of the daily DCB estimates: $\text{std}_{mean} = 0.88\,\text{ns}$, and slot 1 shows the lowest variability with a standard deviation of the daily DCB of $\text{std}_{mean} = 0.48\,\text{ns}$ (Figure 5.19). The apparent signal in the daily DCB variability, visible in the plot, is due to the shift of the common zero-mean when one or more

satellites are missing. Generally, the variability of the GLONASS DCB daily estimates is of one order higher than in the case of the GPS DCB, with mean standard deviation for all satellites $std_{mean} = 0.60$ ns. The mean RMS of the GLONASS satellites DCB for July 2006 is 0.01 ns, corresponding to 0.03 TECU.
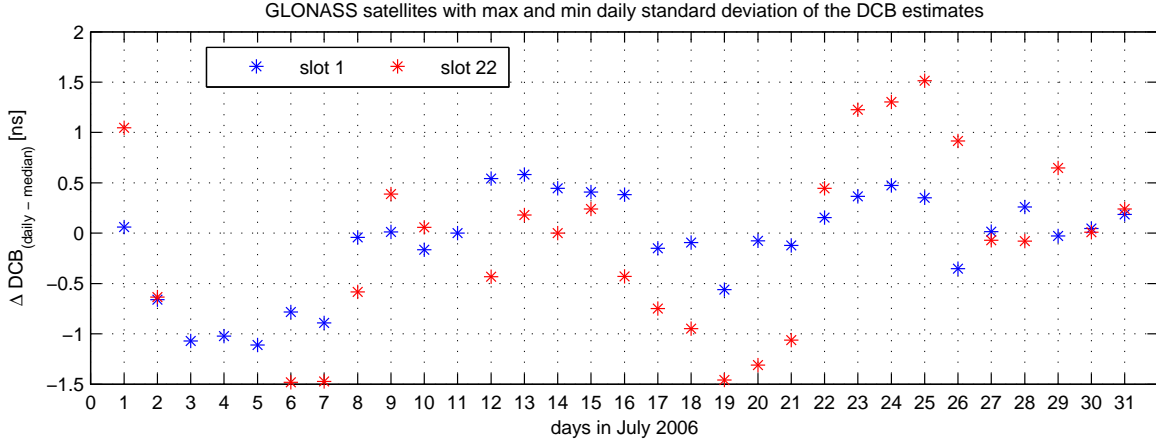
Figure 5.19: Difference between the daily estimates and the monthly median of the most and the least stable GLONASS satellites DCB for July 2006

Correlation between the GPS and GLONASS satellites DCB

The impact of the GLONASS observations involvement on the GPS DCB estimates can be seen in Figure 5.20, showing the differences between the daily estimates of the GPS satellites DCB from the GNSS and the GPS-only solutions for the day 182 in 2006. The mean of the differences between the GPS DCB estimates from the two solutions amounts $1.8 \cdot 10^{-15}$ ns. The maximum absolute difference of 0.027 ns occurs for PRN 5 and the minimum - which is virtually 0.00 ns - is for the DCB estimates of PRN 26 and PRN 29.

The practically non-existent correlation between the GPS and GLONASS satellites DCB estimates allows drawing the conclusion that the differences in the GPS DCB estimates with and without involvement of GLONASS data can be considered as noise. As an example, Figure 5.21 shows the correlation matrix C of the GPS and GLONASS DCB estimates, computed from the GNSS solution for day 022 in 2005 as:

$$C(i,j) = \frac{Q(i,j)}{\sqrt{Q(i,i)\,Q(j,j)}} \qquad \text{with} \qquad Q = \sigma_{apost} \cdot N^{-1} \qquad (5.1)$$

On that day DCB were estimated for 30 GPS and 10 GLONASS satellites. The highest positive and negative correlation coefficients $C_{(i,j)}$ between the GPS and the GLONASS satellite DCB estimates are $C_{(gps,glo)} = 0.05$ and $C_{(gps,glo)} = -0.03$. As for the correlation between the GPS DCB estimates, the highest values are $C_{(gps,gps)} = 0.10$ and $C_{(gps,gps)} = -0.09$. All correlation coefficients between the GLONASS DCB are negative, the highest value being $C_{(glo,glo)} = -0.14$. In Figure 5.21 the diagonal of the matrix is set to zero.
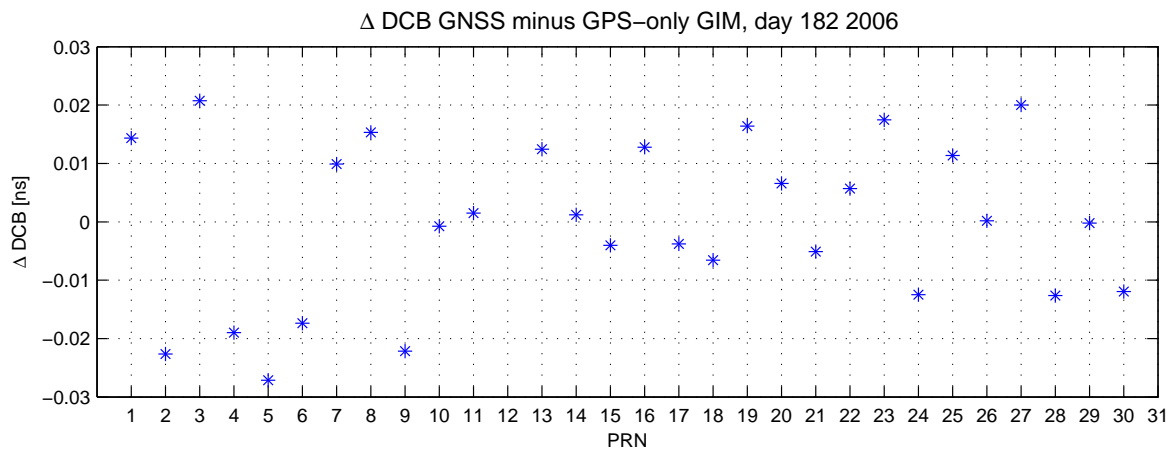
Figure 5.20: Differences between the daily estimates of the GPS satellites DCB from the GNSS and the GPS-only solution for day 182 2006
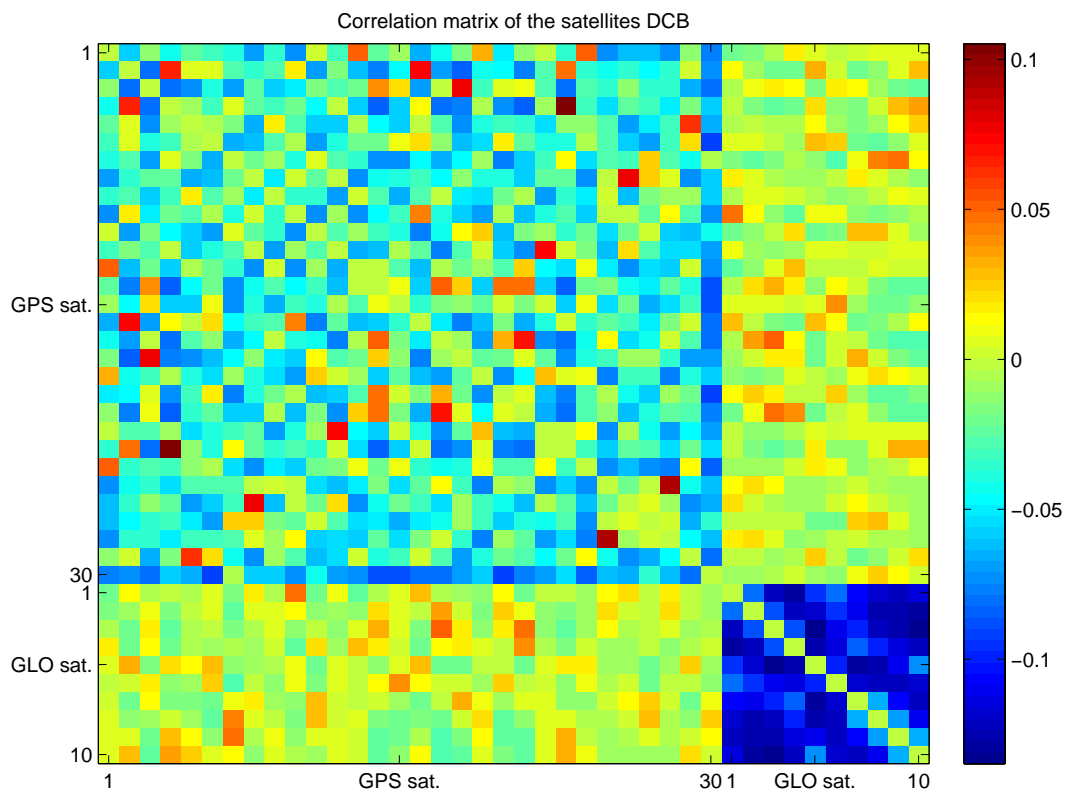
Figure 5.21: Correlation matrix of the satellite DCB estimates, GNSS GIM for day 022 2005; diagonal set to zero

Eventually, in Table 5.2 the estimated median monthly values of the GPS and GLONASS satellites DCB for July 2006 are given.

satellite	PRN1	PRN2	PRN3	PRN4	PRN5	PRN6	PRN7	PRN8
DCB	-3.07	5.87	-2.55	-1.19	-2.46	-2.24	-4.09	-2.85
RMS	0.004	0.004	0.004	0.004	0.005	0.004	0.004	0.004
satellite	PRN9	PRN10	PRN11	PRN13	PRN14	PRN15	PRN16	PRN17
DCB	-1.64	-3.78	2.45	2.05	0.81	-3.69	1.12	0.95
RMS	0.004	0.004	0.004	0.004	0.004	0.004	0.004	0.004
satellite	PRN18	PRN19	PRN20	PRN21	PRN22	PRN23	PRN24	PRN25
DCB	1.56	4.00	-0.95	2.43	6.50	8.70	-4.53	-0.43
RMS	0.004	0.004	0.004	0.004	0.004	0.004	0.004	0.004
satellite	PRN26	PRN27	PRN28	PRN29	PRN30			
DCB	-1.18	-2.41	1.47	-0.88	0.05			
RMS	0.004	0.004	0.004	0.004	0.004			
satellite	slot1	slot2	slot3	slot4	slot5	slot6	slot7	slot8
DCB	1.16	-3.44	5.83	2.53	12.25	13.88	6.12	-1.38
RMS	0.009	0.009	0.011	0.009	0.010	0.009	0.010	0.009
satellite	slot17	slot18	slot19	slot20	slot21	slot22	slot23	slot24
DCB	-3.40	-2.97	-3.54	2.14	-0.34	-7.62	-5.08	-5.55
RMS	0.009	0.009	0.009	0.009	0.009	0.015	0.012	0.012

Table 5.2: GPS and GLONASS satellites DCB (in ns) for July 2006

5.4.2   Receivers DCB

The analysis of the time series of receivers DCB obtained for July 2006 is based on the estimates for the 117 GPS and 25 GPS/GLONASS receivers, the observations of which were used for the GIM throughout the whole period. Figures 5.22 and 5.23 show the daily estimates and monthly mean of the GPS and GLONASS receivers DCB, respectively. As mentioned in section 5.4.1, the variability of the receivers DCB daily estimates is higher than of the satellites DCB. The former are not only determined from a lower number of observations (solely the ones carried out by the particular station), but are also to a larger extend affected from potential VTEC mismodelling. Hence, a higher variability of the DCB estimates for receivers located in areas with higher ionospheric activity (i.e. low latitudes or equator regions at about $\pm 20°$ of the magnetic equator) can be expected.

The mean standard deviation of the daily estimates is $\text{std}_{mean} = 0.36$ ns for the GPS and $\text{std}_{mean} = 0.79$ ns for the GLONASS receivers. Figure 5.24 shows the GPS (upper plot) and GLONASS (lower plot) receivers with the lowest and highest daily variability in terms of differences between the daily estimates and the monthly median. The most stable GPS and GLONASS receivers - `QAQ1` with $\text{std}_{mean} = 0.09$ ns (GPS DCB), and `CRAR` with $\text{std}_{mean} = 0.49$ ns (GLONASS DCB) - are located in high latitudes: 60° and -77°, respectively. The most variable GPS/GLONASS receiver `MTKA`, with $\text{std}_{mean} = 3.20$ ns (GPS DCB) and $\text{std}_{mean} = 1.97$ ns

Figure 5.22: GPS receivers DCB - daily estimates and monthly median, July 2006

Figure 5.23: GLONASS receivers DCB - daily estimates and monthly median, July 2006

(GLONASS DCB), is located at 35° latitude. Both, the GPS and the GLONASS DCB for MTKA seem to become stable after 18 days of high variations, so a receiver specific problem might be supposed in this case. The receivers with most stable DCB estimates for GPS, e.g. BAKE, KIRU, RESO, and for GLONASS - KHAJ, NOVJ, ONSA, THU2, are located at latitudes above 50° and 60°. It has to be noted, that the most unstable receiver DCB estimates for both GPS and GLONASS are for the GPS/GLONASS stations MDVJ, MTKA, and REYZ. The relatively unstable GPS DCB estimates for the low-latitude stations, such as KOUR, MSKU, PIE1, UNSA, could be influenced by the higher ionospheric activity in the equatorial region. Therefore, the larger scatter of their daily DCB values might be induced by this effect without being a real issue of the receiver itself.
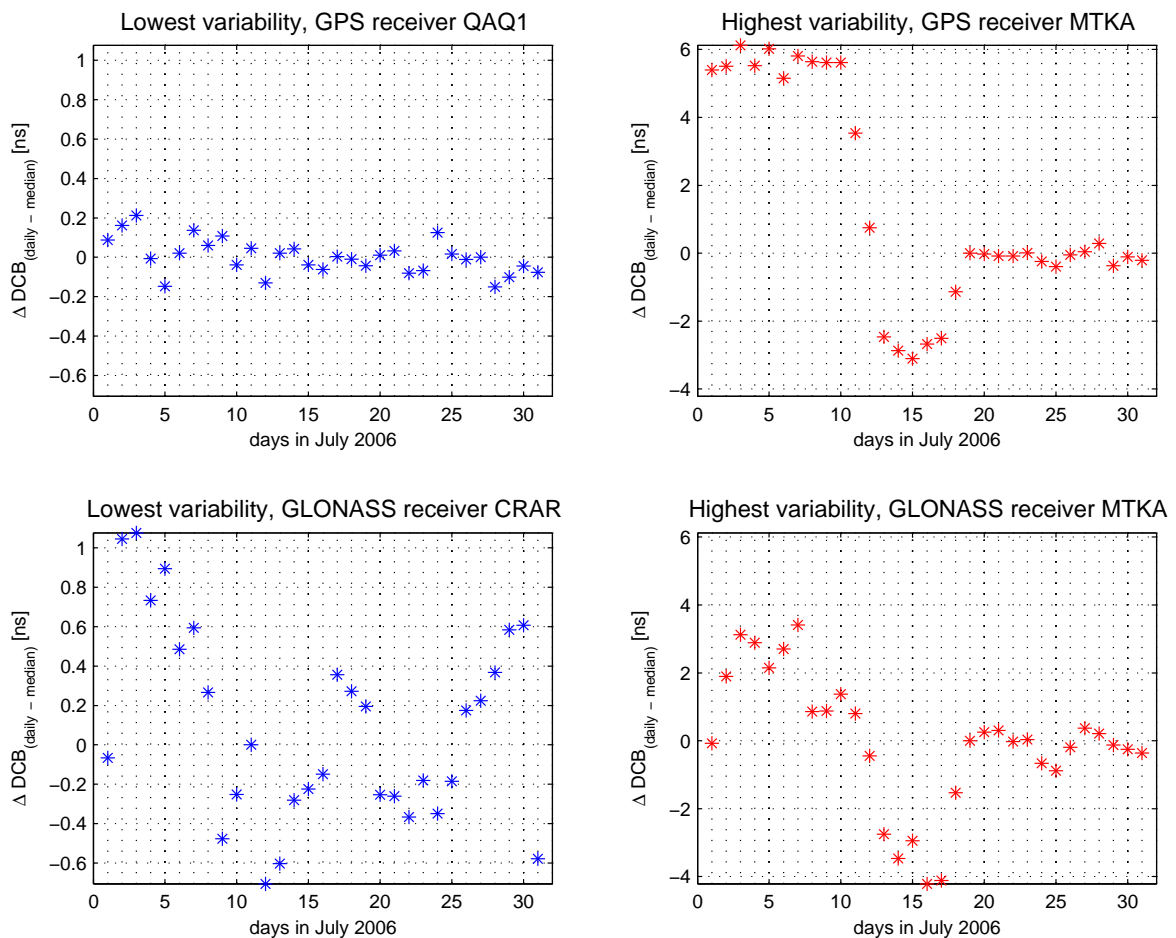
Figure 5.24: Difference between the daily estimates and the monthly median of the most and the least stable GPS (top) and GLONASS (bottom) receivers DCB for July 2006

Correlation between the GPS and GLONASS receivers DCB

The correlation matrix between the GPS and GLONASS receiver DCB estimates for day 022 in 2005 is shown in Figure 5.25, with the diagonal set to zero. The correlation coefi-

cients are predominantly positive. The maximum correlation between GPS and GLONASS receivers DCB is $C_{(gps,glo)} = 0.55$, between the stations DARW ($\beta = $ -12.8°, $\lambda = 131.1$°) and KHAJ ($\beta = 48.5$°, $\lambda = 135.0$°), of which KHAJ is the GPS/GLONASS receiver; the minimal correlation is $C_{(gps,glo)} = -0.005$.

The maximum correlation coefficient between the 170 GPS receiver DCB values estimated on that day is $C_{(gps,gps)} = 0.84$, between the GPS receivers DGAR ($\beta = $ -7.2°, $\lambda = 72.3$°) and NTUS ($\beta = 1.3$°, $\lambda = 103.7$°). Further receiver pairs with correlation higher than 0.7 are:

- DLFT ($\beta = 51.9$°, $\lambda = 4.3$°) and DGAR ($\beta = $ -7.2°, $\lambda = 72.3$°);
- NTUS ($\beta = 1.3$°, $\lambda = 103.7$°) and DLFT ($\beta = 51.9$°, $\lambda = 4.3$°);
- NRC1 ($\beta = 45.4$°, $\lambda = 284.3$°) and DREJ ($\beta = 51.0$°, $\lambda = 14.2$°);
- PERT ($\beta = $ -31.8°, $\lambda = 115.8$°) and MAS1 ($\beta = 27.7$°, $\lambda = 344.3$°);
- SANT ($\beta = $ -33.1°, $\lambda = 289.3$°) and RIOG ($\beta = $ -53.7°, $\lambda = 292.2$°).

The rather significant correlation coefficients between the DCB estimates of the listed GPS receiver pairs are subject of further investigation. As for the 30 GLONASS receiver DCB estimates, the highest correlation of $C_{(glo,glo)} = 0.54$ is between the GPS/GLONASS receivers UNB1 ($\beta = 45.9$°, $\lambda = 293.3$°) and TITZ ($\beta = 51.0$°, $\lambda = 6.4$°).
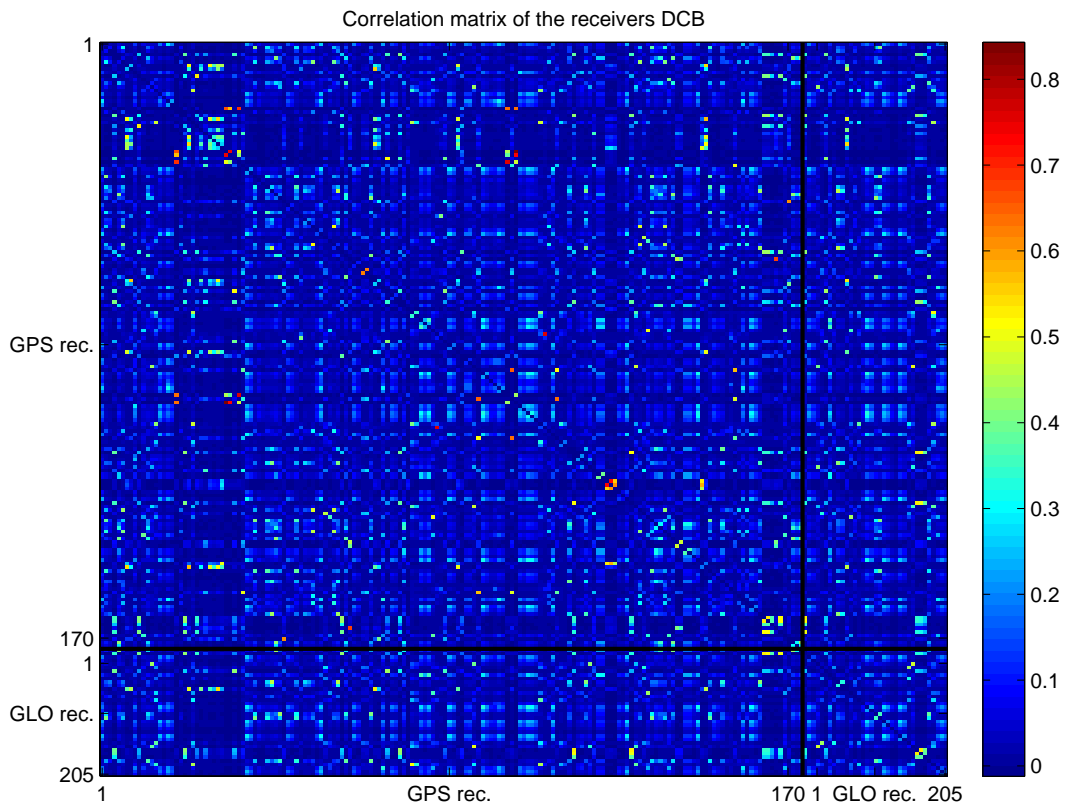
Figure 5.25: Correlation matrix of the receiver DCB estimates, GNSS GIM for day 022 2005; diagonal set to zero

5.5 Validation of the estimated VTEC maps and DCB values

5.5.1 Comparison with global VTEC maps and DCB provided by the IGS

For the sake of distinction, the Global Ionosphere Maps computed within this work are referred to as IGG (Institute of Geodesy and Geophysics) GIM. All IGG GIM are routinely compared with the GIM provided by the IGS Associate Analysis Centre CODE for validation of the obtained results. The CODE GIM (CODE, 2007b) are chosen as a reference for two reasons: the similar way of modelling through spherical harmonics expansion, and the utilisation of GLONASS data in the GIM for two of the four periods investigated in that work (in 2005 and 2006). It has to be mentioned, that the reference epochs of the IGG GIM (01, 03, 05, ..., 23 UT) are set up with regard to the independent day-by-day modelling, so that the reference epoch of each map is in the middle of the corresponding two-hourly data set. Hence, the reference epochs of the IGG maps do not overlap with the ones adopted in the recent (approx. since 2003) IGS GIM that are 00, 02, 04, ..., 24 UT. Therefore, an interpolation in time is performed when computing the differences between the CODE and IGG maps, which can worsen the results of the comparison.

IGG versus CODE VTEC maps

Figure 5.26 shows the two-hourly ΔVTEC maps CODE minus IGG for day 182 in 2006. The maximal and minimal differences for this day are 4.90 TECU and -6.91 TECU, respectively. The bias of the difference is ΔVTEC$_{mean} = -0.25$ TECU, with standard deviation 0.88 TECU. The correlation coefficient between the two VTEC data sets is 0.99. For most of the regarded days, the largest differences occur predominately in the low latitude regions with maximum VTEC. However, this is not a rule, as it can be seen in Figure 5.27, showing the two-hourly sequence of ΔVTEC for day 192 in 2006.

In Figure 5.28 the standard deviation, the bias, and the maximum and minimum of the differences ΔVTEC CODE minus IGG for the 31 days of July 2006 are plotted. The standard deviation does not exceed 1.18 TECU during the whole period and the bias is -0.16 TECU, showing that compared with the CODE maps the IGG GIM slightly overestimate the VTEC. The differences are in the range of ± 12 TECU, with exception of the 9th and 15th of July when large variations occur point wise. As visible in Figure 5.29, showing the ΔVTEC maps for the 15th of July (doy 196), the higher differences of up to -22 TECU appear only in the first three maps and approximately coincide with the location of the GPS station RIOG in the Tierra del Fuego archipelago, Argentina. Data from RIOG is used in both the CODE and IGG GIM for the regarded day. The faulty values appear in the IGG maps and are most probably caused by an undetected problem at this site, resulting in a high VTEC overestimation. The detected outliers disappear after the IGG GIM for that day are recomputed without using data from the RIOG station.
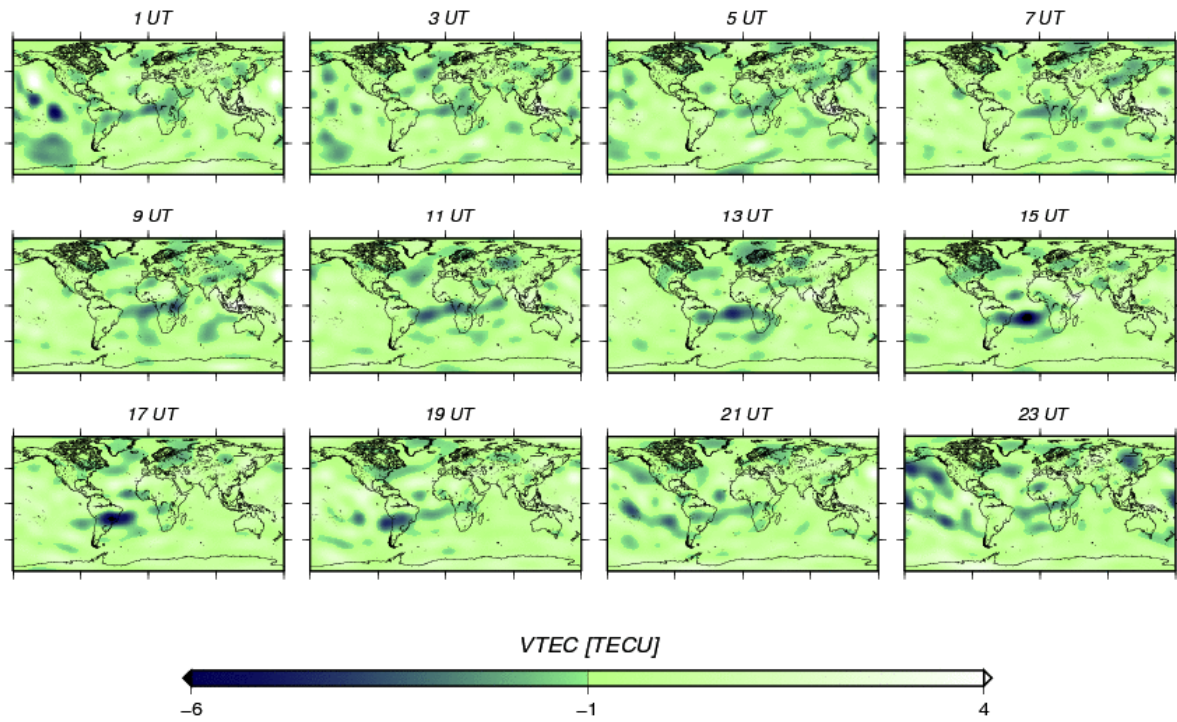
Figure 5.26: Global maps of ΔVTEC between the CODE and the IGG GIM in two-hourly snapshots for day 182 2006
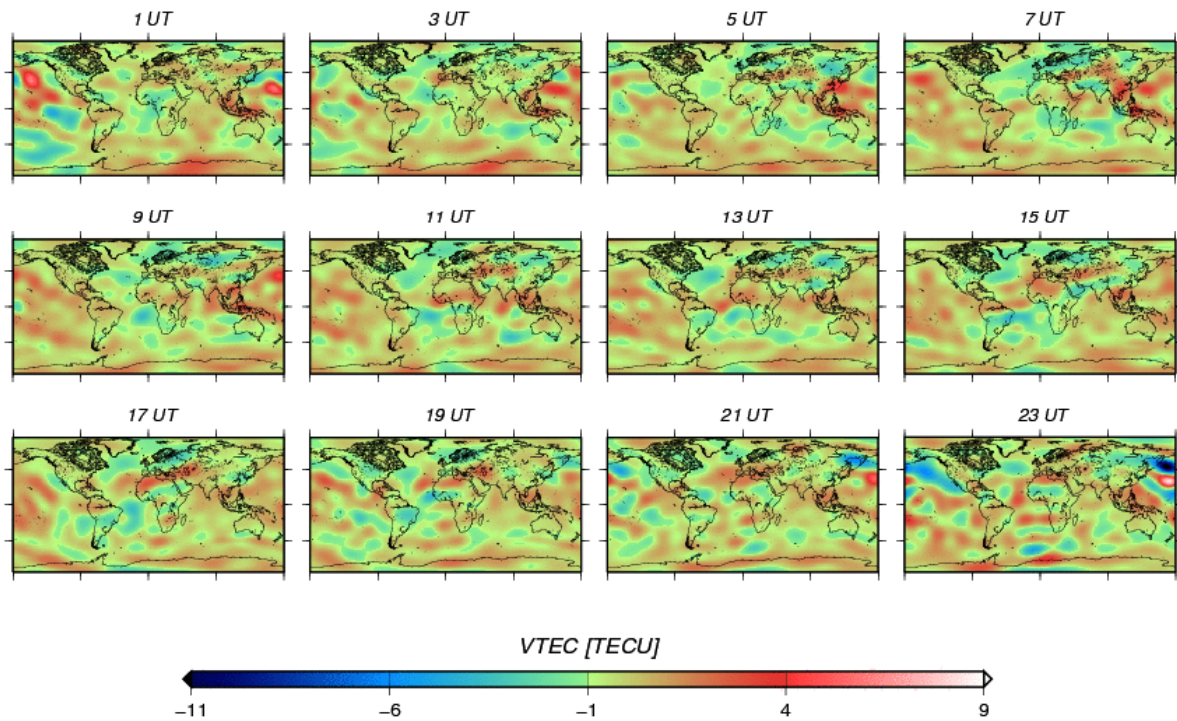
Figure 5.27: Global maps of ΔVTEC between the CODE and the IGG GIM in two-hourly snapshots for day 192 2006
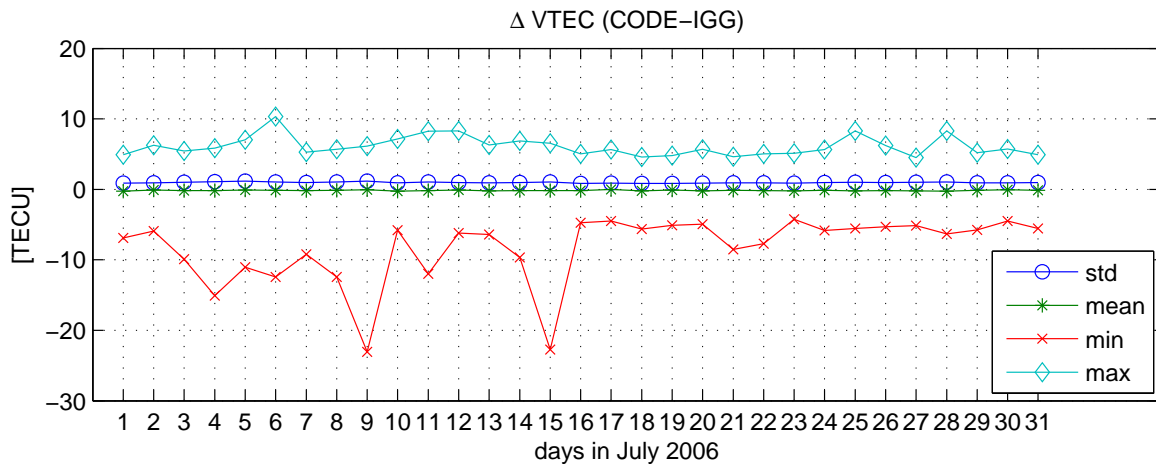
Figure 5.28: Standard deviation, bias, minimum and maximum of the difference ΔVTEC CODE minus IGG for July 2006
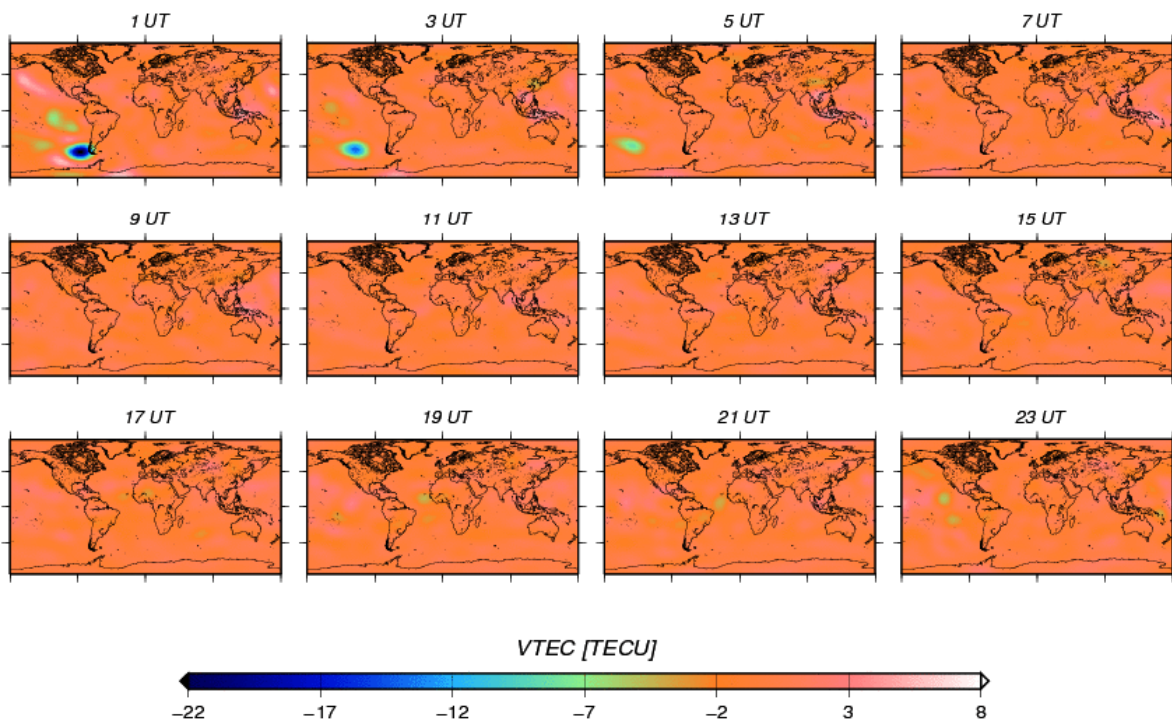
Figure 5.29: Global maps of ΔVTEC between the CODE and the IGG GIM in two-hourly snapshots for the 15th of July 2006

Comparisons of the mean VTEC

The mean VTEC values in terms of the first SH coefficient a_{00} from the CODE and the IGG GNSS GIM for July 2006 are shown in the upper plot of Figure 5.30. The lower plot shows the difference ΔVTEC_{mean} CODE minus IGG. The mean VTEC obtained from the IGG GIM coincides well with the CODE solution: the bias of the difference is -0.08 TECU and the standard deviation is 0.18 TECU. The correlation coefficient between the two time series 0.980.
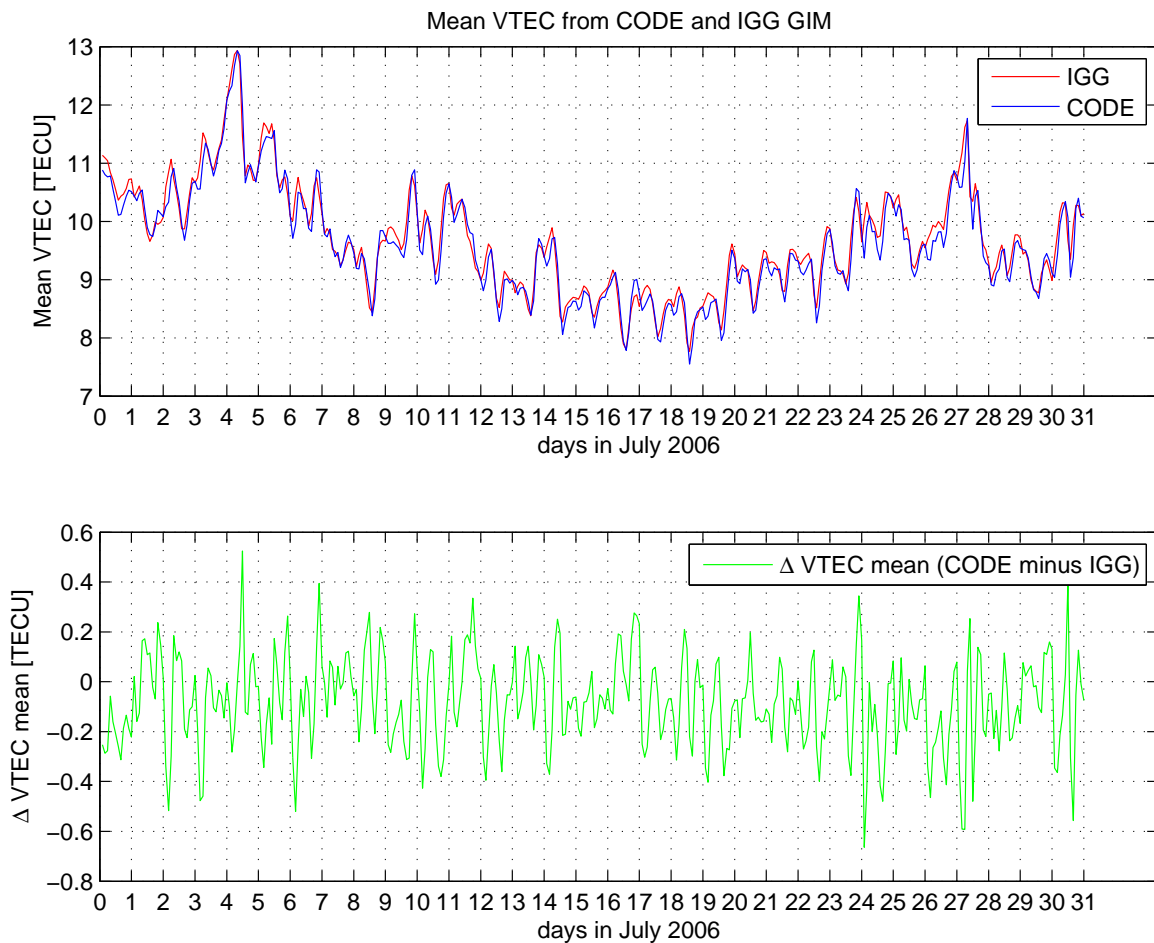
Figure 5.30: Mean VTEC obtained from the IGG and CODE GIM for July 2006 (upper plot) and the corresponding differences ΔVTEC_{mean} CODE minus IGG (lower plot)

To investigate the differences between the two solutions under various ionospheric conditions, the ΔVTEC CODE minus IGG is computed also for the four weeks with different combinations of solar and magnetic activity, mentioned in section 5.2. The results of this comparison are summarised in Table 5.3. It shows the weekly average of the standard deviation, the bias, and the maximum and minimum of the differences ΔVTEC CODE minus IGG for the four investigated periods. It has to be noted that for the first period (in 2001) the degree and order (n, m) of the SH used by CODE and IGG differ, as given in the right columns of

the table. Hence, the comparison for the week in 2001 is not entirely sound. The average values in Table 5.3 clearly show that the agreement between the two types of GIM worsens with increasing ionospheric activity, particularly in periods with higher sunspot number (the weeks in 2001 and 2002). Then, the maximal differences can reach up to ±50 TECU. Looking at the bias and standard deviation of the differences though, it can be stated that in general the two solutions coincide within several TECU.

Period	bias	std	max	min	CODE		IGG	
(doy, year)	[TECU]	[TECU]	[TECU]	[TECU]	data	n, m	data	n, m
267-273, 2001	2.20	7.88	51.37	-42.39	GPS	12, 12	GPS	15, 15
001-007, 2002	1.33	5.74	51.97	-31.39	GPS	15, 15	GPS	15, 15
016-022, 2005	0.02	2.18	21.81	-15.74	GNSS	15, 15	GNSS	15, 15
198-204, 2006	-0.15	0.88	5.08	-5.80	GNSS	15, 15	GNSS	15, 15

Table 5.3: Weekly average of the standard deviation, bias, the maximum and minimum of the difference ΔVTEC CODE minus IGG (in TECU); observations and degree and order of the SH used by CODE and IGG in the given period

For a more detailed view, the twelve two-hourly maps of the difference ΔVTEC CODE minus IGG for the first day of 2002 are plotted in Figure 5.31. Obviously, the largest differences occur predominately in the areas with higher ionospheric values and gradients along the magnetic equator.
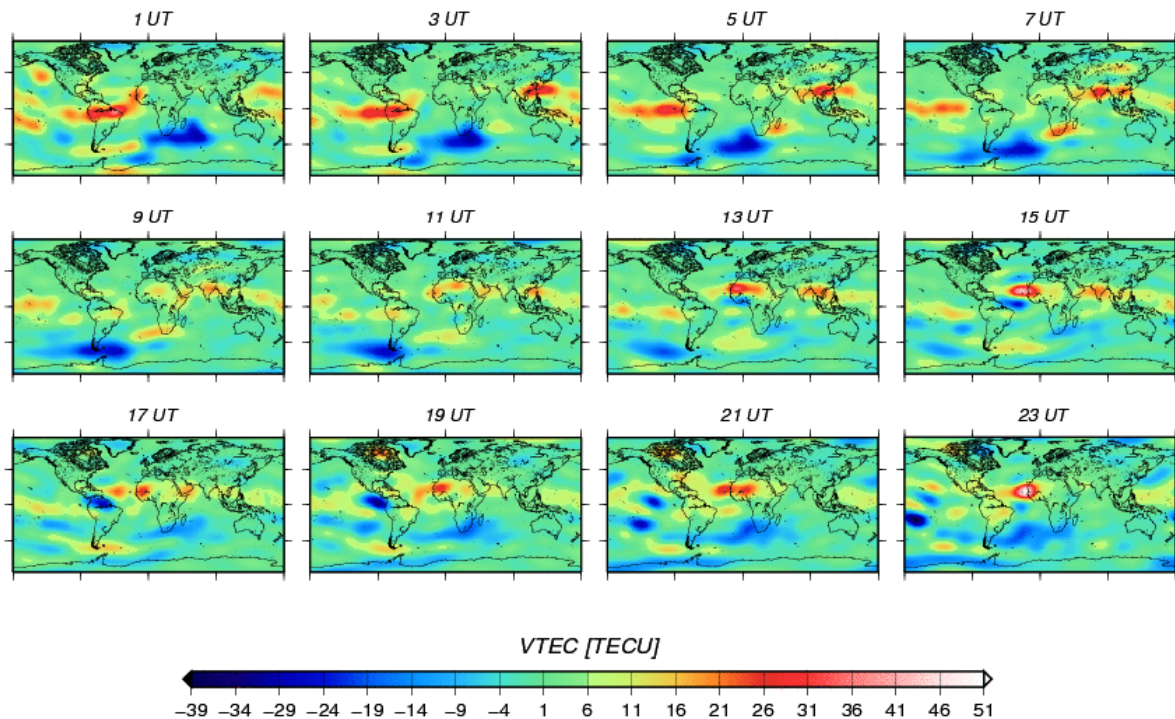
Figure 5.31: Global maps of ΔVTEC between the CODE and the IGG GIM in two-hourly snapshots for day 001 2002

IGG versus CODE satellites DCB estimates

The satellites and receivers DCB estimates are also routinely compared with the values provided by the IGS AAC CODE. In the official monthly DCB set provided by CODE (CODE, 2007c) the daily DCB estimates are aligned to a reference based on all involved satellites in a post-processing step, as already mentioned in section 5.4.1. The latter has not been done for the DCB estimated within that work and therefore the IGG monthly DCB set denotes the median of the daily values over one month. Figure 5.32 shows the comparison between the CODE and IGG GPS satellites DCB for July 2006. The bias between the two DCB sets is -2×10^{-16} ns. The standard deviation is 0.03 ns, corresponding to 0.09 TECU. As for the GLONASS satellites DCB (Figure 5.33), the mean differences are considerably higher with a bias of -0.61 ns or 1.75 TECU, and standard deviation of 0.50 ns or 1.44 TECU.
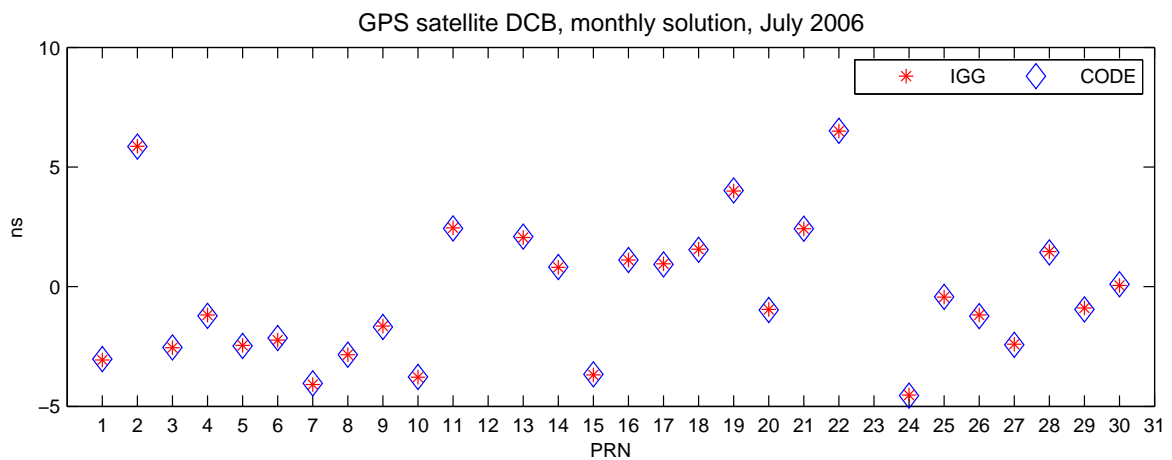
Figure 5.32: GPS satellites: CODE versus IGG DCB for July 2006
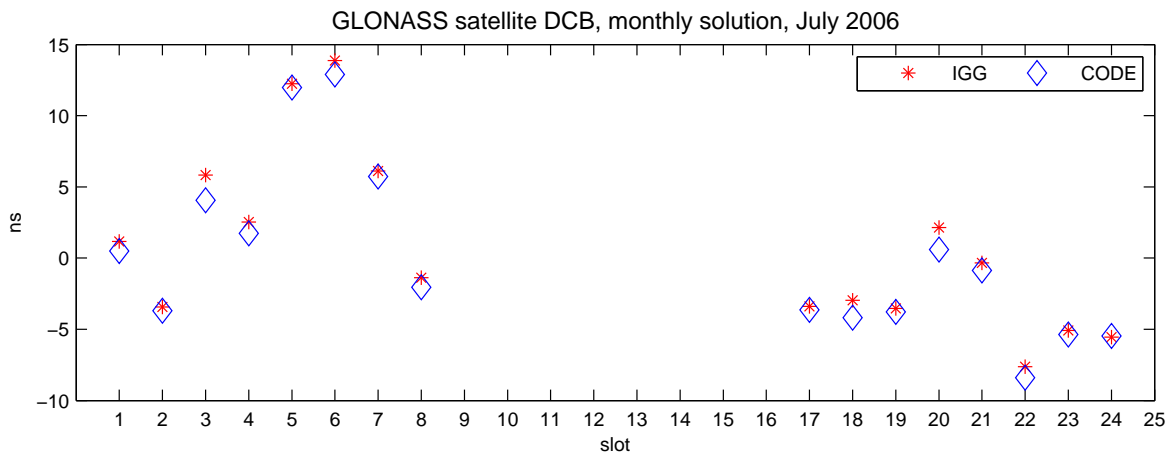
Figure 5.33: GLONASS satellites: CODE versus IGG DCB for July 2006

For each GLONASS satellite the differences between the monthly value and the daily estimates for both the CODE and the IGG solutions are shown in Figures 5.35 and 5.34.
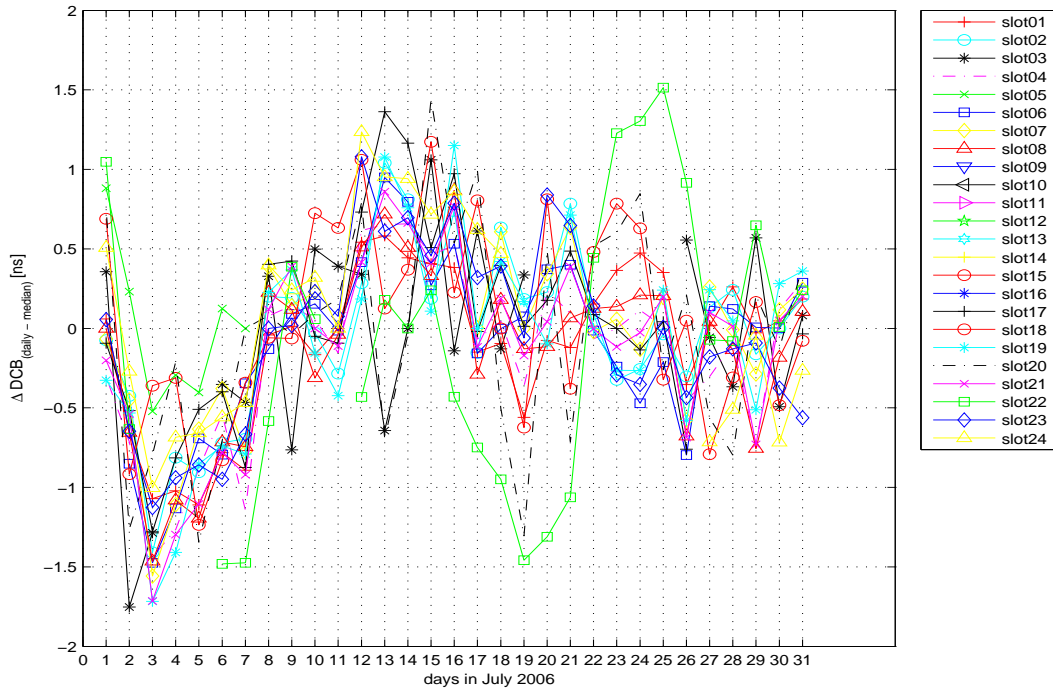
Figure 5.34: IGG GLONASS satellites DCB: daily estimates minus monthly value for July 2006
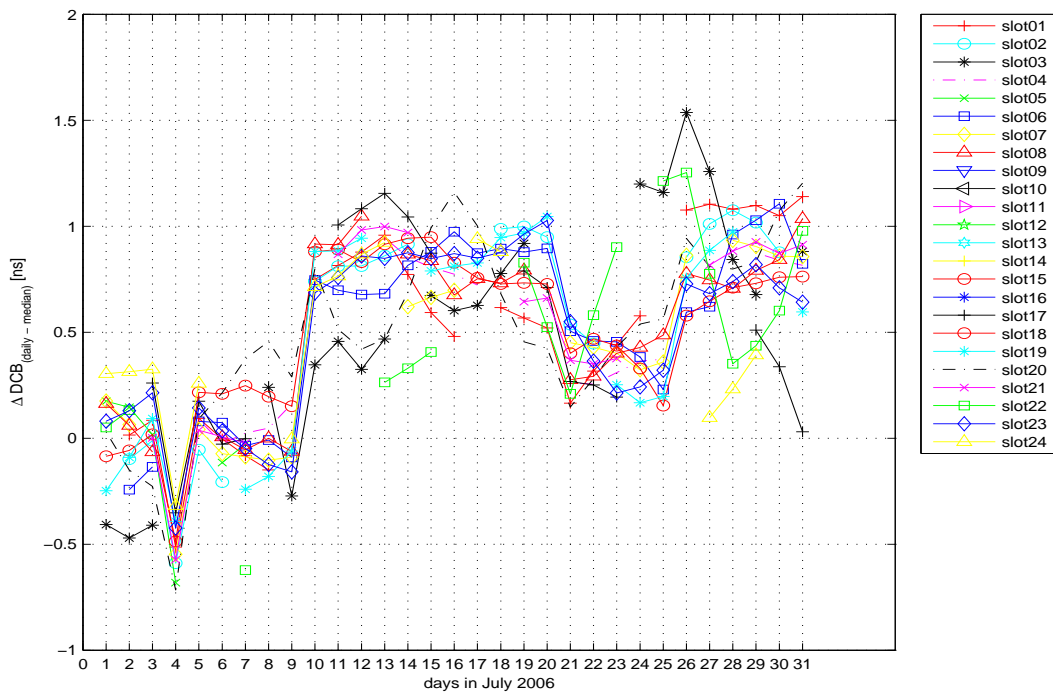
Figure 5.35: CODE GLONASS satellites DCB: daily estimates minus monthly value for July 2006

While in the case of GPS these differences clearly exhibit the behaviour of noise, for most of the GLONASS satellites an apparent signal can be detected. For the IGG GLONASS DCB estimates the differences between the monthly mean and the daily values are in the range of ±1.5 ns (Figure 5.34). Looking at the same differences for the CODE satellites DCB, shown in Figure 5.35, one can see a variability of slightly lower range - about ±1 ns. In both cases most of the satellites seem to follow a similar pattern. This behavior of the GLONASS satellite DCB is most probably caused by the shifting of the zero-mean when data from one or more satellites are missing in some of the days. As already mentioned, the monthly GLONASS DCB values provided from the AAC CODE undergo a second adjustment, relating them to a common monthly zero-mean. Therefore, the similar shifting of the difference between the monthly value and the daily estimates for nearly all satellites is more evident than in the case of the IGG DCB values.

IGG versus CODE receiver DCB estimates

The comparison between the CODE and IGG monthly receivers DCB can be seen in Figures 5.36 and 5.37. For the 91 common GPS receivers the bias between the CODE and the IGG monthly DCB is −0.08 ns (0.19 TECU) and the standard deviation amounts 0.72 ns or 2.04 TECU. The highest difference of 4.46 ns occurs at the GPS station `DAV1`. As for the 18 GLONASS receivers for which both CODE and IGG DCB are estimated, the bias and the standard deviation are −0.61 ns and 0.83 ns, corresponding to 1.77 TECU and 2.39 TECU, respectively. The CODE and IGG GLONASS receiver estimates differ the most (−3.04 ns) for the receiver at station `KIR0`.
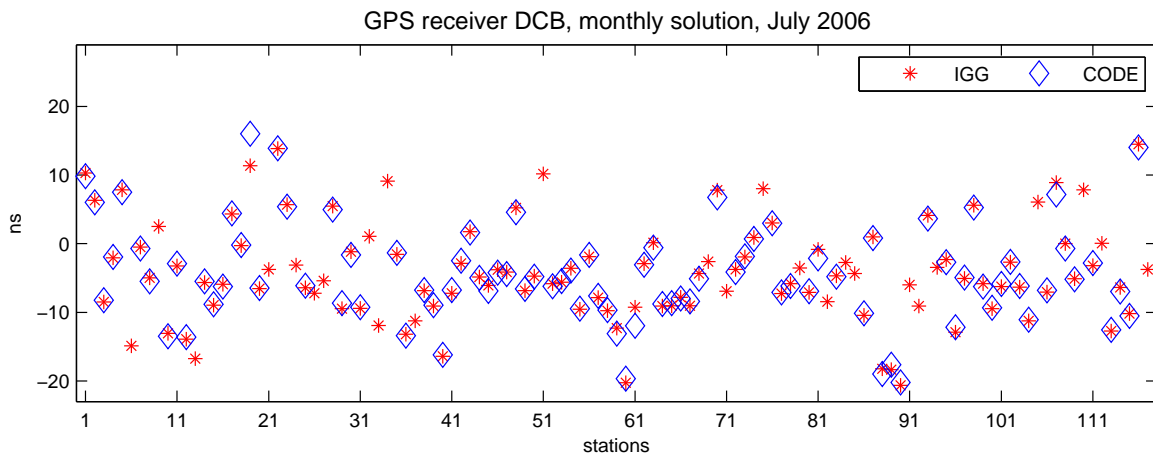
Figure 5.36: GPS receivers: CODE versus IGG DCB for July 2006
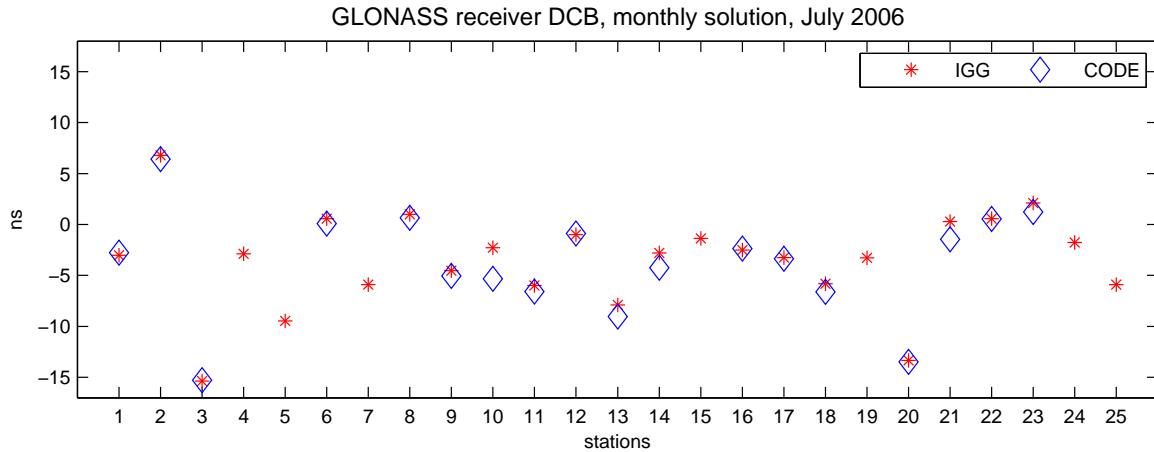
Figure 5.37: GLONASS receivers: CODE versus IGG DCB for July 2006

5.5.2 Comparison with satellite altimetry VTEC

The rapid and final global ionosphere maps produced by the IGS AAC and described in section 3.1.3, are routinely validated with Topex/Poseidon and Jason-1 VTEC (Orús et al., 2003). In order to assess the self-consistency of our approach and the accuracy of the GIM created within this work, the IGG GNSS GIM were also included in this validation procedure, in which the VTEC delivered by Jason-1 along its track is compared with the corresponding values interpolated from the global maps from GNSS data. The comparison was carried out at the UPC by Dr. Manuel Hernández-Pajares. As an example of the results obtained at UPC, the IGG VTEC versus the data delivered by Jason-1 for the interval 21-23 UT on the 31st of July 2006 (doy 212) can be seen in Figure 5.38.
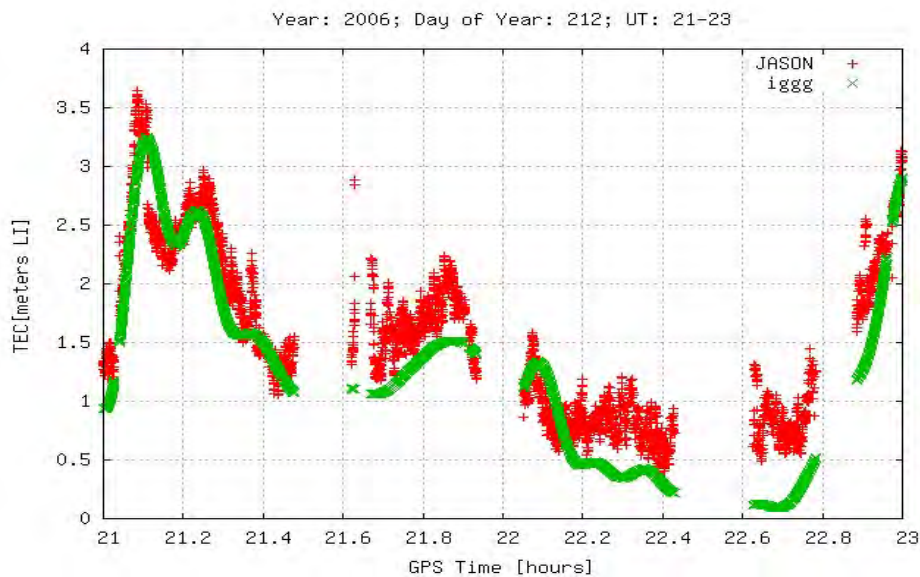
Figure 5.38: IGG versus Jason-1 VTEC, 21-23 UT, day 212 2006

The mean differences for the whole day 212 are shown in Figure 5.39 as a function of time (upper plot) and latitude (lower plot). The mean ΔVTEC Jason-1 minus IGG in time is in the range of 2-4 TECU, the positive sign indicating that Jason-1 overestimates the global VTEC, which is consistent with the phenomena already discussed in section 3.2.3. When looking at the differences as a function of latitude (Figure 5.39, lower plot), it appears that they remain in the mentioned range (about 2-4 TECU) in low and mid latitudes ($\pm 40°$). However, the differences increase at higher latitudes and, on the contrary, in the equatorial area they can become even negative for some of the regarded days.
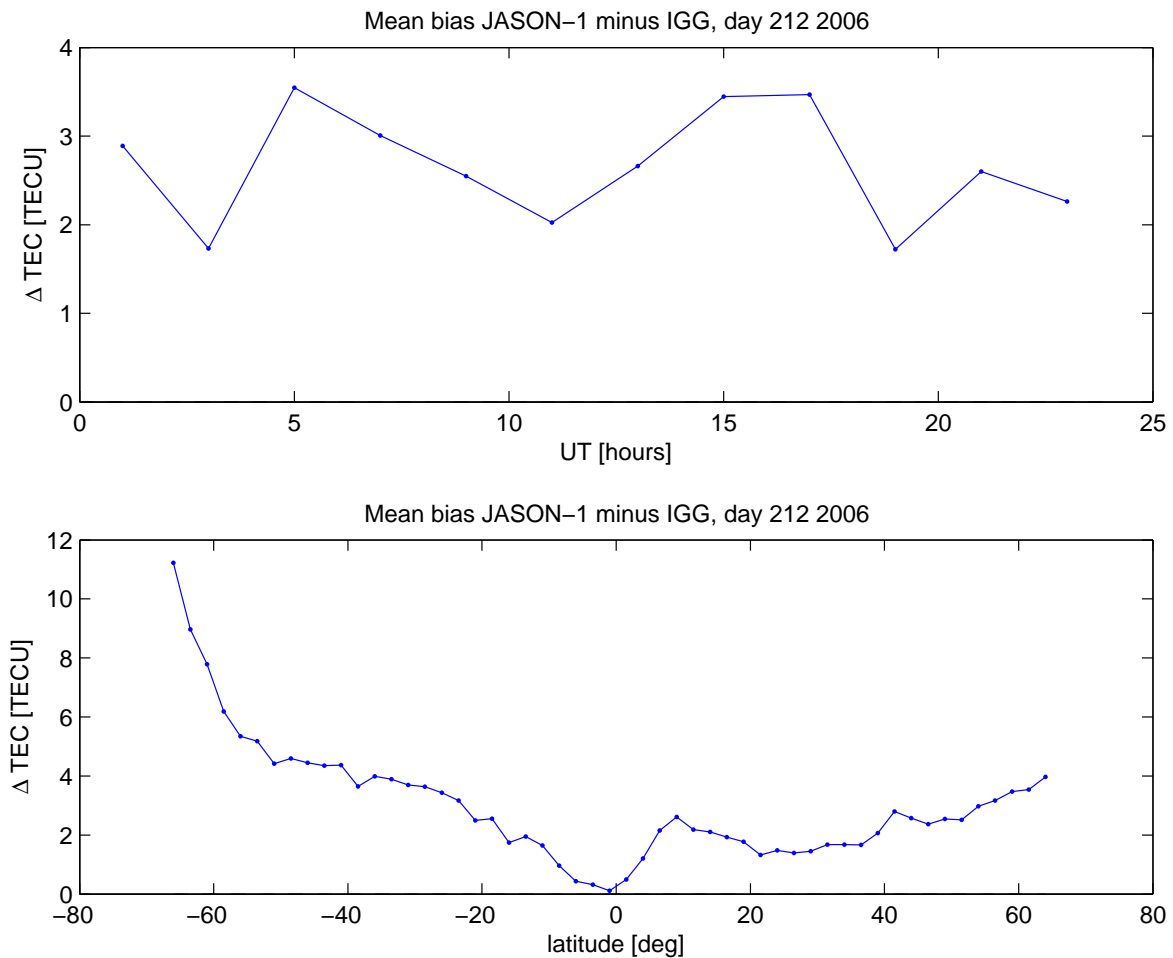
Figure 5.39: Jason-1 minus IGG VTEC in time (upper plot) and latitude (lower plot), day 212 2006

For a general overview, the differences between VTEC interpolated from the IGG GIM and the Jason-1 VTEC for days 182 to 212 in 2006 are averaged on a daily basis. The same is also done for the corresponding differences between Jason-1 and the final GIM provided by the four IGS AAC, as well as the combined IGS GIM (see section 3.1.3). Figures 5.40 and 5.41 show the mean bias, the standard deviation, the root mean square and the percentage error of the differences between VTEC from the various GNSS GIM compared to the data delivered by Jason-1. The comparison is performed in time (Figure 5.40) and in latitude

(Figure 5.41). The IGG model (referred to as 'iggg' in the figures) agrees with the results of the IGS GIM within 1 TECU, and for all GNSS GIM the differences with Jason-1 follow the pattern described above, exhibiting obvious latitudal dependency. As shown in Hernández-Pajares (2004), this behaviour of the differences between GNSS and altimetry derived VTEC can typically be observed for nearly all AAC's GIM and regarded as a visualisation of the insufficient performance of the altimetry measurements in low latitudes, due to the contribution of the topside ionosphere. This problem is treated in more detail in chapter 6.
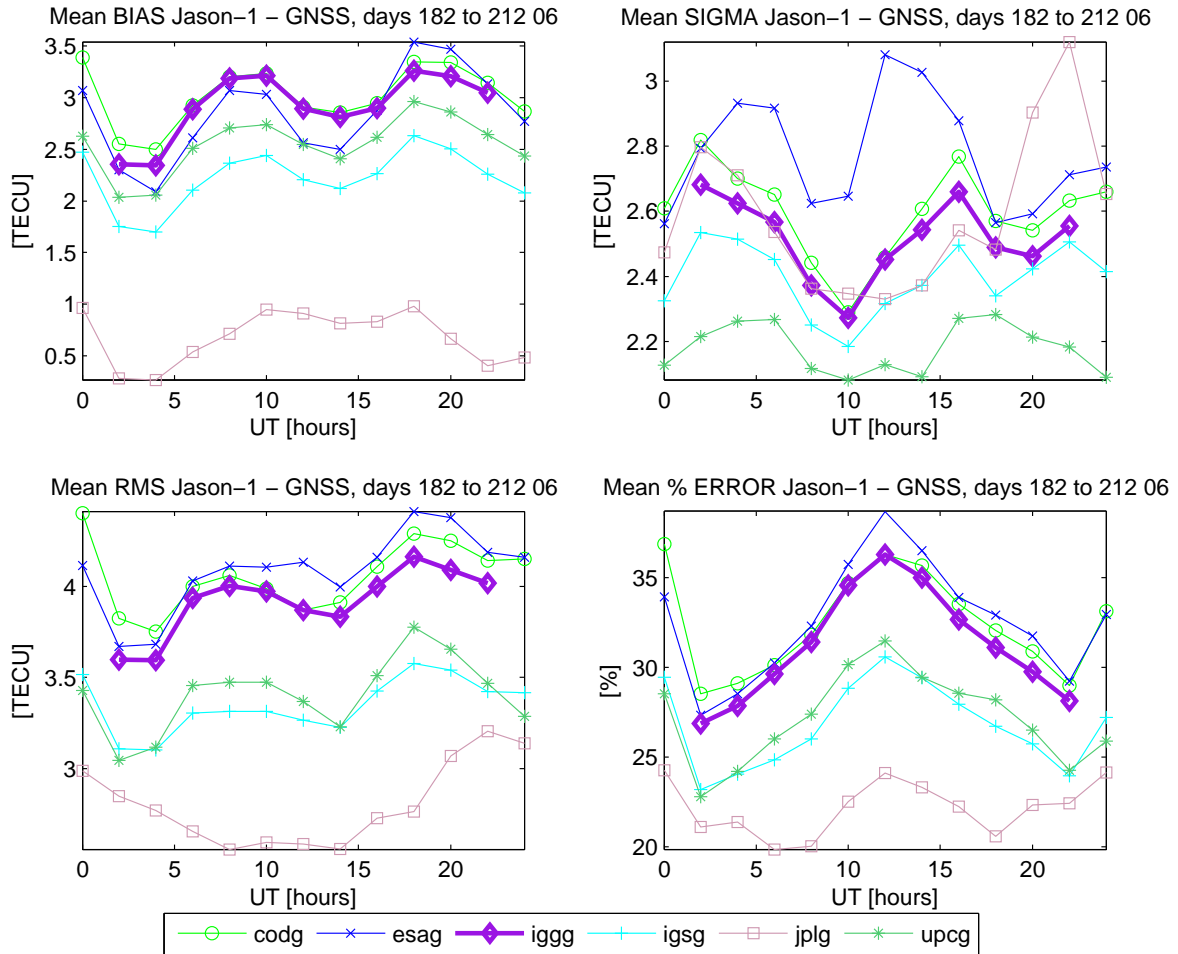
Figure 5.40: Jason-1 minus GNSS GIM VTEC, mean bias, standard deviation, root mean square and percentage error in time for days 182 to 212 2006

Eventually, the daily mean of the bias between the Jason-1 delivered VTEC and the values interpolated from the IGG GIM for the 31 days of July 2006 is shown in Figure 5.42. It can be seen, that the differences slightly increase in the middle of the period, but generally the variations do not exceed ±1 TECU. Their mean value for the whole month is 2.86 TECU. Examples of the differences between IGG GIM and altimetry derived VTEC for the four weeks of different solar and magnetic activity can be found in Appendices B.2 and B.4.
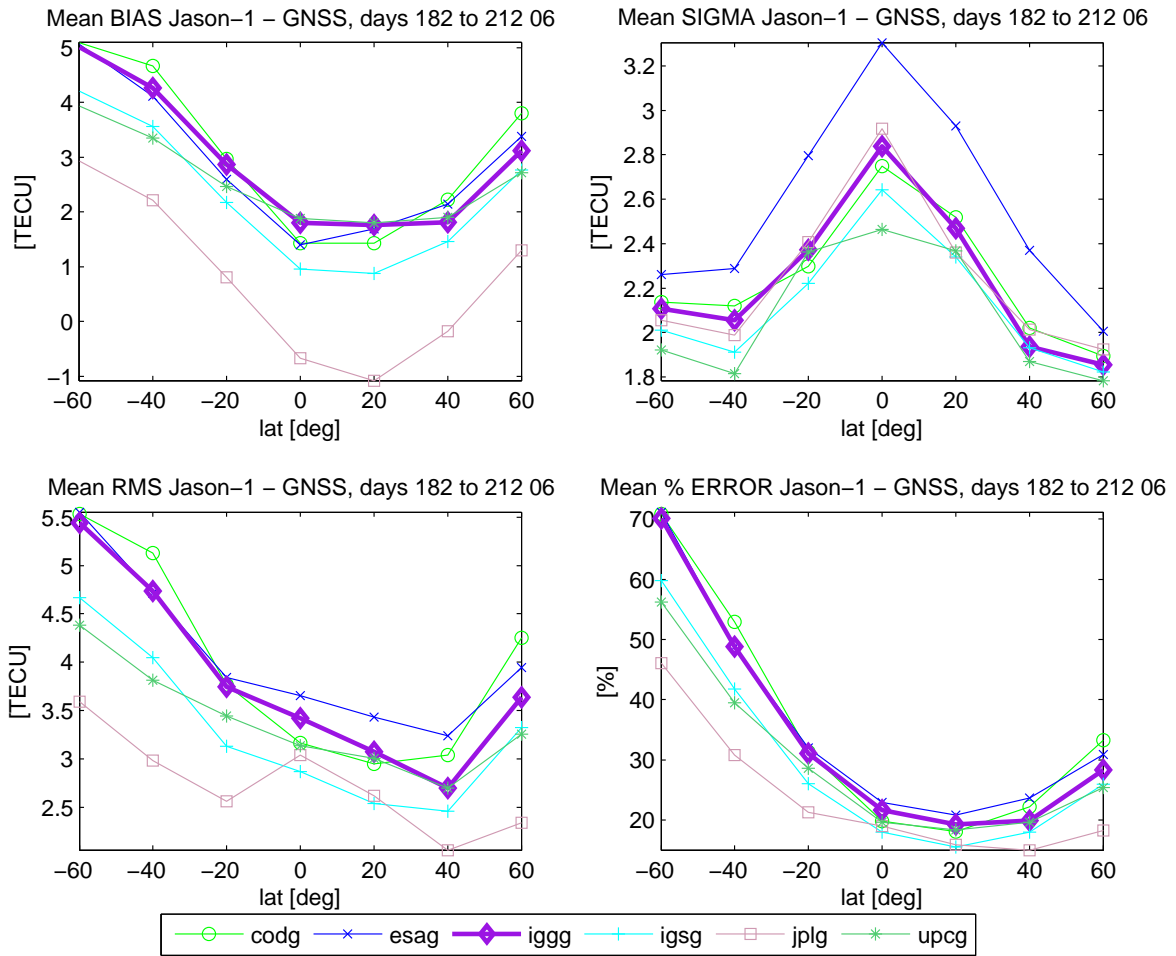
Figure 5.41: Jason-1 minus GNSS GIM VTEC, mean bias, standard deviation, root mean square and percentage error in latitude for days 182 to 212 2006
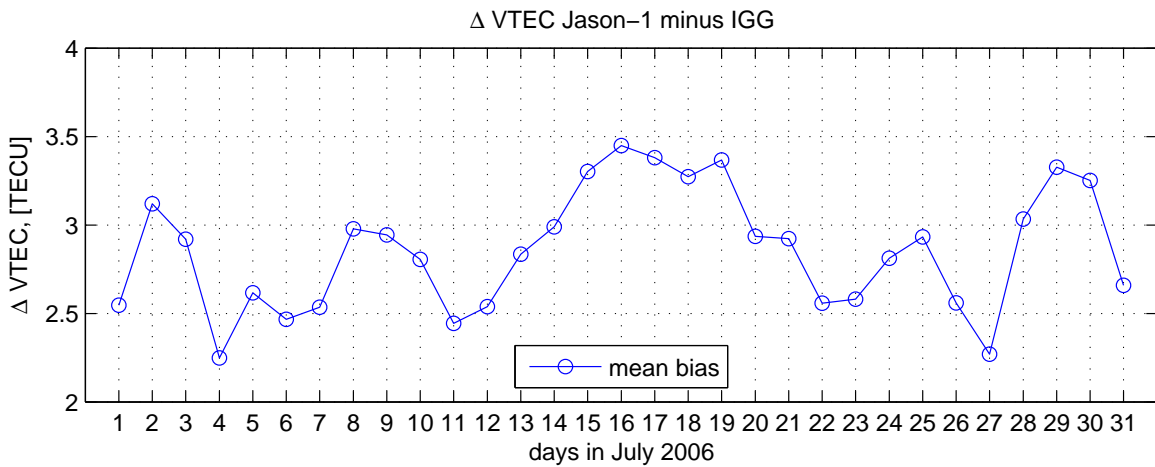
Figure 5.42: Daily mean of the difference Jason-1 minus IGG VTEC, July 2006

Chapter 6

Combined Global Ionospheric Maps

Usually, observations from the Global Navigation Satellite System are used for deriving global maps of the Total Electron Content. As it was shown in the previous chapter, the GIM derived from GNSS data generally provide good representation of the ionosphere. However, the ground stations are inhomogeneously distributed, with large gaps particularly over the sea surface, which lowers the precision of the GIM over these areas. Therefore, the demand for an integrated ionosphere model emerges, which comprises data from different space geodetic techniques. According to section 3.3, several modern geodetic techniques allow the observation and modelling of the ionosphere. Each of them has its specific characteristics, which influence the derived ionosphere parameters. By accounting for these specifics the combined model should make best use of the advantages of every particular method, have a more homogeneous global coverage and be more accurate and reliable than the results of each single technique.

6.1 Combination of GNSS and satellite altimetry observations

As a first step towards an integrated model of the ionosphere, within this study Global Ionosphere Maps from GNSS data are created and additionally satellite altimetry observations are introduced. The latter help to compensate the insufficient GNSS coverage over the oceans and increase the GIM reliability for these areas. The combination of data from about 160 GNSS stations and satellite altimetry observations from Jason-1 or Topex/Poseidon is performed on the normal equation level, as described in chapter 4. The combined global maps of the ionosphere are in two-hourly intervals, like the ones presented in chapter 5. Since the obtained GNSS GIM are used as basis, in the combined model the VTEC is parameterised and estimated in the same way (see section 5.1), and the GNSS data is handled as described in section 5.2. Similar to the GNSS GIM, daily values of Differential Code Biases for all GNSS satellites and receivers are estimated as a by-product of the combined maps. The final daily results of the combination are in the IONEX-format. An excerpt of the IONEX-file obtained for day 182 in 2006 can be seen in Appendix A.

Hence, the global ionosphere models computed within this work are referred to as IGG GNSS-only (estimated solely from GNSS data) and IGG COMB (derived from GNSS combined with satellite altimetry data) GIM.

6.1.1 Altimetry data used for the combination

The way of extracting ionosphere information from satellite altimetry observations is described in details in section 3.2. Therefore, only the basic features of the altimetry derived TEC will be recapitulated:

- similar to GNSS, the ionospheric effect on the Topex/Poseidon and Jason-1 altimeter measurements is proportional to the TEC along the ray path and inversely proportional to the square of the altimeter frequency;

- the precision of the satellite altimetry derived TEC estimates might be affected by systematic effects, such as the SSB;

- the utilised Topex/Poseidon and Jason-1 ionospheric corrections are provided by the Altimeter Database System (ADS) operated by the GFZ (ADSCentral, 2007). In particular, the so-called "DUFT" ionospheric correction is used;

- in a pre-processing step at the ADS the standard SSB correction is applied on the range data;

- the ionospheric range delay dR is directly provided in mm; thus, it first has to be transformed into TECU using (2.33);

- since the altimetry measurements are carried out normal to the sea surface, no mapping function (2.34) is needed in the case of satellite altimetry derived TEC. Therefore, the values obtained by applying (2.33) on the ionospheric range delay are directly referred to as VTEC.

- as initial pre-processing a simple polynomial-fitting procedure is applied for removing the rough outliers in the "raw" VTEC estimates.

For performing the combination on normal equation level, the altimetry derived VTEC is parameterised through spherical harmonic expansions (2.36) in the solar-geomagnetic frame (2.1) and (2.3). After applying the least-squares adjustment (see section 4.1), the resulting normal equations are combined with the ones obtained from GNSS data. This is done by adding the relevant matrices, as given in (4.15).

To visualise the used data, the footprints of the Jason-1 satellite altimeter are shown in Figure 6.1 along with the GNSS stations utilised for the two-hourly GIM for day 182 in 2006. In order to give a more realistic overview of the altimetry coverage, the Jason-1 footprints are plotted in geographical latitude β and sun-fixed longitude s, for the data enters into the model function with these coordinates (see also section 4.2). In the sun-fixed reference frame the number of collocated altimetry observations during one day is very high. Therefore, for each two-hourly interval only observations taken on a distance equal or higher than $0.1°$ from each other are included in the computations. Generally, the altimetry derived VTEC constitutes approximately 0.5% of the total amount of data used for one daily global solution.
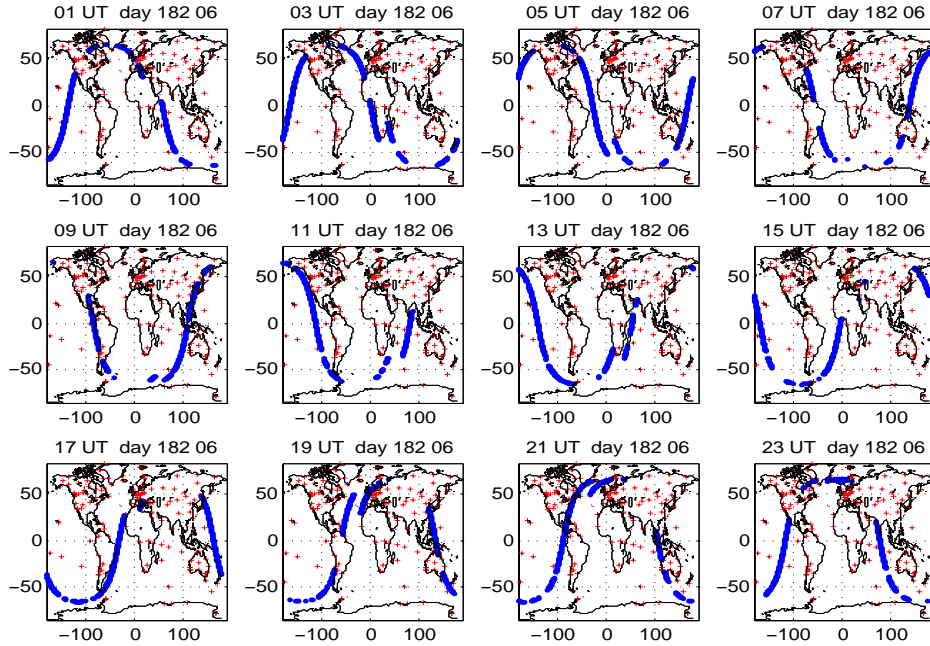
Figure 6.1: Observations used for the twelve two-hourly COMB GIM, day 182 in 2006: Jason-1 footprints (dots) and GNSS stations (crosses)

6.1.2 Impact of the different relative weighting

The relative weighting of the altimetry observations with respect to the GNSS data is a complex matter. In general, two different strategies are possible. On the one hand, due to the much higher number of GNSS measurements compared to satellite altimetry the Topex/Poseidon and Jason-1 data should be over-weighted in order to increase their impact on the combined GIM. In the case of overweighting, however, it becomes crucial to assess the bias between the GNSS and altimetry derived TEC discussed in section 3.2.3. On the other hand, if we take into account the higher noise of the altimetry measurements compared to the carrier-phase smoothed code data from GNSS, a lower weight should be applied on all Topex/Poseidon and Jason-1 derived observations.

To test the impact of the altimetry data relative weighting on the combined GIM, several different weights P_{alt} are applied in (4.15). For the lower-weight supposition $P_{alt} = 0.25^2$ and $P_{alt} = 0.5^2$ are taken. According to the lower number of altimetry observations on the one hand, and their limited distribution in the sun-fixed reference frame on the other, the following weights are chosen to test the higher-weight hypothesis: $P_{alt} = \left\{2^2, 4^2, 10^2\right\}$. Giving equal weights for both types of data (i.e., $P_{alt} = 1$) is tried out as well. For a global overview of the weighting impact, the differences between four of the COMB solutions and the GNSS-only GIM for the map at 19:00 UT on day 182 in 2006 are shown in Figure 6.2. The impact of the altimetry weights is visible mostly along the Jason-1 track (cf. Figure 6.1). Therefore, Figure 6.3 shows the difference ΔVTEC along the Jason-1 track between the GNSS-only GIM and the COMB maps for the whole day with each of the tested altimetry data weights. The results of the comparison are summarised in Table 6.1, which shows the bias, standard deviation, and the maximum absolute difference between the regarded VTEC time series.
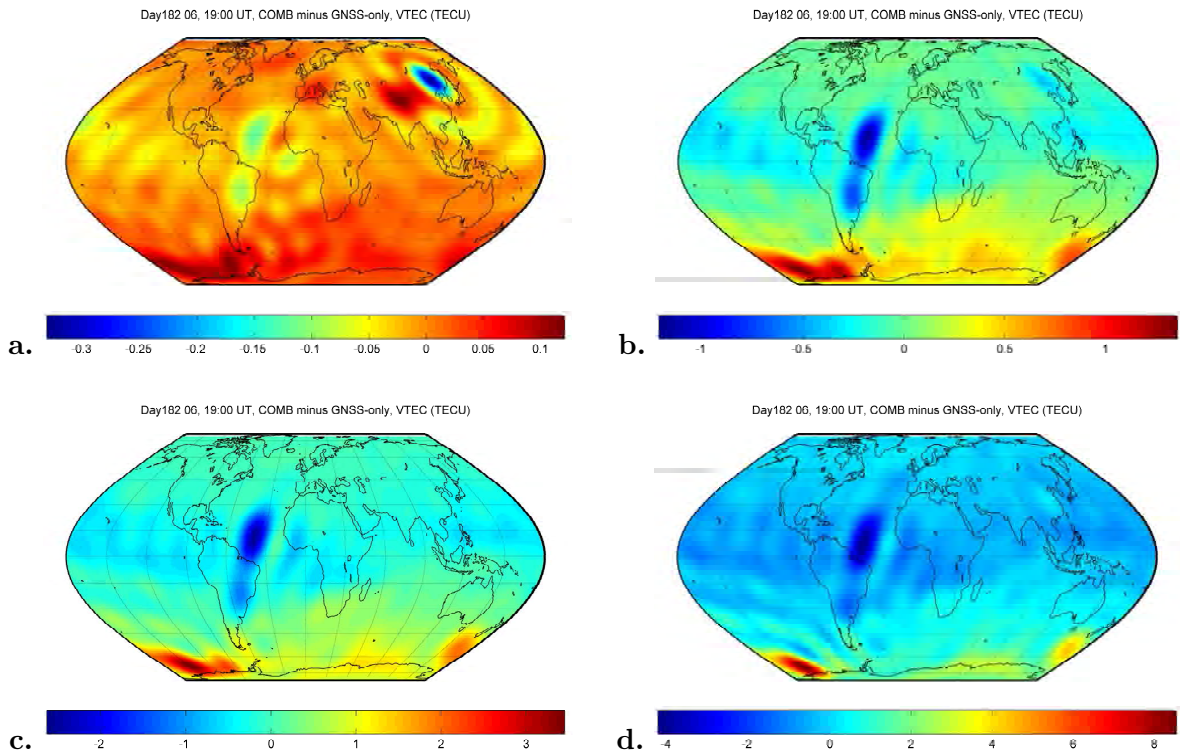
Figure 6.2: COMB GIM minus the GNSS-only GIM at 19:00 UT on day 182 2006, with: **a.** $P_{alt} = 0.5^2$; **b.** $P_{alt} = 2^2$; **c.** $P_{alt} = 4^2$; **d.** $P_{alt} = 10^2$
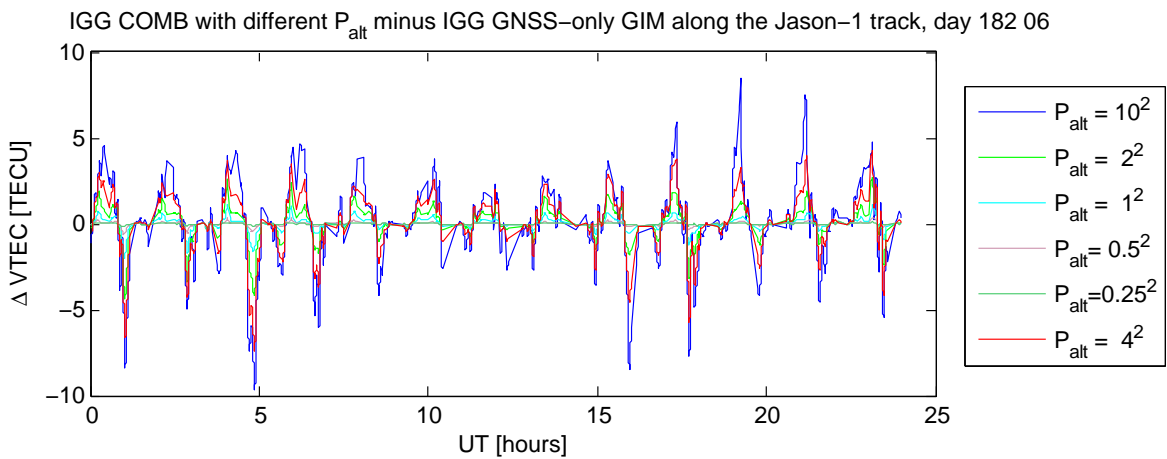
Figure 6.3: ΔVTEC COMB with different P_{alt} minus the GNSS-only GIM along the Jason-1 track, day 182 2006

P_{alt}	0.25^2	0.5^2	1^2	2^2	4^2	10^2
bias, [TECU]	-0.01	-0.02	-0.04	-0.11	-0.22	-0.43
std, [TECU]	0.04	0.13	0.42	1.03	1.77	2.46
max, [TECU]	-0.31	-0.66	-2.02	-4.32	-7.40	-9.63

Table 6.1: Bias, standard deviation, and maximum difference ΔVTEC COMB with different P_{alt} minus the GNSS-only GIM along the Jason-1 track, day 182 2006

Although the amounts of negative and positive differences are rather balanced, for all COMB GIM the bias with the GNSS-only solution along the Jason-1 track is negative. This effect is caused mainly by the high values of the negative differences coinciding with the ionospheric peaks as the VTEC maximum travels with the Sun during the day. Since it is not sampling the whole ionosphere, the altimeter tends to underestimate the VTEC when the plasmaspheric contribution reaches its maximum. This problem is discussed further in section 6.2.

The results show that the relative weighting basically acts like a scaling factor for the contribution of the altimetry data in the combined GIM. When down-weighting the altimetry data, its impact on the combined solution is diminutive - both the standard deviation and the maximum absolute difference between the COMB and GNSS-only GIM are below 1 TECU. The equal weights generate a standard deviation below 0.5 TECU. On the other hand, the weight of 10^2 causes absolute differences reaching nearly 10 TECU. This is rather inconsistent since the plasmasheric contribution above the altimeter altitude is believed to be about 10 to 20% of the TEC (Brunini et al., 2005). Concequently, the proper relative weigth of the altimetry data should be provided approximately between $P_{alt} = 2^2$ and $P_{alt} = 8^2$. It is a very complex issue, depending on the different spatial and temporal distribution of the two types of observations and on their specific systematic errors. In this work a fixed weight of $P_{alt} = 4^2$ is chosen. Among other reasons, this value is taken for in that case the standard deviation between the COMB GIM and the GNSS-only solutions is around or slightly below the range of the estimated offsets for the altimetry satellite (cf. Table 6.3). Certainly, the relative weighting can be optimised and is a matter of further investigation.

6.1.3 Instrumental offset of the altimeters

The bias between GNSS and altimetry derived TEC is a very important issue, especially when higher weight is applied to the altimetry data than to the GNSS measurements. As mentioned in section 3.2.3, several studies show that despite of the lower orbit altitude of the altimetry satellites, the VTEC delivered by these missions is higher than the values obtained from GNSS. Therefore, it can be assumed that the altimetry measurements are biased by an instrumental offset similar to the GNSS DCB.

According to section 4.2, the combination procedure realised by stacking of normal equations (4.15) allows the independent estimation of technique-specific constant time delays. Hence, the combination on normal equation level is used for estimating constant daily offsets for the altimetry satellite along with the combined GIM and the DCB (the latter are discussed in section 5.4). Since only the spherical harmonic coefficients are affected by the combination, the DCB and the altimetry offset remain independent. As an example, Table 6.2 shows the bias and the standard deviation of the difference between the DCB values estimated along

with the GNSS-only and with the combined GIM for day 182 in 2006. In the table's last row the mean RMS of the estimated DCB is given. It can be seen that the bias between the DCB estimates from the GNSS-only and the COMB model is within their formal precision.

	satellites DCB		receivers DCB	
	GPS	GLO	GPS	GLO
bias, [ns]	$5 \cdot 10^{-18}$	$-4 \cdot 10^{-9}$	0.004	-0.023
std, [ns]	0.005	0.004	0.192	0.141
mean RMS, [ns]	0.004	0.009	0.016	0.025

Table 6.2: Bias and standard deviation of the difference ΔDCB GNSS-only minus COMB GIM, and mean RMS of the DCB estimates, day 182 in 2006

In the combined global solution the altimetry offset is computed daily as a single constant value per altimetry satellite. The estimated constant offsets of the Jason-1 satellite for the 31 days of July are shown in Figure 6.4. For the given period the values vary between about 2.5 to 3.5 TECU; the average of their estimated standard deviation is 0.01 TECU. Thus, they generally correspond to the systematic altimetry VTEC overestimation of about 1 to 4 TECU compared to the values delivered by GNSS, as summarised in Brunini et al. (2005). The estimated offsets also match the range of the differences between the VTEC interpolated from the GNSS-only solution and the Jason-1 derived VTEC for the same period, and also follow a very similar pattern (cf. Figure 5.42).
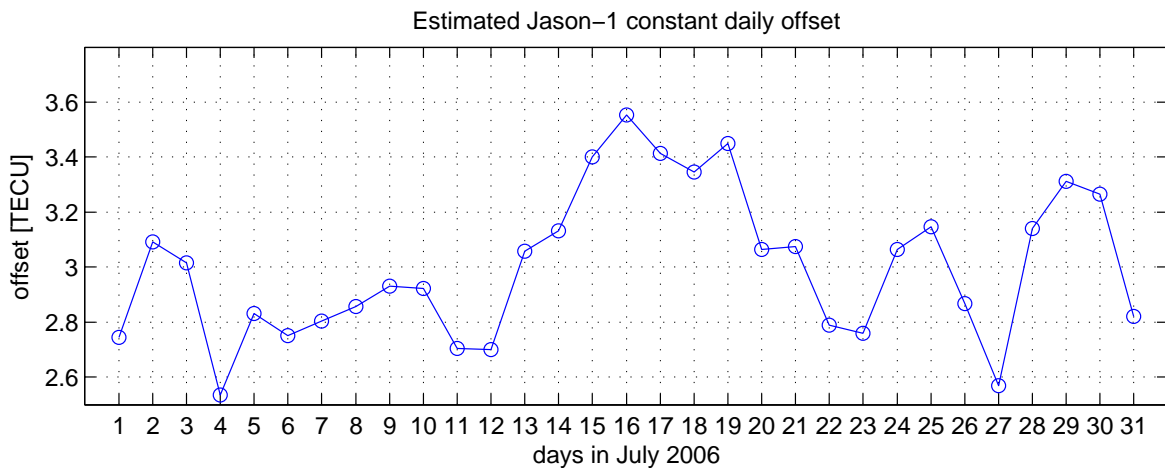
Figure 6.4: Estimated daily offsets of the Jason-1 altimeter for July 2006

The Topex/Poseidon and Jason-1 offsets estimated for four weeks with different ionospheric conditions are shown in Appendix B.3. The weekly averages of the offsets are in the range of 1.5 to 3 TECU, without showing an apparent dependence on the overall ionospheric activity or the particular satellite (see also Table B.1).

To demonstrate the differences between the combined IGG GIM with and without estimation of altimetry offset relative to the GNSS-only solution, the VTEC and RMS values along

the Jason-1 track are interpolated from the different IGG global maps for day 182 in 2006. The compared solutions are: IGG GNSS-only GIM, IGG COMB GIM without estimation of Jason-1 offset, and IGG COMB GIM with Jason-1 offset estimated as a constant. The corresponding VTEC and RMS along the Jason-1 track are plotted in Figure 6.5 as function of the time; the Jason-1 offset is referred to as JOE (Jason-1 Offset Estimate). In the upper plot also the Jason-1 "raw" data is shown for comparison.

Regarding the VTEC values (Figure 6.5, upper plot), the IGG COMB GIM without estimation of Jason-1 offset (IGG COMB, without JOE) predominantly overestimates the VTEC compared to the GNSS-only solution. Along the Jason-1 track, the bias ΔVTEC GNSS-only minus COMB without JOE is -1.56 TECU. The introduction of the altimetry offset (2.75 TECU for the regarded day) compensates the overestimation effect, acting as a negative offset as to the IGG COMB solution without JOE. Correspondingly, the bias ΔVTEC GNSS-only minus COMB with JOE is 0.24 TECU. In this day the standard deviation of the difference with the GNSS-only GIM is 1.78 TECU for both COMB models. As it could be expected, the introduction of the Jason-1 bias has nearly no impact on the formal precision (or RMS) of the combined GIM (Figure 6.5, lower plot).
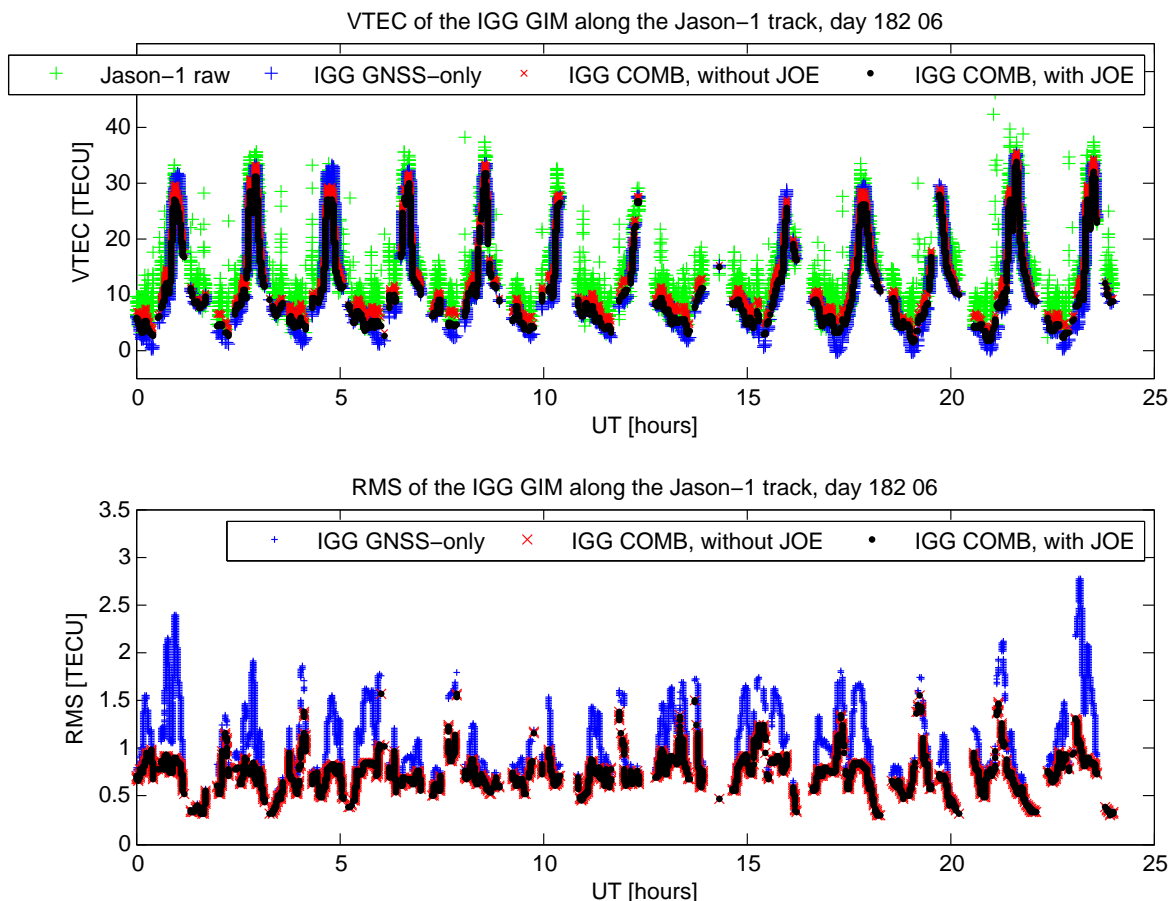
Figure 6.5: VTEC (upper plot) and RMS (lower plot) interpolated along the Jason-1 track from the different IGG GIM for day 182 2006

The behaviour of the differences between the combined IGG GIM with and without estimation of altimetry offset remains similar throughout the investigated periods and shows that in general the computation of an altimetry satellite offset leads to a better agreement between the GNSS-only and the COMB GIM. Therefore, by default the IGG COMB solutions include the computation of daily constant values for this offset. In this way, the estimated offsets still include the plasmaspheric component (i.e., VTEC above approx. 1300 km height, not sampled by the satellite altimeters) additionally to the actual instrumental delay. Along with the differences between the GNSS-only and the COMB GIM with estimation of altimetry offset, this issue is discussed in more detail in the following section.

Eventually, Table 6.3 shows the daily Jason-1 altimeter offset estimate for day 182 in 2006 obtained from the COMB GIM with different weighting of the altimetry data. On average, the value of the offset estimate increases by about 0.05 TECU per weight unit.

P_{alt}	0.25^2	0.5^2	1^2	2^2	4^2	10^2
JOE, [TECU]	2.50	2.51	2.54	2.62	2.75	2.97

Table 6.3: Jason-1 Offset Estimate (JOE) for day 182 2006 obtained from IGG COMB GIM with different P_{alt}

6.2 Examples of combined GIM and comparison with the GNSS-only models

The GNSS-only and the combined global VTEC maps for 19:00 UT on the 1st of July 2006 (doy 182) can be seen in the left and right plot of Figure 6.6, respectively. Since the differences between both GIM are not clearly distinguishable, the corresponding map of the ΔVTEC COMB minus GNSS-only is also shown (Figure 6.7). Positive values denote increase of the estimated VTEC when adding Jason-1 data and vice versa.

Looking at the differences in Figure 6.7, one can recognise an increase of the VTEC values particularly over the oceans and in high southern latitudes, where nearly no GNSS observations are available. The decrease in the equatorial area, coinciding with the region of highest ionospheric activity for this map, can be interpreted as the signature of the plasmaspheric component. As already mentioned, the altimetry measurements do not account for the topside ionosphere. Therefore, despite of the discussed TEC overestimation the integration of altimetry data in the GNSS GIM leads to a decrease of the obtained VTEC over the area where the plasmaspheric contribution reaches its maximum. This pattern of the differences between the GNSS-only and the COMB GIM is kept in all of the twelve two-hourly maps for that day (Figure 6.8), as well as throughout the investigated periods (see also Appendix B.1). For the whole day 182 in 2006, the maximum and minimum ΔVTEC COMB minus GNSS-only is 4.36 and -7.40 TECU, respectively. The mean of the differences is 0.16 TECU, i.e. in general the VTEC obtained from the COMB GIM is slightly higher; the standard deviation of the differences between the two GIM is 0.67 TECU. To concentrate on the differences between the two models especially along the Jason-1 track, the VTEC values interpolated from the GNSS-only and COMB GIM for day 182 in 2006 are shown in Figure 6.9.
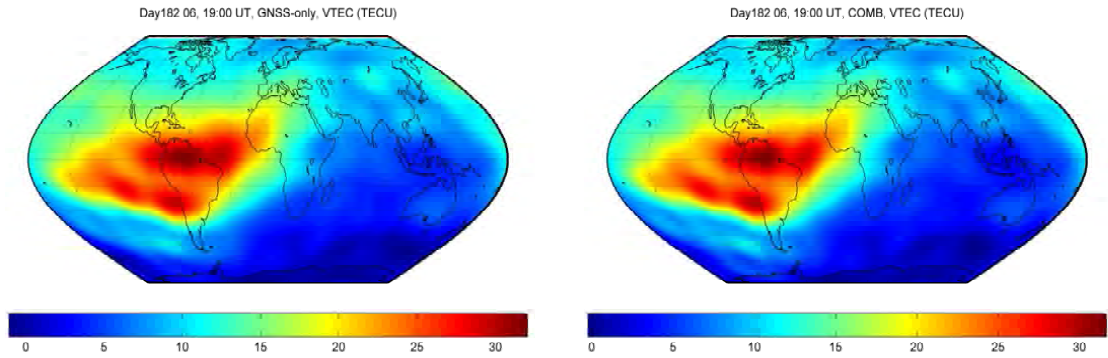
Figure 6.6: GNSS-only (left plot) and COMB GIM (right plot) for 19:00 UT, day 182 2006
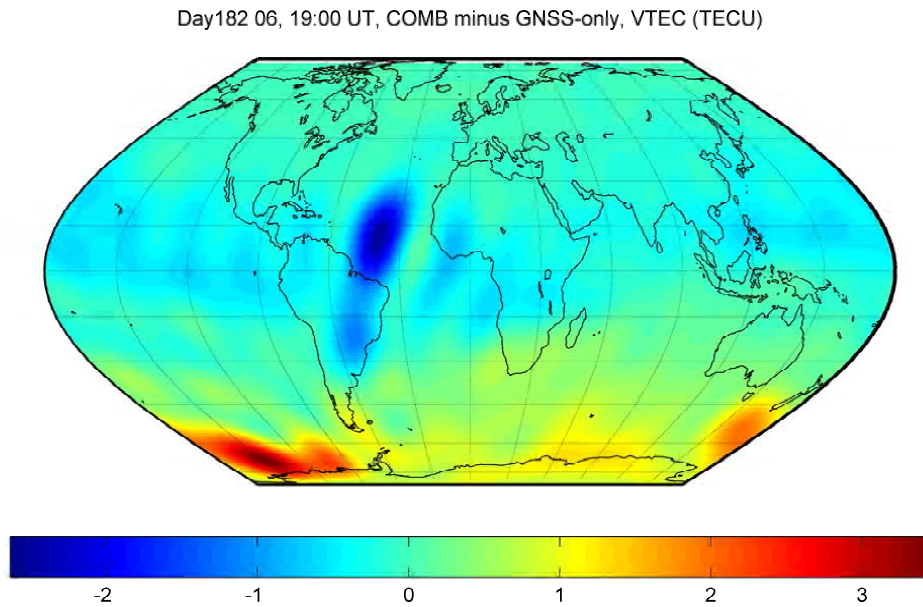
Figure 6.7: ΔVTEC COMB minus GNSS-only GIM, 19:00 UT, day 182 2006

In the domain of low ionosphere activity (in the regarded example VTEC below 10 TECU) at mid and high latitude, a general trend for increase of the VTEC values in the COMB GIM along the Jason-1 track is visible. This effect can be interpreted as the positive contribution of the altimetry data in areas where too few GNSS observations are available, such as the oceans in the higher southern hemisphere. Especially in such regions the GNSS-only model can provide faulty, usually negative values due to absence of observations in a particular two-hourly interval (see section 5.1). Obviously, the altimetry measurements performed just over the seas help to balance this effect. Nevertheless, a decrease of VTEC in the combined model can be observed as well, coinciding with the ionospheric peaks as the VTEC maximum travels with the Sun during one day. This decrease can be related to the insufficient performance of the altimetry measurements in low latitudes, caused by the contribution of the topside ionosphere. The estimation of a constant altimetry offset in the COMB GIM additionally suppresses the obtained VTEC values in this regions (cf. Figure 6.5).

Figure 6.8: Global maps of the ΔVTEC between the combined and GNSS-only GIM in two-hourly snapshots for day 182 2006
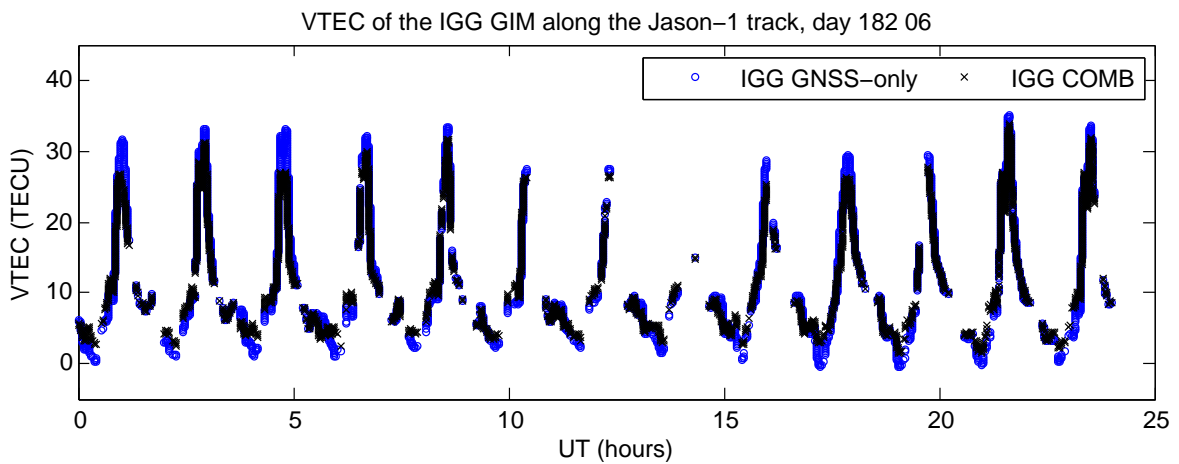
Figure 6.9: VTEC along the Jason-1 track from the GNSS-only and the COMB GIM, day 182 2006

Taking into account the clearly evident latitudal dependency of the differences between GNSS and altimetry derived VTEC (see e.g., Figure 5.41), the estimated constant daily offset must be replaced by an adequate function of the latitude $F(\beta)$, which accounts for both the instrumental altimetry bias and the plasmaspheric contribution. Such approach will improve the combined solution and, on the other hand, it could be used as a tool for rough estimation of the plasmaspheric component.

The modified dip latitude (modip)

The modified dip, or modip, latitude is a coordinate adapted to the real magnetic field i.e., to the magnetic inclination (dip). Proposed by Rawer (1984) for describing the TEC in the F2-layer and the topside ionosphere, it is formulated as (Azpilicueta et al., 2006):

$$tan(\mu) = \frac{I}{\sqrt{cos(\beta_g)}} \tag{6.1}$$

where μ is the modip latitude, I denotes the true magnetic dip, and β_g is the geographical latitude. Close to the equator, the lines of constant modip are virtually identical to the lines of constant magnetic inclination. With increasing latitude they deviate and approach the geographical parallels, so the modip poles merge the geographical ones. Being more closely related to the real magnetic field than the geomagnetic latitude, modip provides a better representation of the VTEC spatial distribution. As shown by Azpilicueta et al. (2006), the bias between the GIM from GNSS data and the altimetry derived VTEC is considerably smaller when modip is utilised for the modelling. Hence, the modip latitude is expected to be more suitable for the combined GIM too. Therefore, a tentative test for using modip in the COMB GIM estimation is made. An example of the results can be seen in the figures below.
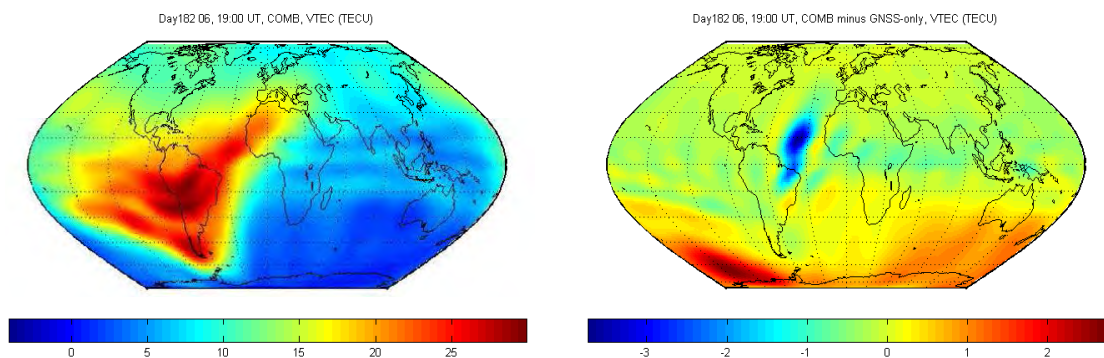
Figure 6.10: COMB GIM (left plot) and COMB minus GNSS-only GIM (right plot) for 19:00 UT, day 182 2006, modip latitude

Figure 6.10 shows the COMB GIM (left plot) and the difference COMB minus GNSS-only GIM (right plot) at 19:00 UT on day 182 2006. Both maps are modelled using modip instead of the geomagnetic latitude in (2.36). For visualising the impact of the two kinds of latitude on the obtained COMB GIM, the differences COMB minus GNSS-only GIM can be compared (cf. Figure 6.7). This comparison is exemplified in Figure 6.11, showing the ΔVTEC COMB

minus GNSS-only GIM (using modip) vs. the ΔVTEC COMB minus GNSS-only GIM (with geomagnetic latitude) for 19:00 UT on day 182 2006. Generally, the two kinds of GIM differ within several TECU, especially in the regions of higher ionospheric activity. This differences have to be further analysed and at this stage of the work the utilisation of modip in the COMB GIM is still under investigation. It has to be taken into account, that modip is closely related to the actual magnetic field and thus more sensitive to the spatial distribution of the VTEC. In order to properly deploy this feature in a sun-fixed reference frame, the observations used for the two-hourly GIM have to be weighted according to their relation to the reference epoch of each map. Such epoch-relative weighting will enhance the spatial agreement between the GNSS and altimetry derived VTEC and allow to take full advantage of the modip latitude potential.
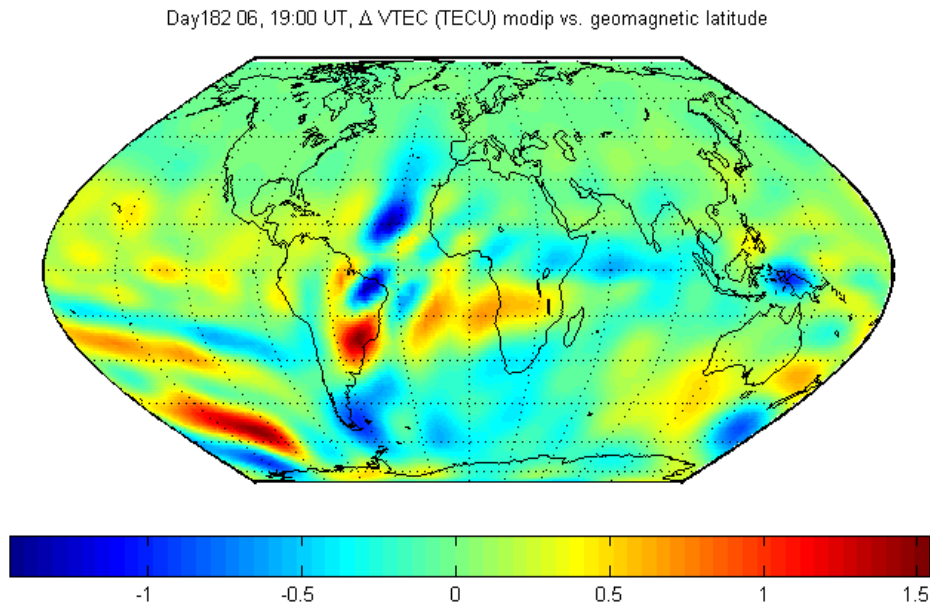
Figure 6.11: ΔVTEC COMB minus GNSS-only GIM (modip) vs. ΔVTEC COMB minus GNSS-only GIM (geomagnetic) for 19:00 UT, day 182 2006

Time series of mean VTEC

The mean VTEC values in terms of the first SH coefficient a_{00} from the COMB and the GNSS-only GIM for July 2006 are shown in the upper plot of Figure 6.12. In the lower plot of the figure the difference ΔVTEC$_{mean}$ COMB minus GNSS-only GIM can be seen. Not surprisingly, the integration of Jason-1 data in the GIM does not significantly influence the mean VTEC except of a very slight increase. The bias of the difference between the two time series is 0.028 TECU and the standard deviation is 0.034 TECU. The correlation coefficient between the two time series 0.9993.
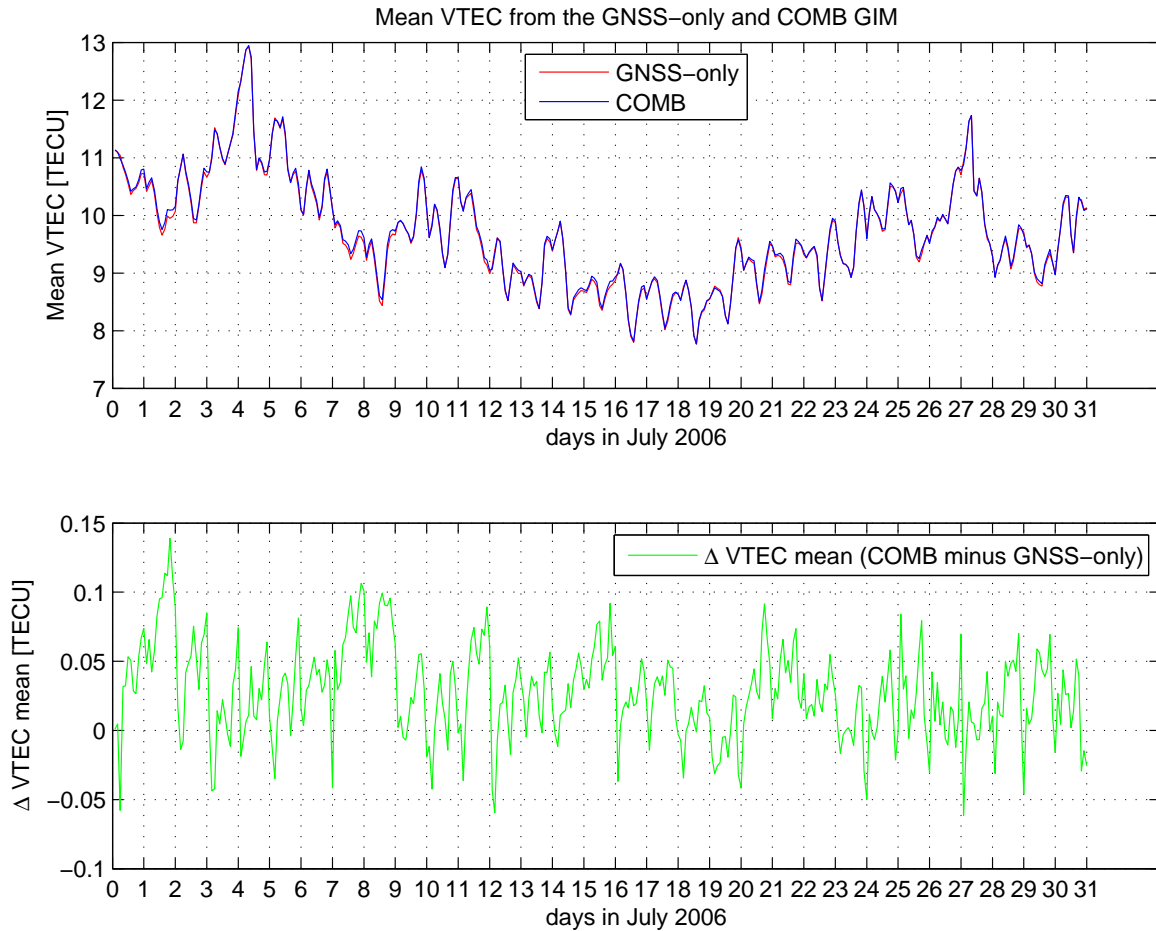
Figure 6.12: Mean VTEC obtained from the GNSS-only and the COMB GIM for July 2006 (upper plot) and the corresponding differences ΔVTEC_{mean} COMB minus GNSS-only (lower plot)

6.2.1 Analysis of the formal errors

As expected, the insertion of additional observations in the COMB GIM leads to lowering of the estimated RMS error compared to the GNSS-only solution. The RMS maps corresponding to the GNSS-only and COMB GIM at 19:00 UT on day 182 in 2006 are shown in Figure 6.13. A closer look at the difference between the combined map and the GNSS-only solution (Figure 6.14) shows a general lowering of the COMB GIM RMS, especially over the areas coinciding with the footprints of Jason-1 (cf. Figure 6.1). In this particular map the RMS decreases up to -0.43 TECU. The same effect can be observed throughout the day (Figure 6.15), with RMS improvement reaching up to -1.74 TECU. The formal precision increase due to the combination can be clearly seen when the RMS of the COMB and GNSS-only GIM is interpolated along the Jason-1 track (Figure 6.16).
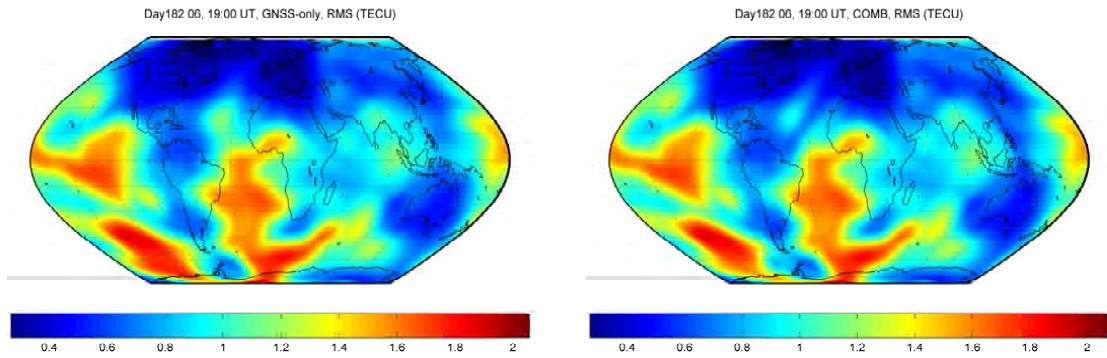
Figure 6.13: RMS of the GNSS-only (left plot) and of the COMB GIM (right plot) for 19:00 UT, day 182 2006
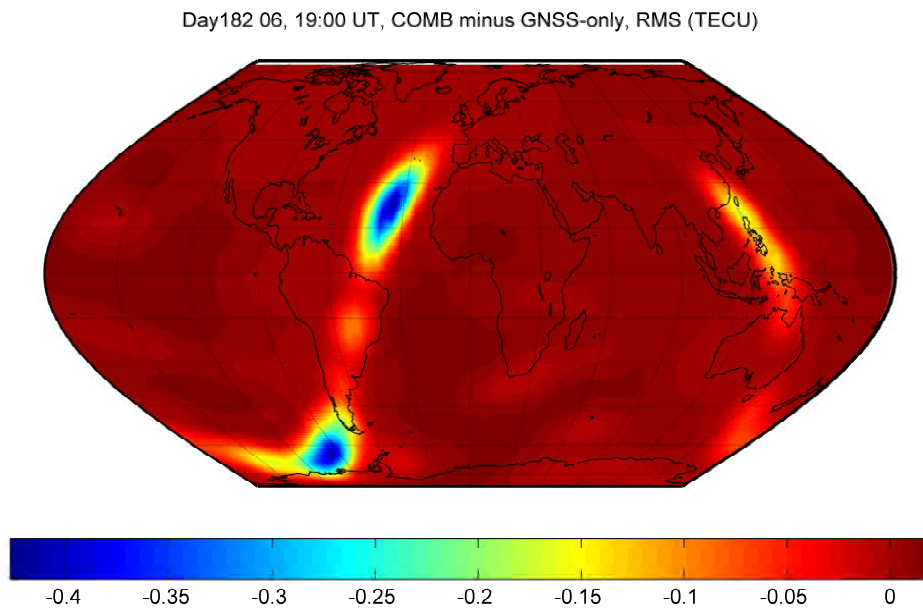
Figure 6.14: ΔRMS COMB minus GNSS-only GIM, 19:00 UT, day 182 2006
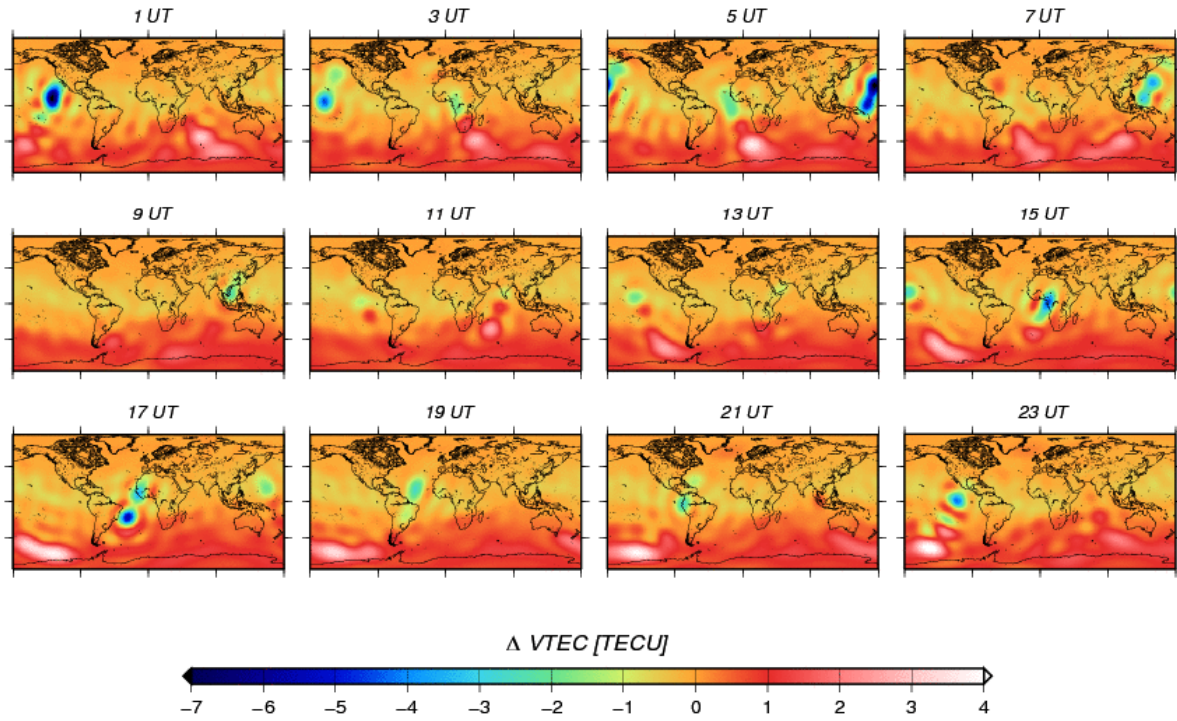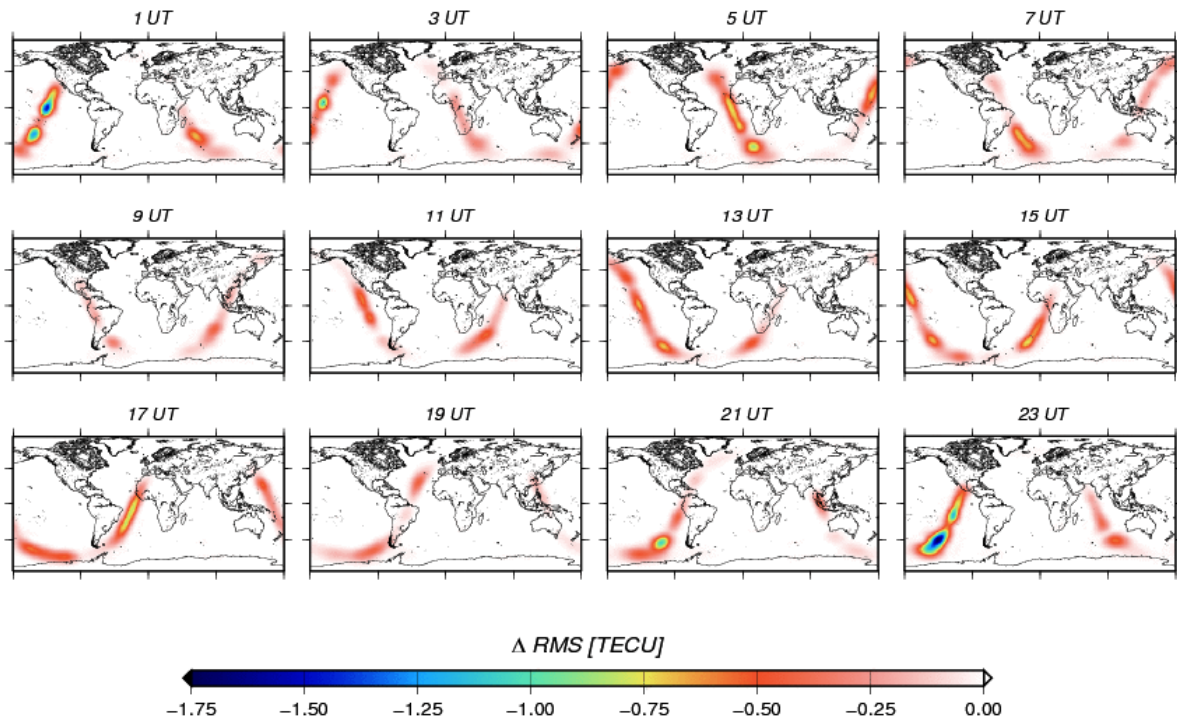
Figure 6.15: Global maps of the ΔRMS between the combined and GNSS-only GIM in two-hourly snapshots for day 182 2006
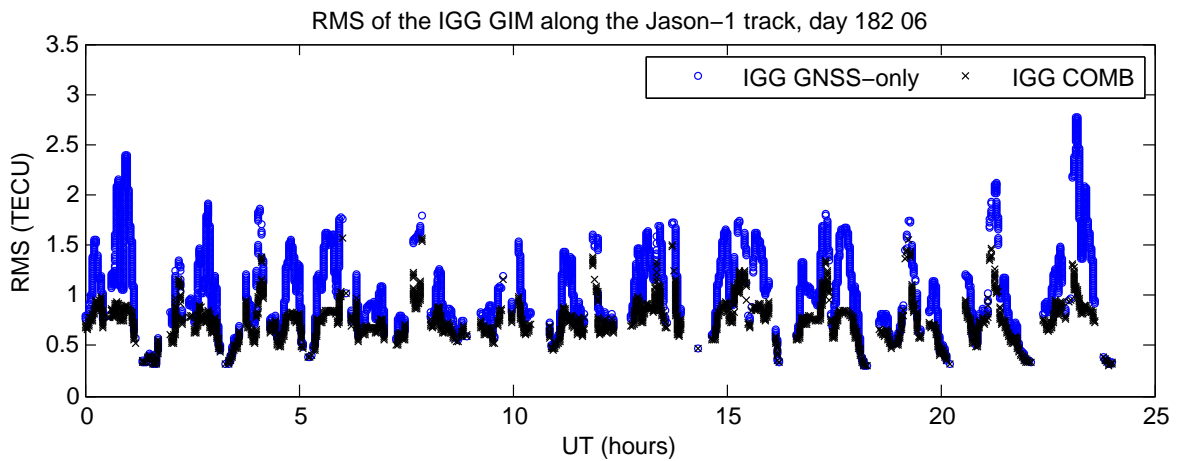
Figure 6.16: RMS interpolated along the Jason-1 track from the GNSS-only and the COMB GIM for day 182 2006

In Figure 6.17 the standard deviation, the bias, and the maximum and minimum of the differences ΔRMS COMB minus GNSS-only for the 31 days of July 2006 are plotted. For the whole period the bias of the difference is -0.01 TECU, showing that in general the COMB GIM have a slightly lower RMS error than the GNSS-only maps. As already discussed, the precision improvement is bigger along the Jason-1 track. There, the negative differences indicating RMS lowering reach up to -2.27 TECU with a mean of -1.40 TECU for the whole month.
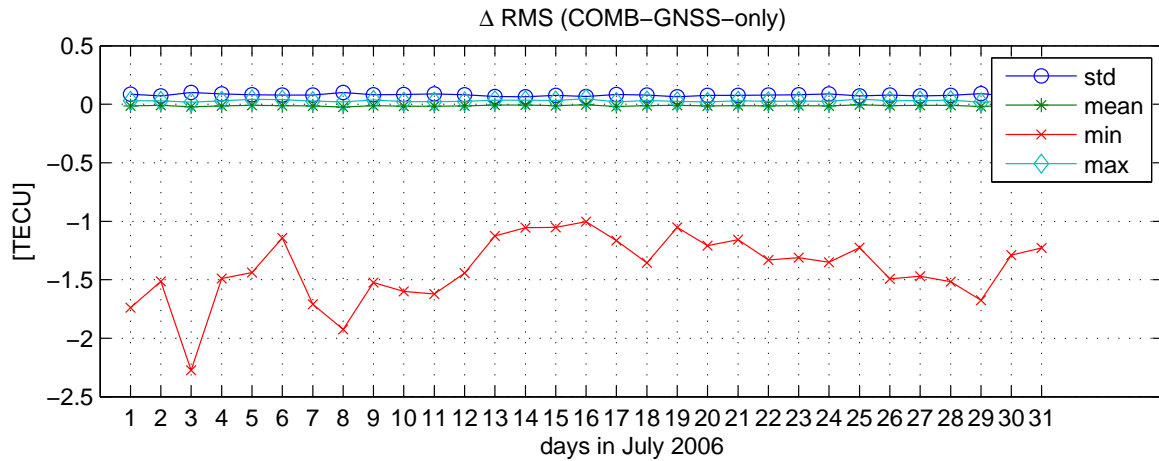
Figure 6.17: Standard deviation, bias, minimum and maximum of the difference ΔRMS COMB minus GNSS-only for July 2006

However, the estimated standard deviation of unit weight (4.11) slightly worsens when altimetry data is included in the GIM. This effect can be related to the the higher noise of the altimetry measurements compared to the GNSS carrier-phase smoothed code observations. The differences between the a posteriori σ of the GNSS-only and the combined solutions for the 31 days of July 2006 are shown in Figure 6.18. The mean of these differences throughout the whole month is 0.05 TECU.
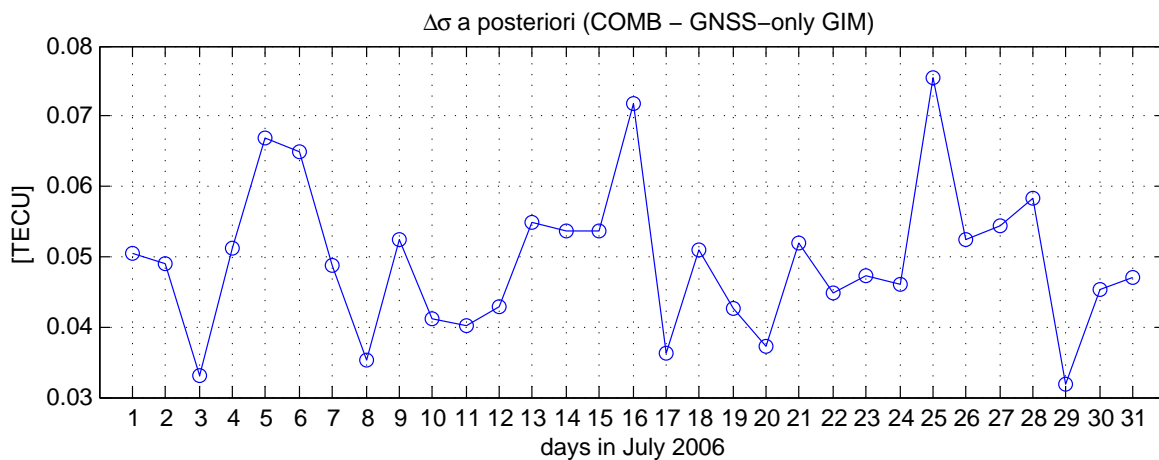
Figure 6.18: $\Delta\sigma$ a posteriori COMB minus GNSS-only GIM for July 2006

6.3 Validation of the combined GIM

One basic problem this study is facing is the validation of the combined GIM. Only the comparison with ionospheric information obtained in a similar way but from a different data source can provide a sound quality assessment of the absolute VTEC delivered by the combined solution. Up to now, there is no global, entirely data-based ionosphere model comprising neither GNSS nor altimetry observations, which could serve as an independent reference for the combined GIM developed within this work. However, it can already be proven that the integration of GNSS and altimetry ionospheric data causes an improvement as to the GNSS-only solution in terms of RMS lowering and better compatibility with the "raw" altimetry observations. Furthermore, utilising the global ionosphere models for single-point positioning (SPP) from GNSS single-frequency observations is a way to provide an objective quality assessment of the COMB GIM. The implementation of the ideas for further optimisation of the COMB GIM, discussed in detail prior in this chapter, will certainly contribute to a distinct improvement of the absolute VTEC accuracy. This concepts deal mainly with the relative weighting of the data and the appropriate modelling of the altimetry specific errors. Still, the validation tests carried out in this section show that the proposed combination method has the potential to improve the GIM reliability and contribute to their global coverage.

6.3.1 Comparison with satellite altimetry data and the IGS GIM

Usually, the GIM from GNSS observations are validated through comparison with altimetry data, as it is done in section 5.5.2. Since measurements from the Topex/Poseidon and Jason-1 altimeters are included in the COMB GIM, this data cannot be used for absolute quality assessment of the combined solution. Obviously, a parallel between the IGG COMB GIM and the IGS ionosphere products (see section 3.1.3) cannot provide a sound evaluation of the COMB GIM accuracy as well. Nevertheless, by applying the procedure presented in section 5.5.2 on the COMB GIM, the self-consistency of the combination approach can be proven. It is expected that the agreement between the "raw" altimetry data and the combined solution will be better than in the case of the GNSS-derived GIM. Moreover, the estimated altimeter offsets can be partly verified by this comparison.

The comparison between altimetry delivered VTEC and the corresponding values obtained from the different global ionosphere models was carried out at the UPC. The final IGS AAC's GIM and the IGG GNSS-only and COMB maps for July 2006 are compared with Jason-1 VTEC in time and in latitude. The altimetry observations used for this validation are obtained from a different data centre and additionally pre-processed at UPC and are thus not identical with the data integrated in the COMB GIM. For each GIM the bias, standard deviation, the root mean square and the percentage error of the differences with Jason-1 are computed and averaged on a daily basis. The results are shown in Figures 6.19 (differences in time) and 6.20 (differences in latitude), and averaged in Tables 6.4 and 6.5. The legend entries "iggg" and "iggc" correspond to the IGG GNSS-only and the IGG COMB GIM, respectively. In order to examine the reasonability of the estimated daily altimeter offsets, the bias between the Jason-1 VTEC and the corresponding values from the COMB GIM is plotted twice in the upper left panels of both figures. The second curve is reduced by the monthly mean of the estimated offsets, which is 3.00 TECU. Both curves are therefore identical, with the reduced one shifted towards zero. In the tables the reduced bias is referred to as "iggc$_{red}$".
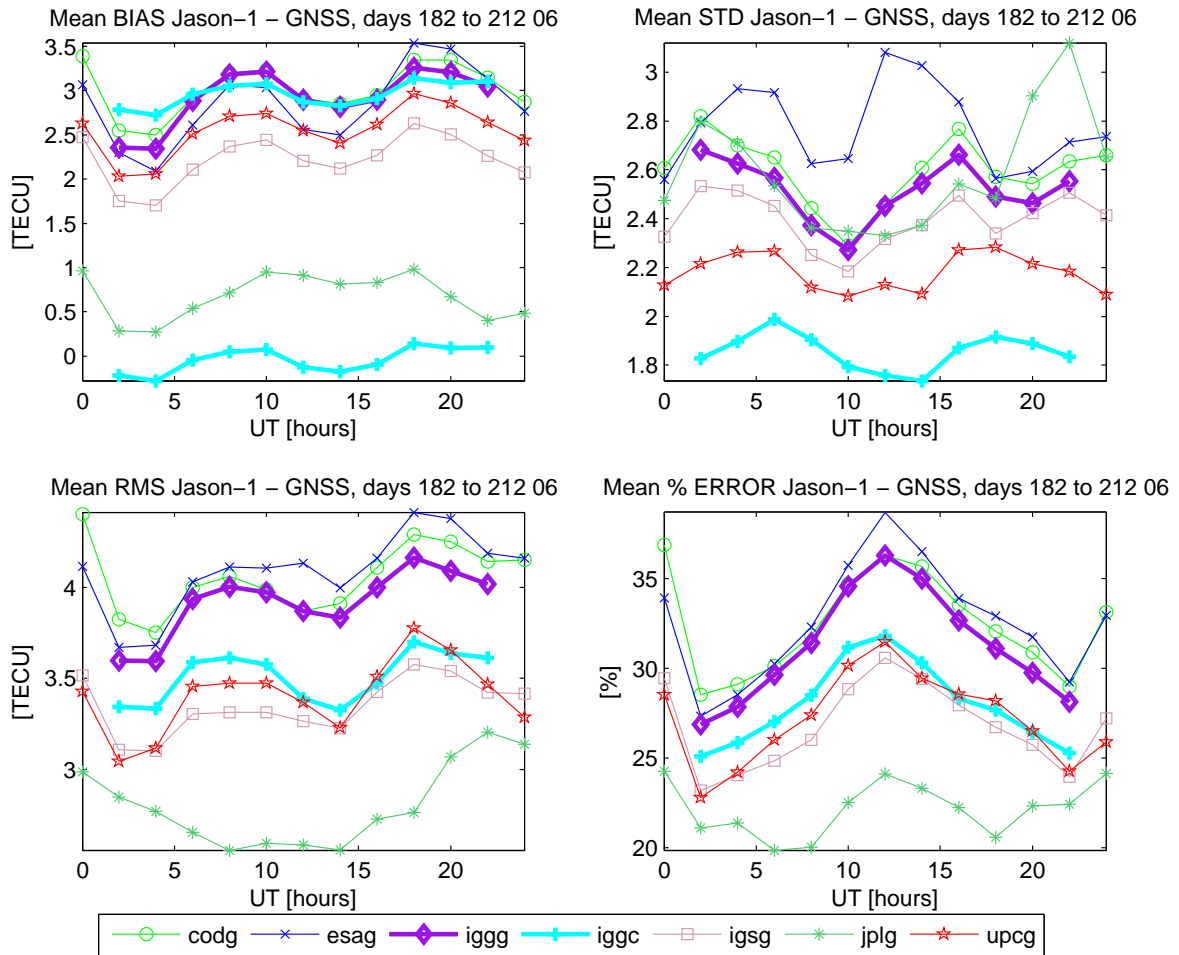
Figure 6.19: Jason-1 minus GNSS and COMB GIM VTEC, mean bias, standard deviation, root mean square and percentage error in time for days 182 to 212 2006

	igs	code	esa	jpl	upc	iggg	iggc	iggc$_{red}$
mean bias, [TECU]	2.22	3.02	2.85	0.68	2.55	2.92	2.96	-0.04
mean std, [TECU]	2.40	2.60	2.77	2.59	2.18	2.52	1.86	-
mean rms, [TECU]	3.35	4.06	4.09	2.80	3.41	3.92	3.51	-
mean error, [%]	26.77	32.44	32.62	22.18	27.19	31.22	27.95	-

Table 6.4: Jason-1 data minus the IGS and IGG GIM, average in time for July 2006
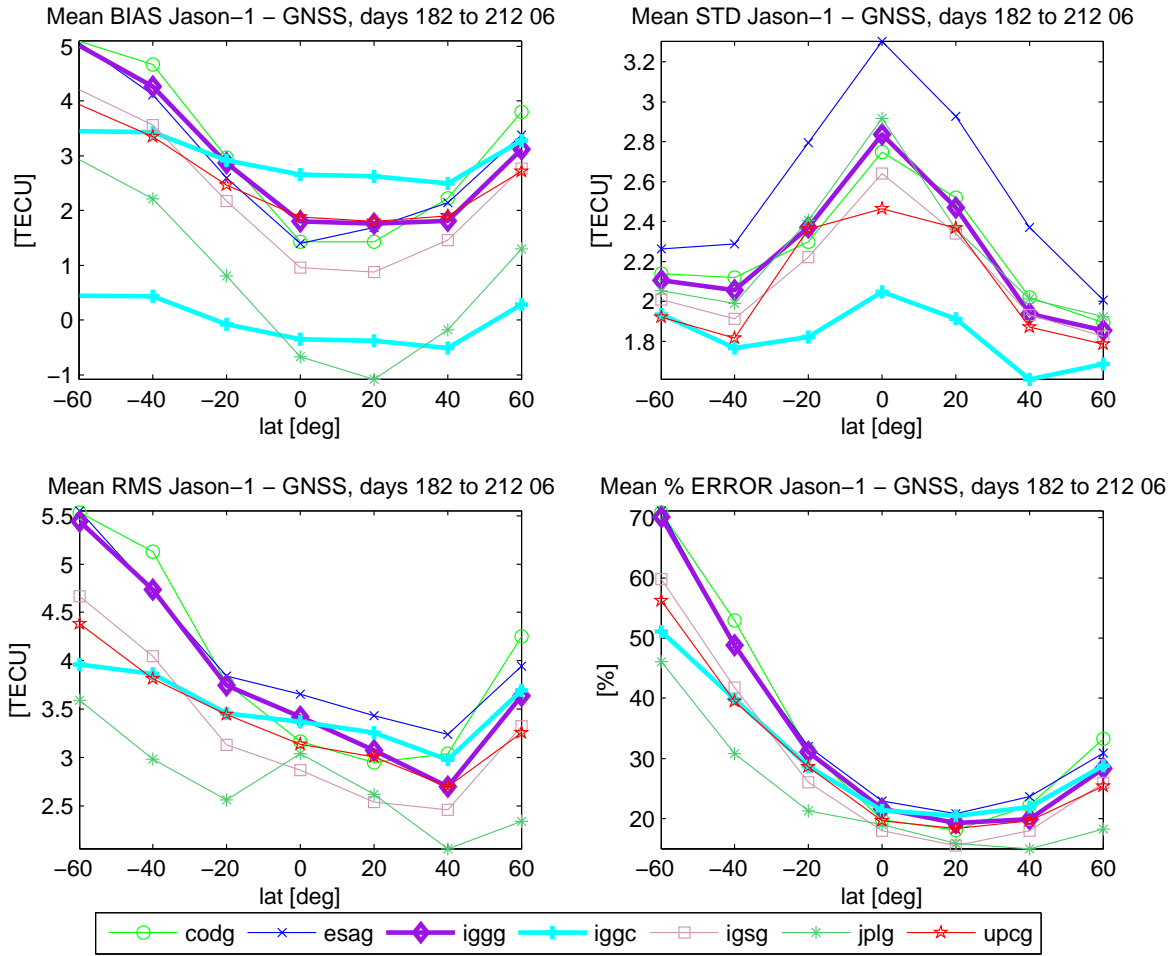
Figure 6.20: Jason-1 minus GNSS GIM and COMB VTEC, mean bias, standard deviation, root mean square and percentage error in latitude for days 182 to 212 2006

	igs	code	esa	jpl	upc	iggg	iggc	iggc$_{red}$
mean bias, [TECU]	2.29	3.09	2.91	0.76	2.58	2.95	2.98	-0.02
mean std, [TECU]	2.13	2.25	2.56	2.24	2.08	2.23	1.83	-
mean rms, [TECU]	3.29	3.98	4.05	2.74	3.39	3.82	3.51	-
mean error, [%]	29.29	35.49	35.73	23.75	29.64	34.16	30.31	-

Table 6.5: Jason-1 data minus the IGS and IGG GIM, average in latitude for July 2006

Several conclusions can be drawn from this comparison:

- the IGG GNSS-only GIM's performance is comparable to the results of the IGS AAC CODE, which can be explained by the similar computation strategy - in both cases VTEC is parameterised using spherical harmonic expansions (2.36);

- except for the bias, the IGG COMB GIM agrees with the altimetry observations better than the IGG GNSS-only GIM;

- however, if the estimated altimetry offset is reduced from the Jason-1 minus IGG COMB bias, the two data sets agree within less than 0.05 TECU;

- the performance of the IGG COMB GIM is generally better than the one of the AAC CODE and approaches the results of the IGS AAC UPC;

- in terms of standard deviation, the IGG COMB GIM yields the best agreement with the observations of Jason-1;

- generally, for all GIM the differences with the altimetry derived VTEC are slightly higher in latitude than in time.

Carrying out the same test for different ionosphere conditions leads to similar results. In Figures 6.21 and 6.22 the standard deviation in time and in latitude between the Jason-1 observations and the various GIM is shown for four days with either remarkably high or low solar and magnetic activity. The differences between the Jason-1 VTEC and the values obtained from the GIM are considerably higher for the days in 2001 and 2002, both periods of very high solar activity. The lowering of the standard deviation for the two more recent periods (in 2005 and 2006) can also be partly explained with the continuous improvement of the IGS ionosphere products. Nevertheless, the strong latitudal dependency of the differences is persistent for each of the investigated periods (Figure 6.22). In both, time and latitude, the IGG COMB solution performs generally better than the GNSS derived GIM. However, the latitudal dependency of the differences is not cancelled by the combination. The complemented plots for the regarded days, showing also the bias, root mean square and percentage error of the differences with the Jason-1 observations can be seen in Appendix B.4.

Recapitulatory, it can be stated that the integration of GNSS and altimetry data leads to better agreement with the "raw" altimetry observations compared to the GNSS-only solutions, which proves the self-consistency of the combination method. The estimated altimetry offset has a reasonable order of magnitude but does not eliminate the latitudal dependency of the bias between the COMB GIM and the altimetry data. Therefore, the estimation of a constant altimetry offset must be replaced by a function in latitude, accounting also for the topside ionosphere.
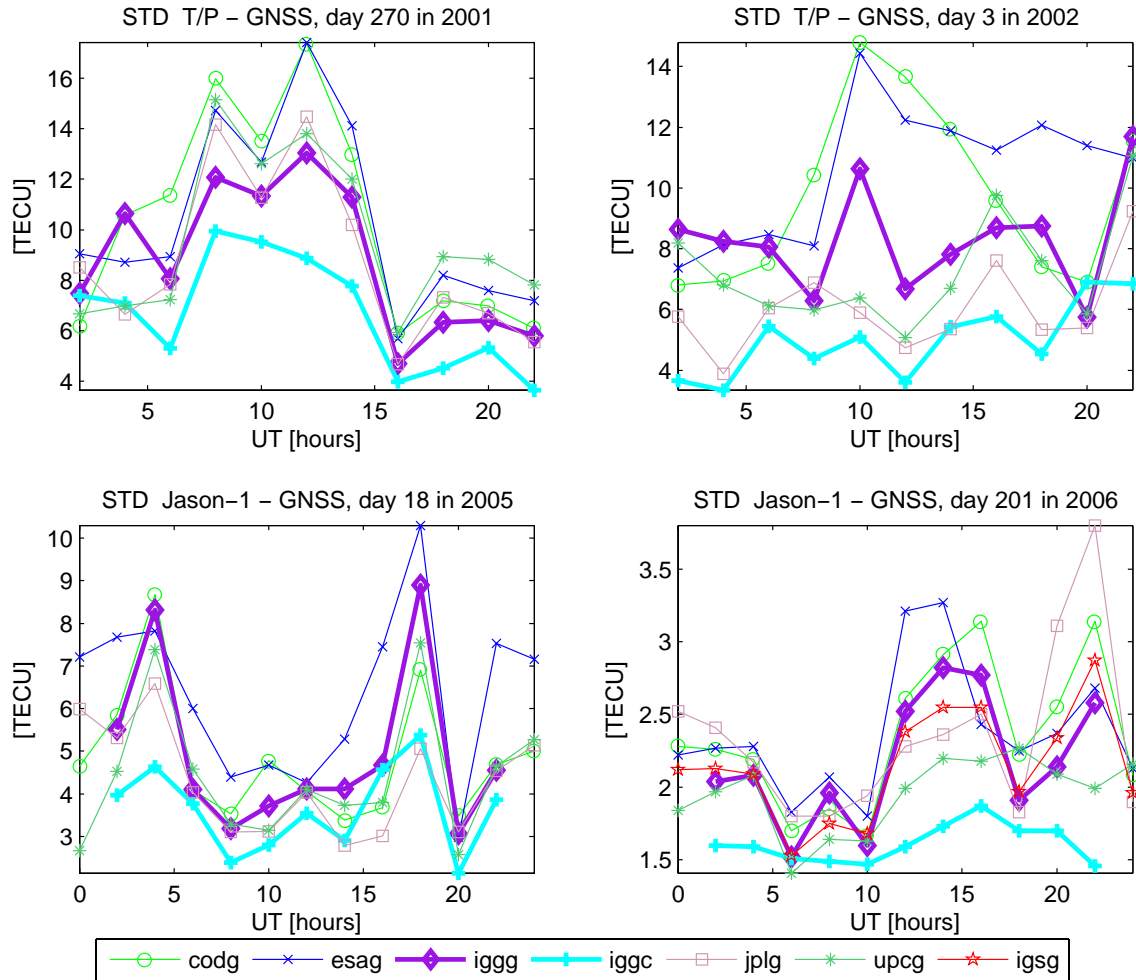
Figure 6.21: Jason-1 minus VTEC from various GNSS and the COMB GIM, standard deviation in time for four days with different ionosphere conditions
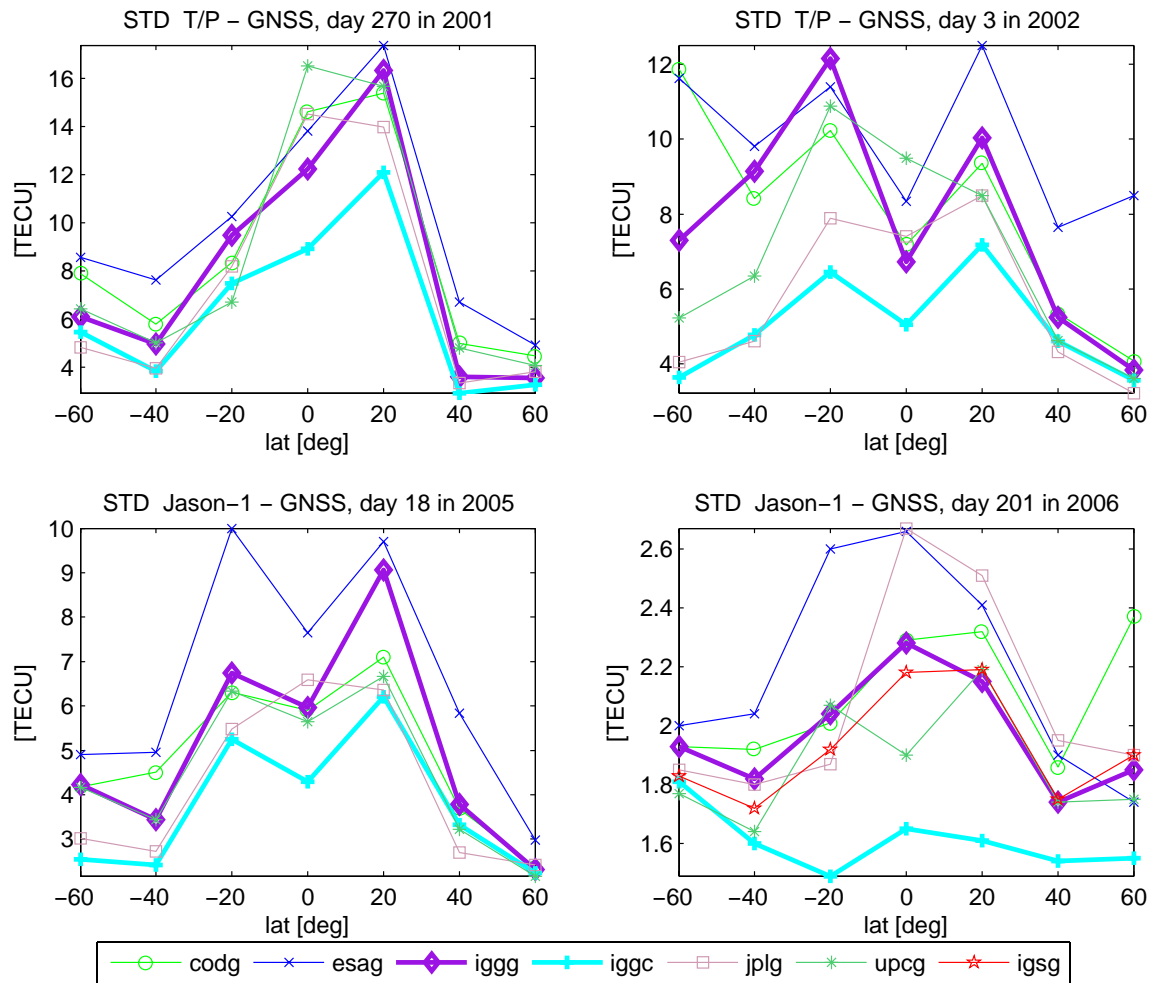
Figure 6.22: Jason-1 minus VTEC from various GNSS and the COMB GIM, standard deviation in latitude for four days with different ionosphere conditions

6.3.2 Verification through GNSS single-point positioning

Single-point positioning is the standard mode of GNSS positioning, which yields the so-called navigation solution. Virtually any GNSS receiver can provide this solution, since SPP can be done with single- or double-frequency code or/and phase data. The main factors that limit the SPP accuracy are the orbit and clock errors, as well as the tropo- and ionospheric refraction (Wasle, 2007). If precise orbital and satellite clock data, e.g. as provided by the IGS, along with double-frequency code pseudoranges and carrier phase observations are used, the accuracy of the obtained single-point coordinates can reach few tens of millimetres. When using single-frequency observations however, a reliable ionosphere model has to be applied for correcting the ionospheric refraction.

In order to test the performance of the IGG GNSS-only and COMB global ionosphere models, SPP for six IGS GNSS stations (shown in Figure 6.23) is carried out for day 182 in 2006 in four different modes:

1. using the ionosphere-free linear combination (3.17) and (3.16) from double-frequency code and phase observations;

2. using single-frequency code and phase observations and the global ionosphere model provided by the IGS AAC CODE;

3. using single-frequency code and phase observations and the IGG GNSS-only global ionosphere model;

4. using single-frequency code and phase observations and the IGG COMB solution.
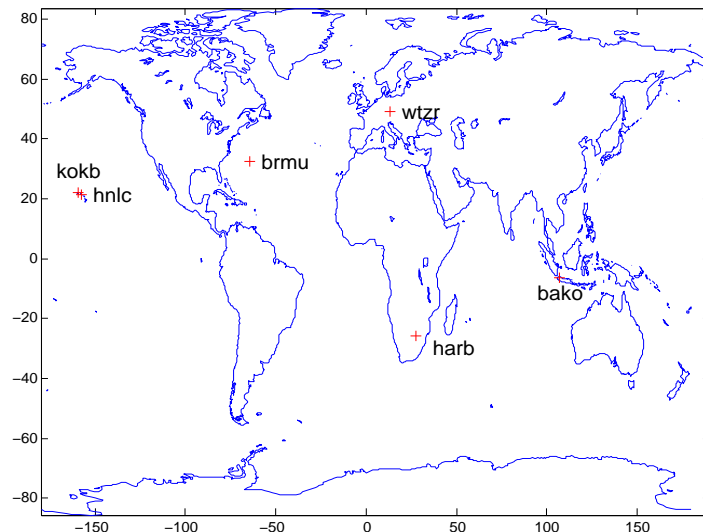
Figure 6.23: SPP test stations

The coordinate estimation is performed with the BERNESE GPS Software (Dach et al., 2007), using the IGS precise ephemerides and satellite clocks. For the single-frequency SPP

the corresponding (CODE or IGG) DCB are utilised. Along with the station coordinates, the site-specific troposphere parameters are estimated as well. The a priori troposphere model is Niell (dry part only), the mapping function used for the delay estimation is the Wet Niell.

For the sake of randomness, the six IGS stations of which the coordinates are estimated are chosen with respect to their involvement in the different GIM for the regarded day as follows:

- observations from the stations `BAKO`, `BRMU`, and `HARB` are not included in the IGG GIM but utilised for the CODE GIM;

- `KOKB` is incorporated in the IGG and in the CODE GIM;

- station `HNLC` is absent in both models;

- `WTZR` is included in the IGG GIM and missing in the CODE model.

The introduction of altimetry data in the GIM is expected to improve the performance of the ionosphere model predominantly over the oceans. Therefore, four of the test stations - `BAKO`, `BRMU`, `HNLC` and `KOKB` - are deliberately chosen for they are not located on the mainland. Eventually, all of the test stations are situated in low and mid latitudes.

As a reference for the estimated coordinates the ITRF 2005 coordinates at epoch 2006/07/01 as provided by ITRF (2007) are used. The results of the SPP in terms of differences between the estimated coordinates and ITRF 2005 can be seen in Table 6.6. A graphical representation of the differences between the ITRF 2005 coordinates and the various single-frequency SPP results is shown in Figure 6.24.

Certainly, the best agreement with the ITRF 2005 coordinates is provided by the double-frequency solution (referred to as SPP DOUBLE), with differences between 1 and 3 cm or less. The accuracy of the single-frequency estimates is within ±70 cm. This roughly agrees with the specification of ±50 cm accuracy for precise point positioning with the BERNESE GPS software given in Dach et al. (2007). The results achieved with the CODE GIM (referred to as SPP CODE) and with the IGG GNSS-only model (referred to as SPP IGGG) are quite similar. The differences between the coordinate estimates obtained with the two GNSS-only models do not exceed ±15 cm and show on obvious trend. Regarding the single-frequency SPP using the IGG COMB model (referred to SPP IGGC), a slight improvement as to the CODE and IGGG SPP results can be seen for several coordinate estimates. Although there is no explicit overall accuracy enhancement when using the COMB GIM, it is significant that the improved coordinate estimates are just for the stations located outside the mainland. Moreover, for the stations `BRMU` (Y-estimate), `HNLC` (X-estimate) and `KOKB` (X- and Y-estimate) the results obtained with the IGG COMB GIM are with up to 7 cm better than both, CODE and IGGG SPP.

Station	Crd.	ITRF 2005	SPP DOUBLE	SPP CODE	SPP IGGG	SPP IGGC
BAKO	X	-1836969.161	-0.0189	0.0009	-0.0834	-0.0779
	Y	6065617.026	-0.0305	-0.2927	-0.2340	-0.2579
	Z	-716257.821	0.0263	-0.5829	-0.7377	-0.7508
BRMU	X	2304703.456	-0.0015	-0.1787	-0.2113	-0.2137
	Y	-4874817.172	0.0119	0.3967	0.3757	**0.3583**
	Z	3395186.962	0.0108	0.1289	0.1725	0.2038
HARB	X	5084657.627	0.0144	-0.2138	-0.2267	-0.2781
	Y	2670325.141	0.0185	-0.1084	-0.0282	-0.0588
	Z	-2768481.127	0.0158	-0.0820	-0.1907	-0.1640
HNLC	X	-5506798.763	-0.0034	0.5875	0.3901	**0.3471**
	Y	-2240049.444	-0.0153	0.0621	-0.0803	-0.1402
	Z	2302720.463	0.0171	-0.0371	0.1329	0.2031
KOKB	X	-5543838.232	0.0120	0.6669	0.5375	**0.4684**
	Y	-2054586.641	0.0119	0.1713	0.0297	**-0.0283**
	Z	2387809.972	-0.0327	-0.0854	0.0700	0.1579
WTZR	X	4075580.535	-0.0146	-0.1682	-0.3303	-0.3284
	Y	931853.826	0.0082	-0.0718	-0.1569	-0.1544
	Z	4801568.157	0.0081	0.1020	0.1203	0.1228

Table 6.6: ITRF 2005 coordinates at epoch 2006/07/01 and differences to the results obtained from double-frequency SPP and single-frequency SPP with different ionosphere models; all values are in [m], the coordinate estimates explicitly improved when using the COMB GIM are marked in bold
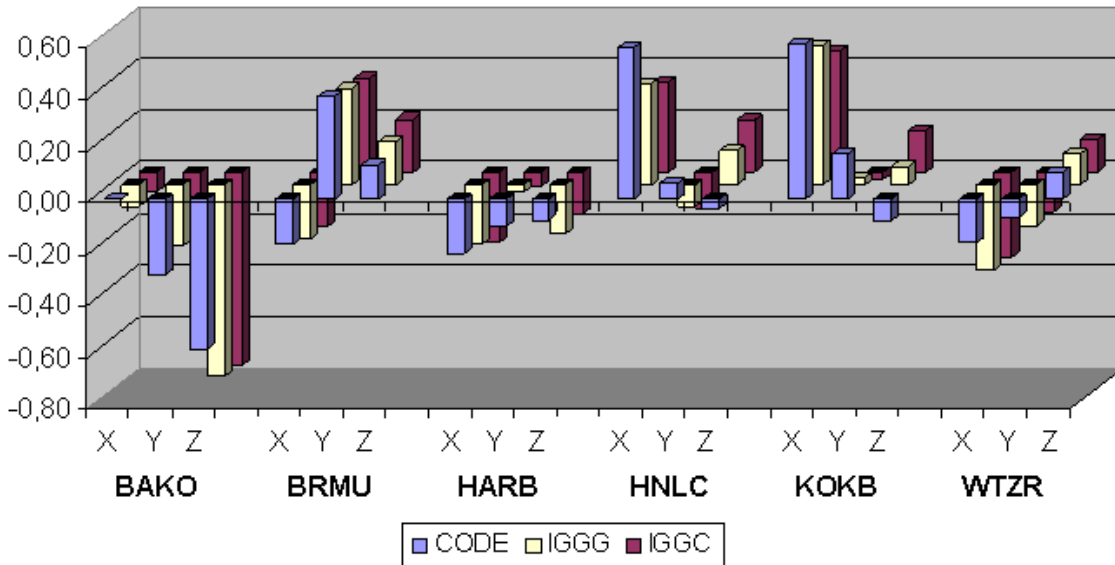
Figure 6.24: Differences between the ITRF 2005 coordinates at epoch 2006/07/01 and the results obtained from single-frequency SPP with different ionosphere models; all values are in [m]

Chapter 7

Conclusion

For the development of Global Ionosphere Maps (GIM) mainly double-frequency GNSS observations are used so far. The GIM represent the ionosphere in longitude, latitude and time, based on the so-called Single Layer Model. Some of the main applications of these maps are correction of the ionospheric refraction in single-frequency GNSS measurements, and space-weather monitoring. Within the Ionosphere Working Group at the International GNSS Service (IGS) four Analysis Centers provide daily GIM since 1998. The individual solutions, which are estimated with different mathematical approaches, as well as one common combined solution are available through the IGS server (IGS, 2007). The IGS global ionosphere models are exerted by a broad number of international users for civil and scientific applications in the navigation and positioning field. Therefore, an increase of their accuracy and reliability is essential. Though the quality of the GNSS derived GIM is generally very good, the ground stations are inhomogeneously distributed, with large gaps particularly over the sea surface. The lack of data lowers the precision of the ionosphere maps over these areas. It can be anticipated however, that some specifics of the ionosphere parameters derived by various non-GNSS techniques, particularly by satellite altimetry missions, will partly balance the inhomogeneity of the GNSS data. The combination of GNSS and satellite altimetry observations, which is subject of development within the dissertation, contributes to the accuracy of the global ionosphere modelling and to the better understanding of the ionosphere as well. An improved knowledge of the processes in the ionosphere is of high importance for all studies of the upper atmosphere and the solar-terrestrial environment, for the radio science, and for climate and plasma studies as well as for civil users, for aviation and marine navigation. Moreover, the integration of observations derived by different geodetic techniques and methods follows the global objective in modern geodetic science towards a better understanding of the processes in the System Earth as a whole.

In this chapter an overview of the work and the essential outcomes is given. Additionally, some ideas for further development and improvement of the results are brought out, as well as the vision for an integrated four-dimensional ionosphere model.

7.1   Summary

The theoretical part of the dissertation summarises the basic knowledge needed for ionosphere study and modelling from the geodetic point of view. It focuses on the specific characteristics

of the medium and its impact on the wave propagation. The modelling and combination procedures implemented in the work are presented and discussed. The utilised space geodetic techniques and the way of extracting ionosphere information from their observations are also emphasised.

In general, the results of the work can be divided in two main categories - global ionosphere maps from GNSS observations, and combined GIM derived from GNSS and altimetry data. The former are used as basis for the combination, but also constitute an independent product, comparable with the IGS GIM. The maps are produced using an autonomous Matlab software, developed within the dissertation. The IGG (Institute of Geodesy and Geophysics) GIM are represented by a spherical harmonic expansion, referred to the sun-fixed geomagnetic reference frame. Their temporal resolution is two hours, resulting in twelve global maps per day. Additionally, the satellites and receivers Differential Code Biases (DCB) are estimated as daily constant values. The developed software gives the opportunity to utilise GPS and GLONASS data, provided by a global network of tracking stations. Using this feature, a detailed analysis of the impact of including GLONASS data in the global ionosphere models is made. The analysis concerns the ionosphere parameters as well as the GPS and GLONSS satellites and receivers DCB, and is based on daily results and on the outcomes over one month. In order to investigate the performance of the developed model, daily GIM and DCB are computed also for four weeks in different ionospheric conditions. The comparison of the IGG GIM with the IGS ionosphere products and with satellite altimetry observations yields a very good agreement, proving the quality of the IGG global ionosphere models obtained from GNSS data.

The combined global ionosphere maps (referred to as IGG COMB GIM) are based on the maps obtained from GNSS data. Therefore, the COMB GIM have the same spatial and temporal resolution as the GNSS-only models, and the incorporated GNSS data is handled in the same way. The combination of GNSS and satellite altimetry ionosphere data is performed on the normal equation level. In the course of adding the altimery observations in the model two basic problems emerge - the relative weighting of the different data sets, and the handling of the systematic errors of the altimeter. In order to determine the relative weight of the altimetry data (P_{alt}), different values are tested. The analysis of the results show that the proper relative weight of the altimetry data should be provided approximately between $P_{alt} = 2^2$ and $P_{alt} = 8^2$. Accordingly, a constant weight of $P_{alt} = 4^2$ is adopted for the IGG COMB GIM. As for the altimeter systematic errors, several studies show that despite of the lower orbit altitude of the altimetry satellites, the Vertical Total Electron Content (VTEC) delivered by these missions is higher than the values obtained from GNSS. This well-known contradiction appears also in the differences between the IGG GIM developed from GNSS data and the "raw" altimetry observations. Based on this phenomena, a purely empirical approach is applied. Assuming that the altimetry measurements are biased by an instrumental offset similar to the GNSS DCB, the combination on normal equation level is used for estimating constant daily offsets for the altimetry satellite, along with the combined ionosphere maps and the DCB. The results show that the computation of an altimetry satellite offset leads to a better agreement between the GNSS-only and the combined GIM. Thus, the IGG COMB maps include the computation of the altimetry offset by default. The estimated values are in the range of about 1.5 to 3.5 TECU, generally corresponding to the systematic altimetry VTEC overestimation of about 1 to 4 TECU compared to the values delivered by GNSS, as

summarised e.g. by Brunini et al. (2005). The estimated offsets also match the range of the differences between the VTEC interpolated from the IGG GNSS-only solution and the Jason-1 derived VTEC.

For assessing the impact of the combination, the developed IGG COMB GIM are compared to the corresponding IGG GNSS-only maps. The differences follow a similar pattern throughout the regarded periods. In general, the introduction of altimetry data causes an increase of the VTEC values especially over the oceans in high southern latitudes, where nearly no GNSS observations are available. The decrease in the equatorial area coincides with the regions of highest ionospheric activity and can be thus interpreted as the signature of the plasmaspheric component, not accounted for by the altimetry measurements. Concerning the formal precision (or RMS) of the GIM, the combination leads to a clear improvement, particularly for the areas corresponding to the altimeter footprints. Eventually, the obtained COMB GIM are validated by two kinds of testing. The final IGS AC's GIM and the IGG GNSS-only and COMB maps for July 2006 are compared with Jason-1 VTEC in time and in latitude at the IGS Analysis Center UPC. The comparison shows that the integration of GNSS and altimetry data leads to better agreement with the "raw" altimetry observations compared to the GNSS-only solutions, which proves the self-consistency of the combination method. Utilising the COMB GIM and the GNSS-only models for single-point positioning (SPP) from GNSS single-frequency observations and comparing the results provides a more objective quality assessment of the combined solution. Thereby, the introduction of altimetry data in the GIM is expected to improve the performance of the ionosphere model predominantly over the oceans. Thus, SPP is carried out for six IGS GNSS stations over one day in three runs. In each of these otherwise identical SPP runs the ionospheric refraction is corrected using the GIM provided by the IGS AC CODE, the IGG GNSS-only, and the IGG COMB GIM, respectively. The results are compared to the ITRF 2005 coordinates of the stations. Although no explicit overall accuracy enhancement appears when using the IGG COMB GIM, some of the obtained results are with up to 7 cm better than the ones achieved with each of the two GNSS-only models. Remarkably, the improved coordinate estimates are just for the stations located outside the mainland.

7.2 Outlook

The presented work shows that the combination of GNSS and altimetry data has a high potential to improve the accuracy and reliability of the global ionosphere maps. Still, for achieving maximum quality of the results the combined GIM need to be further optimised. In the course of the investigations several concrete steps towards the improvement of the COMB GIM performance were identified:

• Modeling of the altimetry satellite offset
The altimetry satellite offsets estimated using the combination procedure are among the most essential results of the work. The analyses show that the computation of an altimetry satellite offset leads to a better agreement between the IGG GNSS-only and COMB GIM and considerably reduces the difference between the COMB GIM and the "raw" altimetry VTEC. For it obviously conciliates both kinds of data, a daily constant value for this offset is com-

puted along with the IGG COMB GIM by default. When estimated as a constant however, the altimetry offset still includes the plasmaspheric component additionally to the actual instrumental delay. Therefore, if does not eliminate the clearly evident latitudal dependency of the differences between GNSS and altimetry derived VTEC, which also shows up in the differences between the IGG GNSS-only and COMB GIM. This leads to the conclusion that the estimated constant daily offset must be replaced by an adequate function of the latitude, accounting for both the instrumental delay and the plasmaspheric contribution. Such approach will contribute to the accuracy of the combined model and can also be used as a tool for approximate estimation of the plasmaspheric component.

- More sophisticated weighting

The weighting procedure can be improved in several aspects. In order to balance the model, the observations of the GNSS stations located in the northern hemisphere can be downweighted relative to ones in the southern hemisphere. The relative weighting of the altimetry data can be further investigated towards a dynamical weightning procedure, which relates the altimetry observations to the latitude and the time at which they were made. Such epoch-relative weighting applied to both the GNSS and altimetry data will enhance the spatial agreement between the GNSS and altimetry derived VTEC and improve the result of the combination. Moreover, it will allow to take full advantage of the potential of the modified dip latitude.

- Implementation of the modip latitude

The modip latitude is a function of the true magnetic dip and therefore more closely related to the real magnetic field than the geomagnetic latitude. When used for global ionosphere modelling, it lowers the bias between the GIM from GNSS data and the altimetry derived VTEC due to the better representation of the VTEC spatial distribution (Azpilicueta et al., 2006). Thus, the modip latitude is expected to be more suitable for the combined GIM as well.

- Others

In order to achieve the best possible performance of the daily GNSS-only and COMB GIM a three-day solution has to be implemented. This will increase the effect of the "relative" constraints discussed in section 5.1, and also allow to conform the reference epochs of the IGG maps to the official IGS products. For the optimal determination of the monthly DCB sets, the daily satellite DCB estimates have to be aligned to a common reference, based on all involved satellites in a further post-processing step.

The presented combination method can be adopted also for ionospheric data from other space geodetic techniques, such as VLBI and DORIS. This will additionally increase the global coverage and enhance the accuracy and reliability of the ionosphere models. A further challenging objective, which increasingly becomes a topic in the ionosphere investigation, is the development of four-dimensional ionospheric models in longitude, latitude, time, and height. The opportunity for four-dimensional modelling is provided by the GPS radio occultation measurements, which allow vertical profiling throughout the ionosphere (see section 2.2.1). Thus, the development of a four-dimensional model of the ionosphere based on combined GIM and in such way integrating data from many different geodetic techniques is an ambitious, but entirely conceivable vision.

Part III

Appendices

Appendix A

Output IONEX-file of a combined GIM

Below, an excerpt of the combined GIM IONEX-file obtained for the 1st of July 2006 is shown.

```
-------------------------------------------------------------------------------
     1.0              IONOSPHERE MAPS    MIX             IONEX VERSION / TYPE
IGGgim 1.0           IGG                 07-Dec-07 21:49 PGM / RUN BY / DATE
IGG GLOBAL IONOSPHERE MAPS FOR DAY 182, 2006            COMMENT
Global ionosphere maps (GIM) are generated on a daily basis DESCRIPTION
at IGG using data from about 190 GNSS sites of the IGS.  DESCRIPTION
Ionospheric data delivered by satellite altimetry       DESCRIPTION
(JASON1 and/or TOPEX-Poseidon) is integrated in the maps DESCRIPTION
through combination on normal equation level.           DESCRIPTION
One constant offset per altimetry satellite is estimated DESCRIPTION
daily.                                                  DESCRIPTION
The vertical total electron content (VTEC) is modeled in DESCRIPTION
a solar-geomagnetic reference frame by spherical harmonics DESCRIPTION
expansion up to degree and order 15. Piece-wise linear   DESCRIPTION
functions are used for representation in the time domain. DESCRIPTION
The time spacing of their vertices is 2 hours, conforming DESCRIPTION
with the epochs of the VTEC maps. Instrumental biases, or DESCRIPTION
differential P1-P2 code biases (DCB), for all GNSS       DESCRIPTION
satellites and ground stations are estimated as constant DESCRIPTION
values for each day, simultaneously with the 12 times 256 DESCRIPTION
or 3072 parameters used to represent the global VTEC    DESCRIPTION
distribution. The DCB datum is defined by a zero-mean    DESCRIPTION
condition imposed on the satellite bias estimates. The   DESCRIPTION
mapping function is evaluated at geodetic satellite      DESCRIPTION
elevation angles. For the computation of the ionospheric DESCRIPTION
pierce points, a spherical layer with a radius of 6821 km DESCRIPTION
is assumed, implying geocentric, not geodetic IONEX     DESCRIPTION
latitudes.                                              DESCRIPTION
Note: Relative a priori constraints between consecutive  DESCRIPTION
TEC maps are added. To balance their a priori sigma of   DESCRIPTION
0.003 TECU, the RMS values are scaled up by a factor of 10. DESCRIPTION
Contact address: stodo@mars.hg.tuwien.ac.at             DESCRIPTION
  2006    07    01     1     0     0                     EPOCH OF FIRST MAP
  2006    07    01    23     0     0                     EPOCH OF LAST MAP
  7200                                                   INTERVAL
    12                                                   # OF MAPS IN FILE
  COSZ                                                   MAPPING FUNCTION
```

```
    10.0                                              ELEVATION CUTOFF
One-way carrier phase leveled to code                 OBSERVABLES USED
   180                                                # OF STATIONS
    55                                                # OF SATELLITES
  6371.0                                              BASE RADIUS
     2                                                MAP DIMENSION
   450.0 450.0   0.0                                  HGT1 / HGT2 / DHGT
    85.0 -85.0  -2.5                                  LAT1 / LAT2 / DLAT
  -180.0 180.0   5.0                                  LON1 / LON2 / DLON
    -1                                                EXPONENT
TEC/RMS values in 0.1 TECU                            COMMENT
List of stations:                                     COMMENT
ajac albh algo alic alrt amc2 ankr antc areq artu bahr bake  COMMENT
bdos bili bjfs bogi bogt cagz cas1 cedu cfag chan chat chur  COMMENT
coco conz copo crar cro1 daka darr darw dav1 dgar dlft drao  COMMENT
drej dubo escu fair fale ffmj flin glps godz gold gope gras  COMMENT
guam guao haly hlfx hob2 holm hrao hueg iisc invk irkj ispa  COMMENT
ista jab1 jama joz2 karr kely kerg khaj kir0 kiru kit3 kodk  COMMENT
kokb kour kuuj lae1 lhaz lpgs mac1 mad2 madr mali mar6 mars  COMMENT
mas1 mat1 maui maw1 mbar mcm4 mdvj mets metz mizu mkea monp  COMMENT
morp msku mtka nain nlib nnor novj nrc1 nril ntus nya1 nyal  COMMENT
ohi2 ohi3 onsa opmt ous2 pert petp pie1 pimo pol2 prds qaq1  COMMENT
qiki quin ramo reso reun reyz riog sant sask sass sch2 scip  COMMENT
scor scub sey1 sio3 sni1 sofi spk1 spt0 stjo str2 sunm suth  COMMENT
sutm sydn thti thu2 thu3 tidb titz tixi tnml tow2 trab tro1  COMMENT
tskb twtf ulab unb1 unfe unsa urum usn3 usud vis0 whit will  COMMENT
wroc wtzj wtzr wtzz wuhn yakt yar2 yarr yell yibl yssk zimj  COMMENT
DIFFERENTIAL CODE BIASES                              START OF AUX DATA
   G01    -3.016     0.004                            PRN / BIAS / RMS
   G02     5.768     0.004                            PRN / BIAS / RMS
   G03    -2.498     0.005                            PRN / BIAS / RMS
   G04    -1.258     0.004                            PRN / BIAS / RMS
   G05    -2.503     0.004                            PRN / BIAS / RMS
   G06    -2.312     0.006                            PRN / BIAS / RMS
   G07    -4.082     0.004                            PRN / BIAS / RMS
   G08    -2.765     0.004                            PRN / BIAS / RMS
   G09    -1.666     0.004                            PRN / BIAS / RMS
   G10    -3.754     0.004                            PRN / BIAS / RMS
   G11     2.507     0.004                            PRN / BIAS / RMS

   ......
   G23     8.664     0.004                            PRN / BIAS / RMS
   G24    -4.527     0.004                            PRN / BIAS / RMS
   G25    -0.451     0.004                            PRN / BIAS / RMS
   G26    -1.145     0.004                            PRN / BIAS / RMS
   G27    -2.447     0.004                            PRN / BIAS / RMS
   G28     1.443     0.004                            PRN / BIAS / RMS
   G29    -0.840     0.004                            PRN / BIAS / RMS
   G30     0.022     0.004                            PRN / BIAS / RMS
   R01     1.215     0.009                            PRN / BIAS / RMS
   R02    -3.512     0.009                            PRN / BIAS / RMS
   R03     6.188     0.009                            PRN / BIAS / RMS
   R04     2.230     0.009                            PRN / BIAS / RMS
   R05    13.129     0.010                            PRN / BIAS / RMS
   R07     6.050     0.009                            PRN / BIAS / RMS
   R08    -1.380     0.009                            PRN / BIAS / RMS
   R17    -3.498     0.009                            PRN / BIAS / RMS
   R18    -2.279     0.009                            PRN / BIAS / RMS
```

```
   R19    -3.863     0.009                              PRN / BIAS / RMS
   R20     2.895     0.009                              PRN / BIAS / RMS
   R21    -0.538     0.009                              PRN / BIAS / RMS
   R22    -6.572     0.009                              PRN / BIAS / RMS
   R23    -5.023     0.012                              PRN / BIAS / RMS
   R24    -5.043     0.012                              PRN / BIAS / RMS
   G  ajac               -9.977     0.021               STATION / BIAS / RMS
   G  albh               10.245     0.012               STATION / BIAS / RMS
   G  algo                6.473     0.019               STATION / BIAS / RMS
   G  alic               -8.624     0.013               STATION / BIAS / RMS
   G  alrt               -1.822     0.011               STATION / BIAS / RMS
   G  amc2                7.992     0.013               STATION / BIAS / RMS
   G  ankr                4.674     0.012               STATION / BIAS / RMS
   G  antc              -14.926     0.015               STATION / BIAS / RMS
   G  areq               -0.306     0.015               STATION / BIAS / RMS
   G  artu               -8.005     0.013               STATION / BIAS / RMS
   G  bahr               -4.864     0.014               STATION / BIAS / RMS
   ......
   G  wtzj               -0.770     0.018               STATION / BIAS / RMS
   G  wtzr               -4.863     0.025               STATION / BIAS / RMS
   G  wtzz               -6.771     0.018               STATION / BIAS / RMS
   G  wuhn               -3.707     0.014               STATION / BIAS / RMS
   G  yakt               -8.895     0.014               STATION / BIAS / RMS
   G  yar2               -7.517     0.014               STATION / BIAS / RMS
   G  yarr                0.078     0.015               STATION / BIAS / RMS
   G  yell                1.570     0.012               STATION / BIAS / RMS
   G  yibl               -1.517     0.014               STATION / BIAS / RMS
   G  yssk              -12.062     0.015               STATION / BIAS / RMS
   G  zimj              -11.192     0.013               STATION / BIAS / RMS
   R  bogi              -16.760     0.040               STATION / BIAS / RMS
   R  cagz               -3.589     0.017               STATION / BIAS / RMS
   R  conz               -8.322     0.023               STATION / BIAS / RMS
   R  crar                7.235     0.022               STATION / BIAS / RMS
   R  darr              -15.974     0.021               STATION / BIAS / RMS
   R  dlft               -3.396     0.015               STATION / BIAS / RMS
   R  drej               -3.537     0.019               STATION / BIAS / RMS
   R  ffmj               -9.859     0.015               STATION / BIAS / RMS
   R  godz                0.247     0.021               STATION / BIAS / RMS
   R  gope               -4.349     0.049               STATION / BIAS / RMS
   ......
   R  thu2                0.639     0.014               STATION / BIAS / RMS
   R  titz               -5.478     0.032               STATION / BIAS / RMS
   R  unb1                2.956     0.016               STATION / BIAS / RMS
   R  unfe               -3.348     0.024               STATION / BIAS / RMS
   R  vis0              -13.030     0.015               STATION / BIAS / RMS
   R  wroc               -7.346     0.015               STATION / BIAS / RMS
   R  wtzj              -13.439     0.023               STATION / BIAS / RMS
   R  wtzr               -0.831     0.034               STATION / BIAS / RMS
   R  wtzz               -6.575     0.022               STATION / BIAS / RMS
   R  yarr               -3.896     0.018               STATION / BIAS / RMS
   R  zimj                3.323     0.016               STATION / BIAS / RMS
DCB and RMS values in ns. Sum of satellite DCB values   COMMENT
constrained to zero.                                    COMMENT
Estimated constant offset of JASON-1 in TECU:           COMMENT
   J1                    2.745     0.013                COMMENT
DIFFERENTIAL CODE BIASES                                END OF AUX DATA
                                                        END OF HEADER
```

```
   1                                                  START OF TEC MAP
2006    07    01    1    0    0                        EPOCH OF CURRENT MAP
  85.0-180.0 180.0   5.0 450.0                         LAT/LON1/LON2/DLON/H
110  112  114  115  116  118  118  119  119  119  118  118  116  115  113  111
109  107  105  104  102  101   99   98   96   95   93   92   91   89   88   87
 87   86   86   87   87   87   88   89   89   90   91   93   94   95   96   96
 97   97   97   97   97   98   98   99   99   99   99   99   98   98   97   97
 97   98   99  100  102  104  106  108  110
  82.5-180.0 180.0   5.0 450.0                         LAT/LON1/LON2/DLON/H
110  112  114  115  117  118  119  120  120  120  119  117  116  114  111  109
107  105  103  102  101  100   99   98   98   97   95   94   92   91   89   88
 87   86   86   86   86   87   87   88   89   90   91   92   93   94   95   96
 96   96   96   96   96   96   97   98   99   99   99   99   98   97   96   95
 95   96   97   99  101  103  105  108  110
 ......
 -82.5-180.0 180.0   5.0 450.0                         LAT/LON1/LON2/DLON/H
 26   27   27   27   27   26   25   24   22   20   17   15   12    9    6    4
  2    0    0    0    0    0    1    4    7    9   12   14   15   15   15   14
 13   12   12   12   12   13   15   15   16   15   14   13   11    8    6    4
  3    2    2    3    3    5    6    7    8    9   10   10   11   11   12   12
 14   15   17   19   21   22   24   25   26
 -85.0-180.0 180.0   5.0 450.0                         LAT/LON1/LON2/DLON/H
 26   26   27   27   27   26   25   25   23   22   20   18   16   13   11    9
  8    6    5    5    5    6    7    9   11   13   15   17   17   18   17   17
 16   15   15   15   15   15   15   15   15   14   13   12   10    8    6    4
  3    2    2    1    2    2    3    4    4    5    6    7    8   10   11   13
 14   16   18   19   21   22   24   25   26
  12                                                  END OF TEC MAP
   1                                                  START OF RMS MAP
2006    07    01    1    0    0                        EPOCH OF CURRENT MAP
  85.0-180.0 180.0   5.0 450.0                         LAT/LON1/LON2/DLON/H
 10   10    9    8    8    7    6    6    5    5    4    4    3    3    3    3
  3    3    3    3    3    3    3    3    3    3    3    3    3    3    3    3
  3    3    3    4    4    4    4    4    5    5    5    6    6    6    7    7
  8    8    9    9   10   10   10   11   11   11   11   12   12   12   12   12
 12   12   12   12   12   11   11   11   10
  82.5-180.0 180.0   5.0 450.0                         LAT/LON1/LON2/DLON/H
 10    9    9    8    7    7    6    6    5    5    4    4    4    3    3    3
  3    3    3    3    3    3    3    3    3    3    3    3    3    3    3    3
  3    3    3    4    4    4    4    4    4    5    5    5    6    6    6    7
  7    8    8    9    9    9    9   10   10   10   10   10   10   10   11   10
 10   10   10   10   10   11   10   10   10
 ......
 -82.5-180.0 180.0   5.0 450.0                         LAT/LON1/LON2/DLON/H
  7    7    8    8    8    9    9   10   11   12   14   16   17   19   20   21
 22   23   23   24   24   25   25   26   26   26   26   26   26   25   25   25
 25   24   24   23   23   22   21   19   18   17   16   14   13   12   11   10
  9    9    8    8    7    7    7    7    7    7    7    7    6    6    6    6
  6    6    6    6    6    7    7    7    7
 -85.0-180.0 180.0   5.0 450.0                         LAT/LON1/LON2/DLON/H
  7    8    8    8    9    9   10   11   12   13   14   16   17   19   20   21
 22   23   24   25   26   27   27   28   28   28   28   28   27   27   26   26
 25   25   24   23   23   22   21   19   18   17   16   14   13   12   11   10
  9    9    8    7    7    7    6    6    6    6    6    5    5    5    5    6
  6    6    6    6    6    7    7    7    7
  12                                                  END OF RMS MAP
                                                      END OF FILE
```

Appendix B

GNSS-only and combined GIM for different ionospheric conditions

B.1 Daily examples of combined GIM and comparison with the GNSS-only maps

One daily example of the estimated two-hourly combined GIM for each of the investigated four weeks is shown in the figures below. Additionally, the corresponding maps of the difference ΔVTEC COMB minus GNSS-only can be seen. Negative values of the differences denote a lowering of the VTEC when altimetry observations are included, and positive differences indicate an increase in the estimated VTEC under deployment of altimetry data. Obviously, the differences between the GNSS-only and the COMB GIM increase proportionally to the general ionosphere activity and typically coincide with the altimeter footsteps. In all regarded days high differences occur predominately in the low latitude regions around local noon, when the VTEC reaches its maximum. Furthermore, large (and mostly positive) differences can be observed over the oceans in the southern hemisphere - a region which is sparely covered by GNSS stations.
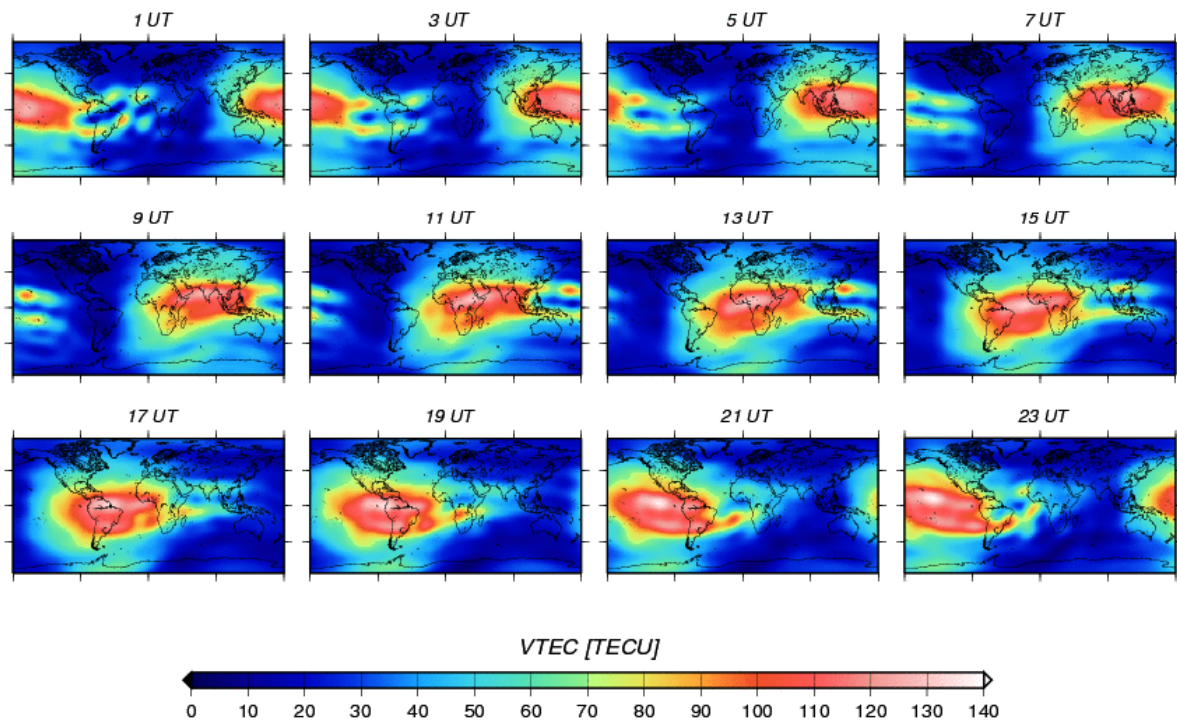
Figure B.1: Global VTEC maps in two-hourly snapshots, COMB GIM for day 270 2001
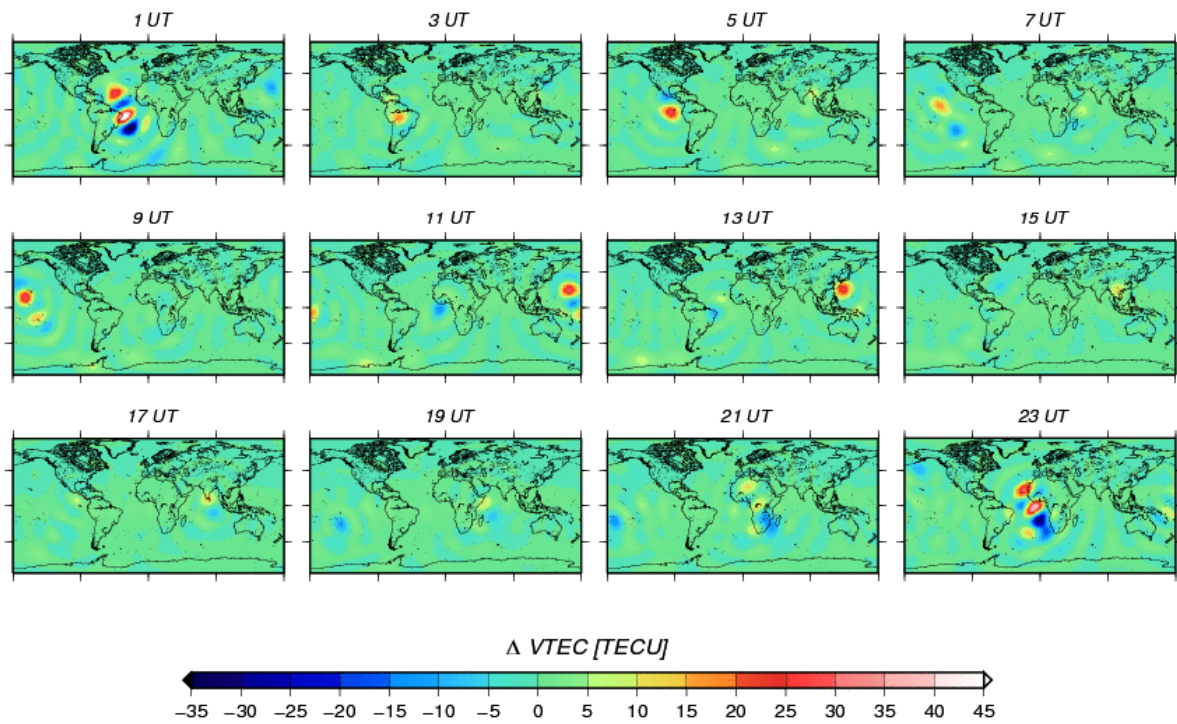
Figure B.2: Global maps of the ΔVTEC between the COMB and GNSS-only GIM in two-hourly snapshots for day 270 2001

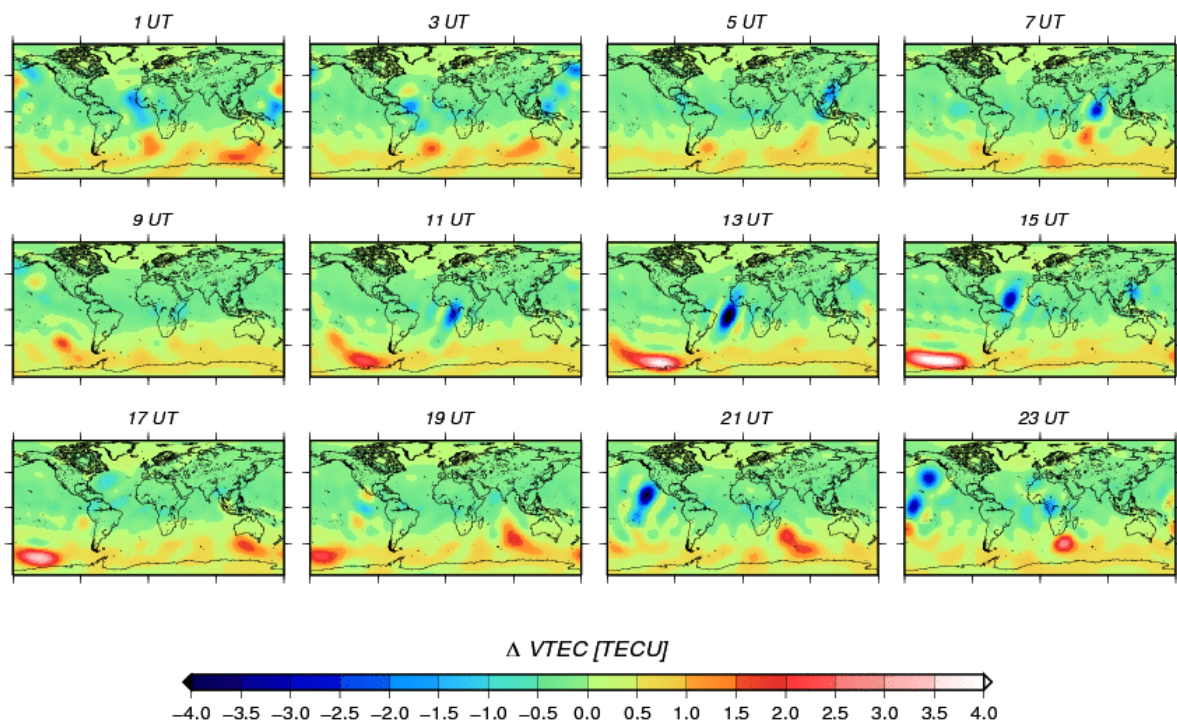Figure B.3: Global VTEC maps in two-hourly snapshots, COMB GIM for day 007 2002
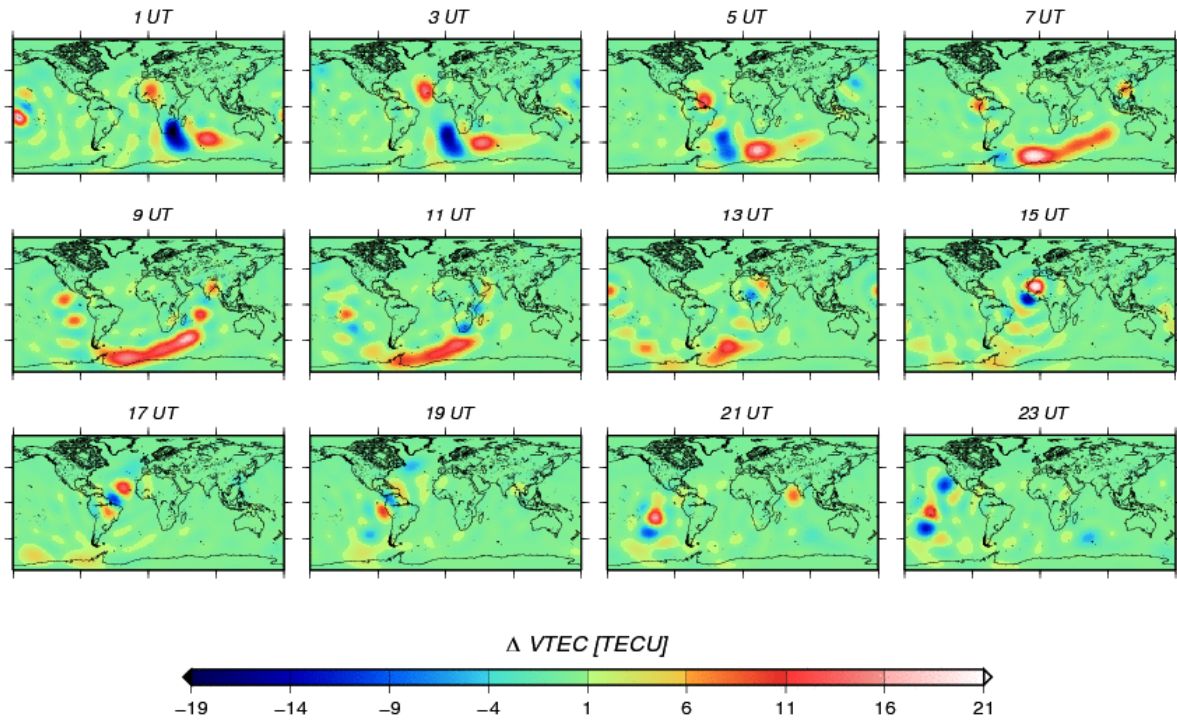
Figure B.4: Global maps of the ΔVTEC between the COMB and GNSS-only GIM in two-hourly snapshots for day 007 2002
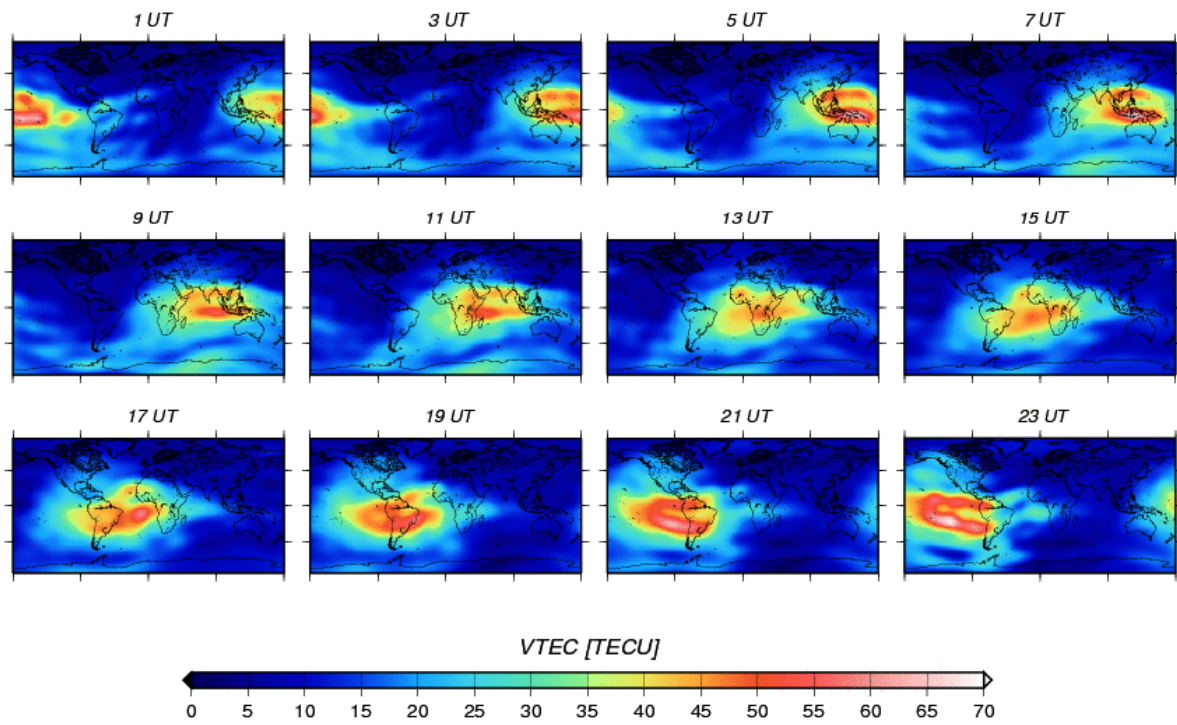
Figure B.5: Global VTEC maps in two-hourly snapshots, COMB GIM for day 016 2005
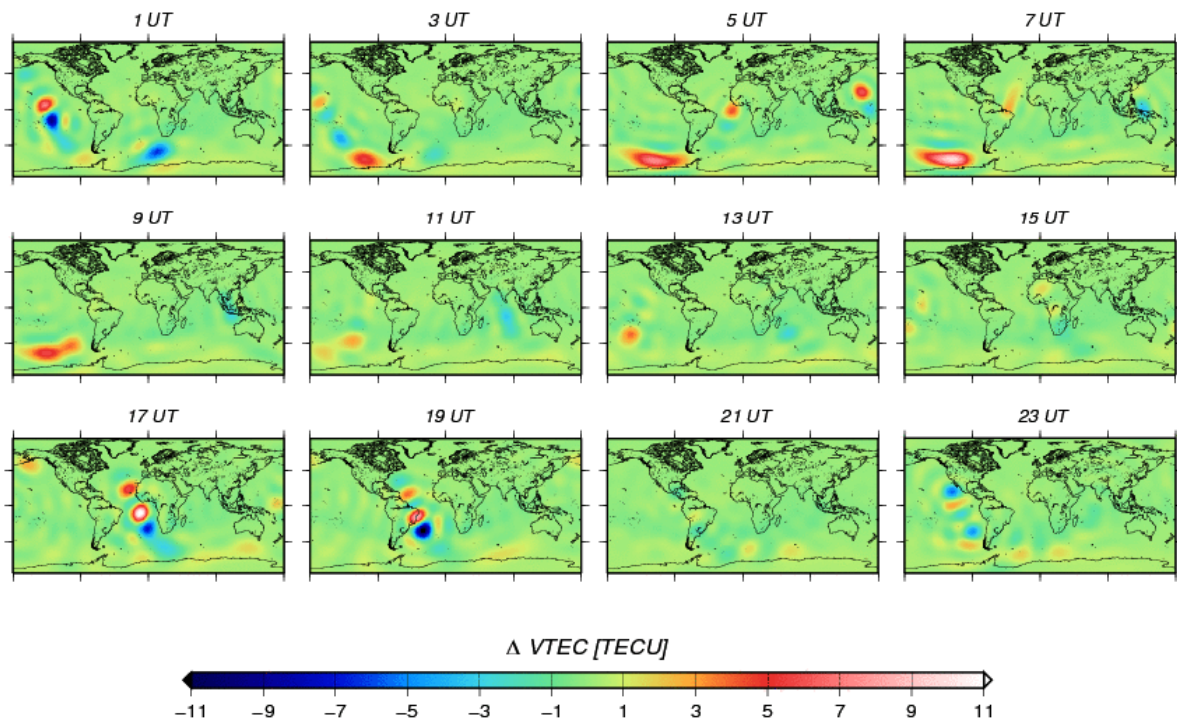
Figure B.6: Global maps of the ΔVTEC between the COMB and GNSS-only GIM in two-hourly snapshots for day 016 2005

Figure B.7: Global VTEC maps in two-hourly snapshots, COMB GIM for day 201 2006

Figure B.8: Global maps of the ΔVTEC between the COMB and GNSS-only GIM in two-hourly snapshots for day 201 2006

B.2 Differences between the IGG GIM and altimetry derived VTEC

Figures B.9 to B.12 show the mean differences between the VTEC delivered by satellite altimetry and the corresponding values interpolated from the IGG GNSS-only and COMB GIM for each of the four investigated weeks of different solar and magnetic activity. The differences are averaged on a daily basis and presented in time and in geographical latitude. For the regarded periods in 2001 and 2002 Topex/Poseidon data is used for both, the comparison and the COMB GIM. For the two weeks in 2005 and 2006 Jason-1 data is used. In order to prove the self-consistency of the combined GIM, the bias between the altimetry derived VTEC and the values obtained from the IGG COMB GIM is reduced by the corresponding daily offsets estimated for the altimetry satellite. As a result, the differences altimetry minus COMB GIM VTEC are shifted towards zero, showing that the estimated offsets are in the order of the bias between the altimetry and GNSS VTEC and proving the self-consistency of the combination approach. However, the latitudal dependency is not entirely omitted, which indicates that the constant altimetry offset should be replaced by an appropriate function of the latitude (see also section 6.2).

It has to be noted, that irrespective of the altimetry satellite (Topex/Poseidon or Jason-1) and the overall ionospheric activity, the absolute bias reference between the altimetry derived VTEC and the values obtained from the GNSS GIM generally remains in a similar range (see Table B.1). The differences are mostly positive, pointing at an overestimated altimetry VTEC in respect to the GNSS derived values. The trend for lowering of the bias close to the equator is present for all of the investigated periods and can be related to the upper plasmaspheric electron content, not measured by the altimeters. In three of the regarded periods (in 2001, 2002, and 2005) an increase of the bias between the altimetry and the GNSS-only VTEC in low latitudes ($\pm 20°$) can be observed, whereas in 2002 and 2005 this effect is higher in the Northern hemisphere. As for the combined GIM, the differences are almost entirely omitted due to the combination and estimation of a constant altimetry offset. Still, in latitudes above $\pm 60°$ the bias remains relatively high.

| Period | av. bias (IGG GNSS-only) | | av. bias (IGG COMB) | | av. estim. | altim. |
(doy, year)	in time	in lat.	in time	in lat.	offset	mission
267-273, 2001	2.41	2.27	0.19	0.32	1.61	T/P
001-007, 2002	2.72	2.42	0.15	0.03	1.85	T/P
016-022, 2005	1.42	1.27	0.005	0.04	1.47	Jas-1
198-204, 2006	3.00	3.34	-0.02	0.22	2.76	Jas-1

Table B.1: Weekly averages of the bias ΔVTEC altimetry minus IGG and of the estimated altimetry offset (all values in TECU); altimetry mission used for the in the given period
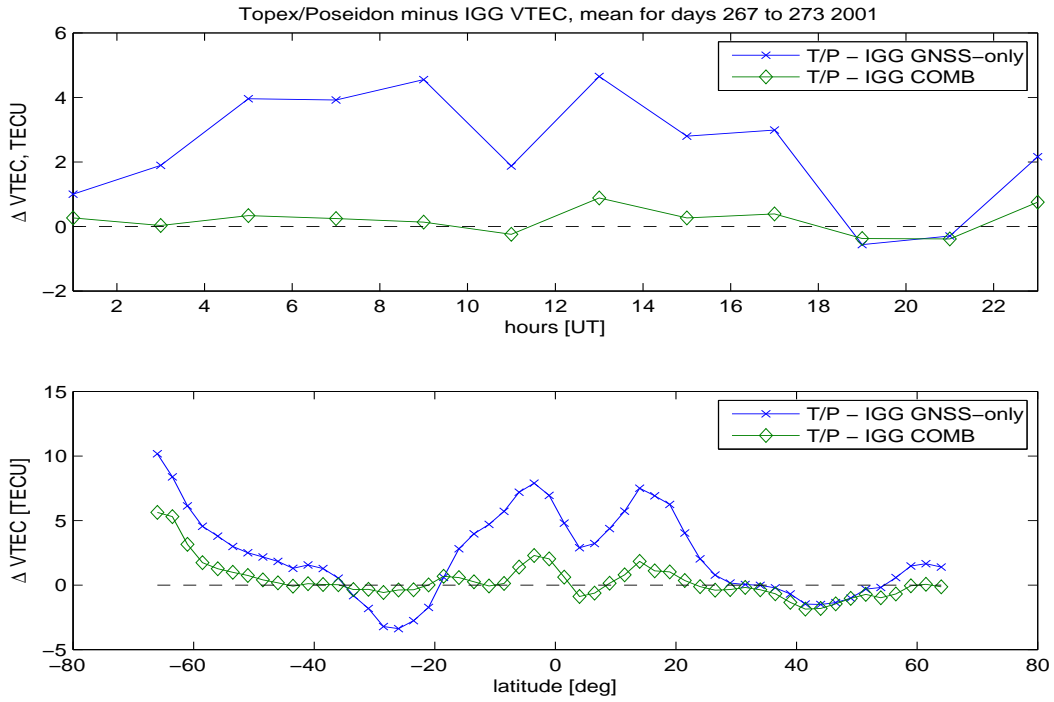
Figure B.9: Mean Topex/Poseidon minus IGG VTEC in time and in latitude, doy 267-273, 2001 (high Kp index, high sunspot number)
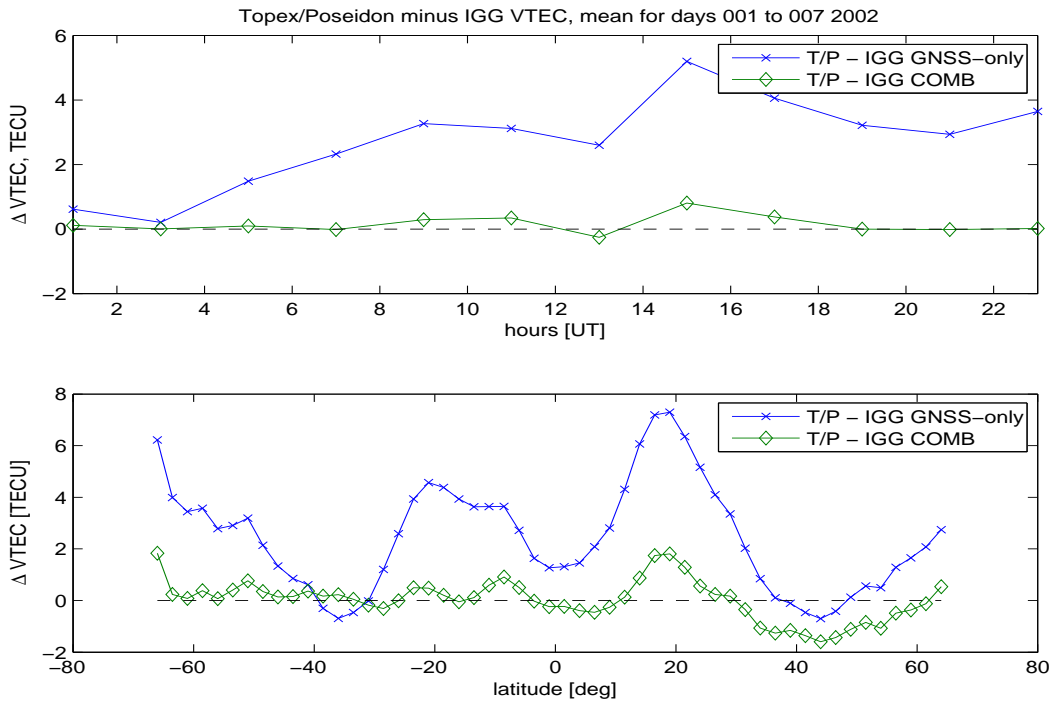

Figure B.10: Mean Topex/Poseidon minus IGG VTEC in time and in latitude, doy 001-007, 2002 (low Kp, high sunspot number)
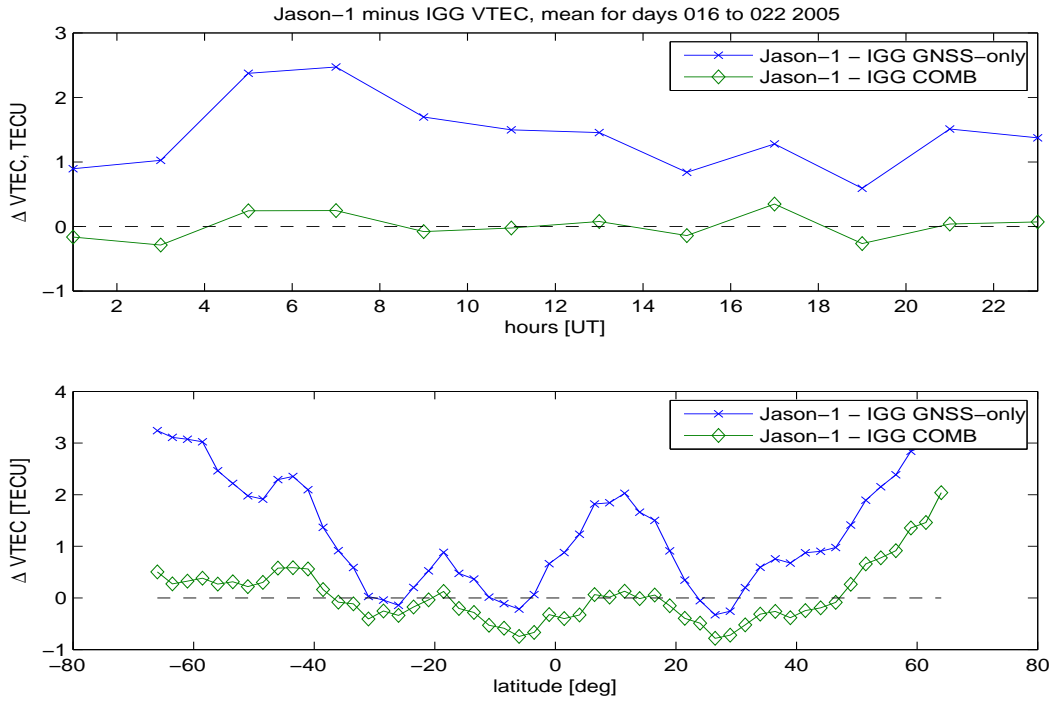
139

Figure B.11: Mean Jason-1 minus IGG VTEC in time and in latitude, doy 016-022, 2005 (high Kp index, low sunspot number)
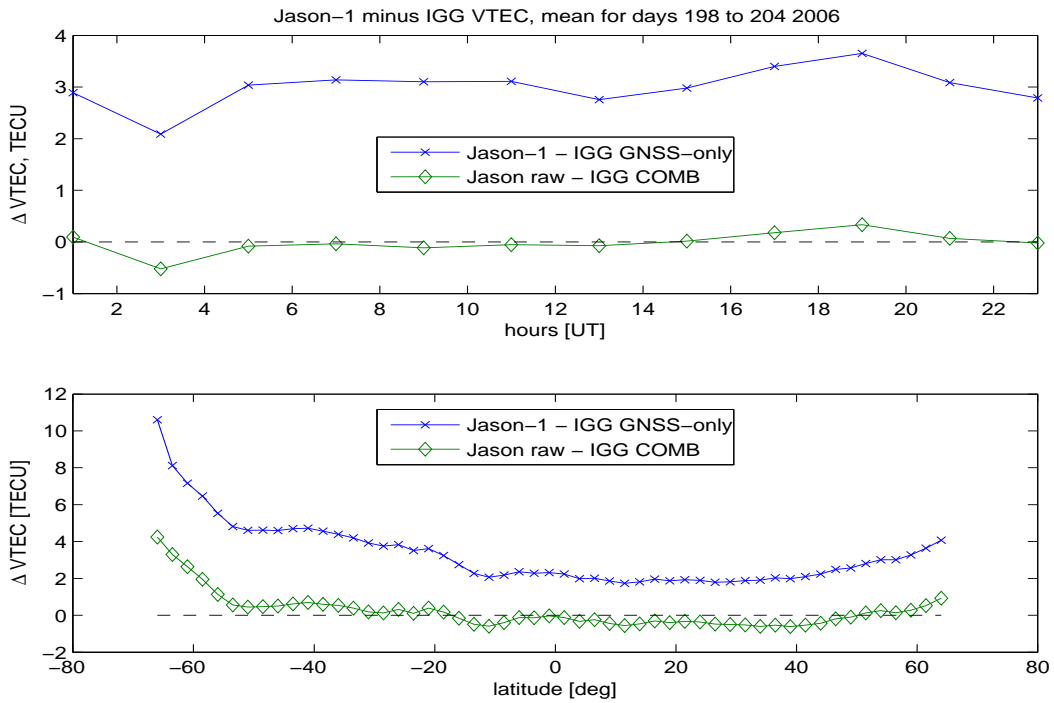

Figure B.12: Mean Jason-1 minus IGG VTEC in time and in latitude, doy 198-204, 2006 (low Kp index, low sunspot number)

B.3 Time series of the estimated constant altimetry offset

For each day of the four weeks in different ionospheric conditions a constant altimetry offset is estimated along with the COMB GIM. The obtained values are shown in Figures B.13 to B.16.
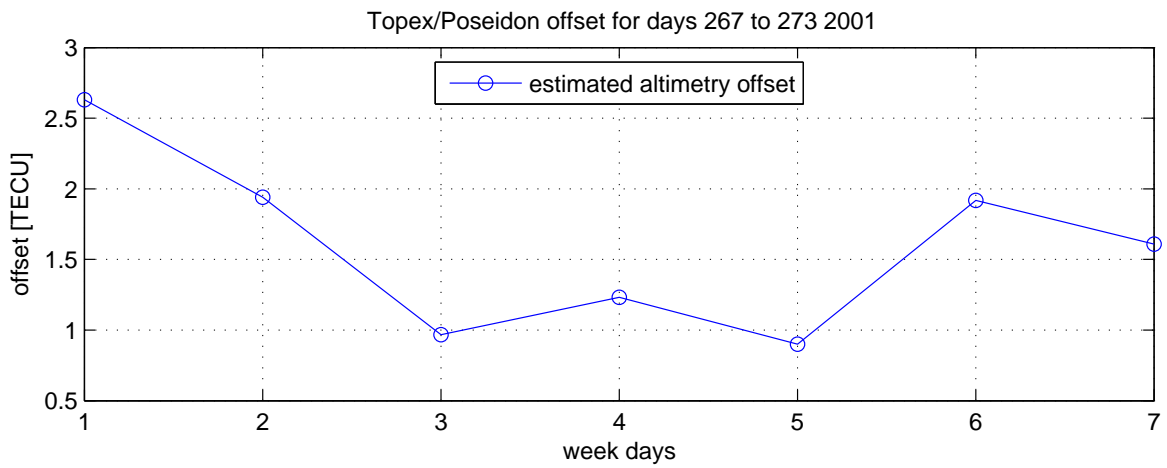
Figure B.13: Estimated daily altimetry offsets, doy 267-273, 2001
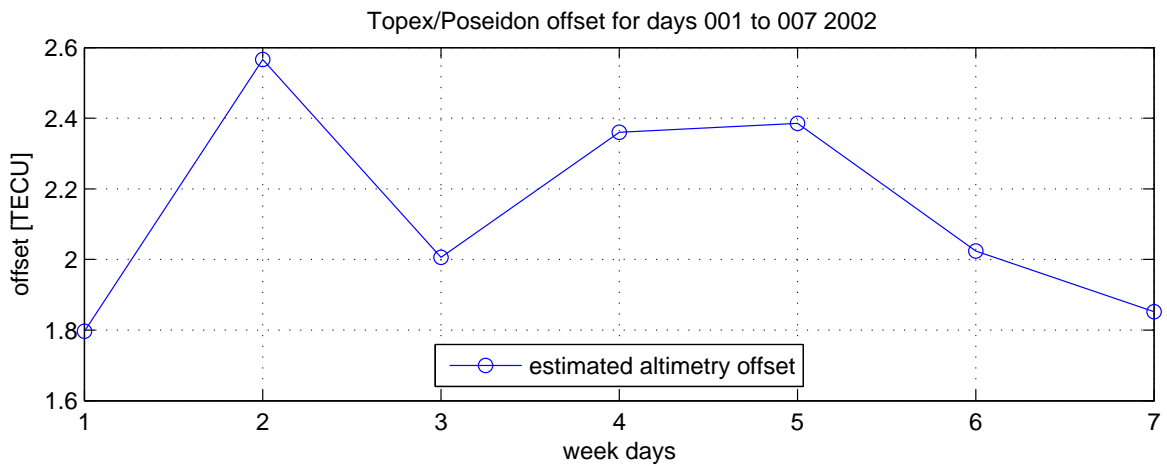
Figure B.14: Estimated daily altimetry offsets, doy 001-007, 2002
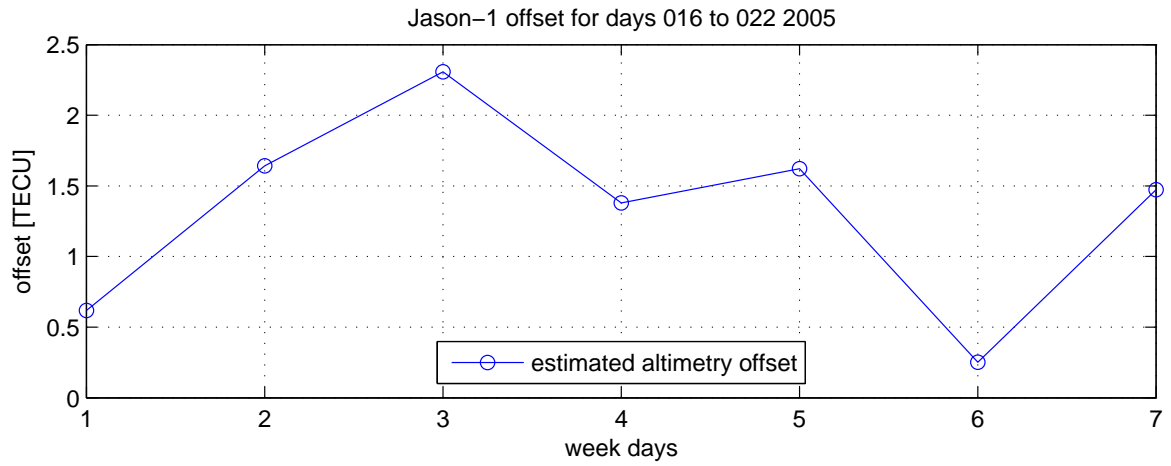
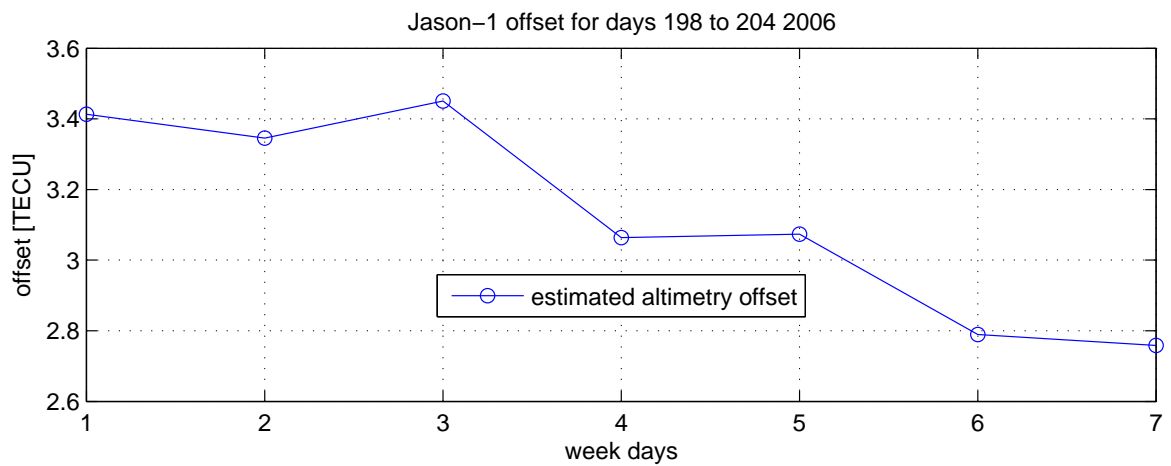Figure B.15: Estimated daily altimetry offsets, doy 016-022, 2005

Figure B.16: Estimated daily altimetry offsets, doy 198-204, 2006

B.4 Comparison of the various GIM and raw satellite altimetry data

Figures B.17 to B.24 show the comparison between altimetry delivered VTEC and the corresponding values derived from the different global ionosphere models. The comparison for four days in various ionosphere conditions is carried out at the UPC. The bias, standard deviation, root mean square and percentage error of the differences are shown in time and in latitude. The legend entries "iggg" and "iggc" correspond to the IGG GNSS-only and the IGG COMB GIM, respectively. In order to examine the reasonability of the estimated daily altimeter offsets, the bias between the altimetry VTEC and the corresponding values from the COMB GIM is plotted twice in the upper left panel of each figure. The second curve is reduced by estimated daily offset. Both curves are therefore identical, with the reduced one shifted towards zero.
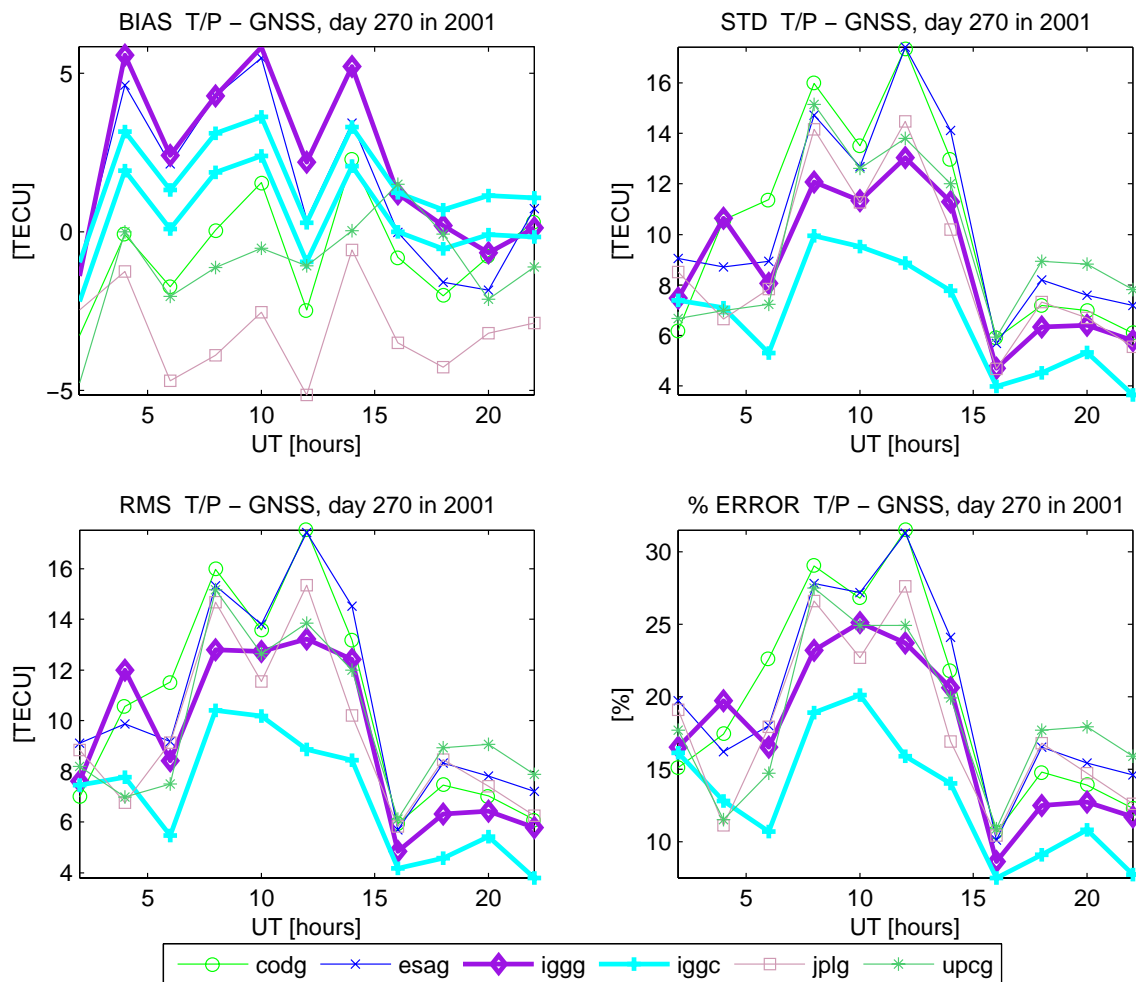

Figure B.17: Jason-1 minus GNSS and COMB GIM VTEC: bias, standard deviation, root mean square and percentage error in time for day 270 in 2001
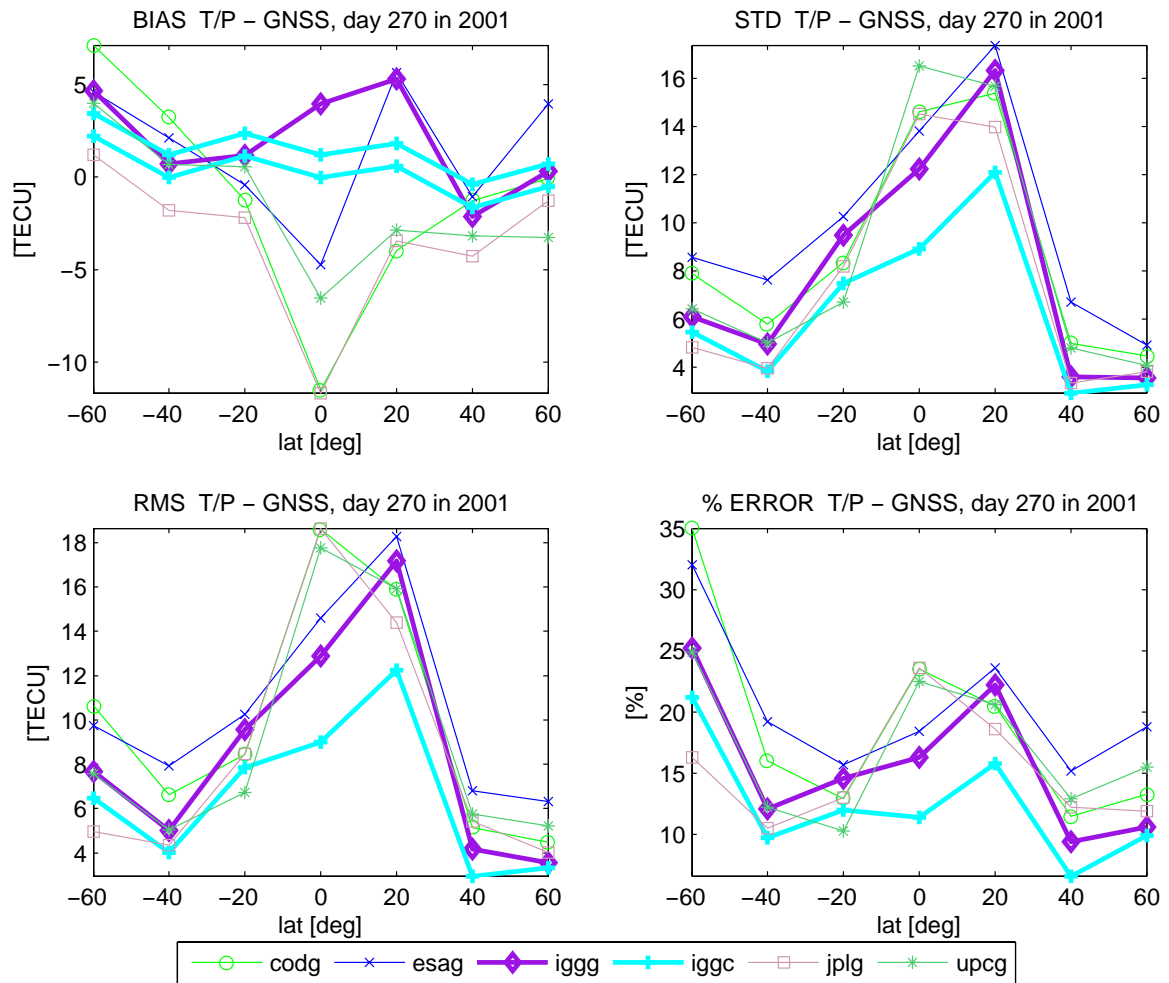
Figure B.18: Jason-1 minus GNSS and COMB GIM VTEC: bias, standard deviation, root mean square and percentage error in latitude for day 270 in 2001
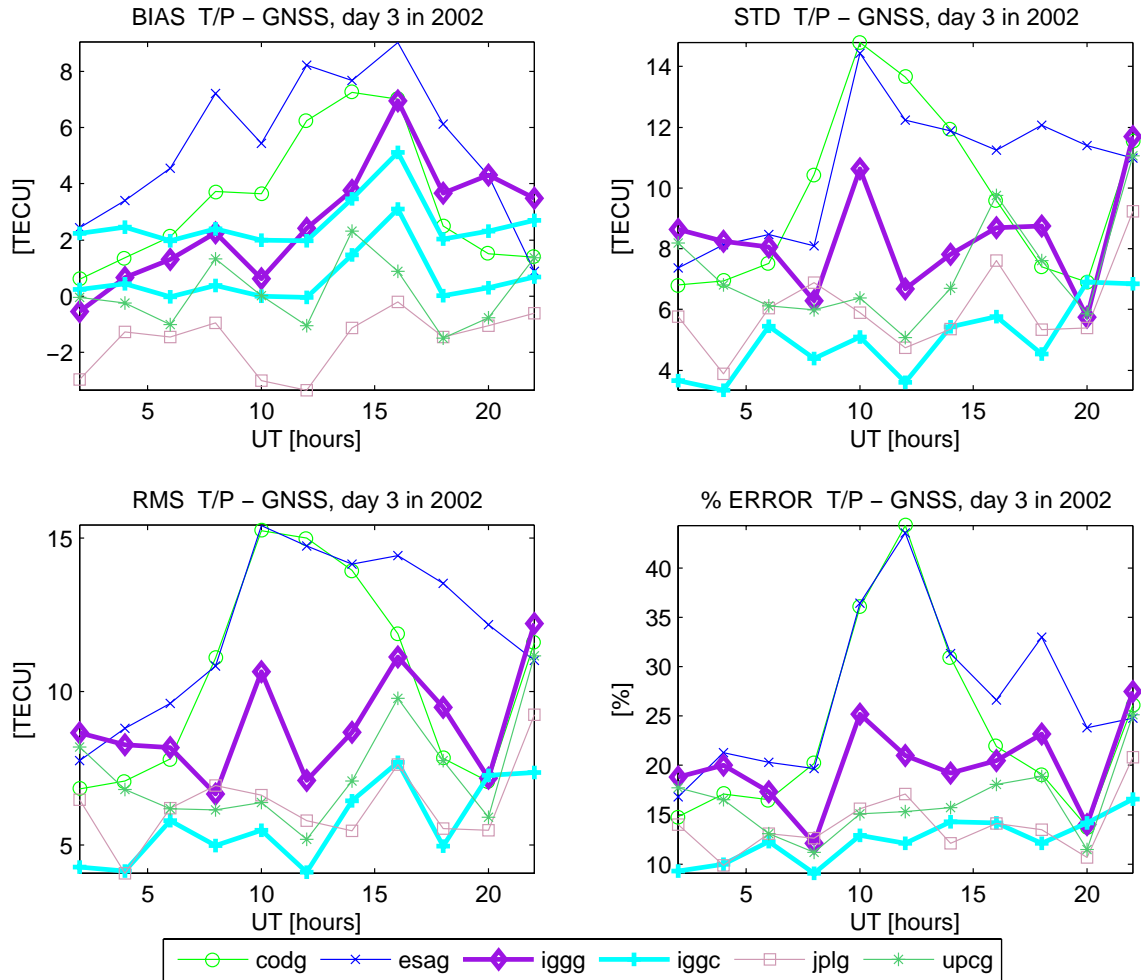
Figure B.19: Jason-1 minus GNSS and COMB GIM VTEC: bias, standard deviation, root mean square and percentage error in time for day 003 in 2002
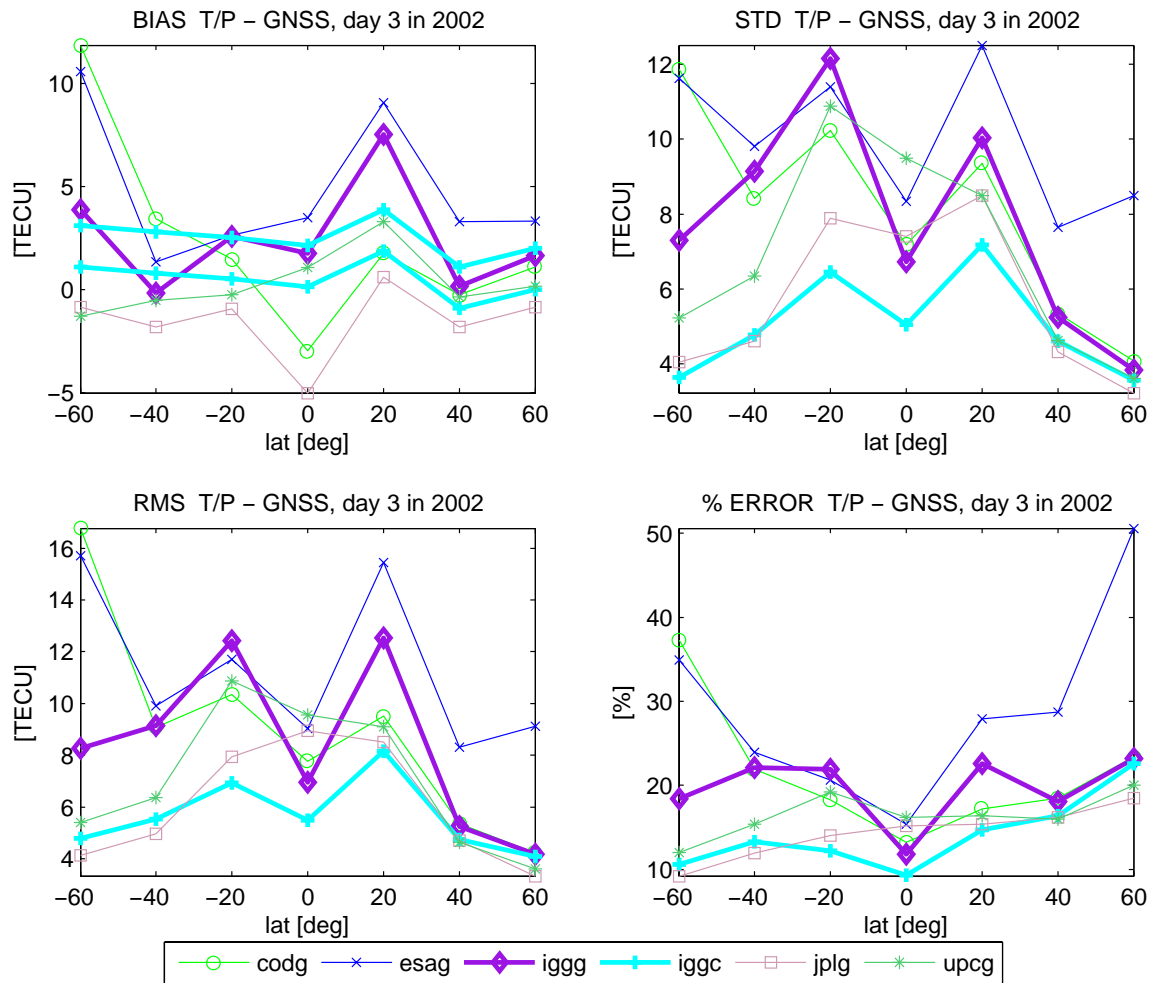
Figure B.20: Jason-1 minus GNSS and COMB GIM VTEC: bias, standard deviation, root mean square and percentage error in latitude for day 003 in 2002
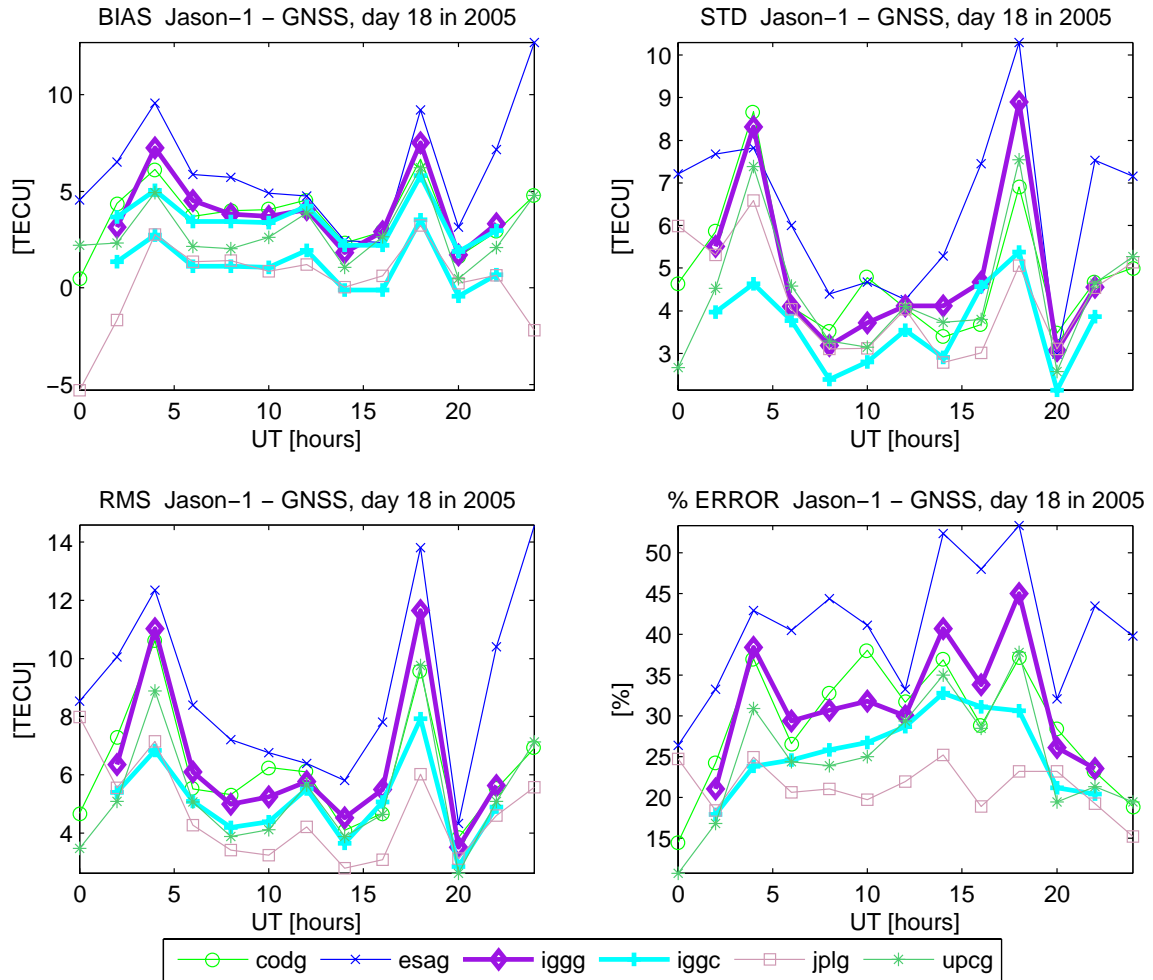
Figure B.21: Jason-1 minus GNSS and COMB GIM VTEC: bias, standard deviation, root mean square and percentage error in time for day 018 in 2005
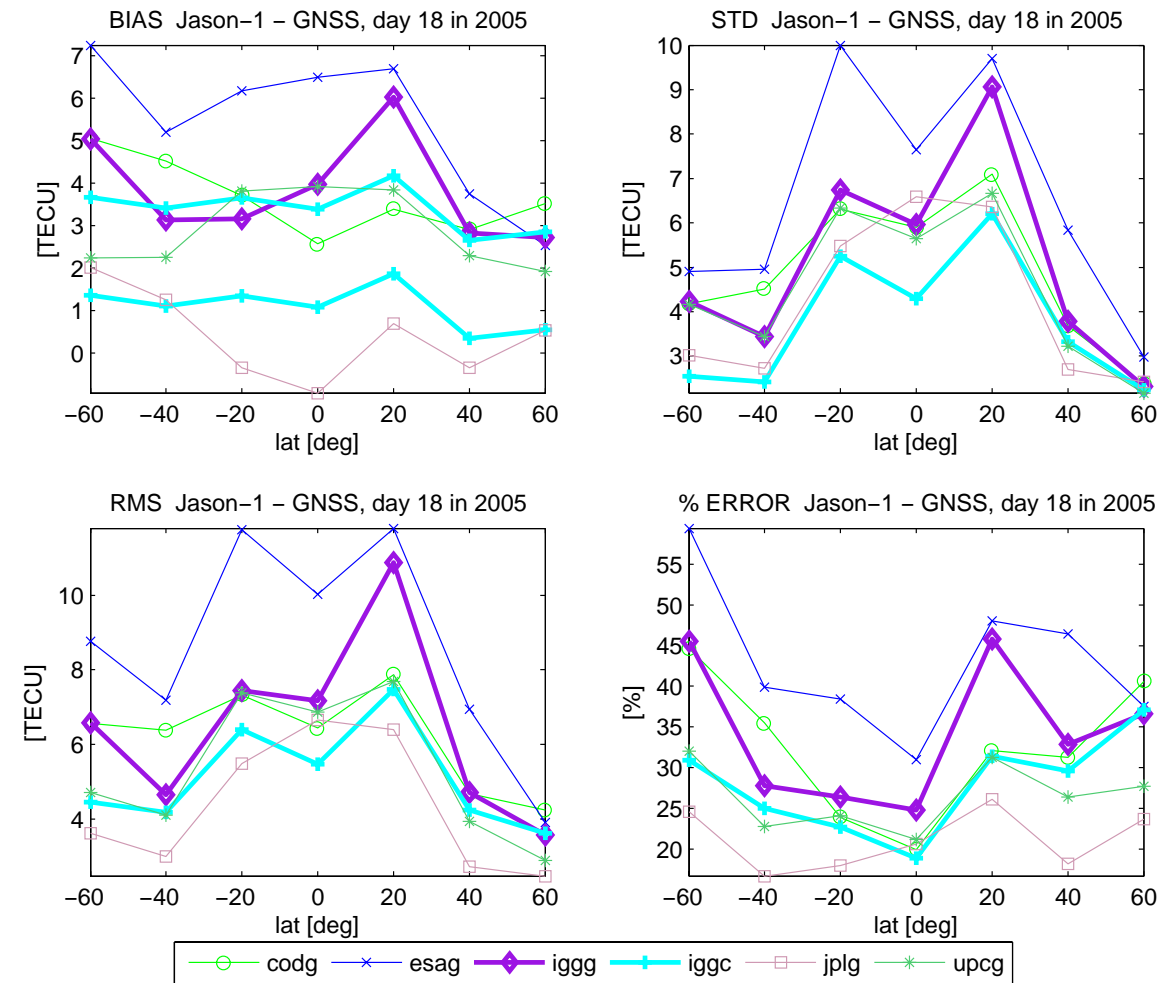
Figure B.22: Jason-1 minus GNSS and COMB GIM VTEC: bias, standard deviation, root mean square and percentage error in latitude for day 018 in 2005
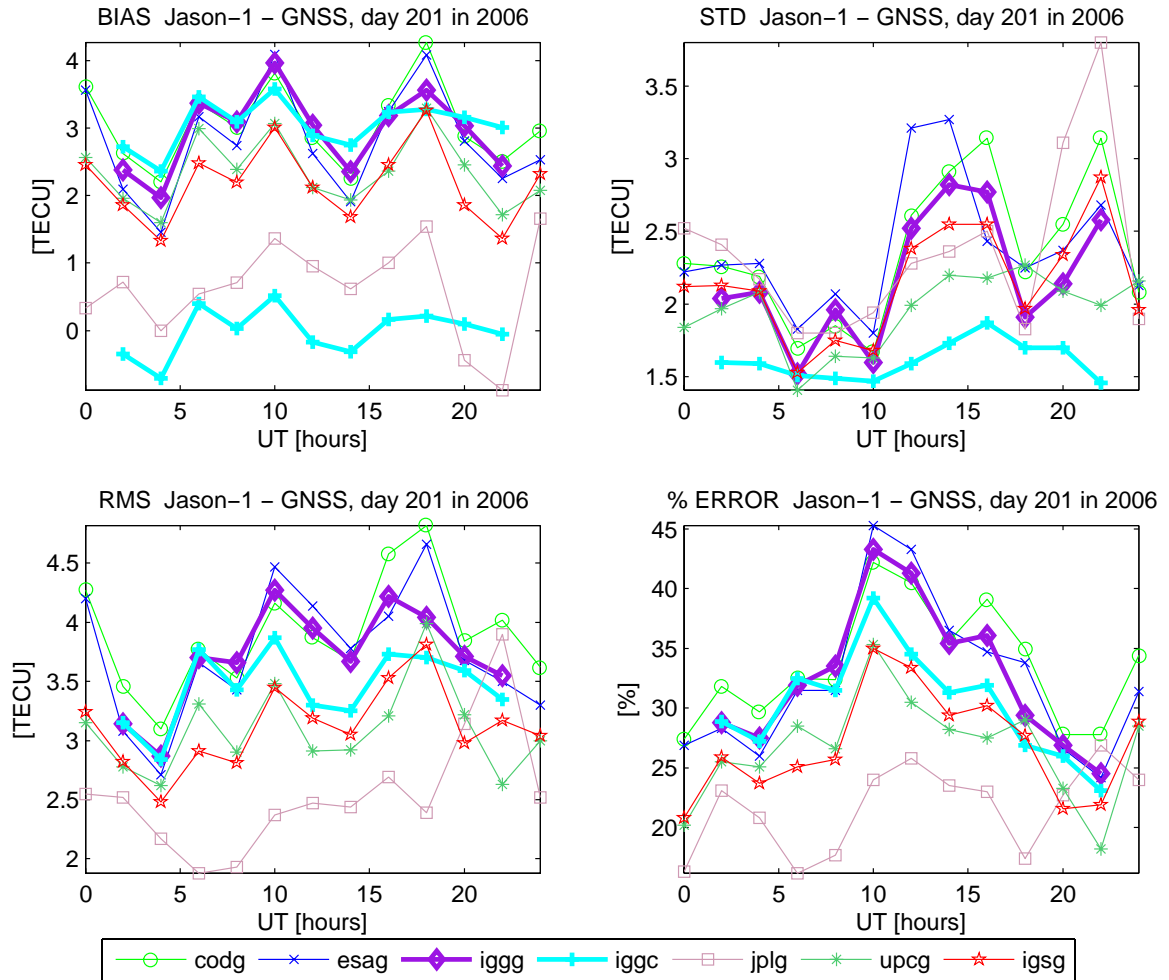
Figure B.23: Jason-1 minus GNSS and COMB GIM VTEC: bias, standard deviation, root mean square and percentage error in time for day 201 in 2006
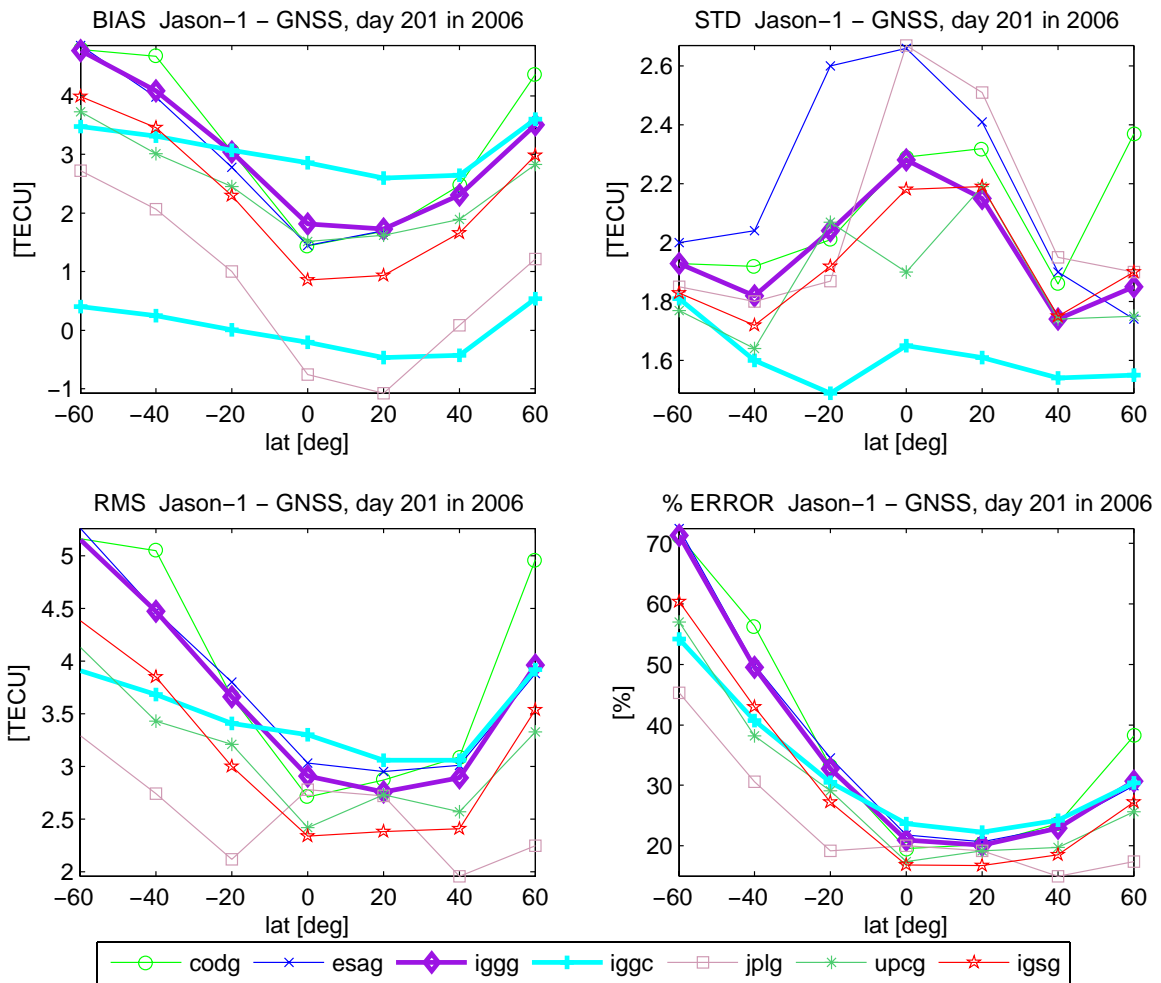
Figure B.24: Jason-1 minus GNSS and COMB GIM VTEC: bias, standard deviation, root mean square and percentage error in latitude for day day 201 in 2006

Appendix C

Combination of GNSS, Jason-1, and Topex/Poseidon data

In September 2002 the Topex/Poseidon satellite assumed a new orbit midway between its original ground tracks, which were taken over by the Jason-1 mission, launched in December 2001 (see section 3.2.1). Till a technical failure in the Topex/Poseidon equipment in October 2005 the two satellites were flying as a tandem mission. During this time it was possible to obtain data from both of them. However, only Topex/Poseidon observations are included in the COMB GIM for the investigated week in 2002, and Jason-1 data for the week in 2005, respectively. The main reason for this decision is the fact that the missions tracks are nearly collocated (Figure C.1). Using observations from both of them would make no significant contribution to the global coverage of the developed ionosphere maps. Since the primary sensor of both missions is the NASA Radar Altimeter, the obtained data and the systematic error effects are expected to be very similar too. Moreover, during the other two periods investigated in this work only one altimetry mission is present; introducing data from both, Topex/Poseidon and Jason-1 in two of the four regarded weeks would bias the comparison between the different periods.
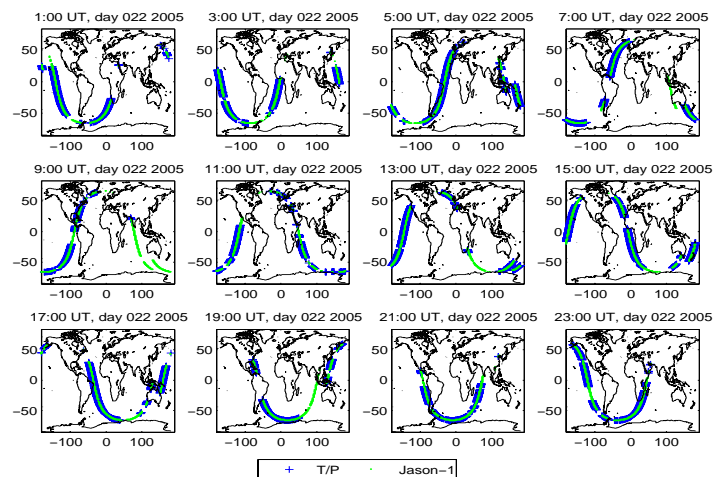

Figure C.1: Topex/Poseidon and Jason-1 footprints in sun-fixed reference frame and two-hourly intervals, day 022 in 2005

By way of trial, for day 022 in 2005 the GIM are computed combining GNSS and both, Topex/Poseidon and Jason-1 observations. This solution, referred to as COMB-2, is compared to the corresponding COMB GIM from GNSS and Jason-1 data. The bias, minimum and maximum of the global VTEC and RMS differences COMB-2 (GNSS, Topex/Poseidon and Jason-1) minus COMB (GNSS and Jason-1) GIM are listed in Table C.1. The corresponding ΔVTEC maps can be seen in Figure C.2. The two solutions are quite consistent with each other. The highest differences of approx. ± 3 TECU appear mainly in the first maps of the two-hourly sequence. The RMS lowering caused by the inclusion of Topex/Poseidon data has a maximum of -0.39 TECU. For the altimetry offset estimates we obtain:

- 1.46 TECU for Jason-1 and 2.89 TECU for Topex/Poseidon (from the COMB-2 GIM);

- 1.51 TECU for Jason-1 (from the COMB GIM).

	ΔVTEC	ΔRMS
bias, [TECU]	-0.01	0.005
min, [TECU]	-2.66	-0.39
max, [TECU]	3.46	0.04

Table C.1: Bias, minimum and maximum of the differences ΔVTEC and ΔRMS COMB-2 minus COMB GIM, day 022 2005
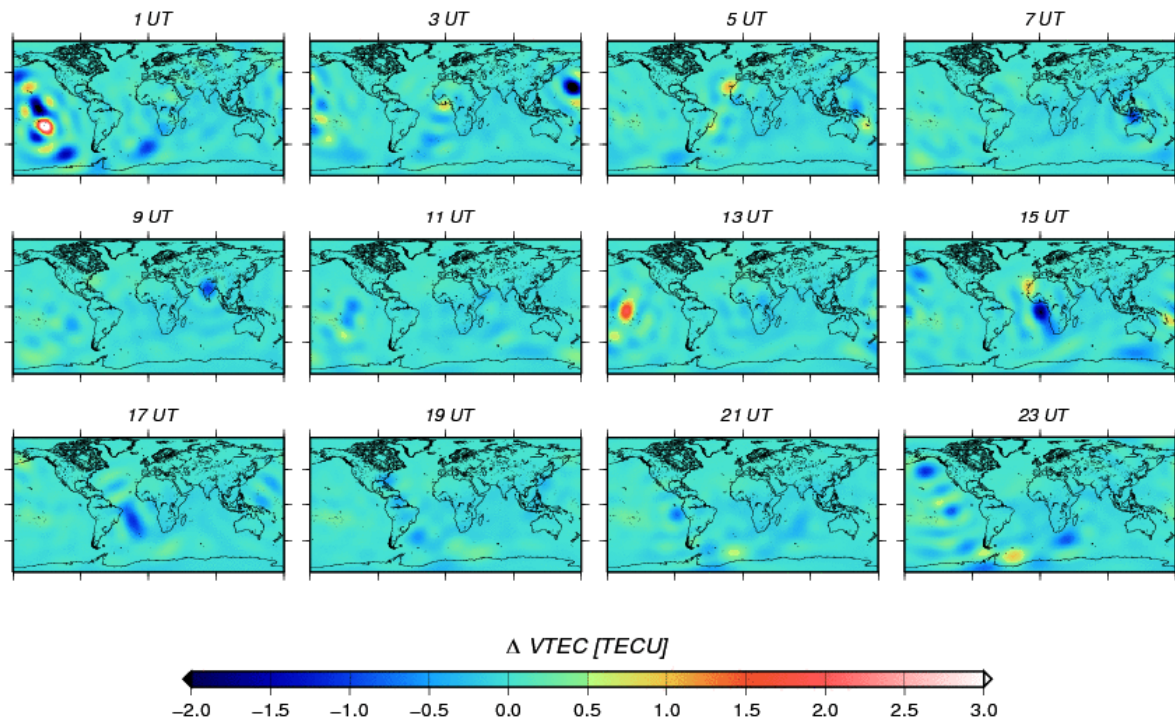

Figure C.2: Global maps of the ΔVTEC between the COMB-2 and COMB GIM in two-hourly snapshots for day 022 2005

Bibliography

ADSCentral (2007). Altimeter Database System Central, Version 4.00. `http://adsc.gfz-potsdam.de/ads/adsCentral_index.html`.

AVISO (2007). The French Active Archive Data Center for multi-satellite altimeter missions. `http://www.aviso.oceanobs.com`.

AVISO/Altimetry (1996). AVISO User Handbook for Merged TOPEX/POSEIDON products, Edition 3.0. AVI-NT-02-101. `www.jason.oceanobs.com/documents/donnees/tools/hdbk_gdrm.pdf`.

Azpilicueta, F., Brunini, C., & Radicella, S. M. (2006). Global ionospheric maps from GPS observations using modip latitude. *Advances in Space Research*, 38(11), 2324–2331.

Bassiri, S. & Hajj, G. A. (1993). Higher-order ionospheric effects on the GPS observables and means of modeling them. *NASA STI/Recon Technical Report A*, 95, 81411–+.

Berthias, J. (2000). DORIS data. Centre National d'Etudes spatiales, DORIS Days, Toulouse, May 2000. `http://lareg.ensg.ign.fr/IDS/doc/DORIS-data10-desc.html`.

Bilitza, D. (2001). International Reference Ionosphere 2000. *Radio Science*, 36(2), 261–275.

Boucher, C. & Altamimi, Z. (2001). ITRS, PZ-90 and WGS 84: current realizations and the related transformation parameters. *Journal of Geodesy*, 75(11), 613–619. doi:10.1007/s001900100208.

Brunini, C. (1997). *Global ionospheric models from GPS measurements*. PhD thesis, Universidad Nacional de La Plata, La Plata, Argentina.

Brunini, C., Meza, A., & Bosch, W. (2005). Temporal and spatial variability of the bias between TOPEX- and GPS-derived total electron content. *Journal of Geodesy*, 79(4-5), 175–188.

Budden, K. G. (1985). *The propagation of radio waves*. Cambridge University Press.

CDDIS (2007). Crustal Dynamics Data Information System (CDDIS) at NASA GSFC. `ftp://cddis.nasa.gov`.

CGNC (2007). U.S. Coast Guard Navigation Center, GPS status and outage information. `http://www.navcen.uscg.gov/gps/status_and_outage_info.htm`.

Chelton, D. B., Ries, J. C., Haines, B. J., Fu, L. L., & Callahan, P. (2001). Satellite altimetry. In L. L. Fu & A. Cazenave (Eds.), *Satellite altimetry and Earth sciences: A handbook of techniques and applications* (pp. 1–132). Academic Press, London. ISBN 0-12-269545-3.

CODE (2007a). Center for Orbit Determination in Europe, Global Ionosphere Maps Produced by CODE. Modified Single-Layer Model Mapping Function. `http://aiuws.unibe.ch/ionosphere/mslm.pdf`.

CODE (2007b). Center for Orbit Determination in Europe, Global Ionosphere Maps Produced by CODE. `http://www.aiub.unibe.ch/ionosphere/`.

CODE (2007c). Center for Orbit Determination in Europe, Global Ionosphere Maps Produced by CODE. `ftp://ftp.unibe.ch/aiub/CODE/`.

CPAR (2007). Centre for RF Propagation and Atmospheric Research, Hampshire, UK. `http://www.cpar.qinetiq.com`.

Dach, R., Hugentobler, U., Fridez, P., & Meindl, M., Eds. (2007). *Bernese GPS Software, Version 5.0*. Astronomical Institute, University of Bern.

Davies, K. (1990). *Ionospheric radio*, volume 31 of *IEE Electromagnetic waves series*. Peter Peregrinus Ltd, London.

de Munck, J. C. & Spoelstra, T. A. T. (1992). *Refraction of transatmospheric signals in geodesy : proceedings of the symposium, The Hague, The Netherlands, May 19-22, 1992*. Delft, The Netherlands : Nederlandse Commissie voor Geodesie, 1992.

Dow, J. M., Neilan, R. E., & Gendt, G. (2005). The International GPS Service (IGS): Celebrating the 10th Anniversary and Looking to the Next Decade. *Advances in Space Research*, 36(3), 320–326. doi:10.1016/j.asr.2005.05.125.

Ducic, V., Artru, J., & Lognonne, P. (2003). Ionospheric remote sensing of the Denali Earthquake Rayleigh surface waves. *Geophysical research letters*, 30(18), 1951–1958.

Eather, R. H. (1980). Majestic lights: The aurora in science, history, and the arts. *Washington DC American Geophysical Union Geophysical Monograph Series*.

Feltens, J. (1998). Chapman profile approach for 3-D global TEC representation. In J. M. Dow, J. Kouba, & T. Springer (Eds.), *Proceeding of the IGS AC Workshop* (pp. 285–297). Darmstadt, Germany.

Feltens, J. & Schaer, S. (1998). IGS Products for the Ionosphere. In J. M. Dow, J. Kouba, & T. Springer (Eds.), *Proceeding of the IGS AC Workshop* (pp. 225–232). Darmstadt, Germany.

Fu, L. L., Christensen, E. J., Yamarone, C. A., Lefebvre, M., Ménard, Y., Dorrer, M., & Escudier, P. (1994). TOPEX/POSEIDON mission overview. *Journal of Geophysical Research*, 99(C12), 2436924382.

GALILEO (2007). European Satellite Navigation System. `http://ec.europa.eu/dgs/energy_transport/galileo/intro/challenge_en.htm`.

Gaspar, P., Ogor, F., Yamarone, P. Y., & Zanife, O. Z. (1994). Estimating the sea state bias of the TOPEX and POSEIDON altimeters from crossover differences. *Journal of Geophysical Research*, 99, 24981–24994.

GGOS (2007). Global Geodetic Observing System. `http://www.ggos.org`.

GLONASS (2007). Russian Space Agency, Information-analytical Centre. `http://www.glonass-ianc.rsa.ru`.

Grüller, R. (2007). NAVSTAR-GPS Das globale Positionierungssystem . `http://www.gpswien.at/Artikel1.htm`.

Habrich, H. (1999). *Geodetic applications of the Global Navigation Satellite System (GLONASS) and of GLONASS/GPS combinations*. PhD thesis, Bern University, Switzerland.

Hargreaves, J. K. (1992). *The Solar-Terrestrial Environment: An Introduction to Geospace - the Science of the Terrestrial Upper Atmosphere, Ionosphere, and Magnetosphere*. Cambridge atmospheric and space science series, Cambridge: Cambridge University Press.

Hartmann, G. K. & Leitinger, R. (1984). Range errors due to ionospheric and tropospheric effects for signals above 100 MHz. *Bulletin Géodesique*, 58, 109–136.

Hernández-Pajares, M. (2004). *IGS Ionosphere WG Status Report: Performance of IGS Ionosphere TEC Map*. Technical report, IGS Workshop, Bern, Switzerland.

Hernández-Pajares, M., Juan, J. M., & Sanz, J. (1999). New approaches in global ionospheric determination using ground GPS data. *Journal of Atmospheric and Terrestrial Physics*, 61, 1237–1247.

Hernández-Pajares, M., Juan, J. M., & Sanz, J. (2000). Improving the Abel inversion by adding ground GPS data to LEO radio occultations in ionospheric sounding. *Geophysical Research Letters*, 27, 2473–2476. 10.1029/2000GL000032.

Hernández-Pajares, M., Juan, J. M., & Sanz, J. (2006). Medium-scale traveling ionospheric disturbances affecting GPS measurements: Spatial and temporal analysis. *Journal of Geophysical Research*, 111(A07S11). doi:10.1029/2005JA011474.

Hernández-Pajares, M., Juan, J. M., Sanz, J., & Orús, R. (2007). Second-order ionospheric term in GPS: Implementation and impact on geodetic estimates. *Journal of Geophysical Research*, 112(B08417). doi:10.1029/2006JB004707.

Hobiger, T. (2003). Die Ionosphäre. Lecture notes (in German), Institute of Geodesy and Geophysics, Vienna University of Technology.

Hobiger, T. (2005). *VLBI as a tool to probe the ionosphere*, volume 75 of *Geowissenschaftliche Mitteilungen*. Veröffentlichung des Instituts für Geodäsie und Geophysik, TU Wien. ISSN 1811-8380.

Hobiger, T., Kondo, K., & Schuh, H. (2006). Very long baseline interferometry as a tool to probe the ionosphere. *Radio Science*, 41(RS1006). doi:10.1029/2005RS003297.

Hofmann-Wellenhof, B., Lichtenegger, H., & Collins, J. (2001). *Global Positioning System (GPS). Theory and practice.* Wien, NY: Springer.

Hugentobler, U., Meindl, M., Beutler, G., Bock, H., Dach, R., Jäggi, A., Urschl, C., Mervart, L., Rothacher, M., Schaer, S., Brockmann, E., Ineichen, D., Wiget, A., Wild, U., Weber, G., Habrich, H., & Boucher, C. (2006). CODE IGS Analysis Center Technical Report 2003/2004. In K. Gowey & et al. (Eds.), *IGS 2004 Technical Reports.* Jet Propulsion Laboratory, Pasadena, California, USA: IGS Central Bureau.

Hwang, C., Shum, C. K., & Li, J., Eds. (2004). *Satellite Altimetry for Geodesy, Geophysics and Oceanography*, volume 126 of *International Association of Geodesy Symposia.* Springer: Proceedings of the International Workshop on Satellite Altimetry, a joint workshop of IAG Section III Special Study Group SSG3.186 and IAG Section II, September 8-13, 2002, Wuhan, China. ISBN 978-3-540-20211-0.

ICD (2002). Global Navigation Satellite System (GLONASS): Interface Control Document (version 5.0). Coordination Scientific Information Center, Moscow. `http://www.glonass-ianc.rsa.ru`.

IDS (2007). International DORIS Service. `http://ids.cls.fr`.

IGRF (2007). International Geomagnetic Reference Field. World Data Center for Geomagnetism, Kyoto. `http://swdcwww.kugi.kyoto-u.ac.jp/index.html`.

IGS (2007). International GNSS Service. `http://igscb.jpl.nasa.gov`.

Imel, D. A. (1994). Evaluation of the TOPEX/POSEIDON dual-frequency ionosphere correction. *Journal of Geophysical Research*, 99(12), 24895–24906.

ITRF (2007). International Terrestrial Reference Frame. `http://itrf.ensg.ign.fr`.

IVS (2007). International VLBI Service for Geodesy and Astrometry. `http://ivscc.gsfc.nasa.gov`.

Jakowski, N., Hocke, S., Schlüter, S., & Heise, S. (1999). Space weather effects detected by GPS based TEC monitoring. In *Proceedings of the Workshop on Space Weather, ESTEC, Noordwijk, WPP-155* (pp. 241–244).

Jakowski, N., Leitinger, R., & Angling, M. (2004). Radio occultation techniques for probing the ionosphere. *Annals of Geophysics*, Supplement to Vol. 47(2/3).

Kelley, M. C. (1989). *The Earth's ionosphere: plasma physics and electrodynamics*, volume 43 of *International Geophysics Series.* Academic Press (San Diego). ISBN 0-12-404012-8.

Kleusberg, A. & Teunissen, P. J. G. (1996). *GPS for geodesy.* Berlin ; New York : Springer, c1996.

Koch, K. R. (1999). *Parameter Estimation and Hypothesis Testing in Linear Models.* Springer, 2 edition. ISBN 978-3-540-65257-1.

Mainul Hoque, M. & Jakowski, N. (2007). Higher order ionospheric effects in precise GNSS positioning . *Journal of Geodesy*, 81(4), 259–268.

Mannucci, A. J., Wilson, B. D., Yuan, D. N., Ho, C. H., Lindqwister, U. J., & Runge, T. F. (1998). A global mapping technique for GPS-derived ionospheric total electron content measurements. *Radio Science*, 33, 565–582. doi:10.1029/97RS02707.

Meza, A. M. (1999). *Three dimensional ionospheric models from earth and space based GPS observations*. PhD thesis, Universidad Nacional de La Plata, Argentina.

NSO (2007). National Solar Observatory. Tucson, Arizona. `http://www.nso.edu`.

Orús, R., Hernández-Pajares, M., Juan, J. M., & Sanz, J. (2003). Validation of the GPS TEC maps with TOPEX data. *Advances in Space Research*, 31(3), 621–627.

Ratcliffe, J. A. (1972). *An introduction to the ionosphere and magnetosphere*. Cambridge University Press. ISBN 0-521-08341-9.

Rawer, K., Ed. (1984). *Encyclopedia of Physics*, chapter Geophysics III, Part VII, (pp. 389–391). Springer-Verlag.

Revnivykh, S. (2005). GLONASS: Status and Perspectives. presented at Munich Satellite Navigation Summit 2005, 9 March, 2005, Munich, Germany.

Ruffini, G., Flores, A., & Rius, A. (2002). GPS tomography of the ionospheric electron content with a correlation functional. *IEEE Transactions on Geoscience and Remote Sensing*, 36(1), 143–153.

Russian Space Web (2007). GLONASS network. `http://www.russianspaceweb.com/uragan.html`.

Schaer, S. (1999). *Mapping and predicting the Earths ionosphere using the Global Positioning System*. PhD thesis, Bern University, Switzerland.

Schaer, S., Beutler, G., Mervart, L., Rothacher, M., & Wild, U. (1995). Global and regional ionosphere modeling using the GPS double difference phase observable. In G. Gendt & G. Dick (Eds.), *Proceedings of the IGS Workshop on special topics and new directions* (pp. 77–92). GFZ, Potsdam, Germany.

Schaer, S., Beutler, G., Rothacher, M., & Springer, T. A. (1996). Global Ionosphere Maps Based on GPS Carrier Phase Data Routinely Produced by the CODE Analysis Center. In *Proceedings of the IGS AC Workshop, Silver Spring MD, U.S.A.*

Schaer, S., Gurtner, W., & Feltens, J. (1998). IONEX: The IONosphere map eXchange format version 1. In J. M. Dow, J. Kouba, & T. Springer (Eds.), *Proceeding of the IGS AC Workshop* (pp. 233–247). Darmstadt, Germany.

Schmidt, M. (2007). Wavelet modelling in support of IRI . *Advances in Space Research*, 39(5), 932–940. doi:10.1016/j.asr.2006.09.030.

Schmidt, M., Shum, C., Bilitza, D., Zeilhofer, C., Potts, L., Ge, S., & Karslioglu, M. (2006). Regional multi-resolution representation of the ionospheric electron density. presented at EGU 2006, Vienna, Austria.

Schreiner, W., Rocken, C., Sokolovskiy, S., Syndergaard, S., & Hunt, D. (2007). Estimates of the precision of GPS radio occultations from the COSMIC/FORMOSAT-3 mission. *Geophysical Research Letters*, 34(4), 4808–+. doi:10.1029/2006GL027557.

Seeber, G. (1993). *Satellite geodesy.* de Gruyter, Berlin; New York. ISBN 3-11-012753-9.

SOPAC (2007). Scripps Orbit and Permanent Array Center: Garner GNSS archive. `ftp://garner.ucsd.edu/rinex`.

Sparks, L., Iijima, B. A., Mannucci, A. J., Pi, X., & Wilson, B. D. (2000). A new model for retrieving slant TEC corrections for wide area differential GPS. In *2000: Navigating into the New Millennium; Proceedings of the Institute of Navigation National Technical Meeting, Anaheim, CA; UNITED STATES; 26-28 Jan. 2000* (pp. 464–473).

SPDIR (2007). Space Physics Interactive Data Resource. National Geophysical Data Center (NGDC), Colorado, USA. `http://spidr.ngdc.noaa.gov`.

Syndegaard, S. (2000). On the ionosphere calibration in GPS radio occultation measurements. *Radio Science*, 35(3), 865–883.

Tavernier, G., Fagard, H., Feissel-Vernierc, M., Lemoine, F., Noll, C., Ries, J., Soudarin, L., & Willis, P. (2005). The International DORIS Service. *Advances in Space Research*, 36(3), 333–341. doi:10.1016/j.asr.2005.03.102.

Tavernier, G., Granier, J., Jayles, C., Sengenes, P., & Rozo, F. (2007). DORIS: New DIODE navigator and beacon network developments. Cnes, France. `http://www.jason.oceanobs.com/html/kiosque/newsletter/news9/tavernier_uk.html`.

Tiberius, C. & de Jong, K. (2002). Developments in Global Navigation Satellite Systems. *Hydrographic Society Journal*, 104. `http://www.hydrographicsociety.org/Articles/journal/2002/104-1.htm`.

Todorova, S. (2003). Regional ionosphere modelling with GPS and comparison with other techniques. Master's thesis, Institute of Geodesy and Geophysics, Vienna University of Technology.

Todorova, S., Hobiger, T., & Schuh, H. (2007a). Using the Global Navigation Satellite System and Satellite Altimetry for combined Global Ionosphere Maps. *Advances in Space Research*, in print. doi:10.1016/j.asr.2007.08.024.

Todorova, S., Schuh, H., Hobiger, T., & Hernández-Pajares, M. (2007b). Global models of the ionosphere obtained by integration of GNSS and satellite altimetry data. *Österreichische Zeitschrift für Vermessung und Geoinformation (VGI) Special Issue - Austrian Contributions to IUGG 2007, Perugia, Italy*, 2, 80–89.

Tolman, B., Harris, R. B., T., G., Munton, D., Little, J., R., M., Nelsen, S., & Renfro, B. (2004). The GPS Toolkit: Open Source GPS Software. In *Proceedings of the 16th International Technical Meeting of the Satellite Division of the Institute of Navigation* Long Beach, California.

UCAR (2007). University Corporation for Atmospheric Research. `http://www.ucar.edu`.

Wasle, E. (2007). *GNSS: GPS, GLONASS, Galileo & more*. PhD thesis, Graz University of Technology.

Weber, R. & Springer, T. A. (2001). The international GLONASS experiment: products, progress and prospects. *Journal of Geodesy*, 75(11), 559–568. doi:10.1007/s001900100199.

Wickert, J., Schmidt, T., Beyerle, G., Michalak, G., König, R., S., H., & Reigber, C. (2006). GPS Radio Occultation with CHAMP and GRACE: Recent Results. In G. K. Ulrich Foelsche & A. Steiner (Eds.), *Atmosphere and Climate Studies by Occultation Methods* chapter 1, (pp. 3–16). Verlag Springer Berlin Heidelberg. ISBN 978-3-540-34116-1 (Print) 978-3-540-34121-5 (Online).

Wooden, W. H. (1984). NAVSTAR Global Positioning System overview. In *Proceedings of the pacific congress on marine technology, Honolulu, Hawaii, April 24-27, 1984* (pp. OST3/10).

Acknowledgements

Curriculum vitae

Name:	Sonya Todorova
E-mail:	stodo@mars.hg.tuwien.ac.at
Date of birth:	June 23, 1979
Place of birth:	Sofia, Bulgaria
Nationality:	Bulgaria

Education

10/2004 - 4/2008	Vienna University of Technology, Doctoral Programme
3/2003 - 10/2003	Vienna University of Technology, research for the MA thesis "Regional ionosphere modelling with GPS and comparison with other techniques"
1998 - 2004	University of Architecture, Civil Engineering and Geodesy (UACG), Sofia Study of Geodesy with specialisation in Advanced Geodesy, graduated with distinction on January 23, 2004
1993 - 1998	German language secondary school "Tsar Ivan Asen II", Sofia

Employment

3/2007 - 2/2008	Scientific research assistant in the FWF-Project "Combination of space geodetic techniques for integrated ionosphere models (COMBION)"
4/2004 - 10/2004 7/2003 - 10/2003	Participant in the FWF-Project "Investigation of the Ionosphere by geodetic VLBI (VLBIonos)"
9/2002 - 12/2002	Construction company "Rumen Vatkov", Sofia, assistant geodesist
2001 - 2002	Participant in the Project "Complex research of the actual geodynamics of South-West Bulgaria" of the UACG and the Bulgarian Academy of Science

Scholarships

10/2004 - 12/2006	Bertha von Suttner-Scholarship for doctoral study financed by BMBWK
3/2003 - 7/2003	Erasmus Scholarship
2001	Student of distinction scholarship, UACG, Sofia

GEOWISSENSCHAFTLICHE MITTEILUNGEN

Bisher erschienen:

Heft 1   Kolloquium der Assistenten der Studienrichtung Vermessungswesen. 1970 - 1973, Dezember 1973.

Heft 2   EGGER-PERDICH-PLACH-WAGENSOMMERER, Taschenrechner HP 45 und HP 65, Programme und Anwendungen im Vermessungswesen. 1. Auflage, März 1974, Special Edition in English, Juli 1974, 2. verbesserte Auflage, November 1974.

Heft 3   Kolloquium der Assistenten der Studienrichtung Vermessungswesen 1973 - 1974, September 1974.

Heft 4   EGGER-PALFINGER-PERDICH-PLACH-WAGENSOMMERER,   Tektronix-Tischrechner TEK 31, Programmbibliothek für den Einsatz im Vermessungswesen, November 1974.

Heft 5   K.LEDERSTEGER, Die horizontale Isostasie und das isostatische Geoid, Februar 1975.

Heft 6   F.REINHART, Katalog von FK4 Horrebow-Paaren für Breiten von +30 bis +60, Oktober 1975.

Heft 7   Arbeiten aus dem Institut für Höhere Geodäsie, Wien, Dezember 1975.

Heft 8   Veröffentlichungen des Instituts für Photogrammetrie zum XIII. Internationalen Kongreß für Photogrammetrie in Helsinki 1976, Wien, Juli 1976.

Heft 9   W.PILLEWIZER, Felsdarstellung aus Orthophotos, Wien, Juni 1976.

Heft 10   PERDICH-PLACH-WAGENSOMMERER, Der Einsatz des programmierbaren Taschenrechners Texas Instruments SR-52 mit Drucker PC100 in ingenieurgeodätischen Rechentechnik, Wien, Mai 1976.

Heft 11   Kolloquium der Assistenten der Studienrichtung Vermessungswesen 1974 - 1976, November 1976.

Heft 12   Kartographische Vorträge der Geodätischen Informationstage 1976, Wien, Mai 1977.

Heft 13   Veröffentlichung des Instituts für Photogrammetrie anläßlich des 80. Geburtstages von Prof.Dr.h.c.K.Neumaier, Wien, Januar 1978.

Heft 14   L.MOLNAR, Self Checking Analytical Relative Orientation and Strip Formation, Wien, Dezember 1978.

Heft 15   Veröffentlichung des Instituts für Landesvermessung anläßlich des 80. Geburtstages von Prof.Dr.Alois Bavir, Wien, Januar 1979.

Heft 16   Kolloquium der Assistenten der Studienrichtung Vermessungswesen 1976 - 1978, Wien, November 1979.

Heft 17   E.VOZIKIS, Die photographische Differentialumbildung gekrümmter Flächen mit Beispielen aus der Architekturbildmessung, Wien, Dezember 1979.

Heft 18   Veröffentlichung des Instituts für Allgemeine Geodäsie anläßlich des 75. Geburtstages von Prof.Dipl.Ing.Dr.F.Hauer, Die Höhe des Großglockners, Wien, 1981.

Heft 19   H.KAGER, Bündeltriangulation mit indirekt beobachteten Kreiszentren, Wien, April 1981.

Heft 20   Kartrographische Vorträge der Geodätischen Informationstage 1980, Wien, Mai 1982.

Heft 21   Veröffentlichung des Instituts für Kartographie anläßlich des 70. Geburtstages von Prof.Dr.Wolfgang Pillewizer: Glaziologie und Kartographie, Wien, Dezember 1982.

Heft 22   K.TEMPFLI, Genauigkeitsschätzung digitaler Höhenmodelle mittels Spektralanalyse, Wien, Mai 1982.

Heft 23   E.CSAPLOVICS, Interpretation von Farbinfrarotbildern, Wien, November 1982.

Heft 24   J.JANSA, Rektifizierung von Multispektral-Scanneraufnahmen - Entwicklung und Erprobung eines EDV-Programms, Wien, Mai 1983.

Heft 25   Zusammenfassung der Diplomarbeiten, Dissertationen und Habilitationen an den geodätischen Instituten der TU Wien, Wien, November 1984.

Heft 26   T.WUNDERLICH, Die voraussetzungsfreie Bestimmung von Refraktionswinkeln, Wien, August 1985.

Heft 27   G.GERSTBACH (Hrsg.), Geowissenschaftliche/geotechnische Daten in Landinformationssystemen - Bedarf und Möglichkeiten in Österreich, Juni 1986.

Heft 28   K.NOVAK, Orientierung von Amateuraufnahmen ohne Paßpunkte, Wien, August 1986.

Heft 29   Veröffentlichung des Instituts für Landesvermessung und Ingenieurgeodäsie, Abt. Ingenieurgeodäsie, anläßlich des 80. Geburtstages von Prof.Dipl.Ing.Dr.F.Hauer, Wien, Oktober 1986.

Heft 30   K.-H.ROCH, Über die Bedeutung dynamisch ermittelter Parameter für die Bestimmung von Gesteins- und Gebirgseigenschaften, Wien, Februar 1987.

Heft 31   G. HE, Bildverbesserung mittels digitaler Filterung, Wien, April 1989.

Heft 32   F.SCHLÖGELHOFER, Qualitäts- und Wirtschaftlichkeitsmodelle für die Ingenieurphotogrammetrie, Wien, April 1989.

Heft 33   G.GERSTBACH (Hrsg.), Geowissenschaftliche/geotechnische Daten in Landinformationssystemen - Datenbestände und Datenaustausch in Österreich, Wien, Juni 1989.

Heft 34   F.HOCHSTÖGER, Ein Beitrag zur Anwendung und Visualisierung digitaler Geländemodelle, Wien, Dezember 1989.

Heft 35 R.WEBER, Lokale Schwerefeldmodellierung unter Berücksichtigung spektraler Methoden zur Geländereduktion, Wien, April 1990.

Heft 36 o.Prof.Dr.Hans Schmid zum 70. Geburtstag. Veröffentlichung der Abteilung für Landesvermessung, Wien, Oktober 1990.

Heft 37 G.GERSTBACH, H.P.HÖLLRIEGL und R.WEBER, Geowissenschaftliche Informationsbörse - Eine Nachlese zu GeoLIS II, Wien, Oktober 1990.

Heft 38 R.ECKER, Rastergraphische Visualisierungen mittels digitaler Geländemodelle, Wien, August 1991.

Heft 39 Kartographische Forschungen und Anwendungsorientierte Entwicklungen, herausgegeben von W.Stams und F.Kelnhofer zum 80. Geburtstag von Prof.Dr.W.Pillewizer, Wien, Juli 1991.

Heft 39a W.RIEGER, Hydrologische Anwendungen des digitalen Geländemodelles, Wien, Juli 1992.

Heft 40 K.STEINNOCHER, Methodische Erweiterungen der Landnutzungsklassifikation und Implementierung auf einem Transputernetzwerk, Wien, Juli 1994.

Heft 41 G.FORKERT, Die Lösung photogrammetrischer Orientierungs- und Rekonstruktionsaufgaben mittels allgemeiner kurvenförmiger Elemente, Wien, Juli 1994.

Heft 42 M.SCHÖNER, W.SCHÖNER, Photogrammetrische und glaziologische Untersuchungen am Gàsbre (Ergebnisse der Spitzbergenexpedition 1991), Wien, Mai 1996.

Heft 43 M.ROIC. Erfassung von nicht signalisierten 3D-Strukturen mit Videotheodoliten, Wien, April 1996.

Heft 44 G.RETSCHER, 3D-Gleiserfassung mit einem Multisensorsystem und linearen Filterverfahren, Wien, April 1996.

Heft 45 W.DAXINGER, Astrogravimetrische Geoidbestimmung für Ingenieurprojekte, Wien, Juli 1996.

Heft 46 M.PLONER, CCD-Astrometrie von Objekten des geostationären Ringes, Wien, November 1996.

Heft 47 Zum Gedenken an Karl Killian "Ingenieur" und "Geodät" 1903-1991, Veröffentlichung der Fachgruppe Geowissenschaften, Wien, Februar 1997.

Heft 48 A.SINDHUBER, Ergänzung und Fortführung eines digitalen Landschaftsmodelles mit multispektralen und hochauflösenden Fernerkundungsaufnahmen, Wien, Mai 1998.

Heft 49 W.WAGNER, Soil Moisture Retrieval from ERS Scatterometer Data, Wien, Dezember 1998.

Heft 50   R.WEBER, E.FRAGNER (Editoren),Prof.Bretterbauer, Festschrift zum 70.Geburtstag, Wien, Juli 1999.

Heft 51   Ch.ÖHRENEDER, A Similarity Measure for Global Image Matching Based on The Forward Modeling Principle, Wien, April 1999.

Heft 52   M.LECHTHALER, G.GARTNER, Per Aspera ad Astra, Festschrift für Fritz Kelnhofer zum 60. Geburtstag, Wien, Jänner 2000.

Heft 53   F.KELNHOFER, M.LECHTHALER, Interaktive Karten (Atlanten) und Multimedia – Applikationen, Wien, März 2000.

Heft 54   A.MISCHKE, Entwicklung eines Videotheodlit-Meßsystems zur automatischen Richtungsmessung von nicht signalisierten Objektpunkten, Wien, Mai 2000

Heft 55   Veröffentlichung des I.P.F. anlässlich der Emeritierung von Prof.Dr. Peter Waldhäusl, Wien.

Heft 56   F.ROTTENSTEINER, Semi-automatic Extraction of Buildings Based on Hybrid Adjustment Using 3D Surface Models and Management of Building Data in a TIS, Wien, Juni 2001.

Heft 57   D.LEGENSTEIN, Objektrekonstruktion aus perspektiven Bildern unter Einbeziehung von Umrisslinien, Wien, Mai 2001.

Heft 58   F.KELNHOFER, M.LECHTHALER und K.BRUNNER (Hrsg.), Telekartographie und Location Based Services, Wien, Jänner 2002.

Heft 59   K.BRETTERBAUER, Die runde Erde eben dargestellt: Abbildungslehre und sphärische Kartennetzentwürfe, Wien, 2002.

Heft 60   G.GARTNER, Maps and the Internet 2002, Wien 2002.

Heft 61   L.DORFFNER, Erzeugung von qualitativ hochwertigen 3D Photomodellen für Internetbasierte Anwendungen mit besonderem Augenmerk auf Objekte der Nahbereichsphotogrammetrie, Wien, Jänner 2002.

Heft 62   CHMELINA, Wissensbasierte Analyse von Verschiebungsdaten im Tunnelbau Wien 2002

Heft 63   A.NIESSNER, Qualitative Deformationsanalase unter Ausnutzung der Farbinformation, Wien 2002

Heft 64   K.BRETTERBAUER; R.WEBER, A Primer of Geodesy for GIS-Users, Wien im Herbst 2003

Heft 65   N.PFEIFER, 3D Terain Models on the basis of a triangulation, Wien, Jänner 2002.

Heft 66   G.GARTNER (Hrsg), Lacation Based Services & Telecartography, Wien, 2004

Heft 67 I.KABASHI, Gleichzeitig-gegenseitige Zenitwinkelmessung über größere Entfernungen mit automatischen Zielsystemen, Wien, 2004

Heft 68 J.BÖHM, Troposphärische Laufzeitverzögerungen in der VLBI, Wien 2004

Heft 69 R.WEBER, W.SCHLÜTER, U.SCHREIBER, O. TITOV Evolving Space Geodesy Techniques (EGS XXVII General Assembly, Nice, France, 2002), Wien 2004

Heft 70 G. WEINWURM, Amalthea's Gravity Field and its Impact on a Spacecraft Trajectory, Wien 2004

Heft 71 Forschungsgruppe Ingenieurgeodäsie, Festschrift anlässlich des 65. Geburtstages von Herrn o.Univ.Prof.Dr.-Ing. Heribert Kahmen, Wien 2005

Heft 72 A. REITERER, A Knowledge-Based Decision System for an On-Line Video-Theodolite-Based Multisensor System, Wien 2005

Heft 73 M. HABERLER, Einsatz von Fuzzy Methoden zur Detektion konsistenter Punktbewegungen, Wien 2005

Heft 74 G. GARTNER, Location Based Services & Telecartography, Proceedings of the Symposium 2005, Wien 2005

Heft 75 Th. HOBIGER, VLBI as a tool to probe the ionosphere, Wien 2006

Heft 76 E. KLAFFENBÖCK, Troposphärische Laufzeitverzögerung von GNSS-Signalen – Nutzen aktiver Referenzstationsnetze für die Meteorologie, Wien 2006

Heft 76a P.J. MENDES-CERVEIRA, Tidal and non-tidal contributions to surface loading processes on station coordinates, Wien 2006

Heft 78 G. KOSTOV, G. BOURDA, L. FERNANDEZ, T. KONDO, Research Projects at IGG Reports, Wien 2007

Heft 79 J. BÖHM, A. PANY, H. SCHUH (Editors), Proceedings of the 18th European VLBI for Geodesy and Astrometry Working Meeting, 12-13 April 2007, Wien 2007

Heft 80 J. BÖHM, Tropospheric Delay Modelling at Radio Wavelengths for Space Geodetic Techniques, Wien 2007

Heft 81 G. Retscher, Mobile Multi-sensor Systems for Personal Navigation and Location-based Services, Wien 2007

Heft 82 R. HEINKELMANN, Bestimmung des atmosphärischen Wasserdampfes mittels VLB als Beitrag zur Klimaforschung, Wien 2008

Heft 83 F. ROTTENSTEINER, Automatic extraction of buildings from airborne laserscanner data and aerial images, Wien 2008